City Research Online

City St George's, University of London

Citation: Dar, T. (2015). Numerical characterisation of label free optical biosensors. (Unpublished Doctoral thesis, City University London)

This is the accepted version of the paper.

This version of the publication may differ from the final published version. To cite this item please consult the publisher's version.

Permanent repository link: https://openaccess.city.ac.uk/id/eprint/13075/

Copyright and Reuse: Copyright and Moral Rights remain with the author(s) and/or copyright holders. Copies of full items can be used for personal research or study, educational, or not-for-profit purposes without prior permission or charge, unless otherwise indicated, provided that the authors, title and full bibliographic details are credited, a hyperlink and/or URL is given for the original metadata page and the content is not changed in any way. For full details of reuse please refer to City Research Online policy.

City Research Online: http://openaccess.city.ac.uk/ publications@citystgeorges.ac.uk

NUMERICAL CHARACTERISATION OF LABEL FREE OPTICAL BIOSENSORS

by

Tuffail Dar

A thesis submitted in fulfilment of requirements for the degree of Doctor of Philosophy at the School of Engineering and Mathematical Sciences

CITY UNIVERSITY LONDON

Northampton Square, London EC1V 0HB

United Kingdom

January 2015

CONTENTS

LIST OF FIGURES

LIST OF TABLES

LIST OF SYMBOLS AND ABBREVIATIONS

ACKNOWLEDGEMENTS

ABSTRACT

1. INTRODUCTION

1.1 Introduction 1

1.2 Aims and objectives 2

1.3 Structure of the thesis 3

2. LITERATURE REVIEW

2.1 Introduction of biosensor 7

2.2 Biosensor classification 9

2.3 Classification according to recognition element 10

2.4 Classification according to transducer 12

2.5 Types of sensing mechanisms 16

2.6 Optical biosensor architectures 21

2.7 Performance comparison 32

2.8 Label-based vs label-free detection 33

2.9 Biosensor applications 36

2.10 Characteristics of biosensors 36

2.11 Optical biosensor performance metrics 37

2.12 Immobilization of recognition receptors 43

2.13 Physical Adsorption 44

2.14 SAM (Self-assembled monolayers) 45

2.15 Covalent Immobilization 49

2.16 Non-covalent Immobilization 53

2.17 Physical Entrapment 54
2.18 Numerical Method Analysis 55
2.19 Numerical Approximation Solutions 56
2.20 Summary 61

3. METHODOLOGY

3.1 Introduction 62
3.2 Simulation tool and modeling parameters 62
3.3 Theoretical Background 63
3.3.1 Basic Equations 65
3.4 Variational Formulations 71
3.4.1 Scalar approximation 71
3.4.2 Vector formulations 72
3.4.3 Natural Boundary Conditions 74
3.5.1 Domain Discretisation 75
3.5.2 Shape Functions 76
3.5.3 Global and Element Matrices 82
3.5.4 Spurious Solution 86
3.6 Summary 88

4. METAL CLAD OPTICAL BIOSENSORS

4.1 Label-free detection of Escherichia Coli (*E.coli*) 89
4.1.1 Modal Solution 91
4.1.2 Sensor structure studied 93
4.1.3 Effective index variation 94
4.1.4 Modal field profile 96
4.1.5 Effect of coupling length 98
4.1.6 Sensing layer growth 99
4.1.7 Optimizing thickness of cladding 101
4.1.8 Effect of outer medium 106
4.1.9 Power in the *E.coli* region 107

4.2 Interaction of metal-clad fibre with sensing materials 108
4.3 Detection of acetone using metal-clad fibre sensor 113
4.4 Summary 118
5. NANOSTRUCTURE OPTICAL BIOSENSORS
5.1 Mach-Zehnder based nanowire biosensor 119
5.2 Mach–Zehnder based sensor structure 120
5.2.1 Modal Solution 121
5.2.2 Effective Index Variation 122
5.2.3 Power confinement 125
5.2.4 Effect of thickness 126
5.2.5 Sensitivity 127
5.3 Slot-waveguide biosensor for DNA hybridisation detection 130
5.3.1 Slot waveguide structure 131
5.3.2 Modal solutions 132
5.3.3 Effective index variation 133
5.3.4 Sensitivity 135
5.3.5 Sensor Detection Limit 144
5.3.6 Power confinement 145
5.4 Simulation results for non-vertical sidewall slot waveguide 150
5.5 Summary 160
6. CONCLUSION AND FUTURE WORK
6.1 Conclusion 162
6.2 Future work 167
APPENDICES 169
BIBLIOGRAPHY 191

LIST OF FIGURES

Figure 2.1: Schematic of a biosensor setup **7**

Figure 2.2: Size of bio-recognition elements **9**

Figure 2.3: Classification of biosensors **9**

Figure 2.4 (a) Scheme representing evanescent field sensing. **(b)** A cross section of a silicon photonic waveguide and the optical electric field distribution of the vertically polarized mode are shown. **(c)** Cross-sectional plot of the evanescent field intensity of optical waveguide. **19**

Figure 2.5 (a) Limited evanescent field of the conventional evanescent field sensors of 250 nm **(b)** Increase in evanescent field of the deep-probe evanescent field biosensor of 1μm **21**

Figure 2.6 The changes in the refractive index in the immediate vicinity of a surface layer are detected with a sensor chip. The plasmonic resonance is observed as a sharp shadow in the reflected light at an angle that depends on the mass of material at the surface – this angle shifts if biomolecules bind to the surface. **22**

Figure 2.6 (a) An evanescent wave corresponds to a TM-mode that propagates along the interface of a metal and a dielectric, where the z-component of the electric field decays exponentially **(b)** Spatial distribution of the magnetic intensity for a surface plasmon at the interface between metal and a dielectric **(c)** A combination of surface plasmons and waveguide modes is possible. **23**

Figure 2.7: Principle of SPR biosensing. **24**

Figure 2.8 SPR sensing structure based on a side-polished single-mode fibre. **26**

Figure 2.9 Scheme of an integrated Mach-Zehnder interferometer. **27**

Figure 2.10 (a) Schematic top view of the slot-waveguide based micro ring resonator (**b)** Cross sectional view of the slot-waveguide based micro ring resonator. **31**

Figure 2.11 Homogeneous sensing where analytes exist in the surrounding aqueous medium that serves as the top cladding. **40**

Figure 2.12 Surface sensing where analyte molecules adsorb on a sensor surface, which can be modelled as an ultrathin film. **41**

Figure 2.13 Schematic representation of functionalization of alkylthiolate self-assembly monolayer **47**

Figure 2.14 Schematic representation of functionalization of alkylsilane self-assembly monolayers **49**

Figure 2.15 Main strategies of chemical grafting; (1) direct reaction to active surface, (2) activation of the surface with homodifunctional linker, and (3) activation of the surface with heterodifunctional linker. **51**

Figure 2.16 Schematic representation of Streptavidin–Biotin immobilization **54**

Figure 3.1 Arbitrarily shaped optical waveguide, divided into arbitrary sub-domains, each having different type of material. **65**

Figure.3.2 Boundary between two media of refractive indices n_1 and n_2, where n, is the unit vector normal to the interface. **68**

Figure 3.3 Finite elements in two-dimension **75**

Figure 3.4 Finite element discretisation of a waveguide with triangular elements **76**

Figure 3.5 Pascal's triangle for complete polynomials in two dimensions **77**

Figure 3.6 Representation of a first order triangular element **78**

Figure 4.1 Schematic of the SPR structure studied **93**

Figure 4.2 Effective index variation with the refractive index of the outer medium, R4 for the inner and outer SPMs at the gold/cladding and the gold/outer medium interfaces respectively for a cladding thickness of R2 = 5,10µm **95**

Figure 4.3 Hx field profile along the y-axis and x-axis for the outer SPM **96**

Figure 4.4 Hx field profile of the outer SPM, R2=5µm **98**

Figure 4.5 Hx field profile of the outer SPM,R2=15µm **98**

Figure 4.6 Coupling length against outer medium refractive index for R4=2 µm **99**

Figure 4.7 Coupling length as a function of the thickness of the E coli region **100**

Figure 4.8 Propagation constant as a function of the thickness of the cladding **102**

Figure 4.9 Variation of effective index with the thickness of cladding **103**

Figure 4.10 Coupling length as a function of the cladding thickness with and without E.coli for an outer medium index, R4 of 1.449 **104**

Figure 4.11 Attenuation constant variation with the cladding thickness R2 for the even and the odd SPMs. **105**

Figure 4.12 Effective index as a function of the outer medium index for the Fibre Mode and (SPM) surface plasmon mode for an outer medium thickness of R4 = 2 & 3µm and cladding thickness, R2 = 5µm. **106**

Figure 4.13 Percentage of power in the E.Coli (R5) region as a function of cladding thickness for different outer medium refractive indices **107**

Figure 4.14 Schematic of the Metal-clad fiber structure **108**

Figure 4.15 Inner radially polarized surface plasmon mode at D = 6 µm. **109**

Figure 4.16 Outer radially polarized surface plasmon mode at D = 6µm and ns = 1.34. **109**

Figure 4.17 Effective index with surrounding medium (n_s) refractive index. **110**

Figure 4.18 Attenuation with surrounding refractive index. **111**

Figure 4.19 Percentage Power with surrounding medium (n_s) refractive index **112**

Figure 4.20 Hx field profiles along the y-axis with metal thickness for acetone in the outer cladding. **114**

Figure 4.21 Effective index variation with metal thickness for D = 6 µm. **115**

Figure 4.22 Modal loss with metal thickness for D = 6 µm. **116**

Figure 4.23 Percentage power in acetone with metal thickness for D = 6 µm. **117**

Figure 5.1 Schematic diagram of (a) the proposed sensor and (b) the cross section view of the composite waveguide, with a specimen layer. **120**

Figure 5.2 (a) 3-D field profile of the Hx mode for the reference and the sensing arm for D = 400 nm **121**

Figure 5.3 Hx along the x axis for a fiber diameter of D = 150 nm. **122**

Figure 5.4 Effective index (n_e) and effective index difference (Δn_{eff}) between the reference and sensing arms as a function of the fiber diameter (D). **123**

Figure 5.5 Change in effective index (ne) and effective index difference (Δn_{eff}) as a function of the wavelength (λ) **124**

Figure 5.6 Power fraction in aqueous solution for the sensing and the reference arms as a function of the fiber diameter (D). **125**

Figure 5.7 Power fraction for the sensing arm as a function of wavelength for a fibre diameter of D = 400 nm **126**

Figure 5.8 Change in propagation constant (β) and power fraction in the E.coli with the variation of the E.coli thickness. **127**

Figure 5.9 Variation of effective index difference, Δn_{eff} and waveguide sensitivity with D (nm) **128**

Figure 5.10a Sensitivity of the sensor as a function of the wavelength **129**

Figure 5.10b Combined power as a function of wavelength, λ (nm) **130**

Figure 5.11 Slot Waveguide Biosensor **132**

Figure 5.12 H_y field of the H_y11 mode **133**

Figure 5.13 H_y Contour of H_y11 mode **133**

Figure 5.14 Variations of the effective index, n_{eff}, with the Slot width for TE Mode **134**

Figure 5.15 Variation of effective index difference, Δn_{eff} and waveguide sensitivity with guide width **136**

Figure 5.16 Variation of effective index difference, Δn_{eff} and waveguide sensitivity with slot width **137**

Figure 5.17 Variation of effective index difference, Δn_{eff} and waveguide sensitivity with guide height **138**

Figure 5.18 Variation of Effective index, n_e with RI **139**

Figure 5.19 Variation of effective index with wavelength **141**

Figure 5.20 Variation of wavelength shift with slot width **142**

Figure 5.21 Variation of wavelength shift with guide width **142**

Figure 5.22 (a) Power confinement factor in ssDNA layer **145**

Figure 5.22 (b) Power confinement factor in dsDNA layer **146**

Figure 5.23 Variation of power density in DNA layer with the slot width for TE mode **147**

Figure 5.24 Variation of power density in DNA layer with the guide width for TE mode **148**

Figure 5.25 Variation of power density in DNA layer with the guide height for TE mode **149**

Figure 5.26: Non-vertical sidewall slot waveguide biosensor **150**

Figure 5.27: H_Y Contour of H_Y11 mode **151**

Figure 5.28: Effective mode index and power confinement in a non-vertical slot waveguide with RI of dsDNA = 1.53 as function of W_{sl} (non-vertical sidewall variation) **152**

Figure 5.29: Effective mode index in a non-vertical slot waveguide with RI of dsDNA = 1.53 as function of slot width **153**

Figure 5.30: Sensitivity in a non-vertical and vertical slot waveguide as function of slot width **154**

Figure 5.31: Variation of power confinement in DNA layer with the guide height for TE mode **155**

Figure 5.32: Variation of waveguide sensitivity with guide height **156**

Figure 5.33: Variation of power confinement in DNA layer with the guide width for TE mode **157**

Figure 5.34: Variation of sensitivity in non-vertical and vertical sidewall structures with the guide width for TE mode **158**

Figure 5.35: Variation of power confinement in DNA layer with the variation of cladding refractive index for TE mode **159**

Figure 5.36 Variation of effective index and power confinement in DNA layer with non-vertical sidewall at an operating wavelength range from 1520 to 1600nm for TE mode. **159**

LIST OF TABLES

Table 2.1 Shows the specific interactions of biomolecules which are commonly used in biosensing devices to increase specificity and discriminate between different substances exist in the same environment **8**

Table 2.2 Overall sensitivity S of a sensor is listed based on two sensing mechanisms and two transducing schemes. **39**

Table 3.1: Modelling parameters of label-free optical biosensors **63**

LIST OF SYMBOLS AND ABBREVIATIONS

Symbol	Meaning
α	Waveguide loss
β	Propagation constant
λ	Wavelength
ε	Dielectric permittivity
μ	Dielectric permeability
σ	Noise in the transduction signal
ϕ	Phase shift
ε'	Real part of complex dielectric permittivity
ε''	Imaginary part of complex dielectric permittivity
k_0	Free space wavenumber
n_e	Effective index
Δn_e	Effective index difference
$\alpha/k0$	Attenuation constant
n_g	Group index
S	Sensitivity
DL	Detection limit
S_z	Pointer vector along the z direction
L_c	Coupling length
BEM	Boundary Element Method
FEM	Finite Element Method
FDM	Finite Difference Method
SPM	Surface Plasmon Mode
SNR	Signal to Noise Ratio
TE	Transverse electric polarised mode
TM	Transverse magnetic polarised mode
VM	Variational Method

ACKNOWLEDGEMENTS

I take this opportunity to thank Almighty Allah for helping me to undertake and complete this research.

I would like to dedicate this thesis to my lovely parents, beloved wife, my brother, my sisters and my mother-in-law for their love and support throughout my life and encouraged all the way from start to completion of this research.

I am immensely indebted to my Supervisor Dr Muttukrishnan Rajarajan for his guidance and support over the years. Without his invaluable advice and wealth of knowledge this work wouldn't have been possible. It has been pleasure to be part of his Research Group. I would also like to thank Professor B.M.A Rahman who has guided and helped me in difficult times of this research work. I wouldn't forget City University London and School of Engineering and Mathematical Sciences in particular for providing excellent research facilities.

Several people have contributed in various ways without their support it would have been impossible to complete this research. I would also like to sincerely thank all my colleagues at the Photonics Research Group for maintaining a friendly and professional work atmosphere.

ABSTRACT

There is a significant need for the development and use of numerical methods to simulate advance and complex optical biosensor structures. Finite Element Method (FEM) has been established as one of the most powerful and versatile numerical method and has been implemented in this thesis to characterize, analyse and optimise label-free optical biosensors for the detection of micron size biological objects like bacteria such as *E.coli* and nanometre size biomolecules such as antibody, nucleic acids and proteins. These sensors are all suitable for deep-probe sensing as large evanescent field can be excited in the sensing medium with substantial penetration depth achieved by techniques like Surface Plasmon Resonance (SPR) and sensor architectures based on nanowires and slot waveguides.

This thesis presents three different architectures of label-free optical biosensors. First, a fiber optic surface plasmon resonance (SPR) biosensor for the detection of *E.Coli* is optically modeled by using the finite-element approach in conjunction with the perturbation technique which is computationally more efficient and can be used for waveguides with low or medium loss values. The same sensing architecture is used when surrounding index is varied from 1.30 -1.44 to cover most of the biological elements that are used in the biosensing applications. Second one is based on evanescent-wave guiding properties of nanowire waveguides a theoretical investigation of silica nanowires employing a wire assembled Mach-Zehnder structure to detect the presence of *E.Coli* is studied second. Finally, a slot-waveguide based micro-ring resonator is investigated for the detection of DNA Hybridization using H-field FEM based full-vector formulation. It is found that all of the numerical methods provide good agreement with the experimental sensitivities and detection limits.

1

INTRODUCTION

1.1 Introduction

Biosensors are increasingly becoming important bioanalytical tools in the biotechnology, pharmaceutical, food control, environmental monitoring and other consumer-oriented industries. The development of biosensors is one of the active areas of analytical research currently. With their high specificity, high sensitivity, portable size and low cost, biosensors hold considerable promise and potential for various analytical purposes.

Infectious disease remains one of the greatest challenges to global health. Today, infectious diseases cause 40% of all deaths worldwide (approximately 20 million deaths a year) [1]. Especially in many developing countries microbial diseases constitute the major causes of death. An estimated 1 million people suffer from food-borne illness each year in the UK. Food-borne illness costs the UK economy an estimated £2 billion each year [2]. Salmonella and *E.coli* are especially dangerous for humans and can cause death. It is extremely important to control the spreading of infectious diseases. In diagnosing and monitoring of infectious diseases molecular techniques has initiated a revolution. The molecular techniques can detect specific nucleic acids or microbial proteins directly in body fluids. Nucleic acid hybridization [3] is one such method which has potential for achieve high sensitivity, specificity, and detection of nucleic acids or proteins. Thus the important demands for a sensor for bacterial detection are high sensitivity and rapid detection.

Intensive research in developing biosensors for fast and sensitive detection has been conducted over several decades and has resulted in various techniques. Especially optical techniques have proven interesting for biosensing due to the possibility of rapid and direct (unlabelled) detection. The research in optical biosensors has resulted in a number of sensor devices which have been applied for biosensing and reported for detection of bacterial pathogens including surface plasmon resonance sensors [4] micro ring resonator sensor [5] and various interferometers [6]. These sensors give rapid and sensitive detection, however some of the sensors are only suitable for sensitive measurements of objects on a size scale up to 100 nm like DNA, proteins and viruses. The beneficial impact on society as a result of availability of such systems is immense therefore investigating any strategy that could reduce development times, costs and reveal alternative designs is of utmost importance. In particular, mathematical modelling and simulation is relatively inexpensive and yet powerful tool for scientific analysis and prediction.

1.2 Aims and objectives

The aim of this thesis is to develop numerical tools which can be used to model, design, and optimise optical biosensor devices at optical frequencies.

The developed numerical tools are applied to analyse the effects of various design parameters of optical biosensor devices such as diameter, metal thickness, biolayer thickness, slot width, guide width, guide height by varying and resolving the problem repeatedly, while an appropriate output metric such as effective index, sensitivity, detection limit, coupling length, power confinement is recorded.

The design and optimisation of optical biosensor devices based on micro and nanotechnology are difficult to fabricate and visualise due to their small size, arbitrary geometry and different scales. The way to design and optimise these complicated structures efficiently is to therefore

carry out numerical analysis, as an approximation to the exact solutions. Finite Element Method (FEM) is a versatile numerical technique that is found to be advantageous in these applications. Its success is mainly due to its versatility and flexible abilities in meshing which allowed its operation in different scales of length in an effective manner.

The developed numerical tools based on finite element formulation are successfully applied to design, characterize and optimise three optical biosensor structures based on metal-clad fibre, silica nanowire and slot-waveguide with a specific objective summarised as:

- To design, characterize and optimize the metal clad fibre biosensor based on surface plasmon resonance technique for detection of *E.*coli, acetone and refractive index range 1.30 -1.5 usually used in biosensing applications.
- To simulate a Mach-Zehnder silica nanowire biosensor for detection of nanometre size biological elements aimed towards achieving the higher sensitivity and improving the power confinement in the sensing area of the device.
- To use the numerical method for modelling, characterization and optimization of slot-waveguide biosensor for detection of DNA hybridisation with high sensitivity and better detection limit.

1.3 Structure of the thesis

The discussion given in this section provides an outline of the structure of the thesis. The work presented in this thesis is based on the research carried out by the author into the use of numerical methods for modelling and characterisation of label free biosensors. Beginning with a general introduction, the first chapter introduces the reader need for biosensor technology. Several key areas of application have been identified which have the potential to provide a significant enhancement of the areas of everyday application.

Chapter 2 provides a detailed insight into optical biosensing and immobilisation of biorecognition elements. The chapter begins with an introduction of optical biosensors and

the suitability of an optical biosensor for a particular application depends upon its performance across a variety of metrics. Furthermore discussion goes to optical biosensor methods, and immobilistaion of biorecognition elements onto optical surface. Based on this general introduction of optical biosensing the focus is aimed at optical biosensors for deep probe sensing.

The theoretical formulation of the Finite Element Method as a powerful numerical tool in analyzing optical biosensors is described in Chapter 3. First a brief overview of the numerical techniques commonly used in waveguide analysis is presented outlining their advantages and limitations in analysing any type of fibre and waveguide. A brief history of the finite element method is also presented focusing on their importance in analysing waveguide problems. The fundamental mathematical relations derived from Maxwell's equations for the application of this approach in the solution of waveguides is also derived. Further, a comparison of several variational formulations is presented with an emphasis on the vector H-field finite element formulation. The utilisation of triangular elements, the shape functions, and the infinite elements is undertaken in order to obtain the propagation constants and the field profiles of various modes supported by a uniform waveguide. The problem of spurious solutions is also investigated and the penalty function method is implemented to avoid the appearance of non-physical solutions.

In chapter 4 the metal-clad biosensors are presented. The metal-clad biosensors are evanescent wave sensors using surface plasmon resonance as sensing principle. Single mode operation of surface plasmon resonance based fibre optic biosensor design is numerically optimised for the maximum penetration of field in the sensing region using finite element based full-vectorial H-field formulation in conjunction with the perturbation technique. Practical metallic elements are not perfect conductors, but suffer a small amount of loss and therefore a rigorous model, which accounts for the modal loss is essential. Therefore H-field

FEM based full-vector formulation, in conjunction with the perturbation technique, has been used for the solution of the metal-clad waveguide modes. The alternative approaches such as classical Sommerfeld waveguiding principle to metal waveguides, 3-D time-harmonic simulation using the finite element method (FEM), FEM solution in terms of the transverse magnetic field H_t formulation and Finite-Difference Time-Domain (FDTD) are computationally very expensive and requires very large computational resources. The influence of the various parameters in the waveguide configurations will be discussed in connection with optimum sensitivity and detection ranges of the sensors. The effect of coupling length, modal confinement and modal loss are studied with and without the presence of *E.coli* for deep-probe sensing. By studying these parameters we search for the optimal design to obtain the best sensing performance in order to enhance the sensitivity and lower the detection limit.

Chapter 5 presents the nanostructure biosensors based on nanowire and slot waveguide structures. The finite element simulation presented here show the detailed dynamics of mode formation, change in mode effective refractive index, power confinement and sensitivity in nanometre scale guiding structures. The optical properties of silica nanowires in a Mach–Zehnder based optical sensor for detecting biomaterial specimens have been studied. Then we analyse the proposed slot waveguide micro ring resonator for the detection of DNA hybridisation. This structure takes advantage of the remarkable property of slot-waveguides to provide high optical intensity in a slot-region which is subwavelength size low refractive index region sandwiched between two high refractive index regions i.e. between two rails or strips. This permits a very high interaction between the slot-waveguide mode probe and a liquid analyte. As a result, the reported slot-waveguide sensor exhibited a bulk ambient sensitivity twice as large as that exhibited by ring resonator optical sensors based on conventional strip waveguides.

Finally in Chapter 6, general conclusions derived from this research work are summarized and explored further. Possible future prospects for this work are also suggested. The thesis concludes with a list of relevant publications in major international journals by the author followed by a list of references cited in this work.

2

LITERATURE REVIEW

2.1 Introduction of biosensor

A biosensor is defined by the International Union of Pure and Applied Chemistry (IUPAC) as a "detecting device that uses specific biochemical reactions mediated by isolated enzymes, immunosystems, tissues, organelles, or whole cells to detect chemical compounds by optical, electrical or thermal signals" [7].

The key component of a biosensor is a biological element, such as an antibody, a single stranded nucleic acid, an enzyme, a membrane receptor, or even a whole cell that form a recognition layer which is immobilised on the surface of a suitable transducer (Figure 2.1).

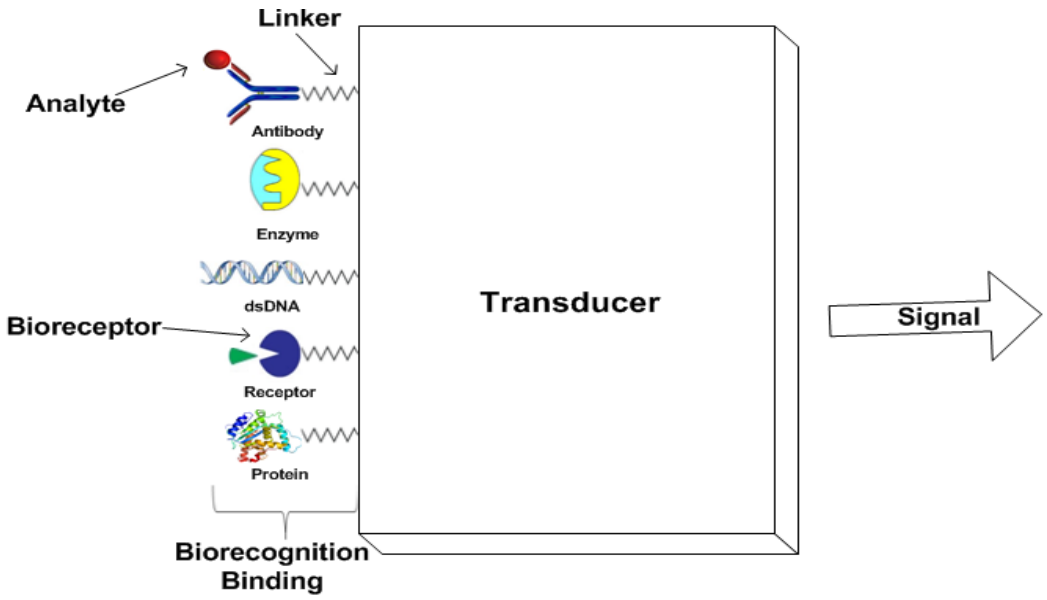

Figure 2.1: Schematic of a biosensor setup [8]

The biological elements are biological molecular species that utilizes a biochemical mechanism for recognition of bioanalytes. The biological element specifically recognizes the analyte in the sample generally via the formation of lock-and-key complexes such as enzyme-substrate, antigen-antibody, single stranded DNA-complementary DNA and so on (Table 2.1). When an analyte (target molecule) interacts with the immobilized biological element (bioreceptor molecules) on a biosensor surface a physical, chemical or biological change is observed [8]. This change is converted to a measurable signal by a detecting device which is called, a transducer.

Element	**Complementary**
Antibody	Antigen
Enzyme	Substrate
ssDNA	Complementary DNA
Carbohydrates	Receptors
Cells	Receptors
Drug	Receptors
Metal ions	Amino acids

Table 2.1: shows the specific molecular interactions which are commonly used in biosensing devices to increase specificity and discriminate between different substances exist in the sample [11].

A key issue in the development of any biosensor is to assure a high functional activity of the biological element immobilized on the transducer surface. The transducer surfaces are miniaturized to a micro or nanometre size scale (Figure 2.2) because of the small amount of biological element that can be deposited thereon.

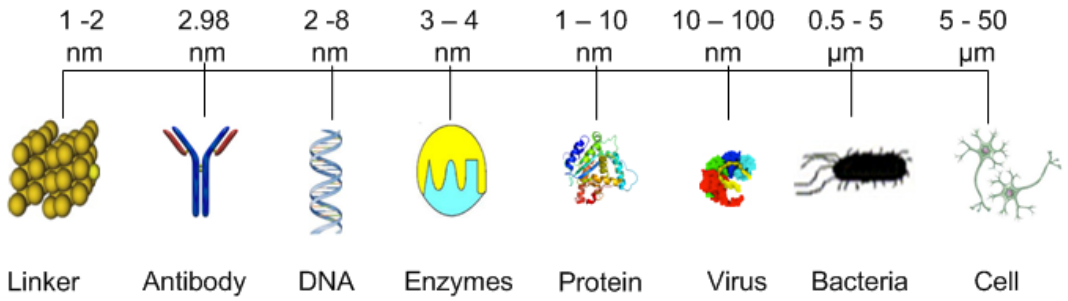

Figure 2.2: Size of biorecognition elements

Directly attaching the biological element to the sensor surface, although sometimes possible, is usually unwise because newly formed chemical linkages can affect the molecule's affinity for the analyte. A linker molecule is commonly used, one end of which has a moiety to anchor to the sensor surface, and the other has a carefully chosen functional group chosen to react with the biological element without damaging it [9, 10, 11, and 12].

2.2 Biosensor classification

Biosensors can be classified either according to their biorecognition element or operating principle of transducer as shown in the Figure 2.3.

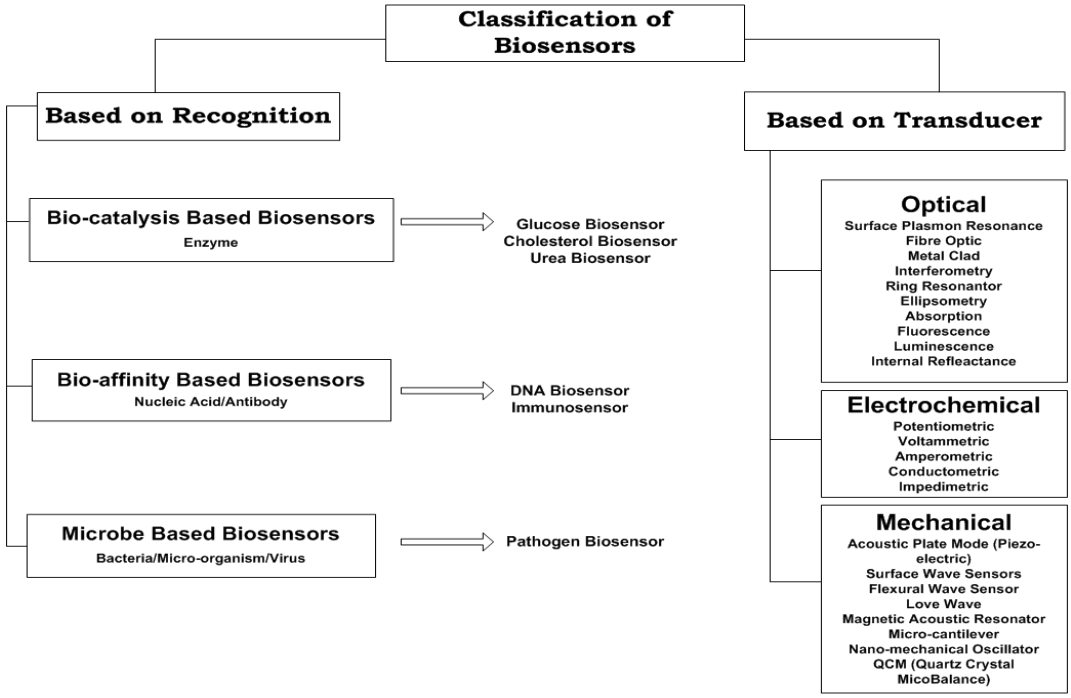

Figure 2.3: Classification of biosensors [13].

2.3 Classification of biosensors according to recognition element

Generally, there are three different biosensors groups classified based on the biorecognition element. The three groups are distinguished from one another by the nature of the process and in terms of their biological element, e.g. biocatalytic (i.e., enzyme), bioaffinity (i.e., antibody and nucleic acid) and microbial (i.e., bacteria, virus) as shown in the Figure 2.3.

i. Bio-catalysis based biosensors

These biosensors use enzymes as their biological element. Enzymes have the ability to specifically recognize to their substrates and to catalyse their transformation hence are proven to be efficient biocatalysts [14].

The bio-catalysis biosensors have two mechanisms of action for operation. The first action involves the catalytic conversion of the analyte by the enzyme. This action can be explained using the following equation:

$$\mathbf{S + E} \underset{k_{-1}}{\overset{k_1}{\longleftrightarrow}} \mathbf{ES} \xrightarrow{k_2} \mathbf{E + P} \qquad (2.1)$$

Where

S = Substrate

E = Enzyme

ES = Enzyme-substrate complex

P = Product

k_1 = Rate of enzyme-substrate complex formation

k_{-1} = Rate of enzyme-substrate complex dissociation

k_2 = Rate of dissociation of enzyme-substrate complex to products

The second mechanism involves detection using the inhibition of the enzymatic activity by the target analyte [14].

The detection limit of these biosensors is mainly determined by the enzyme's activity. However, the major limitation with enzyme-based biosensors is the stability of the enzyme which depends on various conditions such as the pH, ionic strength, chemical inhibitors, and temperature.

ii. Bio-affinity based biosensors

Bio-affinity biosensors use antibodies and nucleic acid as their biological elements and are also known as Immunosensor and DNA biosensor respectively.

The mechanism of action with Immunosensors is based on the ability of an antibody to form complexes with the corresponding antigen [15]. The antibody-antigen reaction is highly selective, and is analogous to a lock and key fit. Antibodies can be chemically conjugated to many different reporter molecules, and they can be coated onto many different surfaces. They can be raised against nearly any biological element, from single stranded (ss) DNA to protein. For these reasons, antibodies have long been an invaluable tool in research and diagnostics of biosensing applications [16]. Though these systems are more specific and sensitive than enzyme-based systems, they face limitations in that they are complex and require multi-step assay configurations [17].

DNA biosensors are made by immobilizing a single stranded DNA probes onto the transducer whose sequence is complementary to the target DNA strands. The detection of specific segments of nucleic acid by complementary probe sequences provides the basis for all nucleic acid probe based biosensors including those for infectious disease monitoring. The specificity of the interaction is dependent on the ability of different nucleotides only to form hydrogen bonds with the appropriate (complementary) partner [18].

iii. Microbe based biosensors

These biosensors utilize microorganisms as their biological element. Their mechanism is based either on the consumption of oxygen and carbon dioxide or the measurement of metabolism of the microorganism [19].

Microbial cells are cheaper than antibodies or enzymes [20]. They can be more stable, and can carry out several complex reactions involving enzymes. However, they are less selective than enzymes. They have longer recovery and response times, [20] and may require more frequent calibration.

2.4 Classification of biosensors according to transducer

Based on the kind of signal or parameter the biological event creates or alters is measured by the transducer. Therefore, biosensors can be classified into four different kinds according the transduction methods they utilize; optical transducers, electrochemical transducers, mechanical transducers and thermal transducers as shown in the Figure 1.3. Special emphasis is placed on describing the optical transducers because research work presented in this thesis is based on the optical transducers.

2.4.1 Electrochemical transducers

When an immobilized biomolecule binds with the target analyte onto an electrochemical transducer ions or electrons are produced or consumed, which affects measurable electrical properties of the solution, such as electric current or potential [21]. There are several approaches used to detect electrochemical changes hence electrochemical transducers are further classified into: potentiometric, amperometric and conductometric.

i. Potentiometric

Potentiometric sensors measure potential between the reference electrode and working electrode at zero current. A logarithmic relationship exists between the potential generated at the electrode surface and the activity of the ion of interest [22].

Most electrodes are made of metals like platinum, gold, silver, and stainless steel, or carbon-based materials that are inert at the potentials at which the electrochemical reaction takes place. However, because some species react at potentials where other species are present, either a selective membrane is used or an electron mediator that reacts at lower potential is incorporated into the immobilization matrix or to the sample containing the analyte [22].

The main advantage of these transducers is their wider detection limits, however the requirement of a very stable reference electrode have limited their application [23]. Nearly all potentiometric sensors, including glass electrodes, metal oxide based sensors as well as ion-selective electrodes, are commercially available.

ii. Amperometric

The measurement of electric current flowing at constant potential is the principle behind amperometric biosensors, which typically utilize electrodes coated with an enzyme which enables the analyte to undergo oxidation or reduction, resulting in a detectable current. The magnitude of the catalysis generated current has been shown to be proportional to the substrate concentration [24].

Each amperometric biosensor is designed for detection of only one or maybe a few molecular species, depending on the specificity of the enzyme. The definitely most commonly used biosensor is the single-use amperometric glucose oxidase based sensor for home glucose assays by diabetic patients. Another common type is sensors for hydrogen peroxide detection in flow systems. Immunoassays can also be performed with amperometric detection, where secondary antibodies are labelled with an enzyme whose product is oxidized at the electrode [25].

iii. Conductometric

Conductometric sensors measure the change in electrical conductivity of the solution due to a change in the ionic strength [26]. The solution conductivity is changed when an enzyme

reaction generates a net change in the concentration of some ionized species. Thus conductometric biosensors can detect any reactive change occurring in the solution. The measured parameter when using this transducer is the electrical conductance/resistance of the solution. The inverse value of resistance is called conductance and thus the name conductometric has been used. Examples of conductometric biosensor are whole cell Chlorella vulgaris microalgae for alkaline phosphatase activity (APA) analysis [27], conductometric biosensor for creatinine determination [28] and the use of conductometric biosensors for biosecurity [29].

2.4.2 Mechanical Transducers

When an electric field is applied across a piezoelectric material, such as quartz crystal, it induces a mechanical stress in the material and creates an oscillating motion of a certain vibrational resonant frequency. The frequency is depending on the mass on the surface of the oscillator and decreases upon increased mass on the surface. Piezoelectric materials have the ability to generate and transmit acoustic waves in a frequency-dependent manner. These waves can propagate on the surface, i.e., surface acoustic wave (SAW) or in the bulk of the resonator, i.e., bulk acoustic wave (BAW). When a piezoelectric sensor surface, which has been coated with a biological substance (i.e., antibody), is placed in a solution containing the virus /bacteria, the attachment of the agent to the antibody coated surface results in an increase in the crystal mass, and this gives rise to a corresponding frequency shift.

The quartz crystal microbalance, QCM, and is undoubtedly the oldest and the most recognized acoustic sensor. QCM technique involves a vibrating crystal which generates the electric current. The mass of material adsorbed on its surface affects the frequency of vibration, which could be related to changes in a reaction [30]. Biosensors based on piezoelectric quartz crystal have been widely investigated and several applications are reported including DNA hybridization, enzyme detections and gas phase biosensors [31].

Other type of a mass-sensitive biosensor is a microcantilever. This sensor detects the changes in cantilever bending or vibrational frequency. The principle of this detection is based on the transduction of specific molecular interactions on a cantilever surface into the mechanical response change of a cantilever [32]. More recently, the microcantilevers operated in vibration mode (oscillation) using RNA aptamers as receptor molecules were fabricated for label free detection of hepatitis C virus (HCV) helicase [33].

2.4.3 Thermal Transducers

These sensors are also referred to as thermal or calorimetric biosensors. Most of the biochemical reactions involve the generation or absorption of heat. These sensors are based on the measurement of heat which can be related to the amount of analyte present [34].

Once the analyte comes in contact with the immobilized biological element onto temperature sensor a heat reaction is measured which is proportional to the concentration of an analyte. The total heat produced or absorbed is proportional to the total number of molecules in the reaction and the molar enthalpy (transfer of heat in a reaction per mol). The measurement of the temperature is via a thermistor, and such devices are called as enzyme thermistors. Thermal biosensors are insensitive to the optical and electrochemical properties of the sample and do not require frequent recalibration [35]. Calorimetric biosensors were used for food, cosmetics, pharmaceutical and other component analysis [36].

2.4.4 Optical transducers

Optical transducers are one of the most common types of transducers used in biosensors which are based on measuring changes in light. After the interaction of the target molecules and probe molecules, a change in light intensity, polarization, phase, peak position, and angular wavelength will be observed and this change can be measured by optical transducers [37]. The optical transducer is generally represented by an optical waveguide (e.g., optical fibre, slot-waveguide, photonic crystal waveguide, photonic nanowire waveguide). By this

way, this photonic device has to satisfy different parallel functions. The first one consists in guiding the light from the optical source (e.g. Laser), to the sensing area. Consequently, the optical waveguide has the rule of transducer, enhancing the interaction between the chemical/biochemical process and the optical signal. By this way, the chemical information can be properly transduced into an optical one. In this context, the transducer can be considered as an engineering prerogative, because several technical solutions have to be implemented in order to maximize the confinement of the optical field in the sensing area [38].

Compared with other transduction methods, optical sensing encompasses the largest number of sub-categories and can be classified as two major types based on the sensing mechanism and the sensing architecture [39]. Moreover, optical biosensors can be classified according to the detection protocols: label-based detection and label-free detection.

2.5 Types of sensing mechanisms

i. Fluorescence

Fluorescence requires an external light source to initiate electronic transitions in a biomolecule immobilized on a waveguide. When a biomolecule absorbs an electromagnetic energy, it reaches to an excited energy level depending on the incident radiation wavelength. The biomolecule from an excited state tends to reach a lower energy level. Relaxation of the biomolecule from the excited state may take place by emission of a photon and this transition is known as fluorescence. Therefore, fluorescence is generated when a substance absorbs light energy at a short (higher energy) wavelength and then emits light energy at a longer (lower energy) wavelength [40]. In fluorescence based detection, either target molecules or biorecognition molecules are labelled with fluorescent tags, such as dyes. The intensity of the fluorescence emitted indicates the strength in interaction between the target and the biorecognition molecules [41].

Typical examples of these sensors are the ones used in the detection of the carcinogen benzo[a]pyrene (BaP) or those used to differentiate BaP and benzopyrene tetrol (BPT) [42]. These sensors are also used in DNA sequencing because of their high read out speed [43].

ii. Raman spectroscopy

Raman spectroscopy is based on the scattering of light. The scattering of light by molecules results in exchange of energy between incident photon and scattering molecules. This energy is either transferred from the scattered photon to the incident photon or vice versa. When the scattered photon has less energy than the incident photon, the method is remarked as Raman to Stokes scattering. Once the scattered photon has a lot of energy than the incident photon, the method is thought as Raman to anti-Stokes scattering [44].

In case of Raman to Stokes scattering, the molecule is at all-time low energetic level. Once a photonic beam of light interacts with the sample, the molecule passes to a higher energetic level then it returns to a lower energetic level by emitting a photon. The difference between incident and emitted photon energy is employed to change the vibration state of the molecule. In case of Raman to anti-Stokes scattering, the molecule at the start is found at higher energetic level and, after the photonic beam interacts with the sample, it reaches the lowest energetic level with a photon emission [45].

Raman signals are very weak and need high precision optical receptors and powerful sources. The advantage of using this kind of sensors is that it overcomes some of the shortcomings of fluorescence sensing such as the ability to sense analytes which do not exhibit fluorescence [46]. It finds application in HIV detection [47] and DNA sequencing [48].

iii. Optical absorption

Absorption is a process in which the energy of a photon is transformed to other forms of energy, such as heat. The absorbance of a molecule at a specific wavelength can be used to determine the concentration according to Beer-Lambert law. The Lambert-Beer law states

that optical absorption (A) is directly proportional to the concentration of the analytes present (C) and the length of the optical path (L), i.e. A α LC. This equation is used to calibrate the presence of analytes in a solution. A common configuration to measure the absorbance is to direct a beam of radiation at the sample and detect the intensity of the radiation that passes through it. This is a very effective and simple method of sensing since most of the analytes are absorbing. This mechanism is used in some optical biosensors to sense biological pathogens or gases such as oxygen or carbon dioxide concentrations and to measure pH in solutions [49]

iv. Evanescent field sensing

For most types of optical biosensors, a solid material medium confines an electromagnetic wave in such a way that the wave has the opportunity to interact with immobilised biosensing element. The electromagnetic wave may be in the form of a traveling wave or a standing wave, depending on the sensor configuration. For light to be guided by the sensor structure but concurrently interact with the external environment, the structure must be designed so that the light wave can extend from the sensor surface into biorecognition layer. With this configuration the change in the optical properties of the surrounding medium is probed by the evanescent tail of the mode propagating along the waveguide structure. An interaction with the surrounding medium will both alter the tail's propagation speed, caused by a change in refractive index, and alter its attenuation, effected by a change in the absorption coefficient. These alterations would then also be detectable as a corresponding change in the phase velocity of the guided wave.

The phase velocity v_p can be used in combination with the speed of light c to introduce a new quantity, the effective refractive index n_{eff}

$$Effective\ Refractive\ Index = \frac{\text{Speed of Light}}{\text{Phase Velocity}} \quad \text{or} \quad n_{eff} = \frac{c}{v_p} \tag{2.2}$$

Since it is obvious that the molecules in the surrounding medium will interact with the

evanescent field, it is easily understood that the result will be a phase velocity v_1 smaller than the speed of light. The binding of antigens with antibody further alters the optical properties of the surrounding medium. This causes a change in the phase velocity v_2 which can be compared to v_1 to obtain a change in the effective refractive index Δ_{neff}.

The evanescent field biosensors have proven to be a highly sensitive tool for interactions in the close vicinity of the sensor surface. Figure 2.4 (a) represents conventional evanescent field biosensor which shows the biomolecular interaction takes place on the waveguide surface inside the evanescent area, which influences the effective refractive index N_{eff} of the transmitted mode light. n: Refractive index. n_e: External. n_c: Core. n_s: Substrate. When target molecules bind to the receptor molecules in the sensor window, the change in local refractive index is felt by the evanescent tail of the optical waveguide mode and shifts the phase velocity of the guided light (Figure 2.4 (b)). Figure 2.4 (c) shows the dashed lines represent the top and bottom extents of the waveguide core. The top surface of the waveguide exposed to the chemical reactions is at x = 0 μm.

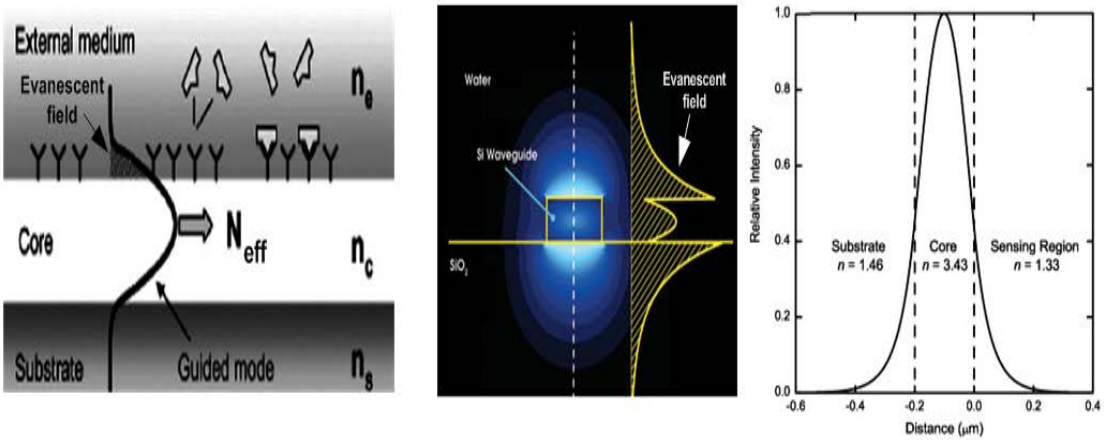

Figure 2.4 (a) Scheme representing evanescent field sensing. **(b)** A cross section of a silicon photonic waveguide and the optical electric field distribution of the vertically polarized mode are shown. **(c)** Cross-sectional plot of the evanescent field intensity of optical waveguide [50].

The evanescent field intensity decays exponentially with distance from the transducer surface, with a decay length of approximately $\lambda/2\pi$, where λ is the wavelength of light. When we consider light for optical biosensors in the typical wavelength range of λ = 600 –1550 nm, the

evanescent field extends only ~100–250 nm (Figure 2.5 (a)) into the test sample. Because the evanescent field distance is so short, the biosensor only interacts with material in direct proximity to its surface, such as DNA, antibody, proteins that are chemically attached to the surface, while being unaffected by unbound material such as bacteria or eukaryotic cell suspended in solution. Different designs for optical biosensors can manipulate the characteristics of the evanescent field so that it either extends deeply into the test sample or is confined tightly to the sensor surface (Figure 2.5 (b)). One key to high sensitivity sensor design is to match the regions of greatest biochemical binding to those regions with the highest evanescent field intensity [51].

Many label-free optical biosensors are based on refractive index changes that results from interactions of biomolecules with evanescent waves. For example, the widely used, state-of-the-art surface plasmon resonance (SPR) sensor uses the evanescent wave of a surface plasmon mode, which is a collective electron oscillation wave existing at the interface between metal and dielectric materials [52, 53]. Several other types of evanescent wave biosensors have been demonstrated on silicon or silica platforms, including fibre optic sensors [54, 55], planar waveguide sensors [56], and, more recently slot-waveguide micro- ring resonator and silicon nanowire sensors [57-58]. The slot-waveguide micro-ring resonators achieve high sensitivity detection through more interaction with analyte molecules binding to the waveguide surface in the slot region and design of very high quality factor resonant structures that allow the evanescent field to interact with biomolecules over multiple cycles of the confined wave. The silicon nanowire waveguide design enables improved detection sensitivity over traditional slab waveguide sensors by utilizing a thinner waveguide core that with biomolecules immobilized on the core a greater fraction of the electric field to leak out into the cladding and interact with biomolecules immobilized on the core surface. Arranged in a Mach-Zehnder configuration, silicon wire waveguides also benefit from longer field-molecule interaction lengths [59].

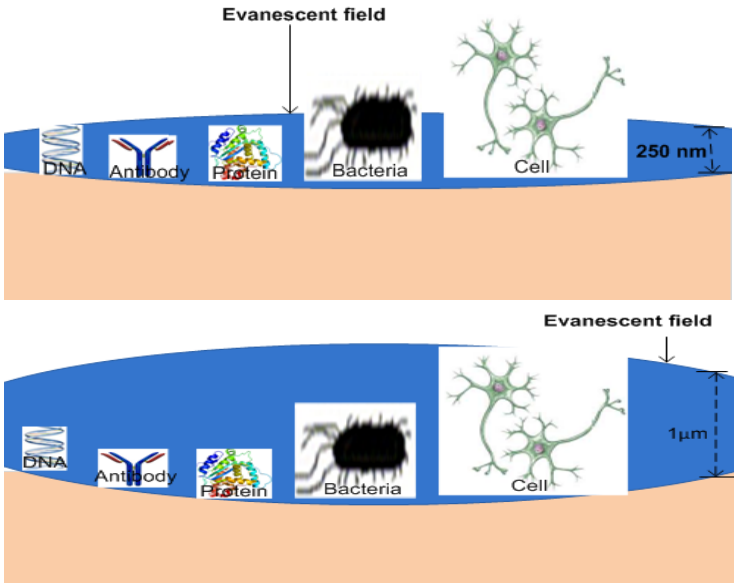

Figure 2.5 (a) Limited evanescent field of the conventional evanescent field sensors of 250 nm **(b)** Increase in evanescent field of the deep-probe evanescent field biosensor of 1µm [60].

2.6 Optical biosensor architectures

Following optical sensor configurations represent widely used architectures in optical label-free sensor development:

- surface plasmon resonance based biosensors
- fibre optic based biosensors
- interferometer based biosensors
- micro ring resonator based biosensors

2.6.1 Surface Plasmon Resonance based biosensors

Introduction

Surface Plasmon resonance (SPR) is one of the successful optical techniques which has applications in chemical and biochemical sensing [61]. In SPR technique, a transverse magnetic polarized light causes the excitation of oscillations of electron density at the metal-dielectric interface [62]. This oscillation of electrons produces a wave known as surface plasmon wave (SPW). When the incident light (which carries energy as well as momentum) and the surface plasmon wave match a resonance occurs which results in a sharp dip in the

reflected light intensity as represented in Figure 2.6.

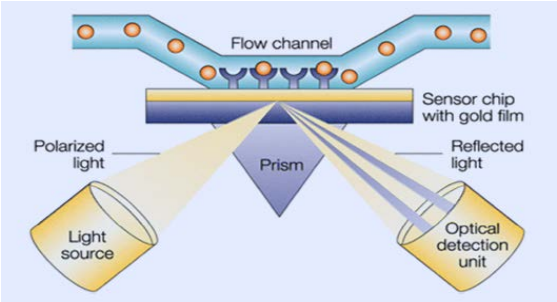

Figure 2.6: The changes in the refractive index in the immediate vicinity of a surface layer are detected with a sensor chip. The plasmonic resonance is observed as a sharp shadow in the reflected light at an angle that depends on the mass of material at the surface – this angle shifts if biomolecules bind to the surface [62].

The resonance condition depends on the angle of incidence, light beam wavelength and the dielectric properties of metal as well as substrate. An angular interrogation takes place when the wavelength is kept constant and the angle of incidence is varied which results in a sharp dip at the particular angle. A spectral or wavelength interrogation takes place when the angle of the incident beam is kept constant and the wavelength is varied which results in resonance at a particular wavelength. The angle of incidence or the wavelength depends on the refractive index of the dielectric medium. Change in refractive index changes the value of the angle of incidence or the wavelength. To excite surface plasmons, generally, a prism is employed [63-70]. The prism based SPR sensing device has variety of shortcomings like its large size, no remote sensing and also the presence of varied optical and mechanical moving elements. To overcome these shortcomings introduction of optical fibre is used in place of prism. The optical fibre SPR probe can be miniaturized which can be advantageous for samples, which are costly and are available in minute quantity. Due to these advantages the surface plasmon resonance based optical fibre sensors have drawn a lot of attention [71-81] and are discussed in section 2.6.2.

2.6.2 Fibre optic SPR based biosensors

In case of optical fibre based SPR sensor evanescent wave is required to excite the surface plasmons. The evanescent wave is resulted due to total internal reflection taking place at the

core-cladding interface as shown in Figure 2.7 (a). To design a SPR based fibre optic sensor, the silicon cladding of the fibre is replaced with a thin metallic layer which is further surrounded by a sensing layer. The guided light is launched into one of the end of the optical fibre to produce an evanescent field which excites the surface plasmons at the metal-dielectric sensing layer interface (Figure 2.7 (b)). The coupling (Figure 2.7 (c)) of evanescent field with surface plasmons strongly depends on wavelength, fibre diameter, metal layer properties and probe geometry. The intensity of the light transmitted after passing through the SPR sensing region is detected at the other end of the fibre as a function of wavelength.

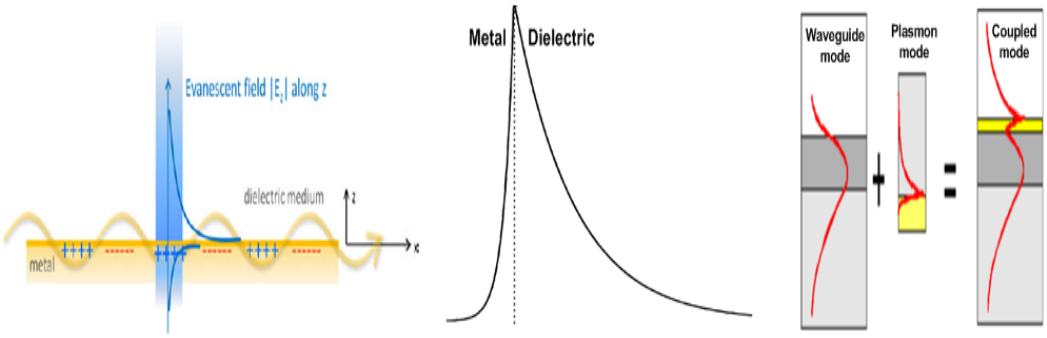

Figure 2.7 (a) An evanescent wave corresponds to a TM-mode that propagates along the interface of a metal and a dielectric, where the z-component of the electric field decays exponentially **(b)** Spatial distribution of the magnetic intensity for a surface plasmon at the interface between metal and a dielectric **(c)** A combination of surface plasmons and waveguide modes is possible [84].

Biomolecular recognition elements immobilized onto the metal surface recognize and bind with an analyte present in a liquid sample producing a local increase in the refractive index at the metal surface. The increase in the refractive index gives rise to an increase in the propagation constant of surface plasmon wave (SPW) propagating along the metal surface which can be accurately measured by optical transducer. The increase in the propagation constant of the SPW is the underlying physical principle of affinity SPR biosensors (Figure 2.7).

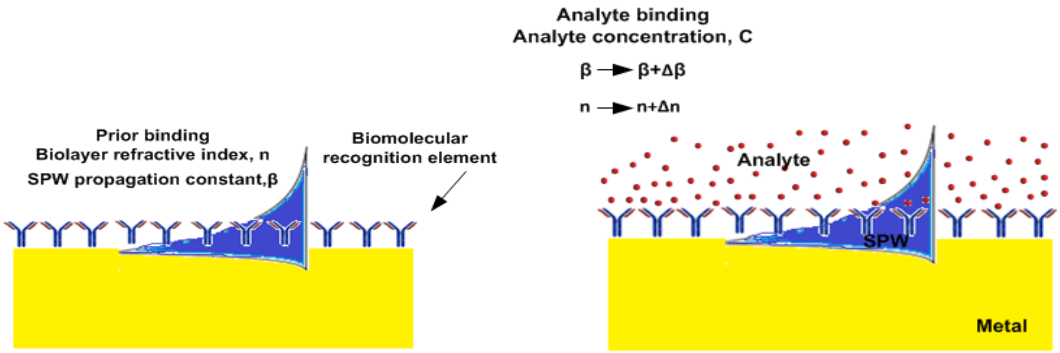

Figure 2.7: Principle of SPR biosensing [85].

SPR Probe Designs

Numerous designs of fibre optic SPR probe are considered to achieve high sensitivity, detection accuracy, reproducibility and operating range of the sensor. The sensitivity and the detection accuracy are determined in the same way as determined in the case of angular interrogation.

Choice of Metals

Gold or silver is used as a choice of metallic coating on the fibre core. Real and imaginary part dielectric constant of gold and silver plays a vital role in achieving sensitivity and detection accuracy. Gold has higher value of the real part of the dielectric constant which results in higher shift of resonance parameter to change in refractive index of sensing layer. Silver, on the other hand has higher value of the imaginary part of the dielectric constant which result s in a narrower width of the SPR curve causing a higher SNR or detection accuracy. Gold is chemically stable while as chemical stability of silver is poor due to its oxidation. The oxidation of silver occurs as soon as it is exposed to air and especially to water, which makes it difficult to give a reproducible result and hence the sensor isn't reliable for practical applications [86].

The ability of other metals to be used for a SPR sensor applications are copper (Cu) and aluminium (Al). Copper is chemically vulnerable against oxidation and corrosion, therefore it isn't widely used as metal for SPR sensor [86].

Effect of Dopants

A theoretical modelling and analysis of SPR based fibre optic sensor has been carried out in [87] to evaluate the effect of dopants on the sensitivity and SNR [87]. Commonly used dopants for pure silica are germanium oxide (GeO_2), boron oxide (B_2O_3), and phosphorus pent-oxide (P_2O_5) which can enhance the sensitivity of the sensor.

Side Polished Fibre

The common sensor configuration among fibre optic SPR probes is the surface plasmon resonance sensor using side polished single mode optical fibre and a thin metal over layer [88]. In this configuration, the guided mode propagating in the fibre excites the surface plasmon wave at the interface between the metal and a sensing medium (Figure 2.8). The resonance occurs if the two modes are closely phase matched. Therefore, variations in the refractive index at the sensor surface induced by the interaction between target analyte molecules and bimolecular recognition element such as antibodies immobilized on the sensor surface may be observed as changes in the resonant wavelength. The single-mode optical fibre based SPR sensor is more sensitive and accurate in comparison to those with multi-mode optical fibre based SPR sensor. However, fabrication of single-mode optical fibre based SPR sensor is much more complex and sophisticated compared with those that use multi-mode fibres [89]. Figure 2.8 shows SPR sensing structure based on a side-polished single-mode fibre.

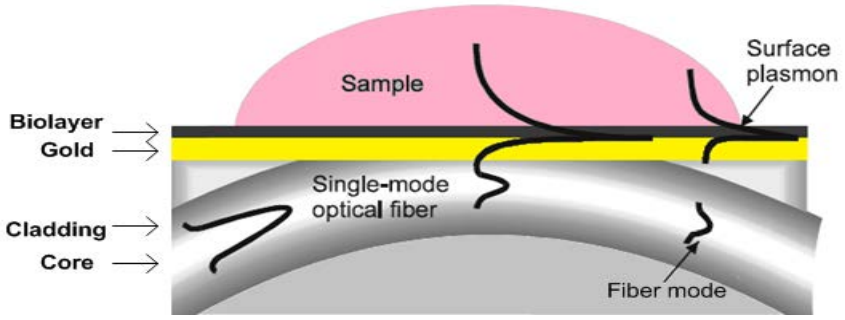

Figure 2.8: SPR sensing structure based on a side-polished single-mode fibre [88].

The side polished multimode optical fibre sensors have been reported [89]. In these sensors the fibre was side polished which increases the sensing area, hence an advantage.

In addition to side polished single mode fibre, D-type single mode optical fibres have also been used for sensing applications utilizing SPR technique with improved sensitivity [90-94]. The other designs for SPR based fibre optic sensor includes SPR probe at one of the ends of the fibre with the reflecting end face [95, 96] and a fibre tip [97, 98]. The photonic band-gap fibre based SPR sensors have also been reported very recently [99].

2.6.3 Interferometer based biosensors

Interferometer based sensors are widely used to detect the phase shift occurred by change in effective index of mode due to interaction between the sample and the guided light propagating in the sensor. Among the interferometer architectures, Mach-Zehnder approach is highly sensitivity for label-free optical biosensing. In these sensors, the guided light interacts with the analyte through its evanescent field or, alternatively, the analyte can propagate in the core of the waveguide if hollow or slot waveguides are employed.

The Mach-Zehnder interferometers are composed of an incident waveguide that is split in two single mode waveguide branches containing a sensing arm and reference arm [100] as represented in Figure 2.9.

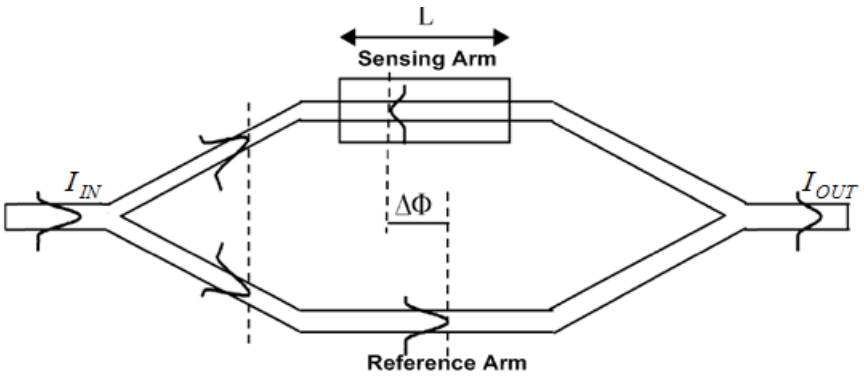

Figure 2.9: Scheme of an integrated Mach–Zehnder interferometer

In an MZI the incident coherent light is split into two separated single mode waveguides. One of these waveguides - the sensing arm - has no cladding. Changes of the optical properties in the region (e.g., bulk superstrate index changes or the addition of a thin biolayer) the evanescent field lead to a change of the effective index (Δn_{eff}) of the waveguide mode which introduces a phase shift in the light traveling in this arm of $\Delta n_{eff}\, k_0\, L$, where $k_0 = 2\pi/\lambda$ is the free space wave number, L the length of the sensor window. The other waveguide - the reference arm - is covered with a cladding and thus isolated from changes of the surrounding media. At the MZI output, where the sensing and the reference arm are recombined, interference occurs due the relative phase shift ϕ induced by the difference of the effective indices. The interference translates this phase shift into a modulation of the optical output Intensity satisfying the condition

$$\frac{I_{OUT}}{I_{IN}} = \frac{1}{2}\left[1 + \mathrm{Cos}\phi\right] \tag{2.3}$$

where I_{OUT}/I_{IN} is the ratio between optical output and input intensity of the MZI. The phase shift ϕ is defined as

$$\Delta\phi = \kappa_0\, L\, [\, n_{eff}^{S} - n_{eff}^{R}\,] \tag{2.4}$$

where $k_0 = 2\pi/\lambda$ is the free space wavenumber, L the length of the sensor window, and (n_{eff}^{S}, − n_{eff}^{R}) the effective index difference between the sensing and reference arm.

Any change in the effective index within the region penetrated by the evanescent field of the light guided in the sensing arm irrespective whether it arises from a refractive index change of the analyte acting as cladding (homogeneous sensing) or from a refractive index change of a thin sensitive film on top of the core layer (surface sensing) leads to a change of the relative phase shift Δϕ and thus to a change of the output signal.

The input optical power I_{IN} is split into two optical beams with an half power $I_{IN}/2$ in the sensing and reference arm respectively. If any optical phase delay is applied to the guided mode in the sensing arm ($\Delta\phi = 0$), light will be combined at the output Y-branch exhibiting an output optical power $I_{OUT} = I_{IN}$. In all different cases ($\Delta\phi \neq 0$ in sensing arm), the optical output power will be different from the input one ($I_{OUT} \neq I_{IN}$), according to

$$I_{OUT} = I_{IN}\,\mathrm{Cos}^2\frac{\phi}{2} = I_{IN}\,\mathrm{Cos}^2\frac{\pi\,\Delta n_{eff}\,L}{\lambda} \tag{2.5}$$

Typically, increasing the length of the sensor increases the sensing signal. One of the penalty of using the MZI device as a sensor is a cosine-dependent intensity function whereby signal change is not easily resolvable near the maximum and minimum of the cosine function as compared to sensors that have a linear intensity response.

The sensitivity S of sensors based on Mach-Zehnder interferometer can be expressed as;

$$S = \frac{2\pi\,L}{\lambda} S_w \tag{2.6}$$

where S_w is the waveguide sensitivity, defined in case of homogeneous sensing, as

$$S = \frac{2\pi\,L}{\lambda}\left(\frac{\partial n_{eff}}{\partial n_c}\right) \tag{2.7}$$

and, in case of surface sensing, as:

$$S = \frac{2\pi\,L}{\lambda}\left(\frac{\partial n_{eff}}{\partial \rho}\right) \tag{2.8}$$

where n_{eff} is the effective index of optical mode propagating in guiding structure, n_c is the cover medium refractive index and ρ is the thickness of molecular layer deposited on guiding cover medium interface. The sensitivity of an integrated optical sensors adopting Mach-Zehnder architecture depends on sensing arm length, L. An undesired shift in propagating

mode of an effective index may be introduced due to for example because of change in temperature which can affect the sensitivity. Thus, a trade-off between device length and device sensitivity has to be usually achieved [101].

Recently nanowire sensor employing a wire assembled Mach-Zehnder interferometer was developed for optical sensing. Several different types of nanowire, either metallic [102] or drawn from bulk glasses [103], as well as chemically grown nanoribbons [104], have been successfully fabricated and used as building blocks for potential future micro or nanophotonics applications in fields such as biosensing and nonlinear optics [105]. Further, the combination of nanotechnology, biology, chemistry, and photonics allows the exploration of new opportunities for the development of optical sensors with subwavelength or nanometer structures. Silica nanowires [106] offer several advantages over other types of nanowires since they are based on materials used in the most important photonic and opto-electronic applications within the visible and the near-infrared ranges and as a result their optical properties are familiar. Light guided along such a nanowire leaves a large fraction of the guided field outside the wire as evanescent waves [107, 108], making it highly sensitive to the index change of the surrounding medium.

2.6.4 Micro Ring Resonator based biosensors

Optical microring resonators are an emerging biosensing technology that has recently been under intensive investigation [109 - 113] for achieving higher sensitivities and finding application in multiplexed analysis. The device size reduction by some orders of magnitude without compromising the device sensitivity is due to large photon lifetime within the resonator at resonance which provides a long interaction length to achieve a detectable phase shift, makes micro-resonators an ideal optical biosensors.

Recently, a slot-waveguide based ring resonator has made a huge impact among biosensors due to the fact larger light analyte interaction is achieved in the slot through which biomolecules flow. The slot waveguide based micro ring resonator can be used as a biosensor by applying a proper surface chemistry to the waveguide surface. This will result in a thin layer on top of the waveguide that contains receptor molecules that are specific to the analyte. When the resonator is brought into contact with a fluid containing this analyte, the analyte will bind to the receptor molecules at the surface of the waveguide, causing a thickness change of the layer on top of the waveguide. A binding event will change the local refractive index, which results in a change of the effective refractive index of the optical mode and hence in a resonance wavelength shift which is expressed as;

$$\Delta\lambda = \frac{\Delta n_{\text{eff}} \cdot \lambda_{res}}{n_g} \tag{2.9}$$

where Δn_{eff} is the change of the effective index caused by the analyte binding, λ_{res} is the initial resonance wavelength, and n_g is the group index of the slot waveguide at the resonance wavelength and is given by;

$$n_g = \mathrm{n}_{\text{eff}} - \lambda \frac{\Delta n_{eff}}{\Delta\lambda} \tag{2.10}$$

There are two important routes to improve the detection limit of the sensor: one approach is to maximize the quality factor of the resonator, which will decrease the impact of noise on the determination of the resonance wavelength [114]. Another approach is to maximize the average resonance wavelength shift per binding event by increasing the interaction of light and biomolecules that get attached to the waveguide surface. When using a normal photonic waveguide with a rectangular cross section, only the evanescent tail of the waveguide mode will interact with the biomolecules. By etching a narrow slot in the middle of the waveguide, however, a vast fraction of the quasi-TE mode will be concentrated in that

slot [115], causing it to have more interaction with analyte molecules binding to the waveguide surface in the slot region and improving the sensitivity of the sensor.

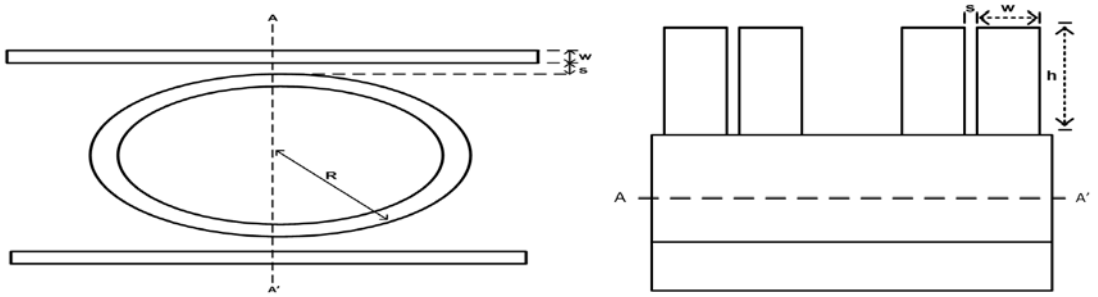

Figure 2.10 (a) Schematic top view of the slot-waveguide based micro ring resonator **(b)** Cross-sectional view of the slot-waveguide based micro ring resonator

Figure 2.10 (a) shows a schematic top view of the slot-waveguide micro ring resonator. A straight slot-waveguide is used to couple light into a slot-waveguide ring. Only one particular wavelength of light called the resonance wavelength gets coupled into the slot-waveguide ring and vice versa.

Figure 2.10 (b) illustrates a schematic cross section of the straight-ring slot waveguides coupling region. Both straight and ring slot-waveguides consist of two strips (rails) on a bottom cladding layer. The top of the whole device (cover) is exposed to the environment, that is, the top cladding region (refractive index=n_B) constitutes the sensing region.

2.7 Comparison, advantages and disadvantages of sensor architectures

The most common evanescent wave sensor is the Surface Plasmon Resonance (SPR) sensor [61]. The SPR biosensor has been used commercially because of its outstanding performance in evaluating complex bimolecular interactions [63]. However SPR sensors have a relatively large size and its miniaturization in lab-on-chip platforms is complex. Moreover, the sensitivity is usually limited to the nanomolar range, which is extremely useful in diverse applications [72] but not enough for applications requiring lower detection levels, which are usual in the clinical practice. In order to overcome these disadvantages, SPR-based optical fibre sensors

have attracted significant interest [94]. A fibre based sensing configuration allows for a compact sensing element and sample volume, the capacity for remote sensing and the potential for disposable miniaturized sensing devices. In the past decade, various fibre based SPR sensors have been proposed and demonstrated, including the use of either single mode fibres [96] or multimode fibres [97].

Conventional SPR biosensors have a Detection Limit (DL) between 1×10^{-6} to 1×10^{-7} RIU and a mass surface density DL around 1 pgmm^{-2}. The Detection Limit (DL) in optical fibre coupled SPR biosensor is typically around 10^{-5} to 10^{-6} RIU. A better DL of $5–7\times10^{-7}$ RIU has been achieved by multiple peak SPR fibre optic sensors and by spectral interrogation in a side-polished single mode fibre using depolarized light [89].

Mach-Zehnder based sensors are usually sensitive but are not as compact as micro ring resonator based sensors. The Mach-Zehnder based sensors require long structures whereas micro ring resonator based sensors have reduction in length of three orders of magnitude and exhibit a sensitivity which is comparable to that of Mach-Zehnder based sensors. The sensitivity of an integrated optical sensors adopting Mach-Zehnder architecture depends on sensing arm length L. An undesired shift in propagating mode of an effective index may be introduced due to for example because of change in temperature which can affect the sensitivity in Mach-Zehnder based sensors [100, 101]. The sensitivity of the Mach-Zehnder sensor based on silica nanowire is about 7.5/μm as compared with conventional Mach-Zehnder sensors based on integrated planar waveguides is much lower, e.g., below 0.7/μm [209], showing that much higher sensitivity can be achieved when sensing with optical nanowires.

The large photon lifetime within the micro ring resonator at the resonance provides a long interaction length to interact with biomolecules to achieve a detectable phase shift. Therefore, sensor configurations based on microring resonator show very important

advantages related to dimension reduction without significantly affecting the device sensitivity. Silicon slot waveguides has been emerged as very attractive nanometre ultra-sensitive optical biosensors [109-115]. The slot-waveguide ring resonator showed a RI sensitivity of over 298nm RIU−1 and a DL of 4.2×10−5 RIU and an estimated protein DL of approximately 20 pgmm−2 as compared to 70 nm/RIU for a normal-waveguide-based ring resonator [215].

The ring resonators require a tunable laser source when the resonance wavelength is monitored, which increases instrumentation costs. They also do not offer a means for internal referencing for temperature drifts, wavelength drifts and non-specific binding of molecules. Mach-Zehnder devices can be used with a low cost, fixed wavelength diode laser source over a large dynamic range and offer internal referencing capabilities for the above parameters through the use of the reference arm. Therefore, the optimal choice of transducer design will depend on the application and acceptable instrumentation costs [101].

2.8 Label-based vs label-free detection

Label-based systems use tags, dyes and probes to label biomolecules [116]. Labels are relatively small modifying agents that can be used to tag, dye and probe proteins, antibodies, nucleic acids and other molecules. These compounds often contain groups that provide sensitive detectability by virtue of some intrinsic chemical or atomic property such as fluorescence, visible chromogenic character, radioactivity, or bioaffinity toward another protein. Most probes can be designed to contain a reactive portion capable of coupling to the functional groups of biomolecules. After modification of a protein via this reactive part, the probe becomes covalently attached, thus permanently tagging it with a unique detectable property. Subsequent interactions that the labelled protein is allowed to undergo can be followed through the tag's visibility [117]. The most conventional label-based methods available are chromogenic, radioactivity and fluorescence based detection systems [118].

In chromogenic detection antigen-antibody interactions can easily be detected by chromogenic reactions. A chromogenic substrate is a molecule which is catalysed by the enzyme linked to the antibody to provide a coloured product which can be easily detected [118].

Radioactivity is a process by which certain elements spontaneously emit energy in the form of waves or particle by disintegrating the unstable atomic nuclei in to a more stable form. There are various applications where radioactivity labeling has been employed. Antigen-antibody, protein-protein, protein-DNA and protein-RNA interactions can be studied by using the radio labeled query protein on antigen that gives out radiation on binding to the corresponding target molecule [119].

Fluorescence is a phenomenon by which a substance absorbs radiation of one wavelength and emits another, usually longer wavelength and that is known as fluorescence. The fluorescent label uses a reactive derivative of a fluorescent molecule known as a fluorophore which chemically attaches to a biomolecule such as antibody, protein, or amino acid. The fluorophore selectively binds to a specific region or functional group on the target molecule before being exposed to probe molecules and serves as a marker or dye, or tag, or reporter for antibodies, peptides, nucleic acids [120]. A light source is then used to excite the fluorophores attached to the sensor; the fluorophores absorb photons of the excitation slight, which cause the fluorophores to emit light at a longer wavelength (e.g., fluorescent light is lower energy compared to incident light). The fluorescence is detected by a photodetector, which identifies the presence of the labeled target molecules [121].

The technique of bioconjugating fluorophores onto biomolecules is time consuming and low yield often results. Moreover, the fluorophore modification process can inhibit the biomolecular binding efficiency, adversely affecting the sensor performance. In addition, since the fluorescence intensity is typically weak and the lifetime is short, optical detection

instruments often must be of high quality [123]. Label-free biosensors that do not require the use of fluorescent molecules for biomolecule detection have the advantage of eliminating complex sample preparation techniques and improving reliability [124]. Optical label-free biosensors often operate based on a change in refractive index due to affinity binding events of biomolecules, such as DNA hybridization or antigen-antibody binding.

The labelling of biomolecules exhibit interference with the binding site and often alter surface characteristics and natural activities of the query molecule. The labelling procedure is laborious, lengthy and limits the number and types of query molecules. Therefore, Label-free detection techniques are now attracting significant attention to overcome the issues with label based detection techniques. The Label-free detection techniques simplify the bioassays by eliminating the need for secondary reactants. Label-free techniques avoid interference due to the tagging molecules. Moreover, they provide quantitative information for the binding kinetics [122].

Label based detection methods are not suitable for portable or hand-held diagnostic devices because attaching the dyes is a complex exercise. Detecting the fluorescence requires expensive lab-based equipment. Label-free method of biosensing detect the binding of complex biomolecules directly using portable or hand-held devices requiring no expertise and are less costly [125].

2.9 Biosensor applications

Applications of biosensors include medical, environmental, public security, and food safety areas. Medical applications include clinical, pharmaceutical and device manufacturing, and research. Environmental applications include spill clean-up, monitoring, and regulatory instances. Public safety applications include civil and military first responders as well as unattended monitoring. Food safety applications include monitoring of food production,

regulatory monitoring, and diagnosis of food poisoning. Biosensors allow multi-target analyses, automation, and reduced costs of testing.

2.10 Characteristics of biosensors

The key characteristics of biosensors are the following:

- Fast or real-time detection provides almost immediate interactive information about the sample tested, enabling users to take corrective measures before infection or contamination can spread.
- Biosensors can be used for point-of-care or on-site testing where state-of-the-art molecular analysis is carried out without requiring a state- of-the-art laboratory.
- Many biosensor technologies can be configured to allow continuous flow analysis. This is beneficial in food production, air quality, and water supply monitoring.
- Biosensors can be miniaturized so that they can be integrated into powerful lab-on-a-chip tools that are very capable while minimizing cost of use.
- Biosensors can be integrated with on-line process monitoring schemes to provide real-time information about multiple parameters at each production step or at multiple time points during a process, enabling better control and automation of many industrial and critical monitoring facilities.

2.11 Optical biosensor performance metrics

The suitability of an optical biosensor for a particular application depends upon its performance across a variety of metrics including sensitivity, detection Limit, resolution, and sensor cost. In this section, we will define some of the methods used to compare optical biosensors. Some metrics, such as sensitivity or cost, can be defined numerically. Others, such as ease-of-use or instrument robustness, are subjective but can have a significant impact on the commercial success of an approach.

2.11.1 Sensitivity

For optical biosensors, sensitivity is fundamentally determined by how efficiently the electromagnetic field associated with the optical transducer couples to biomolecules in contact with the sensor surface. The design goal for achieving high sensitivity is to produce a structure that allows as much of the electric field as possible to reside outside the transducer and within the surrounding media. Factors affecting the sensitivity of optical biosensors include electromagnetic field strength, penetration depth of evanescent field, optical power contained in the sensing region and geometric factors which include the metal thickness, length and diameter of core.

In sensor development, sensitivity is an important parameter to evaluate the sensor performance. Fundamentally, sensitivity is determined by the strength of interaction between the light and sample, therefore, sensitivity is the magnitude of sensor transduction signal change in response to the change in analyte [126]. In most evanescent wave based sensors sensitivity is determined by the light intensity at the sensor surface or the fraction of light in solution.

Sensitivity is defined as the ratio of the change in transducing optical parameters ($\Delta\lambda$ in the resonant wavelength shift scheme and ΔI in the intensity variation scheme) to the change in the waveguide parameters affected by analytes. According to the definition the sensitivity S for four different combinations is listed in the Table 2.2. From the mathematical expressions sensitivity can be further divided into two parts, which are named as device sensitivity and waveguide sensitivity respectively.

(a) Device Sensitivity

Device sensitivity is defined as the ratio of the change in the transducing optical parameter to the effective index change. Device sensitivity only depends on device properties and it is related to the variation of transducing optical parameters, and thus depends on the

transducing method. For the resonant wavelength shift scheme, device sensitivity is expressed as;

$$S = \partial\lambda/\partial \mathrm{n}_{\mathrm{eff}} \tag{2.11}$$

$$\partial\lambda = \frac{\partial \mathrm{n}_{\mathrm{eff}} \cdot \lambda_{res}}{n_g} \tag{2.12}$$

Where ∂λ is the resonant wavelength shift, ∂n_{eff} is the change of the effective index caused by the analyte binding, λ_{res} is the resonance wavelength, and n_g is the group index.

While for the intensity scheme it becomes

$$S = \partial I/\partial \mathrm{n}_{\mathrm{eff}} \tag{2.13}$$

From 2.11 and 2.12, device sensitivity will be enhanced by using longer resonant wavelength or smaller effective refractive index for either case.

(b) Waveguide Sensitivity

Waveguide sensitivity is defined as the ratio of the effective index change to the change in the waveguide parameter affected by analytes. Waveguide sensitivity is relevant to waveguide structures regardless of the type of devices. Waveguide sensitivity is determined by the effective index change resulting from the analyte-induced change in waveguide parameters. The effective index change is produced either by a change of cover medium refractive index or by a change of thickness of sensing layer which is immobilized on waveguide surface [127]. It varies with the sensing mechanism used and is expressed as

$$\partial \mathrm{n}_{\mathrm{eff}} / \partial \mathrm{n}_{\mathrm{c}} \quad \text{(homogeneous sensing)} \tag{2.14}$$

$$\partial \mathrm{n}_{\mathrm{eff}} / \partial \mathrm{t} \quad \text{(surface sensing)} \tag{2.15}$$

		Sensing scheme	
		Resonant wavelength shift	Intensity variation
Sensing mechanism	Homogeneous	$S = \frac{\partial \lambda}{\partial n_c} = \frac{\partial \lambda}{\partial n_{eff}} \cdot \frac{\partial n_{eff}}{\partial n_c}$	$S = \frac{\partial I}{\partial n_c} = \frac{\partial I}{\partial n_{eff}} \cdot \frac{\partial n_{eff}}{\partial n_c}$
	Surface	$S = \frac{\partial \lambda}{\partial t} = \frac{\partial \lambda}{\partial n_{eff}} \cdot \frac{\partial n_{eff}}{\partial t}$	$S = \frac{\partial I}{\partial t} = \frac{\partial I}{\partial n_{eff}} \cdot \frac{\partial \eta_{eff}}{\partial t}$

Table 2.2 Overall sensitivity S of a sensor is listed based on two sensing mechanisms and two transducing schemes

(c) Homogeneous Sensing

In homogenous sensing, the analytes are suspended in a fluid (gaseous or liquid) medium around the surface of the waveguide. When there is a change in the amount of homogeneously present analytes in the medium, the cladding index changes. This change in cladding index results in change in the effective index of the guided mode and moves the resonance wavelength. In this mechanism, all materials including the detected analyte in the solution can contribute to the effective-index shift, which leads to no specificity. To solve this problem, surface sensing can be employed. The sensitivity of a homogenous sensor can be defined as the ratio of change in cladding index (∂n_c) to the change in resonance wavelength ($\partial \lambda$), it is represented as;

$$S = \partial \lambda / \partial n_c \tag{2.16}$$

Figure 2.11 represents surface sensing diagrammatically;

Figure 2.11: Homogeneous sensing where analytes exist in the surrounding aqueous medium that serves as the top cladding [127].

Homogeneous sensing enables to measure concentration of a wide spectrum of chemical species as glucose or ethanol, usually present in a solution. Moreover, this kind of sensing mechanism allows estimating some gas concentration changes because some polymeric materials have the refractive index sensitive to specific gas concentrations. In all these cases, a chemical analyte concentration change induces the refractive index change in a solid or a liquid material serving as cover medium in the guiding structure. For example, when glucose concentration in an aqueous solution changes, a shift of the solution refractive index is induced [128].

(d) Surface Sensing

In surface sensing the exterior of the waveguide are treated with a layer which selectively attracts the analytes. Hence the analytes adhere to the surface of the waveguide. This solves the selectivity/specificity problem. When the analytes adhere to the waveguide surface, it increases the thickness of the waveguide and this layer of analytes is called the addlayer (t). The sensitivity of surface sensors is defined as the ratio of change in addlayer (∂t) to the change in resonance wavelength (∂λ).

$$S = \partial\lambda/\partial \mathrm{t} \tag{2.17}$$

Figure 2.12 represents surface sensing diagrammatically.

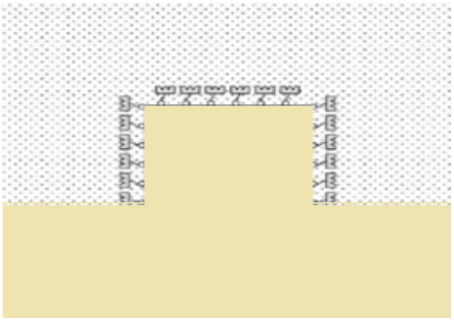

Figure 2.12: Surface sensing where analyte molecules adsorb on a sensor surface, which can be modelled as an ultrathin film [127].

Surface sensing is exploited in a wide range of biochemical applications, such as DNA sequencing by hybridization, antigen-antibody reactions study or pollution concentration measure in water. This kind of sensing is based on immobilization of an ultra-thin layer of receptor molecules on the guiding film surface. The interaction between analyte and receptor molecules produces a change of molecular adlayer thickness, affecting the effective index of propagating optical mode [129].

2.11.2 Detection Limit

Sensor detection limit (DL) is another important parameter to characterize the sensor performance. The DL can be deduced by taking into account the noise in the transduction signal, σ, i.e., the minimum resolvable signal:

$$DL = \sigma / \mathrm{S} \tag{2.18}$$

Where S is the sensitivity. Improvement in the DL can be accomplished by reducing the noise level or increasing the sensitivity. The sensitivity can be enhanced by increasing the interaction of light with the solution. The most commonly seen noise is from thermal expansion and temperature fluctuations in both sensor substrate and buffer solution which results in temperature dependent refractive index changes. To overcome the temperature related noise, non-specific binding and bulk RI change various methods are being employed to enhance the sensor performance by controlling these effects. The thermally induced noise can be reduced by implementing a temperature control, such as a thermoelectric cooler to

stabilize temperature. Another method is to balance the thermo-optic and thermo-mechanic effects. Third method is to employ a reference channel, which is either built into the same sensor or placed on a different sensor nearby to reduce so called common mode noise [130,131].

2.11.3 Resolution (or Limit of Determination)

Resolution is a critical performance criterion for detection of analytes present at low concentration or detection of adsorbed molecules with low molecular weight. To determine the resolution of a sensor, one must characterize the noise of the sensor when operated with its detection instrument. Noise can be easily characterized at a basic level by allowing the sensor to reach a steady-state condition and recording the measured output many times in sequence without any intentional change to the sensor. The noise is thus defined as the standard deviation, σ, of all the repeated measurements. If one defines a signal to be detectable if the signal has a magnitude of 3σ, then the *limit of determination* (LOD), defined as the smallest measurable mass density change of the sensor, is

$$LOD = 3\sigma / \mathrm{S} \tag{2.19}$$

The sensitivity and the resolution are related but are entirely different Figures of merit. Sensitivity is used to define the lowest value determined above zero concentration while the resolution describes the minimum resolvable difference between two measurements at any concentration.

2.11.4 Sensor Cost

Adoption of biosensor technology for most applications in diagnostics or pharmaceutical screening will be driven to some extent by the cost of performing an individual assay. For a primary screen used in the pharmaceutical research industry, for example, a screening

campaign to determine a set of candidate chemicals that has a desired affinity level for a protein can involve over 1 million assays. Researchers working on high-volume industrialized assays describe the need to minimize the cost per data point in such a campaign. Though optical biosensors offer tremendous advantage over labelled assay technologies by not requiring the use of tag reagents, the cost of the transducer in each assay must be low enough to compensate the cost of additional reagents. This cost goal challenges the wide acceptance of optical biosensors, which are often high-precision optical components fabricated from expensive materials (such as glass, silicon, or optical fibre) using highly exacting processes such as photolithography, dielectric or metal deposition, and plasma etching. Even if a sensor is inexpensive to fabricate, the cost of packaging and testing it must be efficient.

Two main methods have been used to bring the cost/assay to acceptable levels. First, if a sensor is expensive to fabricate and package, it can be regenerated and used for several successive assays. Second, sensors can be designed to be compatible with mass production by using inexpensive materials and methods, so they can be used one time before disposal, much like typical labelled assays.

2.12 Immobilisation of recognition receptors

Immobilisation step is critical in the development of any class of biosensor. It makes the detection easier and more sensitive. A wide variety of biomolecules can be used as bioreceptors, i.e. antibodies, nucleic acid sequences, peptides, enzymes, cell receptors and many others. Optical biosensors exploit the evanescent wave phenomenon to characterize interactions between bioreceptors that are attached to the biosensor surface and analytes that are in solution above the surface. Binding of molecules in solution to surface immobilized bioreceptors alters the refractive index of the medium near the surface which results in a change of the effective refractive index of the optical mode and thus to a change of the output signal [132].

The performance of a biosensor comes from its ability to immobilize bioreceptors while maintaining their natural activity, the bioavailability (accessibility) of the bioreceptors to targets in solution and a low nonspecific adsorption to the solid support. These specifications govern the specificity and sensitivity of such devices and can be tailored by an appropriate choice of the solid–liquid interface where the bioreceptors are immobilized. The chemical preparation of the surface is a key parameter. The physical and chemical properties of the interface play an important role in achieving optimal recognition of the target and limiting the nonspecific adsorption. Given the complexity and variability of biorecognition elements, there is no universal immobilization method. The choice of immobilization chemistry is therefore made based on the properties of a specific biorecognition element [133].

Several methods are used to biofunctionalize the sensor surface: (i) physical adsorption as a result of direct deposition of the biomolecule (ii) covalent binding of the biomolecule to the surface using a cross-linker previously immobilized on the surface (iii) noncovalent interactions to a previously deposited active layer, either by non-specific electrostatic interactions or by non-covalent affinity binding (i.e. biotin-avidin systems) (iv) physical entrapment in a polymer layer.

2.13 Physical Adsorption

Adsorption from solution takes place if the molecules interact with the surface by means of attractive interactions. Therefore, part of the molecules goes to the surface and a residual part remains in solution. A dynamic equilibrium is established where molecules in solution adsorb at the surface, while adsorbed molecules leave the surface. The system is equilibrated when the rate of adsorption and desorption are equal. The surface concentration and residual concentration are related, the larger the concentration in solution, the larger the adsorbed amount. The surface concentration is termed surface excess; it is expressed in mol/m^2. From a thermodynamic point of view, the standard

chemical potential of the molecule at the surface is lower than that in solution, so that the molecules are in a more favourable environment at the surface [134]. There are several drawbacks related to the immobilization by means of adsorption only. Adsorption depends on the interaction of the biomolecule and the surface, so that the amount of adsorbed molecules may vary from spot to spot. Release to the solution is possible when the solid support is immersed in the analyte solution; this causes a loss of the signal and possible cross contamination of the spots. The reversal of the roles of probes and target allows the immobilization process to work again [135].

Physical adsorption of a biomolecule to a surface occurs via dipole-dipole interactions, van der Waals forces or hydrogen bonding, depending on the nature of the substrate surface and the absorbate. However, physical adsorption in general is not only strongly influenced by changes in the ambient conditions, such as pH and the solvent used, but may also be reversible process. Furthermore, adsorption may not provide as high density of immobilized biomolecules as covalent immobilization. Physical adsorption is generally unspecific, random and multi-oriented in nature, often resulting in the inaccessibility of the active binding site.

The adsorption of proteins on solid surfaces is influenced by the physical and chemical characteristics of the real sample (blood, urine, waste water etc.). Changes in pH, ionic strength or particular additives in the sample can cause desorption of the adsorbed proteins. These problems can be overcome using covalent coupling procedures.

2.14 SAM (Self-assembled monolayers)

The interface between the sensor surface and the biomolecules deposited onto the interface is a key component of optical biosensors. The sensor surface must have ability to attach to receptors without changing their native conformation and binding activity. This attachment must be stable over the course of a binding assay and sufficient binding sites should be presented to interact with the analyte. Most importantly the interface should be resistant to non-specific binding of the sample.

Self-assembly monolayers (SAMs) are organized layers of molecules which spontaneously forms on a solid surface. The process of self-assembly is governed by inter and intra-molecular forces that drive the molecules into a stable, low energy state. These forces include hydrogen bonding, electrostatic interactions, hydrophobic interactions, and van der Waals forces. These nanometer thick layers are easily fabricated from commercially available substances or can at least be synthesized with relative ease [136]. The first applications of SAM for biosensor were described in the late 1980s and originally developed for Biacore instruments [137].

Many coupling strategies use a chemical-linker layer between the sensor base (for example, a gold layer) and the biological component to achieve these ends. Functionalized alkane thiols and alkoxy silanes form stable, self-assembled monolayers on planar surfaces and act as ideal linkers [138].

Two of the most widely studied systems of SAMs are alkylsilane monolayers and alkylthiolate monolayers.

(a) Alkylsilane Monolayers

Alkylsiloxane monolayers are usually prepared by a covalent adsorption process of self-assembling molecules, such as trichloro (R-SiCl3), trimethoxy (R-Si(OMe)3) or triethoxy silanes (R-Si(OEt)3), onto the surface of optical transducer. The self-assembling molecule consists of three parts: the head group, the alkyl chain and the terminal end group.

The head group, i.e., trichloro-, trimethoxy or triethoxy silane, is responsible for the tie up of the biomolecule onto the sensor surface. Because of the strong interaction between the head group and the sensor surface, the molecules attempt to adsorb at all surface sites, resulting in a close-packed monolayer [139]. The alkyl chain provides the stability of the monolayer, due to van der Waals interactions, and influences the ordering of the SAM [140]. The terminal end group introduces chemical functionality into the monolayer system. The simplest terminal functionality is a methyl group however, the chain may be terminated with a number of

different groups (e.g., NH2, OH, or COOH), allowing SAMs to be tailored to a particular application. Functionalization of the end group also allows multiple layers to be adsorbed on top of the monolayers [141].

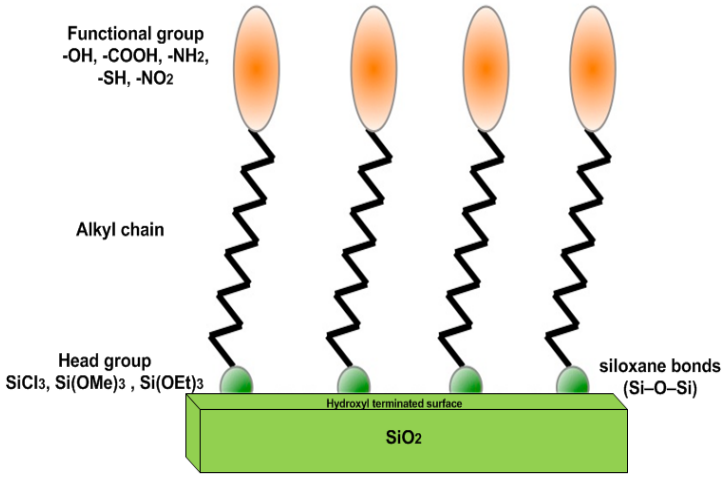

Figure 2.13: Schematic representation of functionalization of alkylsilane self-assembly Monolayers [142].

The general formula of alkylsilane $R_nSiX_{(4-n)}$ shows a dual behavior, organic and inorganic. R is organic moiety and X is a hydroxyl or a reactive hydrolysable group (–Cl, –OMe, –OEt, etc.) that reacts onto hydroxyl-terminated supports. Reaction of silane molecules to surface silanol groups of silica leads to the formation of quite stable siloxane bonds (Si–O–Si). The siloxane bond is thermally stable and is relatively chemically stable.

The functionality of silane is the number of reactive groups present at the silicon atom. Monofunctional silanes (n = 3) having only one reactive group at the silicon extremity bind to silica by means of a single bond. Multifunctional silanes (n = 1 or 2) bear several (2 or 3) reactive groups the silicon atom and can bind to the surface by several bonds. Binding by several bonds is stronger but the reaction is more difficult to be controlled in a reproducible manner [143].

(b) Alkylthiolate Monolayers

The high affinity of thiols (R–SH), disulfides (R–S–S–R) and sulfides (R–S–R) for metals (gold,

silver, copper, palladium, platinum, and mercury) drive the formation of well-defined organic surfaces with useful chemical functionalities displayed at the exposed interfaces for biosensor applications [144].

Alkanethiol SAMs on metals, and particularly on Au, have attracted considerable attention due to its ease of preparation and to the strength of the S–Au bond [145]. The general formula of alkanethiols is HS(CH2)nX. A thiol molecule consists of three parts: the sulfur head, the hydrocarbon chain (of variable length), and the terminal group, which can have different functionalities. The thiol head group acts as an anchor group which is covalently bond to the gold. The carbon chain is referred as the backbone which is assumed to stabilize the SAM due to Van der Waals interactions. The end group (or tail group) in the simplest case consists of a methyl-group. However, a lot of other functionalized end groups have been attached so far and the possibility to chemically modify the end group makes SAMs a powerful system [146].

Gold is usually the surface material of choice due to its chemical inertness and the well-defined structure of the obtained film (densely packed and ordered array of long chain molecules). Gold does not oxidize at room temperature, does not react with atmospheric oxygen and is biocompatible compared to silver that oxidizes readily in air and is toxic to cells [146].

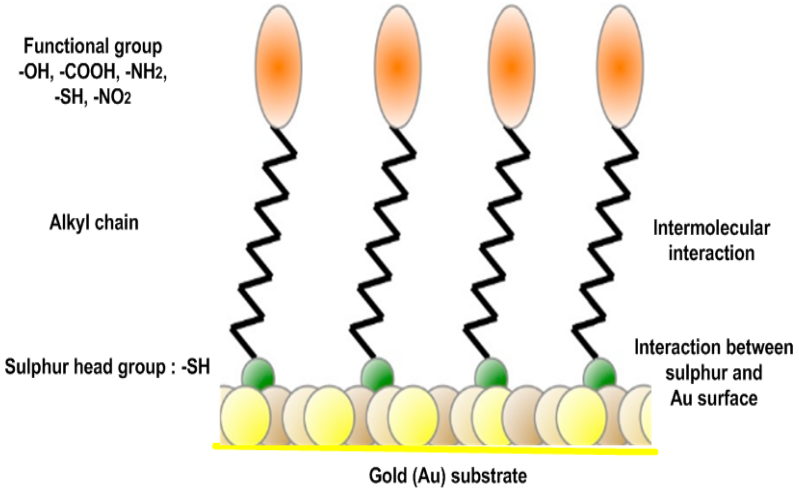

Figure 2.14: Schematic representation of functionalization of alkylthiolate self-assembly monolayers [147].

For biosensor application purpose, mixed SAMs are easily prepared. Mixed monolayers allow to control the density of the reactive species (diluting), to increase its accessibility and to bring chemical inertness to the underlying surface.

2.15 Covalent Immobilization

Currently, there is a growing interest in the covalent coupling of proteins, e.g. antibodies, to solid substrates. The use of covalent coupling procedures in DNA or protein micro-array technology and in enzyme-linked immunosorbent assay (ELISA) is increasing because of the higher robustness of this approach. For immunosensor applications the affinity biosensor interface consists of antibodies, which are preferably covalently attached onto the transducer surface. In most cases, the surface should be activated before the attachment of proteins [148].

Covalent immobilization method involves formation of a covalent bond between the sensor surface and a biorecognition element such as a protein, enzyme, antibody or DNA. The biorecognition elements cannot be coupled directly to the surface. Therefore, a chemical modification of the surface is performed before the biomolecule immobilization step itself. The surface modification often involves several steps, at least two. The most difficult step of the grafting process is the binding of the biomolecule. Indeed it has to accommodate the different constraints presented above: aqueous solvent, low concentration, low temperature, etc. The strategy consists in choosing the grafting reaction of the biomolecule first and adapting the surface functionalization to this choice. Once the chemical functionality of the surface is chosen, a process is devised for attaching this reactive function to the surface. The surface chemistry of the transducer is the next constraint to be managed. Indeed, the transducer is not chosen for its ability to be grafted but for its sensitivity to the

chemical signal. Typical surfaces are inorganic materials such as silica, glass, gold, etc. There is not so much choice regarding reactions and reagents for grafting organic molecules to such inorganic surface. The involved chemistry is often quite vigorous, that is, not compatible with the functionality to be attached. For example, silanes cannot contain carboxylic acid or hydroxyl group; primary amino group is compatible with ethoxysilane but reacts strongly with chlorosilane. Because of this limitation, a coupling agent is often used in a second step after the first derivatization step performed directly on the transducer surface. A coupling agent is a difunctional molecule that reacts by one end to functionalized surface and leaves its second group for further reaction with the biomolecules. Coupling agents (Figure 2.15) are either homodifunctional if the two reactive functions are identical (e.g. phenylenediisothiocyanate) or heterodifunctional if they are different. The coupling agent is used for functionalization of the surface and/or for the chemical modification of the biomolecules as well [149].

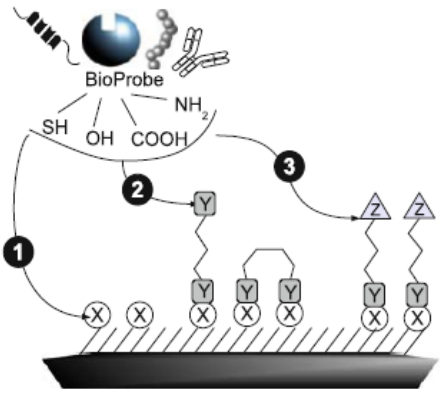

Figure 2.15: Main strategies of chemical grafting; (1) direct reaction to active surface, (2) activation of the surface with homodifunctional linker, and (3) activation of the surface with heterodifunctional linker [149]

2.15.1 Main coupling strategies

There are three main types of coupling chemistry, which utilize, respectively, amine (e.g. lysine), thiol (cysteine) or aldehyde (carbohydrate) functional groups on glycoproteins. All covalentcoupling methods utilize free carboxymethyl groups on the sensor surface. They can therefore be used for any of the sensor chips that have such carboxymethyl groups. If the protein to be immobilised has a surface exposed disulphide or a free cysteine, ligand-thiol coupling is probably the method of choice. Failing this, amine coupling should be tried in the

first instance. If amine coupling inactivates the protein, aldehyde coupling can be attempted, provided that the protein is glycosylated [150].

(a) Amine Coupling

Amine coupling is the most generally applicable covalent coupling chemistry used to immobilize protein ligands. Immobilization is via free primary amine groups such as lysine residues that are abundant in most proteins or the N-terminus of proteins and peptides [151]. This procedure has several advantages including:

- Highly versatile as the vast majority of biomolecules may be immobilized without derivatization, or without requiring tags.
- Produces a highly stable covalent bond that prevents ligand from leaching from the surface.
- Is effective over a wide pH range
- Does not require exposure of the biomolecule to harsh conditions
- Immobilization conditions are easily controlled to prevent excessive cross-linking with the surface
- Reagents may be prepared and stored frozen for a few months

(b) Thiol Coupling

Covalent coupling strategies using thiol groups allow site-specific reactions. The sulfur atom of cysteine belongs to form a sulfhydryl (or thiol) group. The low likelihood of cysteine's presence or accessibility in protein restricts the use of thiol groups to immobilization of native molecules [152]. This turns out advantageous in order to introduce solvent accessible reactive groups on protein surface. Cysteine residues involved in disulfide bonds can be chemically or enzymatically cleaved [153] before a subsequent reaction with activated surfaces.

Thiol groups allow very specific reactions because they are very reactive toward various chemical functions that are quite stable in water. The simplest approach is the reaction of thiol group onto supported thiol groups by formation of disulfide linkage. But disulfide bonds are unstable under reducing conditions. Alternatives involve formation of stable thioether bonds by Michael addition on maleimide groups or reaction with haloacetamide groups.

Thiols are prone to self-oxidation. The reactions of oxygen with thiols in aqueous solution give disulfides quite easily (pH 7–9). Radiolytic oxidation is also possible [154].

(c) Aldehyde Coupling

Aldehyde coupling involves the formation of a hydrazone bond via condensation of hydrazide groups on the sensor surface with aldehyde groups on the ligand molecule. These aldehyde moieties may be native to the protein or introduced through mild oxidation of cis-diols present in the ligand molecule. Aldehyde coupling is particularly useful for site directed immobilization of glyco-conjugates, glyco-proteins, and polysaccharides, and may also be useful for orientation-specific immobilization of proteins containing functional groups that may be converted to aldehyde moieties [155].

2.16 Non-covalent Immobilization (Streptavidin–Biotin System)

The strong interaction between avidin and biotin was discovered as early as 1941 [156]. Avidin is a protein commonly purified from chicken egg white while biotin is a vitamin found in all cells. Streptavidin, a bacterial homologous protein to avidin, isolated from the actinobacterium Streptomyces avidinii, is more frequently used than avidin and is commercially available also in a number of engineered forms [157].

The binding between avidin/streptavidin and biotin has long been regarded as the strongest, noncovalent, biological interaction known, having a dissociation constant, K_d, in the order of

4×10^{-14} M [4]. The bond formation between biotin and avidin/streptavidin is very rapid. Once bond is formed, it is unaffected by extremes of organic solvents, pH, temperature, and other denaturing agents [158].

The strong interaction has led to a large number of research and diagnostic applications using avidin-biotin or streptavidin-biotin technology. The strength and reliability of the interaction underlie its importance in biotechnology, but the interaction is also a model for high-affinity receptor ligand binding. In most assays, streptavidin is coupled to a solid phase, such as a biosensor chip, while biotin is coupled to the moiety of interest, often a nucleic acid, protein, or antibody [159] as shown in Figure 2.16.

Streptavidin is a protein and has four high affinity binding sites for the small water soluble vitamin biotin. The Biotin can be combined to a variety of biomolecules including antibodies and many biotin molecules can be attached to a single molecule of protein. The biotinylated protein can thus bind to more than one molecule of Streptavidin [161].

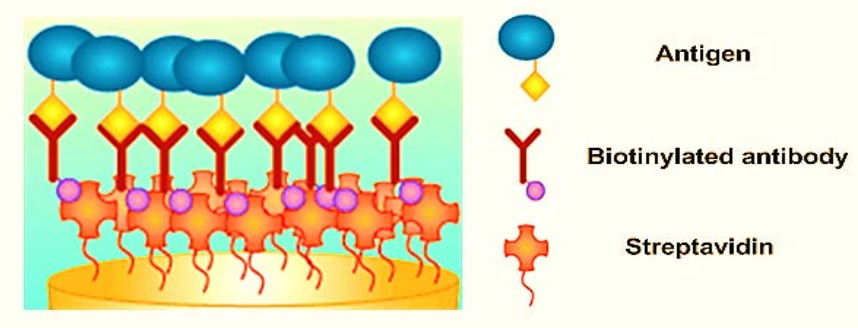

Figure 2.16: Schematic representation of Streptavidin–Biotin immobilization [160].

2.17 Physical Entrapment

In this method, the biorecognition element is entrapped within the body of a matrix such as sol–gel processed glass. The sol–gel process has emerged as powerful approach to immobilize heat sensitive and fragile biorecognition elements such as enzymes, proteins, antibodies etc. This is due to its simplicity of preparation, low-temperature encapsulation, easy for immobilization, chemical inertness, tunable porosity, optical transparency,

mechanical stability, and negligible swelling behavior [162].

The two major advantages with a sol–gel system is that it can retain a large content of water; this feature makes the encapsulated bio-recognition agents or enzyme catalytic centers long-term stable and the process can be performed at room temperature [163] Furthermore, the use of a porous matrix such as a sol–gel processed glass, where the size of porosity can be tailored, offers the opportunity to introduce size-dependent specificity toward analytes [164]. A disadvantage of this method is that the biomolecules are randomly oriented. Therefore, many of them may have their active sites buried in the matrix, thus unavailable.

The sol–gel process involves hydrolysis of alkoxide precursors under acidic or basic conditions, followed by condensation and polycondensation of the hydroxylated units, which leads to the formation of a porous gel. The resulted sol–gel is an interconnected rigid network with pores of sub-micrometer dimensions and polymeric chains whose average length is greater than a micrometer [165].

The Sol–gel processed glass containing the entrapped biorecognition elements have been used in the forms of films, coatings, or monoliths. In recent biosensor work, the surface of an optical sensing element (fibre, waveguide, or a surface plasmon resonance device) has been coated by a sol–gel processed film [166].

2.18 Numerical Method Analysis

Advances made in modern device fabrication techniques and the continuous emergence of novel exotic materials has resulted in fibre and integrated optic waveguides and related components used in today's optical biosensors having an intricate geometry and having materials with complex refractive indices. A robust and highly accurate simulation method is often required to address the challenges in defining and characterizing such waveguides and

devices. Defining and characterizing such waveguides can be performed with various methods which can be classified into analytical approximation solutions and numerical solutions through computer aided simulations. Analytical approximation solutions are very widely used in many applications for the determination of the propagation characteristics of various types of optical waveguides, with relatively simple geometry. Such solutions are the Marcatili Method [167], the Effective Index Method [168], and the Equivalent Network Method (ENM) [169].

For three dimensional waveguides which are more commonly used in today's photonics systems and circuits, analytical solutions in compact form are not always obtainable. In addition, the analytical solutions do not always treat the modes in complex waveguides as hybrid modes but rather as purely of a single polarization. For that reason their accuracies are sometimes questionable in certain cases. Whenever exact analytical solutions are not available, approximate methods are often sought. Most engineering problems involve the derivation of partial differential equations, relating the variables of interest, which are based on physics and engineering principles. The development of approximate methods for the numerical solution of partial differential equations has attracted the attention of mathematicians, physicists and engineers for a long time. There are number of approximate theoretical and numerical technique that could be used to determine the useful characteristics of propagation in waveguides.

2.19 Numerical Approximation Solutions

The numerical solutions of waveguides can be classified into two groups. These are the domain solutions, also known as differential solutions, in which the whole domain of the optical waveguide is considered as the operational area, and the boundary solutions, also known as integral solutions, which include only the boundaries as the operational area. The Variational Method (VM), the Finite Element Method (FEM), the Finite Difference Method

(FDM), and the Multilayer Approximation Method (MAM) are some of the most commonly used domain solutions, while, the Boundary Element Method (BEM), the Point Matching Method (PMM) and the Mode Matching Method (MMM), are typical boundary solutions [170].

Most of the numerical solutions are concerned with methods of finding a numerical solution to the Helmholtz's wave equation, which can be derived directly from Maxwell's equations and can be expressed as [171]:

$$\nabla^2\varphi + \kappa^2\varphi = 0 \tag{2.20}$$

Equation (2.20) is valid over the entire cross section of an arbitrarily shaped waveguide, bounded by the closed curve. The equation is also subject to boundary conditions which can be of both Dirichlet and Nuemann type. In Dirichlet type, the boundary condition is enforced by forcing $\Phi = 0$ whereas for the Nuemann type this is enforced by $\partial\Phi/\partial n = 0$ where Φ is the corresponding field (E or H), k is the wavenumber and n is the normal unit vector.

2.19.1 The Variational Method

In the variational approach, a field solution of the optical waveguide problem, usually based on the wave equation is assumed, where the unknown parameters are chosen to match the assumed field to the actual field solution. The above solution is then expressed in integral form, in terms of a functional satisfying the boundary conditions of the problem. By minimizing the expression, the stationary value of the functional about the correct solution, with respect to small variation of the field values, is achieved. Then by using trial functions to represent the field solutions, the integral equations are reduced to a set of linear equations which can be solved by standard numerical techniques. The accuracy of the results depends on the choice of the trial functions [172], which must be sufficiently differentiable and satisfy the boundary conditions. The variational method forms the basis of

other fundamental numerical techniques, such as the Finite-Element and the Finite-Difference methods, which are discussed in the following sections.

2.19.2 The Finite Difference Method

The finite difference method (FDM) [173] is one of the most rigorous and perhaps the most commonly used numerical method used for the solution of boundary value problems. In FDM, a finite cross-section is defined by enclosing the optical waveguide under investigation in a rectangular box, where the side walls may be either electric or magnetic walls, in order to include coupled structures. At the boundaries of the enclosing rectangular box, the fields are assumed to be negligibly small therefore infinite elements with an associated decay factor can be introduced, to approximate the infinite exterior region. The cross-section of any non-homogeneous optical waveguide is implemented by a rectangular grid, where it is essential that all the dielectric boundaries must lie on points of the above grid. By considering any arbitrary nodal point of the rectangular grid, the corresponding nodal field value can be expressed in terms of the neighbouring nodes, in the two transverse directions, by the five point formula of infinite differences, which is based on a Taylor series expansion. The Helmholtz wave equation (shown earlier in equation (2.20), or a variational expression, can be arranged into a set of two coupled wave equations, one for each transverse direction H_x and H_y, which can be discritized in the five point finite difference form. By imposing the correct continuity conditions of the fields between the adjacent cells of the grid, an eigenvalue matrix equation of the type $[A]x - \lambda [B]x = 0$, can be formed (where λ is the eigenvalue), which can be solved by using sparse matrix techniques.

The main disadvantage of finite difference methods are the lack of geometrical flexibility in fitting irregular boundary shapes, and in concentrating points in regions of the solution domain where the variable changes rapidly. Moreover, using the finite difference methods

difficulties also arise in treating singular points and when any boundary or interface boundary does not coincide with constant coordinate surfaces.

2.19.3 The Beam Propagation Method

The research on integrated optical circuits (IOC) and optical planar devices has emerged from the necessity of calculating the propagation of a light wave in an optical circuit having an arbitrary refractive index distribution. This type of field propagation can be simulated numerically by the beam propagation method (BPM), an approach that was developed in underwater acoustics and seismology before it was adapted to optical waveguide problems by Feit and Fleck [174]. Since then, it has been widely used for analyzing the performance of a light beam propagated in an optical planar circuit that has a nearly stripelike waveguiding structure and in which the refractive index varies smoothly compared with the wavelength. The main features of the BPM are that the electromagnetic fields are Fourier transformed with respect to the direction normal to that of light propagation and that a stepwise method is used for successively calculating the electromagnetic field along the axial direction.

In the BPM, the optical field is transported within one propagation step, from the transverse plane at the longitudinal coordinate z, to the transverse plane at $z + \Delta_z$. Calculations are performed, to relate the optical fields at the input and output planes, which are based on the assumption that the dielectric profile within one step, Δ_z, remains unchanged [188]. As the optical field propagates through a medium, it is subject to diffraction due to its wave nature, and the light rays of the wave experience a certain amount of phase shift, depending on their x; y positions. The above influences can be applied one at a time, provided that the space along the path is subdivided into very small sections, Δ_z. By doing so, the continuous medium can then be realized as a series of lenses separated by short sections of homogeneous space, where the contribution of the lenses in the phase shift is expressed in the solution of the wave equation. For computational purposes, the wave between the

lenses can be decomposed into its spectrum of plane waves by applying a Fast Fourier Transform (FFT) algorithm, and then it is reconstructed halfway, (Δ_z / 2), before the next lens, by applying the inverse FFT. The above process is repeated for each section along the whole propagation path. The propagation step size Δ_z, which must be at most one wavelength of the light beam, must ensure that the contribution of evanescent waves, which are part of the plane wave, is negligible, and that the rays associated to the wave, travel parallel to the z-axis, with minimum phase shift.

The BPM is widely accepted as the most powerful method for the analysis of non-uniform structures but it is not as efficient as the methods specifically developed for the analysis of uniform structures, where discretization's in both the transverse and the longitudinal plane are required [175]. To handle the discretization in the transverse plane, two-dimensional methods can be employed, such as the FDM [176] and the FEM [177]. The latter can be used in many devices, such as directional couplers, optical fibres, bent optical waveguides, Bragg and diffraction gratings, tapered optical waveguides and optical Y-junctions. It can also be used in conjunction with other numerical techniques such as the Fresnel approximation [178].

2.19.4 Finite Element Method

The finite element method (FEM) has emerged as one of the most successful numerical methods for the analysis of waveguides from low frequency to microwave to optical region. It is indeed capable of solving waveguide of arbitrary refractive index distribution. In the work presented in this thesis, a full-vectorial H field based FEM has been used to characterise waveguides operating at terahertz frequencies. Such methods are capable of handling a wide range of inhomogenous problems with greater ease. It is also capable of solving anisotropic problems. In this approach, any waveguide cross-section can be divided into a patchwork of triangular elements, where the appropriated field components are approximated by

polynomial expressions over these elements. Each element can have different dielectric material, which may be, anisotropic, non-linear or lossy. The FEM, which is based on the Ritz-Galerkin approach, converts a continuous system into a discretized model. By applying the variational principle [179] to the functional of the system, the problem reduces to a standard eigenvalue matrix equation $[A]x - \lambda [B]x = 0$, which can then be solved by using standard matrix solver algorithms. The FEM can be used effectively for the analysis of various optical waveguides, with any shape, including 2D and 3D optical waveguides, axisymmetrical and non- axisymmetrical optical fibre, and non-linear optical waveguides.

The FEM is based on the same principles as the FDM, therefore a comparison of the two methods can be attempted. Although in the FDM simpler matrix eigenvalue equations are formed, which are formulated with less computer programming, less computer memory storage and execution time, and the solution is free of spurious modes (H_x - H_y formulation), the above approach cannot be easily applied to structures with odd-shaped boundaries. The triangular elements used in the FEM can give a better fit to such structures and also the change of the density or the order of the elements, in regions where there is more rapid field variation, is performed more easily with the FEM. Additionally, in the FEM, the field is defined explicitly everywhere and this makes for easier manipulation, such as when evaluating spatial derivatives to give related fields [180].

2.20 Summary

This Chapter serves as the background knowledge of biosensors. The discussion started with underlying principle of evanescent wave sensing phenomenon and performance criterion of optical biosensors including sensitivity, detection limit and sensor cost. The sensitivity is an important parameter to evaluate the sensor performance. The design goal for achieving high sensitivity is to produce a structure that allows as much of the field as possible to reside in the sensing medium. For this reason various architectures of optical biosensors are elaborated

that allowed interaction of guided mode with the sensing medium so that the minimum detectable change in the sensing medium changes the effective refractive index of mode and thus to a change of the output signal. Interface between the sensor surface and the chemical or a biological system is a key component of the optical biosensors. The physical and chemical properties of the interface play an important role in achieving optimal recognition of the target and limiting the nonspecific adsorption. Bioreceptors such as enzymes, antibodies, nucleic acids, proteins, peptides and carbohydrates, surface chemistry and strategies to immobilize bioreceptors on the functionalized surface are discussed. The performance of a biosensor comes from its ability to immobilize receptors while maintaining their natural activity, the bioavailability of the receptors to targets in solution and a low nonspecific adsorption to the solid support. These specifications govern the specificity and sensitivity of such devices and can be tailored by an appropriate choice of the interface where the bioreceptors are immobilized.

3

METHODOLOGY

3.1 Introduction

Computer simulation provides an easy way to predict the optical behaviour, optimize the biosensor's performance and understand the physical principles behind the observed phenomenon in experiment. Biosensor modelling and simulation is a rich source of mathematical challenge. The main components of biosensors are based on well-understood physical processes as well as chemical and biological reactions, all of which are amenable to mathematical modelling using ordinary and partial differential equations. Finite Element Methods are well suited for solving partial differential equations. The objective of this chapter is to provide a foundation for mathematical and computational modelling of label free optical biosensors through the Finite Element Method with a view to optimising their design process. This chapter first describes simulation tool and parameters of optical biosensors then theoretical background of the Finite Element Method based on variational principle is presented.

3.2 Simulation tool and modelling parameters

FORTRAN programming is used to carry out the numerical modelling and simulation of optical biosensors. The Finite Element Method formulation of optical biosensor structures is applied in the program to perform modal analysis of these structures. The program includes mesh generation subroutine, finite element discretization for optical waveguides, assignment of

nodes, elements, and material index, boundary nodes for each layer, complex refractive index, transformation from polar to rectangular coordinates, material variation in the azimuthal generation, implementation of differential Maxwell's equations, numerical equation for calculating modal parameters, input of waveguide and biomolecular parameters and generating 2-D and 3-D modal field profiles.

The parameters used for modelling of label-free optical biosensors are shown below in the tabular form including waveguide parameters, device parameters, modal parameters and biomolecular parameters. The Finite Element Method based numerical technique is used to analyse the effects of waveguide and biomolecular parameters by varying and resolving the problem repeatedly, while an appropriate output metric such as modal and device parameters are recorded. Graphs are built relating the parameters to the results, from which optimum parameters are picked with fabrication limitations taken into consideration.

Waveguide Parameters	Device Parameters	Biomolecular Parameters	Modal Parameters
guide width	*length*	*RI of biomolecules*	*propagation*
guide height	*bending radius*	*thickness of biolayer*	*constant*
slot width	*device sensitivity*	*thickness of linker*	*effective index*
fibre diameter	*detection limit*	*thickness of DNA*	*attenuation constant*
thickness of metal	*coupling length*	*thickness of E.coli*	*power confinement*
			wavelength shift

Table 3.1: modelling parameters of label-free optical biosensors

3.3 Theoretical Background

Mathematically, the FEM is a numerical technique for obtaining approximate solutions to boundary-value problems, and it is the extension of two classical methods, the Raleigh-Ritz variational method, and the Galerkin method of weighted residuals. A boundary value problem can be defined by a governing differential equation in a domain, together with the

boundary conditions on the boundary that encloses the domain. In the variational approach the boundary-problem is formulated in terms of variational expressions, referred to as functionals, whose minimum corresponds to the governing differential equation. The approximate solution is obtained by minimising the functional with respect to its variables [181]. The Galerkin method is based on the method of weighted residuals [180], in which the domain of the differential equation is discretized, and the solution is approximated by the summation of the unknown solutions for each subdomain weighted by known functions, relating them to the domain. The overall solution is obtained by minimising the error residual of the differential equation.

Research on the application of the FEM to electromagnetic-wave engineering began during the last years of the 1960's and since then, with the availability of larger and faster computers, it has been established as a very powerful tool dealing with the analysis of optical waveguides, particularly structures with arbitrary shapes, index profiles nonlinearities and anisotropies.

A cross section of an arbitrarily shaped optical waveguide, Ω, in the *x*-*y* transverse plane, as shown in Figure 3.1, is considered, divided into a number of sub-domains, called elements, being composed of several different materials, each of which can be described by arbitrary permittivity and permeability tensors, $\hat{\varepsilon}(x,y)$ and $\hat{\mu}(x,y)$ respectively. A uniform shape of the waveguide along the longitudinal *z*-axis, is assumed and time and axial dependencies are given by $\exp(j\omega t)$ and $\exp(-\gamma z)$, where, ω is the angular frequency and the complex propagation constant, γ, given by:

$$\gamma = \alpha + j\beta \tag{3.1}$$

where α (Np/m) is the attenuation constant and β (rad/m) is the phase constant.

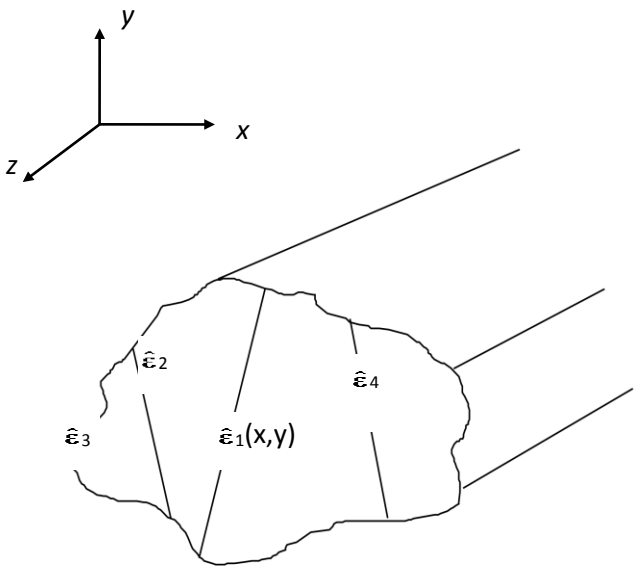

Figure.3.1 Arbitrarily shaped optical waveguide, divided into arbitrary sub-domains, each having different type of material.

For the loss-free case the propagation constant is considered to be equal to the phase constant, $j\beta$. The electric, **E**(*x,y,z,t*), and the magnetic, **H**(*x,y,z,t*) fields over the region of the waveguide can be expressed by:

$$\mathbf{E(x,y,z,t) = E(x,y)[expj(\omega\, t - \beta z)]} \tag{3.2}$$

$$\mathbf{H(x,y,z,t) = H(x,y)[expj(\omega\, t - \beta z)]} \tag{3.3}$$

where **H**(*x,y*) and **E**(*x,y*), are the spatial time-independent electric and magnetic fields respectively.

3.3.1 Basic Equations

For the application of the FEM in the analysis of optical waveguide problems, some fundamental electromagnetic field equations should be considered, such as the Maxwell's equations, the boundary conditions and the Helmholtz's wave equations.

3.3.1.1 Maxwell's Equations

Maxwell's equations comprise a set of four electromagnetic field vectors, which represent the governing laws of the electromagnetic wave phenomena. The four vectors are: the electric field intensity **E** (Volts/meter), the magnetic field intensity **H** (Amperes/meter), the electric flux density **D** (Coulomb/meter^2) and the magnetic flux density **B** (Tesla). For source-free, time dependent fields they can be written in differential or integral form. Since, the FEM is a boundary-value problem which is defined by differential equations, Maxwell's equations are presented in differential form as follows:

$$\nabla \times \mathbf{E} + \frac{\partial \mathbf{B}}{\partial t} = 0 \qquad \text{(Faraday's law)} \qquad (3.4)$$

$$\nabla \times \mathbf{H} - \frac{\partial \mathbf{D}}{\partial t} = 0 \qquad \text{(Maxwell-Ampere law)} \qquad (3.5)$$

$$\nabla \cdot \mathbf{D} = \rho \qquad \text{(Gauss's law)} \qquad (3.6)$$

$$\nabla \cdot \mathbf{B} = 0 \qquad \text{(Gauss's law-magnetic)} \qquad (3.7)$$

where ρ, is the (scalar) electric charge density (Coulomb/meter^3).

The associated constitutive equations for the medium can be written as:

$$\mathbf{D} = \varepsilon \mathbf{E} \qquad (3.8)$$

$$\mathbf{B} = \mu \mathbf{H} \tag{3.9}$$

where ε, is the permittivity and μ the permeability of the medium and can be defined by:

$$\varepsilon = \varepsilon_0 \varepsilon_r \tag{3.10}$$

$$\mu = \mu_0 \mu_r \tag{3.11}$$

where ε_0, ε_r, μ_0, μ_r are the permittivity of the vacuum (8.854 x10^{-12} Farad/meter) , the relative permittivity of the medium, the permeability of the vacuum (4π x 10^{-7} Henry/meter) and the relative permeability of the medium respectively.

Additionally, the flow of energy carried by an electromagnetic field is expressed by the Poynting vector **S** (W/m^2) and can be expressed by:

$$\mathbf{S} = \mathbf{E} \times \mathbf{H} \tag{3.12}$$

3.3.1.2 Boundary Conditions

Boundary conditions are conditions that must be met at the boundary surface when two different media 1 and 2 come into contact. If the unit normal vector ***n***, is directed from medium 1 to medium 2, as shown in Figure 2.2, in the absence of any surface currents (J=0) and surface charges (ρ=0), the following boundary conditions apply:

1) The tangential component of the electric field must be continuous

$$\mathbf{n} \times (\mathbf{E}_1 - \mathbf{E}_2) = 0 \tag{3.13}$$

2) The tangential component of the magnetic field must be continuous

$$\mathbf{n} \times (\mathbf{H}_1 - \mathbf{H}_2) = 0 \tag{3.14}$$

3) The normal component of the electric flux must be continuous

$$\mathbf{n}.(\mathbf{D}_1 - \mathbf{D}_2) = 0 \tag{3.15}$$

4) The normal component of the magnetic flux density must be continuous

$$\mathbf{n}.(\mathbf{B}_1 - \mathbf{B}_2) = 0 \tag{3.16}$$

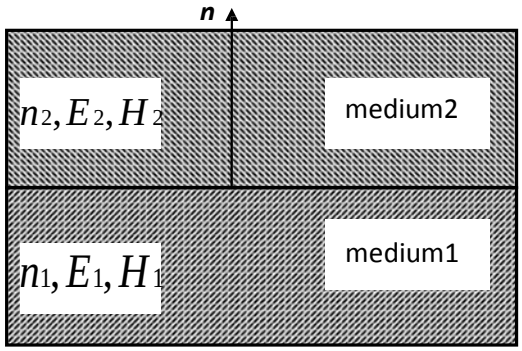

Figure.3.2 Boundary between two media of refractive indices n_1 and n_2, where ***n***, is the unit vector normal to the interface.

In certain cases, one of the two media can be considered, either as a perfect electric conductor or a perfect magnetic conductor. When one of the two media becomes a perfect electric conductor, an *electric wall* boundary condition is imposed as:

$$\mathbf{n} \times \mathbf{E} = 0 \quad \text{or} \quad \mathbf{n}.\mathbf{H} = 0 \tag{3.17}$$

Such condition ensures the continuity of the normal component of the electric field vector, **E**, and vanishes the magnetic field vector, **H**, at the boundary. When one of the two media becomes a perfect magnetic conductor, a magnetic wall boundary condition is imposed as:

$$\mathbf{n} \times \mathbf{H} = 0 \quad \text{or} \quad \mathbf{n}.\mathbf{E} = 0 \tag{3.18}$$

The above condition, vanishes the electric field vector, **E**, and ensures the continuity of the normal component of the magnetic field at the boundary.

3.3.1.3 Natural and Forced Boundary Conditions

In the case of a closed surface, such as the boundary of an optical waveguide, additional boundary conditions are considered. These boundary conditions can be *natural*, in cases where the field decays at the boundary, therefore they can be left free. In some other cases they can be *forced*, in order to take advantage of the symmetry of a waveguide, to reduce the number of elements in FEM (and the order of the matrices), or to impose complementary symmetry to the waveguide, in order to achieve the required polarization. The above boundary conditions can be classified as follows [180]:

$$\varphi = 0 \qquad \text{(Homogeneous Dirichlet)} \qquad (3.19)$$

$$\varphi = \kappa \qquad \text{(Inhomogeneous Dirichlet)} \qquad (3.20)$$

where φ can be the Electric (E), or Magnetic (H) field, and k is a prescribed constant value.

$$\partial\varphi/\partial\mathrm{n} = 0 \qquad \text{(Homogeneous Neumann)} \qquad (3.21)$$

where ***n*** is the unit vector normal to the surface.

The Neumann boundary conditions represents the rate of change of the field when is directed out of the surface, and it can be used in the FEM to impose the field decay along finite-elements, adjacent to the boundary elements of a waveguide structure.

3.3.1.4 Wave Equations

In an isotropic lossless medium with no wave source (J=0, ρ=0), with uniform permeability $\mu=\mu_0$, and uniform and constant permittivity, by eliminating the magnetic flux density in and the electric flux density components from Maxwell's equations, (3.5) and (3.6) respectively, these can be written as :

$$\nabla^2 \mathbf{E} + \kappa^2 \mathbf{E} = \mathbf{0} \tag{3.22}$$

$$\nabla^2 \mathbf{H} + \kappa^2 \mathbf{H} = \mathbf{0} \tag{3.23}$$

where the wavenumber, *k* (rad/m) is

$$\kappa = \omega\sqrt{\varepsilon\mu_0} \tag{3.24}$$

If $\varepsilon=\varepsilon_0$, then the wavenumber k_0, is called free space wavenumber and is defined by:

$$\kappa_0 = \omega\sqrt{\varepsilon_0\mu_0} \tag{3.25}$$

Equations (3.22) and (3.23) are known as vector Helmholtz wave equations [181] for homogeneous media, and in addition to the physical solutions, they also support non-physical, spurious solutions, since the condition ∇**.**H=0, is not satisfied.

In a rectangular coordinate system, if only one component of the electric or magnetic field is considered, suppose E_x, vector Helmholtz wave equation can lead to the scalar Helmholtz wave equation as [171]:

$$\nabla^2 \mathrm{E}_x + \kappa^2 \mathrm{E}_x = 0 \tag{3.26}$$

3.4 Variational Formulations

The finite-element formulation is based on the variational or Raleigh-Ritz approach, therefore, several variational formulations have been proposed for the analysis of the optical waveguide problem. These can be in a scalar form [182], where the Electric or Magnetic field is expressed only in terms of one component, according to the predominant field component, or, can be in vector form, where the Electric or Magnetic field is expressed in terms of at least two of the constituent field components.

It should be noted that most of the formulations applied in the finite element method, yield to a standard eigenvalue problem:

$$[\mathrm{A}]\{x\} - \lambda[\mathrm{B}]\{\times\} = 0 \tag{3.27}$$

where A and B are real symmetric sparse matrices, and B is also positive definite. The eigenvalue λ, can be chosen as β^2 or k^2, depending on the formulation, and the eigenvalues represent the nodal field values of the finite-elements. It is desirable for the above matrix equation to be of this canonical form, to allow an efficient solution.

3.4.1 Scalar approximation

Scalar approximation can be applied in situations where the field can be described as predominantly TE or TM and it can be expressed in terms of the longitudinal components of the above modes. It has been used for the solution of homogeneous waveguide problems [183], open boundary problems [184], and for the analysis of anisotropic waveguides [185]. For the quasi-TE modes over a region Ω, where the dominant field component is E_x, the formulation can be written as [183]:

$$L = \iint_{\Omega} \left[\left(\frac{\partial E_x}{\partial x} \right)^2 + \left(\frac{\partial E_x}{\partial y} \right)^2 - k_0 n^2 E_x^2 + \beta^2 E_x^2 \right] d\Omega \tag{3.28}$$

where, β is the propagation constant and *n* is the refractive index. For the quasi-TM modes, where H_x is the dominant field component, the formulation can be written as [183]:

$$L = \iint_{\Omega} \left[\frac{1}{n^2} \left(\frac{\partial H_x}{\partial x} \right)^2 + \frac{1}{n^2} \left(\frac{\partial H_x}{\partial y} \right)^2 - k_0 H_x^2 + \frac{1}{n^2} \beta^2 H_x^2 \right] d\Omega \tag{3.29}$$

3.4.2 Vector formulations

The scalar formulation is inadequate to handle general anisotropic or inhomogeneous problems and it can be used only as an approximation in such cases. For a more accurate representation of general waveguide fields, a vector formulation, with at least two components is essential. Several vector formulations dealing with optical waveguide problems have been proposed by many authors. However, some of them are affected by non-physical spurious solutions, which appear mixed with the correct ones in the computations, and therefore several methods have also been proposed to overcome such problems.

The E_z-H_z formulation which is one of the first formulations used in finite-element analysis [183] , [185] cannot treat general anisotropic problems without destroying the canonical form of the eigenvalue equation (3.27), and also some problems arise in enforcing boundary conditions for a waveguide with an arbitrary dielectric distribution. Additionally, this approach is based on the axial field components which are the least important of the **E** and **H** fields.

A vector **E**-field formulation [186], [187], [188] which can handle general anisotropy, but loss-less problems, has also been applied to the solution of several types of optical waveguides. For such a formulation, the natural boundary conditions correspond to a magnetic wall, and

therefore it is essential to enforce the electric wall (***n***×**E**=0) as a boundary condition, which is difficult to implement for irregular shaped structures.

The vector **H**-field formulation is more suitable for dielectric waveguide problems, because the magnetic field is continuous everywhere, and the natural boundary conditions correspond to those of the electric wall, therefore no forced boundary conditions at the boundaries are required. This formulation can be written as [189], [190]:

$$\omega^2 = \frac{\int (\nabla \times \mathrm{H})^* . \hat{\varepsilon}^{-1} . (\nabla \times \mathrm{H}) \mathrm{d}\Omega}{\int \mathrm{H}^* . \hat{\mu} . \mathrm{H} \mathrm{d}\Omega} \tag{3.30}$$

where ω, is the natural frequency, Ω is the waveguide cross-section and $\hat{\varepsilon}$and $\hat{\mu}$ are the permittivity and permeability tensors respectively. To obtain the stationary solution of the functional (3.30), the expression is minimised with respect to each of the variables, which are the unknown nodal field components H_x, H_y and H_z. This minimisation leads to a matrix eigenvalue equation as stated in equation (3.27), where **[A]** is a complex hermitian matrix and **[B]** is a real symmetric and positive-definite matrix. Because of the general 90^0 phase difference between the axial and transverse components of **H** [191] the Hermitian matrix **[A]** can be transformed to a real symmetric matrix for a loss-less problem. In general, the matrices **[A]** and **[B]** are quite sparse. The eigenvectors {x} represents the unknown field components at the nodal points for different modes with λ as their corresponding eigenvalues and also λ is proportional to ω^2. In order to obtain a solution for a given wavelength, the propagation constant, β value has to be changed iteratively until the output eigenvalue corresponds to that wavelength. By varying β over the range of interest, it is possible to calculate the dispersion characteristics for the various modes.

However, the above formulation (as well as the E-field), yields spurious solutions, because the divergence condition, ∇**.H**=0 is not satisfied, therefore alternative approaches, such as the

penalty coefficient method [190], [192] have been proposed to eliminate those non-physical solutions. This method will be discussed in a later section.

3.4.3 Natural Boundary Conditions

The term natural boundary condition arises in the calculus of variations, and since the finite element method is fundamentally one of minimisation of an error functional, the term arises also in this context. The boundary condition, which is automatically satisfied in the variational procedure, is called the `natural boundary condition'. In variational formulations these can be automatically satisfied, if left free. The scalar functional defined earlier in equation (3.28) has the continuity of $\partial E_x/\partial n$ as the natural boundary condition, and the functional defined in equation (3.29) has the continuity $(1/n^2)$ $(\partial H_x/\partial n)$ as the natural boundary condition, where **n** is the outward normal unit vector. The vector H-field formulation described in equation (3.30), has the natural boundary condition of an electric wall, i.e. $n \cdot \mathbf{H} = 0$. Therefore there is no need to force any boundary condition on conducting guide walls. But for regular shaped waveguides and at the symmetric walls (if applicable) the natural boundary condition can be imposed to reduce the matrix problem size. However, it may be necessary to analyse the structure with complementary symmetry conditions to obtain all the modes, although the exploitation of the symmetry greatly reduces the computational cost.

The key to using the finite element method is to find the solution of a complicated problem by replacing it with a simpler one. The differential operator equations which describe the physical problem are replaced by an appropriate extremum functional J, which is the variational for the desired quantity. The problem can be regarded as obtaining the solution H over a specified region in the transverse plane so that the boundary conditions and also the extremum requirement are satisfied. The axial dependence is assumed in the form $e^{-j\beta z}$, and the transverse plane is used for the discretisation.

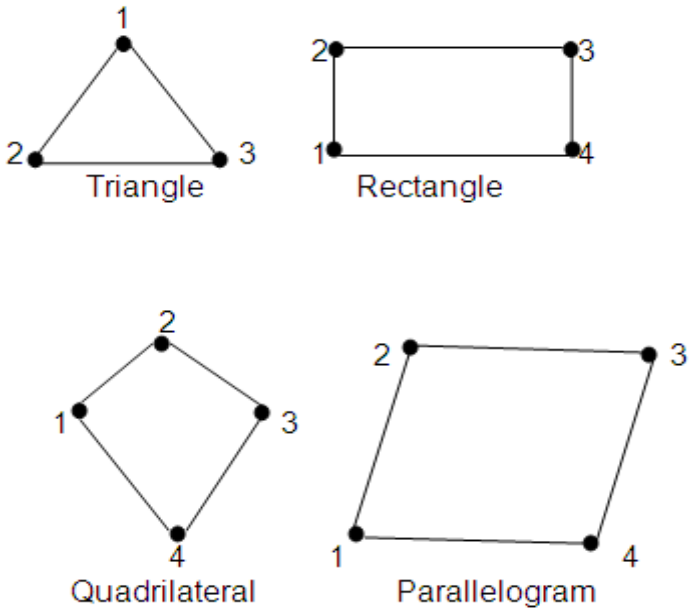

Figure 3.3: Finite elements in two-dimension

3.5.1 Domain Discretisation

The discretisation of the domain into sub-regions (finite elements) is considered as the initial in the finite element method. The shapes, sizes, number and configurations of the elements have to be chosen carefully such that the original body or domain is simulated as closely as possible without increasing the computational effort needed for the solution. Each element is essentially a simple unit within which the unknown can be described in a simple manner. There are various types of elements available for use in finite element formulations. These elements can be defined to be as one, two and three dimensional elements. When the geometry and material properties can be described in terms of only one spatial coordinate, then a one-dimensional element can be used. However, when the configuration and other details of the problem can be described in terms of two independent spatial coordinates, the two-dimensional elements shown in Figure 3.3 can be used. The simplest and indeed the most basic element typically considered for two-dimensional analysis is the triangular element. The size of the element also dictates the accuracy of the final solution as the higher order elements

tend to provide more accurate solutions. A typical representation of an arbitrary waveguide structure using triangular elements is shown in Figure 3.4. By dividing the waveguide cross section into triangular elements, the unknown **H**

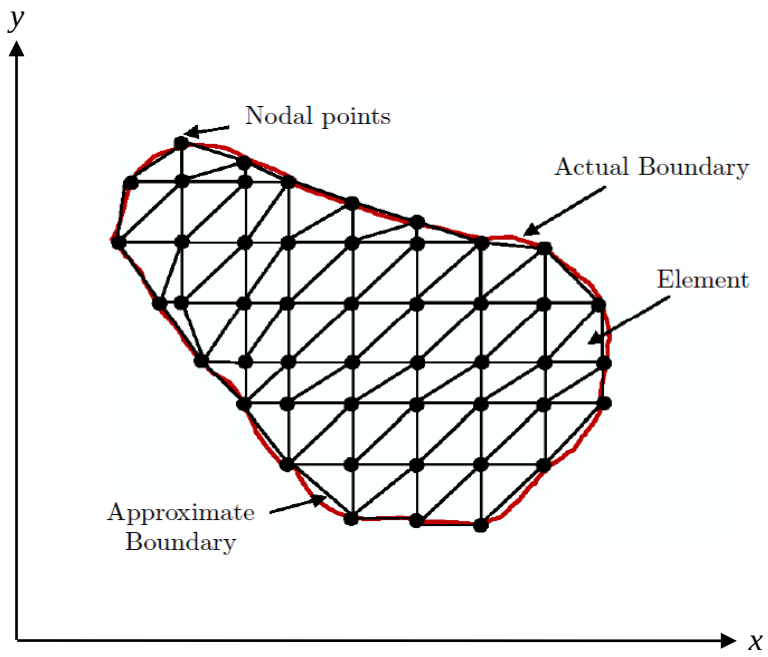

Figure 3.4: Finite element discretisation of a waveguide with triangular elements

is discretised into corresponding sub-regions. These elements are easier to analyse rather than analysing the distribution over the whole cross section. As shown in Figure 3.4, the transverse plane is covered with a grid of discrete nodes which are the vertices of each triangular element. The values of **H** at these nodal points are the basic unknowns. The intersections of the sides of the triangular elements are called the nodal lines.

3.5.2 Shape Functions

In two-dimensional problems, the element assumes a linear interpolation between the field values at the vertices of the triangle. Within each element the unknown field **H**, is approximated by means of suitably chosen set of polynomials. These functions are called shape functions. For a simple triangular element the interpolation polynomial should include a constant term and both the x and y terms rather than only one of them. The field variable

representation within an element should not alter the local co-ordinate system. In order to achieve this geometric isotropy, the polynomial should be complete according to Pascal's triangle as shown in Figure 3.5. The final consideration in selecting the order of the interpolation polynomial is to make the total number

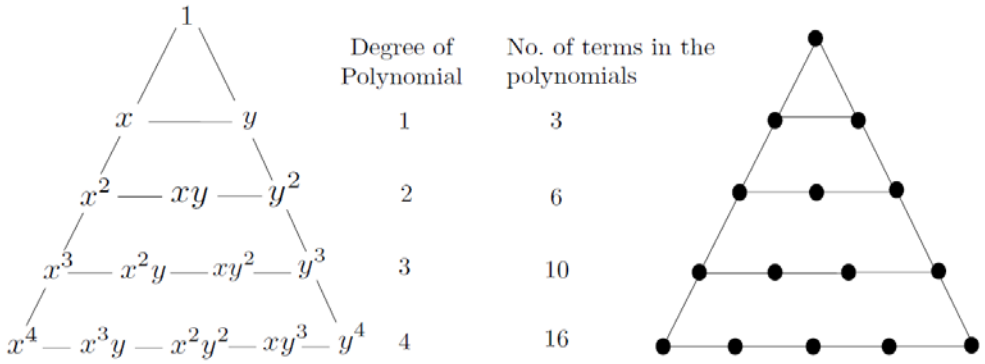

Figure 3.5: Pascal's triangle for complete polynomials in two dimensions

of terms in the polynomial equal to the number of nodal degrees of freedom of the element. For example, the first degree polynomial involves three coefficients and so can be expressed in terms of three nodal values at the triangle vertices. The second degree polynomial needs six coefficients and can similarly be expressed in terms of values of six nodes as shown in Figure 3.5.

The continuous field function Φ(x, y) in the problem domain may be replaced by a set of discrete values (Φ_i, i = 1, 2, 3 ..... m), where m is the total number of nodes. This function will be continuous across the triangles. To be admissible functions, there must be some specific conditions between the elements usually the continuity of the field across the boundaries is preferred. A typical first order triangular element used in finite element discretisation is shown in Figure 3.6.

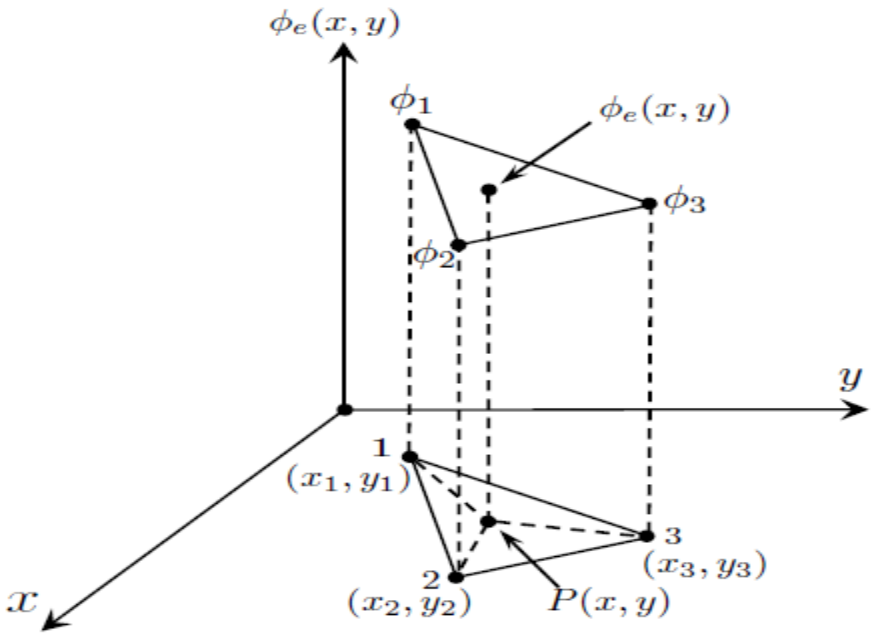

Figure 3.6: Representation of a first order triangular element

Inside each first oder element, the nodal field values Φ is interpolated continuously. This can be achieved by introducing the interpolation functions, $N_i(x, y)$. Thus, using the interpolation functions, the elemental field values can be written as:

$$\varphi_e(x,y) = \sum_{i=1}^{3} N_i(x,y).\varphi_i \tag{3.31}$$

where Φ_i are the nodal field values. The functions $N_i(x, y)$ are called `shape functions'. Equation (3.31) can also be written in matrix form as:

$$\varphi_e(x,y) = [N_1 N_2 N_3]\begin{Bmatrix}\varphi_1\\ \varphi_2\\ \varphi_3\end{Bmatrix} \tag{3.32}$$

$$\varphi_e(x,y) = [N]\{\varphi_e\} \tag{3.33}$$

where [N] is the shape function matrix and the column vector $\{\Phi_e\}$ is vector corresponding to the field values at the 3 vertices of the triangular element. In order to obtain the shape functions, $N_i(x,y)$ (where i = 1; 2; 3), a linear approximation of the of the field inside the element must be performed:

$$\varphi_e(x,y) = \alpha_1 + \alpha_2 x + \alpha_3 y \tag{3.34}$$

for which α_1, α_2 and α_3 are constants. By re-writing the above relation, such that the following conditions are satisfied:

$$\varphi_e(x_i, y_i) = \varphi_i \qquad i = 1,2,3 \tag{3.35}$$

where (x_i, y_i) (i = 1; 2; 3) are the global co-ordinates of the three vertices of the triangle. Hence the nodal field values Φ_i can be expressed as:

$$\varphi_1 = \varphi_e(x_1, y_1) = \alpha_1 + \alpha_2 x_1 + \alpha_3 y_1$$

$$\varphi_2 = \varphi_e(x_2, y_2) = \alpha_1 + \alpha_2 x_2 + \alpha_3 y_2$$

$$\varphi_3 = \varphi_e(x_3, y_3) = \alpha_1 + \alpha_2 x_3 + \alpha_3 y_3 \tag{3.36}$$

This can also be written in the matrix form as:

$$\begin{Bmatrix} \varphi_1 \\ \varphi_2 \\ \varphi_3 \end{Bmatrix} = \begin{bmatrix} 1 & x_1 & y_1 \\ 1 & x_2 & y_2 \\ 1 & x_3 & y_3 \end{bmatrix} \begin{Bmatrix} \alpha_1 \\ \alpha_2 \\ \alpha_3 \end{Bmatrix} \tag{3.37}$$

By solving the above matrix, the constants α_1, α_2, α_3 can be determined in terms of Φi; i = 1, 2, 3:

$$\alpha_1 = \frac{1}{2A_e}\left[\varphi_1(x_2y_3 - x_3y_2) + \varphi_2(x_3y_1 - x_1y_3) + \varphi_3(x_1y_2 - x_2y_1)\right]$$

$$\alpha_2 = \frac{1}{2A_e}\left[\varphi_1(y_2 - y_3) + \varphi_2(y_3 - y_1) + \varphi_3(y_1 - y_2)\right]$$

$$\alpha_3 = \frac{1}{2A_e}\left[\varphi_1(x_3 - x_2) + \varphi_2(x_1 - x_3) + \varphi_3(x_2 - x_1)\right] \quad (3.38)$$

Where A_e is the area of the triangular element given by:

$$A_e = \frac{1}{2}\begin{bmatrix}1 & x_1 & y_1\\ 1 & x_2 & y_2\\ 1 & x_3 & y_3\end{bmatrix} = \frac{1}{2}(x_2y_3 - x_3y_2) + (x_3y_1 - x_1y_3) + (x_1y_2 - x_2y_1) \quad (3.39)$$

Substituting the values of α_i from equation (3.38) into equation (3.34) results in the formation of the following equation:

$$\varphi_e(x, y) = N_1(x, y).\varphi_1 + N_2(x, y).\varphi_2 + N_3(x, y).\varphi_3$$

$$\therefore \varphi_e(x, y) = [N]\{\varphi_e\} \quad (3.40)$$

The above relation has close resemblance to the matrix relation given earlier in equation (3.33) and $N_i(x,y)_{\ i}$ = 1, 2, 3 are shape functions given by the matrix notation [180]:

$$[N]^T = \begin{bmatrix}N_1\\ N_2\\ N_3\end{bmatrix} = \frac{1}{2A_e}\begin{bmatrix}x_2y_3 - x_3y_2 & y_2 - y_3 & x_3 - x_2\\ x_3y_1 - x_1y_3 & y_3 - y_1 & x_1 - x_3\\ x_1y_2 - x_2y_1 & y_1 - y_2 & x_2 - x_1\end{bmatrix}\begin{bmatrix}1\\ x\\ y\end{bmatrix} \quad (3.41)$$

Where N_1, N_2 and N_3 are the three nodal points of the triangular element and N^T denotes a transpose of the N matrix. The shape function matrix can also be re-written as:

$$[N]^T = \begin{bmatrix} N_1 \\ N_2 \\ N_3 \end{bmatrix} = \begin{bmatrix} a_1 + b_1 x + c_1 y \\ a_2 + b_2 x + c_2 y \\ a_3 + b_3 x + c_3 y \end{bmatrix} \tag{3.42}$$

and a_i , b_i, c_i (i = 1; 2; 3) are the constants calculated as:

$$a_1 = \frac{x_2 y_3 - x_3 y_2}{2A_e}$$

$$b_1 = \frac{y_2 - y_3}{2A_e}$$

$$c_1 = \frac{x_3 - x_2}{2A_e} \tag{3.43}$$

Similarly a_2, b_2, c_2, a_3, b_3 and c_3, can be calculated by cyclic exchange of 1 → 2 →3 in equation (3.43). The shape functions N_i can also be expressed in terms of the areas of the triangle shown earlier in Figure 3.6 as:

$$N_i = \frac{\text{area of sub triangle } P_{23}}{\text{area of sub triangle } 1_{23}} \tag{3.44}$$

Similarly N_2 and N_3 can be defined in the same way. Hence, N_i has the following property:

$$\sum_{i=1}^{3} N_i = 1 \tag{3.45}$$

Thus evaluating the shape function N_1 gives a value of 1 at the node 1(x_1, y_1), whereas at nodes 2 and 3 a value of 0 is obtained. Hence it is the unique first degree interpolation function for node 1. Similarly the shape functions N_2 and N_3 gives a value of 1 at nodes 2 and 3 respectively and - at other nodes.

3.5.3 Global and Element Matrics

The solution of the optical waveguide problem by the FEM can be transformed to a standard eigenvalue problem as in equation (3.27) where matrices **[A]** and **[B]** are known as global matrices and consist of the summation of the element matrices for each triangular element of the discretised cross-section of the optical waveguide. In this section, the assembly of the element and global matrices is shown, with respect to the shape functions and the nodal field values of each triangular element, based on the variational formulation. Throughout the procedure, the full H-field formulation in terms of the three axial components is assumed and first-order triangular elements are being used. Within each of the triangular elements the three unknown field H-components Hx, Hy and Hz of the magnetic field can be represented as following:

$$\mathbf{H}_x(x,y) = [\mathbf{N}_1 \quad \mathbf{N}_2 \quad \mathbf{N}_3]\begin{bmatrix}\mathbf{H}_{x1}\\ \mathbf{H}_{x2}\\ \mathbf{H}_{x3}\end{bmatrix}$$

$$\mathbf{H}_y(x,y) = [\mathbf{N}_1 \quad \mathbf{N}_2 \quad \mathbf{N}_3]\begin{bmatrix}\mathbf{H}_{y1}\\ \mathbf{H}_{y2}\\ \mathbf{H}_{y3}\end{bmatrix}$$

$$\mathbf{H}_z(x,y) = [\mathbf{N}_1 \quad \mathbf{N}_2 \quad \mathbf{N}_3]\begin{bmatrix}\mathbf{H}_{z1}\\ \mathbf{H}_{z2}\\ \mathbf{H}_{z3}\end{bmatrix} \qquad (3.46)$$

where H*xi*, H*yi* and H*zi* for i = 1, 2, 3 are the x, y and z components of the nodal magnetic fields. Hence the magnetic field over the element $[H]e$ can be described as:

$$[H]_e = \begin{bmatrix} H_x(x,y) \\ H_y(x,y) \\ H_z(x,y) \end{bmatrix} = \begin{bmatrix} N_1 & N_2 & N_2 & 0 & 0 & 0 & 0 & 0 & 0 \\ 0 & 0 & 0 & N_1 & N_2 & N_2 & 0 & 0 & 0 \\ 0 & 0 & 0 & 0 & 0 & 0 & N_1 & N_2 & N_2 \end{bmatrix} \begin{bmatrix} H_{x1} \\ H_{x2} \\ H_{x3} \\ H_{y1} \\ H_{y2} \\ H_{y3} \\ H_{z1} \\ H_{z2} \\ H_{z3} \end{bmatrix} \tag{3.47}$$

In a more compact form, the above equation (3.46) can be written as:

$$[H]_e = [N]\{H\}_e \tag{3.48}$$

Where $\{H\}_e$ is the column vector representing the three components of the nodal field values in the element and [N] is the shape function matrix. Also using equation (3.48), the curl of H equation can be written as:

$$(\nabla \times \tilde{H})_e = \nabla \times [N]\left\{\tilde{H}\right\}_e = \begin{bmatrix} 0 & -\partial/\partial z & \partial/\partial y \\ \partial/\partial z & 0 & -\partial/\partial x \\ -\partial/\partial y & \partial/\partial x & 0 \end{bmatrix} [N]\left\{\tilde{H}\right\}_e = [Q]\left\{\tilde{H}\right\}_e \tag{3.49}$$

Where the matrix [Q] can be written as:

$$[Q] = \begin{bmatrix} [O] & \dfrac{-\partial}{\partial z} & \dfrac{\partial [N]}{\partial y} \\ \dfrac{\partial [N]}{\partial z} & [O] & \dfrac{-\partial [N]}{\partial x} \\ \dfrac{-\partial [N]}{\partial y} & \dfrac{\partial [N]}{\partial y} & [O] \end{bmatrix} \tag{3.50}$$

Where [0] = [0 0 0] and [N] = [N_1 N_2 N_3] and the some of the shape function derivatives are substituted using equation (3.43) as shown:

$$\frac{\partial N_1}{\partial x} = b_1, \frac{\partial N_2}{\partial x} = b_2, \frac{\partial N_3}{\partial x} = b_3$$

$$\frac{\partial N_1}{\partial y} = c_1, \frac{\partial N_2}{\partial y} = c_2, \frac{\partial N_3}{\partial y} = c_3 \qquad (3.51)$$

the values of the constants b_1, b_2, b_3, c_1, c_2 and c_3 were given earlier in equation (3.43). By substituting the expressions shown in equations (3.48) and (3.49) in to the variational formulation of equation (3.30), the vector H-field formulation functional for an element can be obtained as:

$$\omega^2 = \frac{\int (\nabla \times H)^* . \hat{\varepsilon}^{-1} . (\nabla \times H) d\Omega}{\int (H^* . \hat{\mu} . H) d\Omega}$$

$$\Rightarrow \omega^2 = \frac{\int_\Delta ([Q]\{H\}_e)^* . \hat{\varepsilon}^{-1} . [Q]\{H\}_e d\Omega}{\int_\Delta ([N]\{H\}_e)^* . \hat{\mu} . ([N]\{H\}_e d\Omega}$$

$$\Rightarrow \omega^2 = \frac{\int_\Delta \{H\}_e^T [Q]^* . \hat{\varepsilon}^{-1} . [Q]\{H\}_e d\Omega}{\int_\Delta \{H\}_e^T [N]^T . \hat{\mu} . [N]\{H\}_e d\Omega} \qquad (3.52)$$

Re-arranging the last part of the above equation (3.52), the following can be obtained:

$$J_e = \int_\Delta \{H\}_e^T [Q]^* . \hat{\varepsilon}^{-1} . [Q]\{H\}_e d\Omega - \omega^2 \int_\Delta \{H\}_e^T [N]^T \hat{\mu} [N]\{H\} d\Omega \qquad (3.53)$$

where Δ represents the integration over the triangular element domain. T and * denote the transpose of a matrix and the complex conjugate transpose, respectively. The [Q] matrix was defined earlier in equation (3.49). A transpose operation on this matrix would define the $[Q]^*$ matrix. For isotropic material, the relative permittivity is a scalar quantity. For waveguides consisting of anisotropic material the relative permittivity can be taken as a tensor represented by a 3 x 3 matrix and the inverse of the matrix should be implemented. The total function, J, associated with the whole cross section of the waveguide can be obtained by summing J_e of all the individual elements as:

$$J = \sum_{e=1}^{n} J_e \tag{3.54}$$

where n is the number of elements.

The minimisation of the functional given in equation (3.54) can be performed by differentiating with respect to the field nodal values and equating it to zero as below:

$$\frac{\partial J}{\partial \{H\}_e} = 0 \tag{3.55}$$

Thus the following relation can be obtained:

$$\frac{\partial J}{\partial \{H\}_e} = 2\int_{\Delta} \{H\}_e [Q]^* \hat{\varepsilon}^{-1} [Q]\, d\Omega - 2\omega^2 \int_{\Delta} [N]^T \hat{\mu}\, [N]\{H\}_e\, d\Omega = 0 \tag{3.56}$$

$$\therefore \int_{\Delta} [Q]^* \hat{\varepsilon}^{-1} [Q]\, d\Omega . \{H\}_e - \omega^2 \int_{\Delta} \mu [N]^T [N] d\Omega . \{H\}_e = 0$$

Thus the following eigenvalue equation can be obtained:

$$[A]\{H\} - \omega^2 [B]\{H\} = 0 \tag{3.57}$$

where the matrices [A] and [B] can be defined as:

$$[A] = \sum_{e=1}^{n} [A]_e = \sum_{e=1}^{n} \int_{\Delta} \frac{1}{\hat{\varepsilon}} [Q]^* [Q] d\Omega$$

$$[B] = \sum_{e=1}^{n} [B]_e = \sum_{e=1}^{n} \hat{\mu} \int_{\Delta} [N]^T [N] d\Omega \qquad (3.58)$$

Matrix {H} contains all the H-field nodal values over the whole cross section of the waveguide considered. $[A]_e$ and $[B]_e$ represent the element matrices whose assemblage over the whole cross section result in formation of the so called global matrices of the eigenvalue equation, given by [A] and [B], respectively.

When solving waveguide problems by using finite elements, the key factor affecting storage requirements and computational effort is the choice of algorithm to solve the matrix equation. The global matrices [A] and [B] shown in equation (3.58) are highly sparse. The sparsity increases with the order of the matrices and decreases with the polynomial order of the shape functions. It is obvious that using higher order basis functions, one may obtain a more accurate solution of the problem under consideration. However, the added disadvantage to that is that the process involves increasing programming effort, particularly when considering waveguide problems with material anisotropy, infinite elements and penalty functions. In addition to that using higher order polynomials for a given matrix order increases the density of the matrix although this can be handled with reasonable effort by using a sophisticated matrix solver.

3.5.4 Spurious Solution

The usage of vector formulations in analysing waveguide problems, results in generating some non-physical, spurious solutions along with the physical solutions of the system. Spurious solutions may evolve due to several reasons such as: (i) enforcement of boundary condition (ii) positive definiteness of the operator and (iii) non-zero divergence of the trial fields. In the

H-field formulation, the associated Euler equation is consistent with the two curl Maxwell's equations (3.4), (3.5), but does satisfy the $\nabla \cdot \mathbf{B} = 0$ condition which may be the reason behind the appearance of spurious modes [190].

The identification of the spurious modes amongst the physical modes can be difficult, when a set of eigenmodes is computed. Sometimes spurious modes can be spotted, from their dispersion curves, or by their eigenvectors, where the field varies in an unreasonable, sometimes in a random way along the cross section of the waveguide. Rahman and Davies [192] have developed a procedure which gives a reasonable identification of the spurious modes. In the above approach, the divergence of the magnetic field, $\nabla \cdot \mathrm{H} = 0$, is calculated for each eigenvector, and when the value obtained is high, it is assumed that the eigenmode does not satisfy the divergence condition, and therefore it is a spurious mode.

Several approaches have been used, most of them aiming to force the condition $\nabla \cdot \mathrm{H} = 0$, which is considered the main cause of spurious modes. In the method developed by Rahman and Davies [192] an integral is added the H-field formulation, so that the resulting Euler equation is the Helmholtz equation, plus the $\nabla \cdot \mathrm{B} = 0$ condition. The variational formulation then becomes as [190, 192]:

$$\omega^2 = \frac{\int (\nabla \times \mathrm{H})^* \frac{1}{\varepsilon} . (\nabla \times \mathrm{H}) \mathrm{d}\Omega + \frac{\alpha}{\varepsilon_0} \int (\nabla \cdot \mathrm{H})^* (\nabla \cdot \mathrm{H}) \mathrm{d}\Omega}{\int (\mathrm{H}^* \cdot \mu \mathrm{H}) \mathrm{d}\Omega} \qquad (3.59)$$

where α is the dimensionless penalty factor. The value of α is often taken to be around $\frac{1}{\varepsilon_n}$

where ε_n is the dielectric constant of the core of the waveguide. In this method the divergence free constraint is imposed in a least-squared sense and larger the penalty factor the more heavily the constraint is implemented giving a further reduction of the spurious modes from

the spectrum. The penalty function also improves the quality of the eigenvectors without increasing the order of the matrix in the eigenvalue problem.

3.6 Summary

The aim of this chapter was to present a theoretical background of the Finite Element Method based on variational principle to perform modal analysis of various waveguide structures. The properties of various numerical methods often used in analysing waveguide problems have been examined. An elaborate mathematical description is given for the vector H-field based FEM formulation. Several aspects of the method such as the boundary conditions, shape functions and methods aimed at eliminating spurious solutions has been extensively analysed. This chapter thus serves as the underlying principle of the numerical method used to analyse waveguides used in optical biosensing of which will be presented in the subsequent chapters.

4

METAL CLAD OPTICAL BIOSENSORS

4.1 Label-free detection of Escherichia Coli (*E.coli*)

This chapter starts with characterization of a biosensor using the finite element based numerical tools for detection of specific *E.coli* strain. Most of the *E.coli* detection systems use a reporter method to determine if two or more molecules interact. As a result, these conventional methods of pathogen detection require a number of time consuming steps to achieve at a useable measurement. However, the development and use of more effective biosensor technology could significantly reduce this time, as well as allow the detection of even smaller amounts of pathogens with fewer false positives. Today optical methods are widely used to study the interaction of molecules in fields ranging from genomics to biophysics.

Escherichia Coli (*E.Coli*) have emerged as an important enteric pathogen posing a tremendous challenge to public health. Illnesses caused by *E.Coli* can range from mild, watery diarrhoea to life threatening conditions, such as haemolytic uremic syndrome and haemorrhagic colitis [193].

E.Coli is a bacterium that commonly lives in the intestines of people and animals. The organism can be found on a small number of cattle farms and can live in the intestines of healthy cattle. Meat can become contaminated during slaughter, and organisms can be thoroughly mixed

into when it is ground. Bacteria present on the cow's udders or on equipment may get into raw milk [194-197].

Several optical sensing mechanisms have been proposed and developed so far in particular surface plasmon resonance has been exploited for the detection of pathogens. The surface plasmon resonance based sensors when compared to other biosensing techniques offer high degree of sensitivity, no labelling of biomolecules, real-time measurement of kinetics of biomolecular interaction, and immunity from electromagnetic interference [193-199].

Although, SPR in Planar structure can be more compact and integrable with other photonic devices, however, Fibre based sensors would be easy to fabricate and overall cheaper. The Fibre optic biosensors are easily miniaturized and integrated for the determination of different target compounds in a wide variety of application fields. The Fibre optic sensors consume less analyte, smaller in size, occupy less space, light in weight, more durable and have greater geometry versatility, hence, so less expensive. They also provide numerous ways of performing the rapid, remote, in-line and on-line determination of a lot types of analytes in a wide range of application fields.

In the present work, the **H**-field Finite Element Method (FEM)-based full-vector formulation in conjunction with the perturbation technique is used for the solution of the metal-clad fibre modes, where the transverse and longitudinal magnetic field components are analyzed with respect to the rectangular coordinates. Therefore, the optical fibre modes are initially presented in terms of the transverse magnetic field components, H^x_{mn} and H^y_{mn}, as commonly used for integrated optical waveguide problems, where the *m* and *n* subscripts denote the field maxima along the *x*- and the *y*-axes, respectively. As an example of this notation, the H^y_{mn} mode (also known as the quasi-TE mode) indicates that the H_y (or E_x) field is dominant compared to the non-dominant H_x (or E_y) field component.

The transverse and longitudinal magnetic field components only excite the surface plasmon waves. Excitation occurs when the surface plasmon waves and the TM modes are phase matched, resulting in a coupled wave system.

4.1.1 Modal Solution

The key modal parameters in the design of any waveguide are their propagation constants, confinement factor, loss coefficients and the modal field profiles. First of all it is essential to develop modal solution approach, which can provide this information for practical optical waveguides with arbitrary shape, size, and material profile. Practical metallic conductors are not perfect conductors and hence suffer significant loss of the electromagnetic waves, and therefore, the modelling of loss in the analysis of optical waveguides, incorporating metallic films and the interaction of the metallic films with dielectric materials in order to accommodate guided waves, is considered to be important for the accurate design of various biosensor devices. As surface plasmon technology has reached maturity, the associated devices have, themselves, become more complex. The optimisation of such advanced devices requires the accurate characterisation of their lightwave propagation characteristics. Unfortunately analytical methods are not adequate to model these advanced sensing devices without significant approximation. Only the simplest planar waveguides can be analyzed by solving their corresponding transcendental equations, which are developed by applying field continuity conditions at the interface boundaries. Even then, it is not possible to find a closed-form solution of such transcendental equations, and iterative procedures must be used to find the zeros of such equations. From the boundary conditions for multilayered planar structures, a matrix equation can be generated, and similarly the roots of the determinants can be found iteratively, to yield that propagation constant of such planar structures. However, in all practical optical waveguides the optical power is confined in both the transverse directions, and for such a waveguide, an analytical solution is not possible. It is not possible to find an

exact analytical solution for even the simplest arrangement, i.e. one with perfect circular symmetry, a step-index difference between core and cladding, and infinite cladding. Therefore the optimisation of existing realistic designs or the evaluation of new designs has created great interest in the development and use of effective numerical methods. Hence there is a significant need for the development and use of numerical methods to simulate complex structures in order to optimise existing designs and evaluate novel devices, either prior to or instead of fabrication and experimental testing, which is time consuming and expensive.

Several approaches for the analysis of SPMs, such as field expansion approaches for matching the field continuity at the metal dielectric interface of axially symmetric copper wire, the classical Sommerfeld waveguiding principle to metal waveguides operating in the millimetre-wave region, and more recently, a 3-D time-harmonic simulation using the finite element method (FEM) have been considered, but the last one, being a 3-D approach, requires very large computational resources [200 - 204].

Of the different numerical approaches considered so far, the FEM is now established as one of the most powerful and versatile methods in many branches of engineering [205]. In the FEM approach the problem domain is divided into a patch work of finite number of regions called elements. Each of these elements can have different shapes, sizes and material. Using this approach a complex structure can be accurately represented. Most of the formulations used in the FEM, such as the scalar and **H**-field formulations are restricted to structures without modal loss or gain. Due to necessity for analysis of practical waveguides that suffer from loss or gain various alternative approaches have been developed, such as the FEM solution in terms of the transverse magnetic field H_t formulation. However, this formulation generates a complex eigenvalue equation and therefore, is computationally more expensive. On the other hand the vector H-field formulation used in conjunction with

the perturbation technique, which is computationally more efficient, can be used for waveguides with low or medium loss values. The FEM **H**-field formulation has been previously successfully applied in the characterization of optical and THz waveguides [206]. In such cases, the perturbed fields were approximated by the fields obtained from the solution of the variational formulation using only the real part of the dielectric constant. The attenuation constant was the calculated from the fields obtained from the loss-free system by using a simple matrix multiplication, thus reducing the calculation time and the large memory requirements necessary in other formulations, such as H_t formulation.

4.1.2 Sensor structure studied

The structure studied here is shown in Figure 4.1. This kind of structure has become common in many sensors because it has been observed that its behaviour is strongly dependent on the refractive index of the surrounding medium. Although, a side polished fibre may also be used, however, to study the effect of fibre parameters on optical properties, a circularly symmetric structure is considered here.

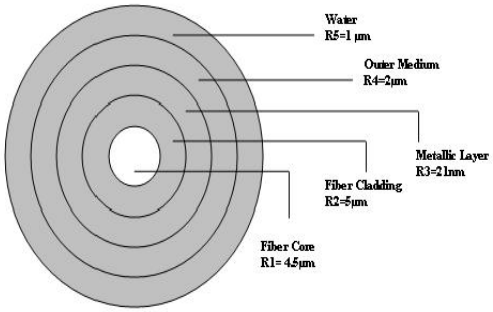

Figure 4.1 Schematic of the SPR structure studied

A metal-coated mono-mode optical fibre is considered for the understanding of the various loss mechanisms and, subsequently, the design and optimization of the biosensor for the detection of *E coli*. The thickness of the gold metallic layer is taken as 21 nm with a refractive index of $n = 0.52 + 10.7j$ [226]. The refractive index (RI) of the core and cladding is taken as 1.44868 and 1.44439, respectively at an operating wavelength of 1550nm. Here, R_1 is the

radius of the core and R_2, R_3, R_4, and R_5, are the thicknesses of the cladding, gold, outer medium and water layers respectively. Firstly, effect of index variation of R4 and thickness of R2 layer is studied. The purpose of changing index values of R4 and thickness of R2 layer is to find an optimum index and desirable thickness where the phase matching is better. Finally, with the new optimum index and desirable thickness of R4 and R2 respectively *E.coli* layer is introduced.

A two fold symmetry has been employed for the present analysis, where only a quarter of the waveguide cross section has been divided into 100 and 120 azimuthal and radial divisions, respectively, thus forming a mesh of 23900 first-order triangular elements. It takes about 48 seconds of CPU time to obtain a single modal solution on a 3.4-GHz Pentium processor.

4.1.3 Effective index variation

FEM based model investigation is devoted to study the influence of geometrical parameters of metal clad optical fibre sensor on the effective index of mode by varying the refractive index of surrounding medium in order to achieve better coupling between the SPR modes in order to maximize the modal field penetration depth into the sensing medium.

Initially, R_1, the radius of the core is taken as 4.5 μm, the thickness of the gold, R_3 is taken as 21nm, and R_4, the outer medium thickness was varied from 2μm to 3μm and R_2 the cladding thickness was varied from 5-10 μm. The values of the effective indices for the modes of the structures are represented as a function of the outer medium refractive index, R_4. The refractive index of outer medium is varied from 1.440 to 1.453 to study the coupling between the inner surface plasmon mode (ISPM) and the outer surface plasmon mode (OSPM). There are two metal/dielectric interfaces which can support SPM: one at the outer gold/dielectric boundary and the other at the inner gold dielectric boundary. In this waveguide, the mode with the dominant H_x field at the upper and lower metal-dielectric interfaces is tangential to these boundaries, which satisfies the electric-wall boundary

condition n.H = 0 and supports two SPMs along these metal/dielectric interfaces. These two surface plasmon modes have different propagation constants. However, if the propagation constants are closer for these two modes then the two modes can couple and form a supermode or super SPM.

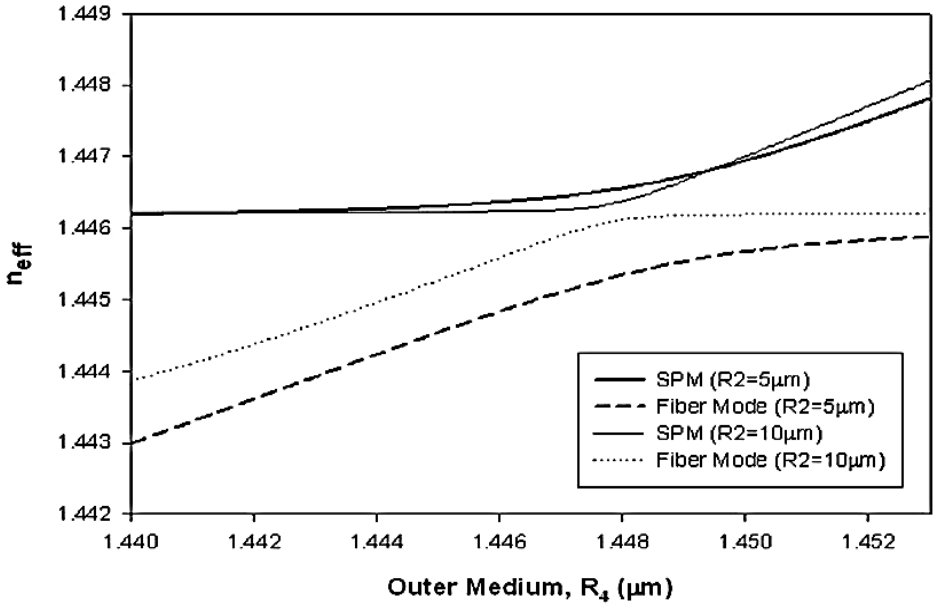

Figure 4.2: Effective index variation with the refractive index of the outer medium, R4 for the inner and outer SPMs at the gold/cladding and the gold/outer medium interfaces respectively for a cladding thickness of R2 = 5 and 10μm

As shown in Figure 4.2, as the refractive index of the outer medium increases the effective index difference between the outer surface plasmon mode (OSPM) and the inner surface plasmon mode (ISPM) becomes closer and at phase matching condition they are nearly equal. The propagation constants of the two SPMs are close at refractive indices of 1.449, 1.448 for cladding thickness of 5μm and 10μm respectively. In this case the outer medium thickness was fixed at R_4=2 μm.

4.1.4 Modal field profile

This section shows the model field profile of metal clad optical biosensor when *E.Coli* layer is added to the sensing structure. This layer consists a chemical linker MUDA [mercapto undecanoic acid], its RI is 1.463 and thickness is 1.69nm and is used as linker for antibody (RI is 1.41 and thickness is 2.98nm) and the target antigen *E.coli* with average RI of 1.37 and average thickness of 0.4 – 0.7 microns [221]. This layer is added on top of the outer medium layer, R_4 with phased matched refractive index values of 1.449 and 1.448 for cladding thickness of 5µm and10µm respectively.

The variation of the optical properties with the metal thickness, t, and the outer cladding materials can be better explained with the aid of the field distribution along the radial direction of the fibre and particularly near the dielectric/metal and metal/dielectric interfaces. Variations of the H_x field along the *y* - axis and the *x* -axis for the outer SPM are shown in Figure 4.3.

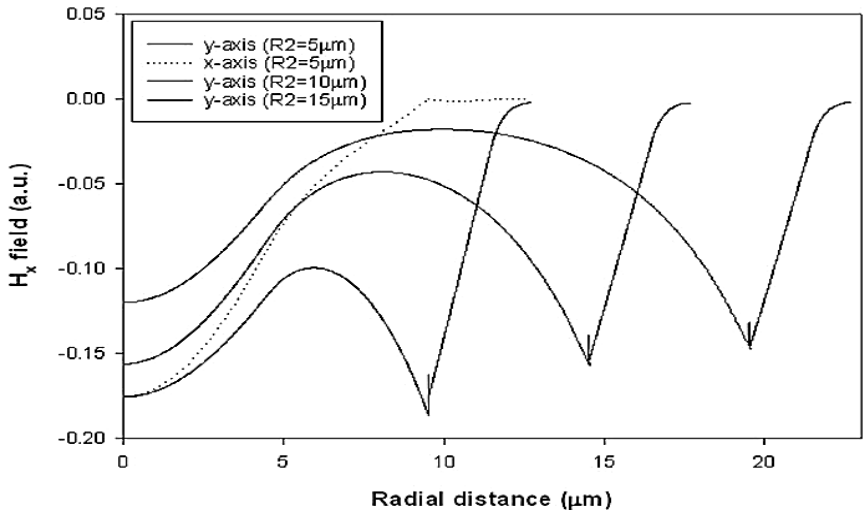

Figure 4.3: H_x field profile along the y-axis and x-axis for the outer SPM

It can be observed that the field profile along the *y*-axis, as shown by the solid line, exhibits its maximum field intensity at the dielectric/metal interface at the radial distance of 9.5µm, 14.5µm and 19.5 µm for R_2=5µm, R_2=10µm and R_2=15µm respectively and decays rapidly in the metal region. In this configuration the H_x does not see the SPM along the x-axis as

n.H=0 forces the H_x field to be zero at the metal interface but that is not true along the y-direction. On the other hand, the H_y is forced to zero along the metal interface on the x-axis and sees the SPM along the y-axis at the metal dielectric. As can be seen from Figure 4.3 when R_2 = 5µm there is a strong interaction between the fibre core mode and the surface plasmon mode and most of the field is in the core region. However, as the R_2 is increased to 15µm the separation between the core and the SPM modes become larger weakening the phase matching. Hence the core mode and the SPM will be weakly coupled and as shown by dashed-dotted line that most of the field is at the metal interface.

When the radial distance is greater than the thickness of the cladding, the optical field profile along the x-axis has the maximum field intensity at the centre, shown by a dashed line and gradually decreases along the radial distance reaching zero value at the cladding/metal interface.

The 3-D contour profile of the H_x fields for this SPM at the outer metal/dielectric interfaces are shown in Figures 4.4 and 4.5 for R_2=5µm and R_2=15µm respectively. Here, it can also be seen that the field intensity is maximum at the upper and lower interfaces, where the electric wall boundary condition allows the H_x component to have its maximum value. It can also be noticed that there are 3 peaks along the y-direction, one in the core and two at the two vertical metal/dielectric interfaces. Along the x-direction the field is forced to zero at the metal/dielectric interface and has a maximum in the core region with no surface plasmon mode at this part of the metal/dielectric interfaces.

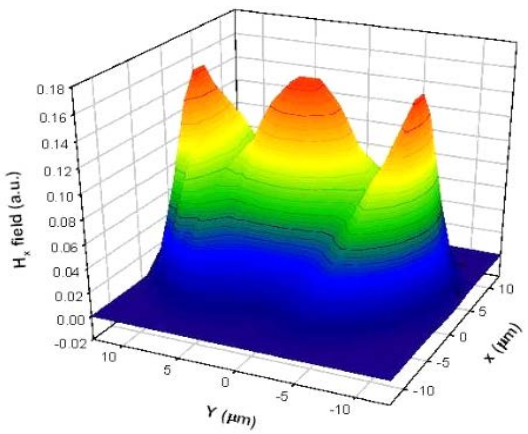

Figure 4.4: H_x field profile of the outer SPM, R2=5μm

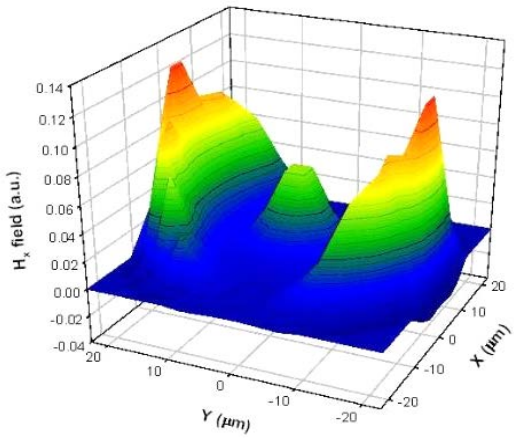

Figure 4.5: H_x field profile of the outer SPM,R2=15μm

Figure 4.5 shows similar characteristics to Figure 4.4; however, as R_2 is larger here, the interaction between the core and SPM modes is smaller. It can also be seen clearly that the field is higher at the metal/dielectric boundaries.

4.1.5 Effect of coupling length

The coupling length is an important parameter in investigating the phase matching condition of the fibre mode and the surface plasmon mode. The coupling length can be defined as the minimum distance at which a maximum power transfer occurs. Through the calculation of the propagation constants of the inner surface plasmon modes and outer surface plasmon modes using the VFEM, the coupling length, L_c, can be calculated as;

$$L_c = \frac{\pi}{\beta_{OSPM} - \beta_{ISPM}} \tag{4.1}$$

Where, β_{OSPM} and β_{ISPM} are the propagation constants of the surface plasmon mode and fibre mode, respectively. One can understand this by noting that the coupling length is related to the difference between β_{OSPM} and β_{ISPM}.

Figure 4.6 shows the coupling length as a function of the outer medium refractive index. The maximum coupling length is observed when it is phased matched. As can be seen from this

Figure as the cladding thickness, R_2 is increased from 5µm to 15µm although similar phase matching can be achieved, however, due to increased separation between the core mode and SPM mode, the coupling length is increased.

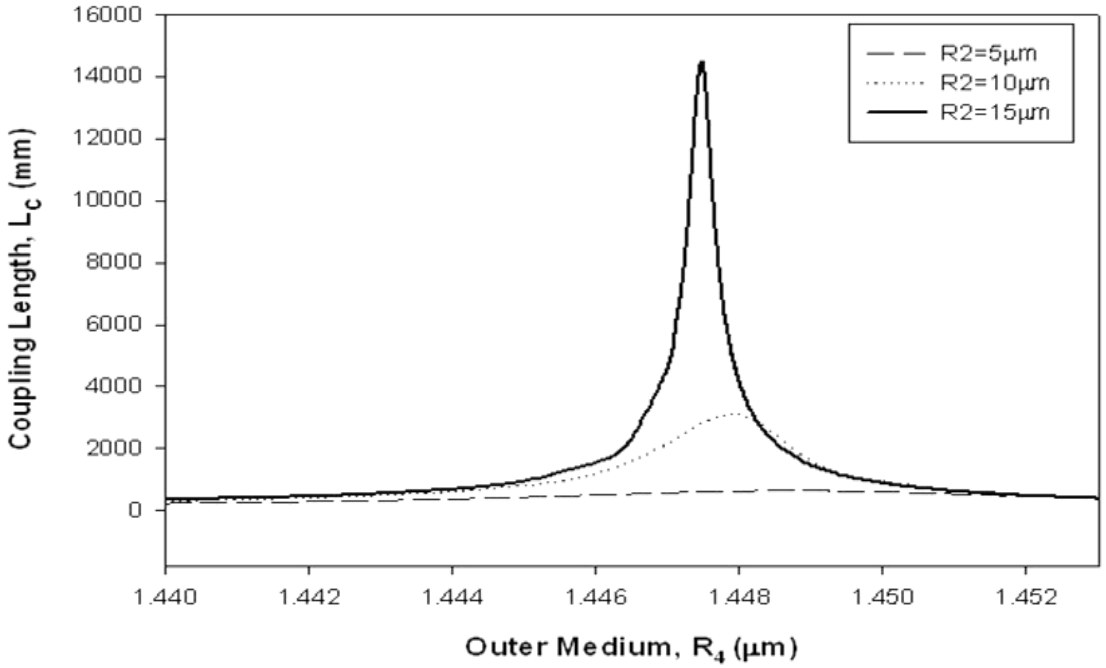

Figure 4.6: Coupling length against outer medium refractive index for R4=2 µm

This can be explained with the help of Figure 4.2. When the cladding thickness, R_2 is 5µm the inner and the outer SPMs are very strongly coupled hence the difference between their propagation constant is large giving a shorter coupling length. However, when R_2 is 15µm the inner and the outer surface plasmon modes are weakly coupled and hence the difference between their propagation constant is small giving rise to an increased coupling length. It can also be noticed that the peaks of the coupling length curves correlate with the phase matching points from Figure 4.2.

4.1.6 Sensing layer growth

An important question for the modelling of sensor performance is how the sensing layer composed of recognition and target molecules is modelled. The simple model that is generally adopted describes changes of an equivalent sensing layer. This layer is characterized by its

thickness and its refractive index. Molecular deposition is modelled as a change in thickness or refractive index of this layer. In simple model the molecular interactions correspond directly to changes in refractive index or thickness of the sensing layer. Using this model the quantity to be measured is the change of the effective index upon changes of the sensing layer thickness.

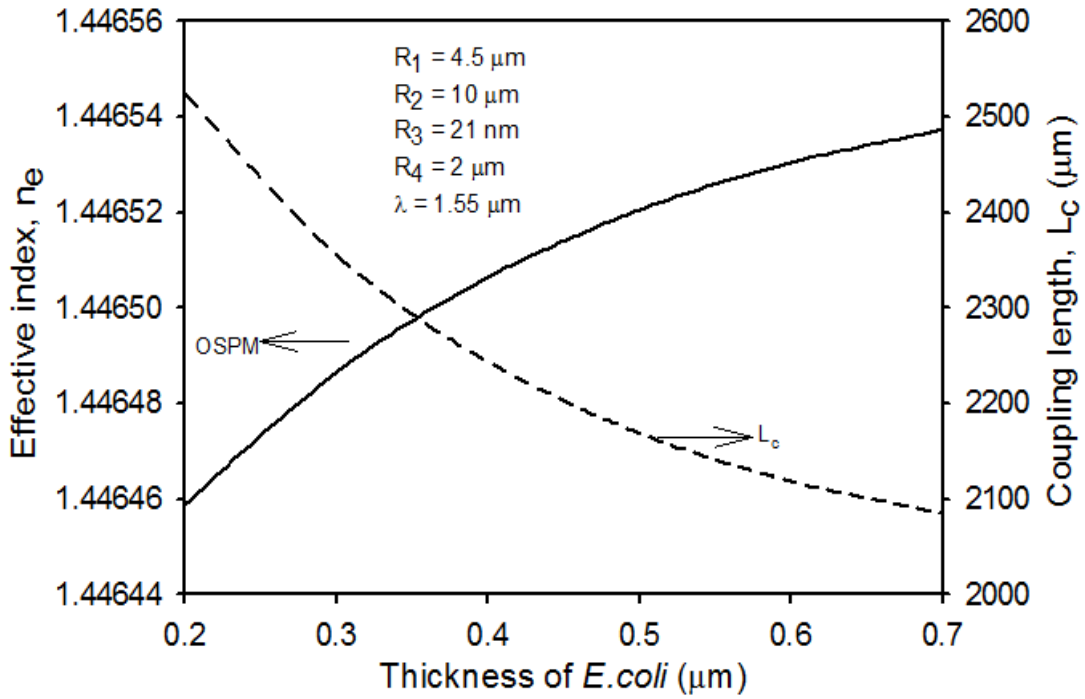

Figure 4.7: Coupling length as a function of the thickness of the *E.coli* region

Therefore, thickness of the *E coli* layer is an important parameter in the design of the optical biosensors. To study the effect of the thickness of the *E.coli* on the effective index and coupling length the thickness was varied from 0.2 – 0.7μm. As can be seen from Figure 4.7 as the thickness of the *E.coli* is reduced from 0.7 to 0.2μm the coupling length is increased from 2084μm to 2524μm respectively. This shows that maximum power coupling can be achieved at a much shorter device length for larger thickness of the *E.coli*. The solid line shown in Figure 4.7, indicate the variations of the effective indexes for the SPM at outer interface. Effective index of the outer SPM increases with the thickness of E.coli. The outer SPM being associated with the higher refractive index RI=1.449 of R4 layer shows the features of an oddtype first supermode. Similarly, with the inner SPM mostly being confined near the core and cladding

region with lower refractive index, and this mode shows evenlike second supermode properties. The effective index of outer surface plasmon mode increases from 1.44646 to 1.44654 with the increase of thickness of *E.coli* from 0.2 to 0.7 µm respectively. Similarly, the effective index of inner surface plasmon mode increases from 1.446152 to 1.446166 with the increase of thickness of *E.coli* from 0.2 to 0.7 µm respectively. This shows that coupling length decreases with the increase of effective index for larger thickness of the *E.coli*. The evanescent field of outer surface plasmon mode penetrates more into the *E.coli* layer due to higher refractive index of buffer layer, R4 in between outer metal interface and *E.coli* layer hence power confinement increases. The inner surface plasmon doesn't penetrate deep into the E.coli layer because it is confined near the core region, R1 of lower refractive index. Therefore, for the detection of E.coli excitation of outer surface plasmon mode is very important.

4.1.7 Optimizing thickness of cladding

The majority of the fibre optic SPR sensors are based on evanescent field interactions. A typical single mode optical fibre has a core diameter between 8 and 10.5 µm, a cladding diameter of 125 µm and light propagates confined in the core [201]. Therefore, the penetration depth is far smaller than the cladding thickness and there is almost no interaction between the optical signal and the external medium. The evanescent field can be exposed by removing partially or totally the cladding of the optical fibre. This can be done by chemical etching, tapering or side polishing techniques [201]. Therefore, leaving too much of the cladding around the core weakens the interaction between the fundamental mode and the SPR mode. For this reason we have varied the thickness of cladding, R_2 from 5 to 15 µm with R_1 core diameter kept 4.5 µm. The thickness of metal layer, R_3 is 21nm and thickness of buffer layer, R_4 is 2µm with higher refractive index of 1.449. We will first study the effect of cladding thickness with difference in propagation constant, Δβ in presence of *E.coli.*

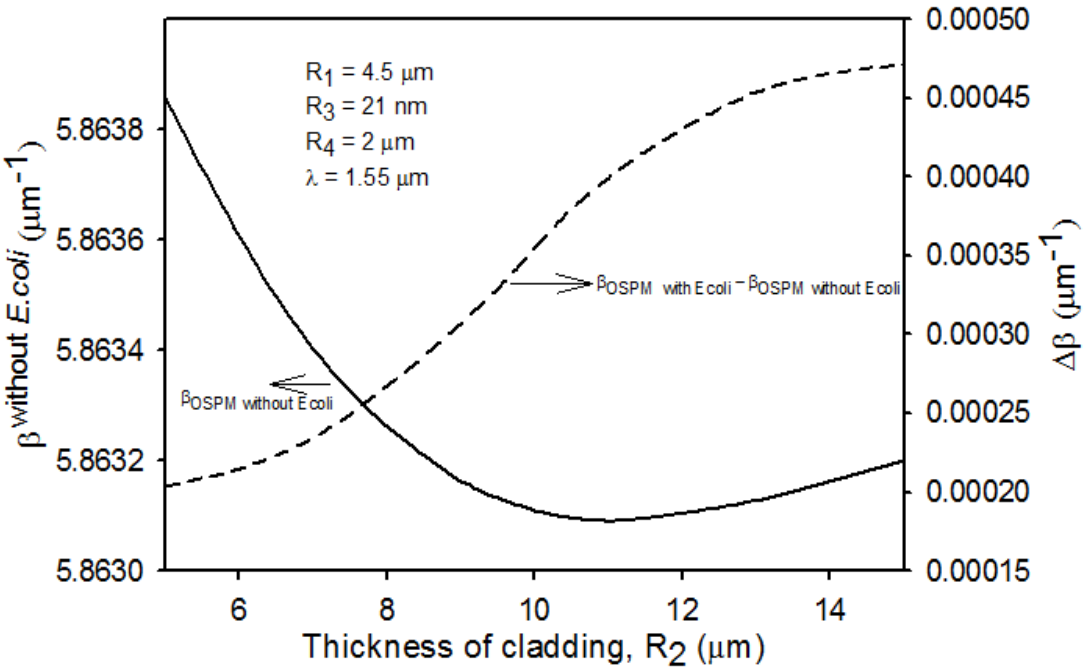

Figure 4.8: Propagation constant as a function of the thickness of the cladding

The solid line shown in Figure 4.8, indicate the variation of propagation constant of outer SPM with or without presence of *E.coli.* Here, the propagation constant of outer SPM without presence of *E.coli* and the propagation constant difference between outer SPM with *E.coli* and outer SPM without *E.coli* is plotted against thickness of cladding, R_2. As can be seen from the aforementioned characteristics, as R2 increases the propagation constant of outer SPM without presence of *E.*coli decreases. The propagation constant difference, Δβ, between the outer SPM without *E.coli* and the outer SPM with *E.coli* is shown in dotted lines in the figure, increases with increase in the thickness of cladding.

Next, the variation of effective indexes for the SPMs at the inner and outer interfaces as shown in dotted and solid lines in the Figure 4.9 respectively in presence of *E.coli*. As shown in the figure the effective index of outer SPM with presence of *E.coli* is higher for the cladding thickness of 5μm. Since the variation of the cladding thickness changes the effective index of the inner SPM. It increases with the cladding thickness and is highest value is when cladding thickness, R_2 is 10 μm.

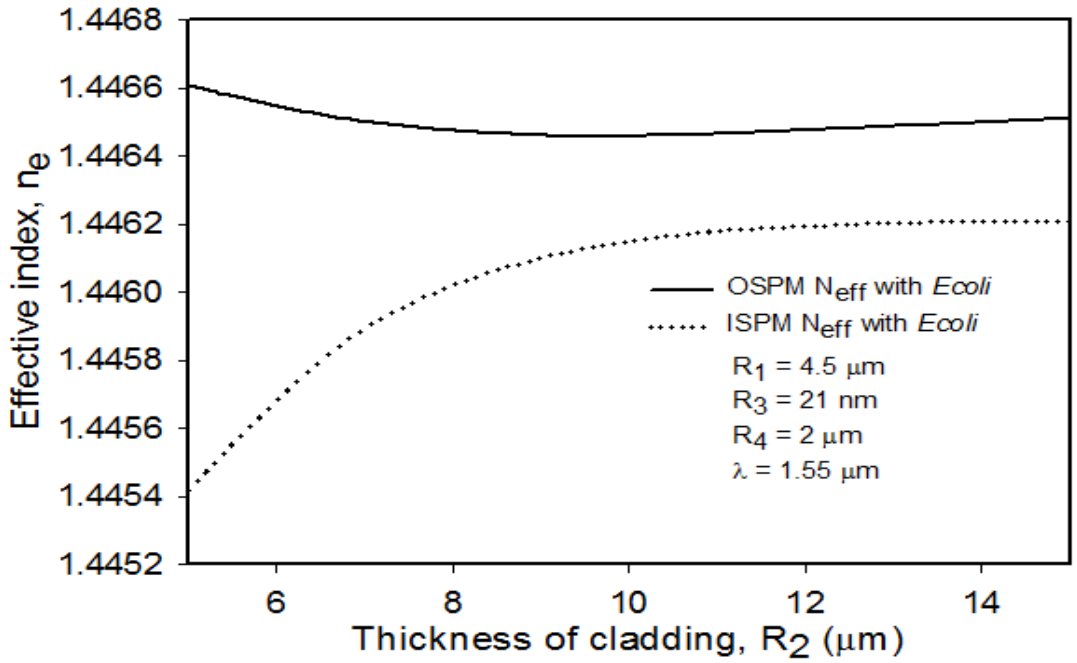

Figure 4.9: Variation of effective index with the thickness of cladding, R_2

The outer SPM being associated with the higher refractive index RI=1.449 of R_4 layer shows the features of an oddtype first supermode. Similarly, with the inner SPM mostly being confined near the core and cladding region with lower refractive index 1.44439, and this mode shows evenlike second supermode properties. However, it can be clearly observed that these two lines do not cross each other. For coupled SPMs, the oddlike SPM has a higher effective index than the evenlike SPM. The effective index of the inner SPSM strongly depends on the thickness of cladding and increases monotonically. On the other hand, the effective index of the outer SPM reduces with the cladding thickness.

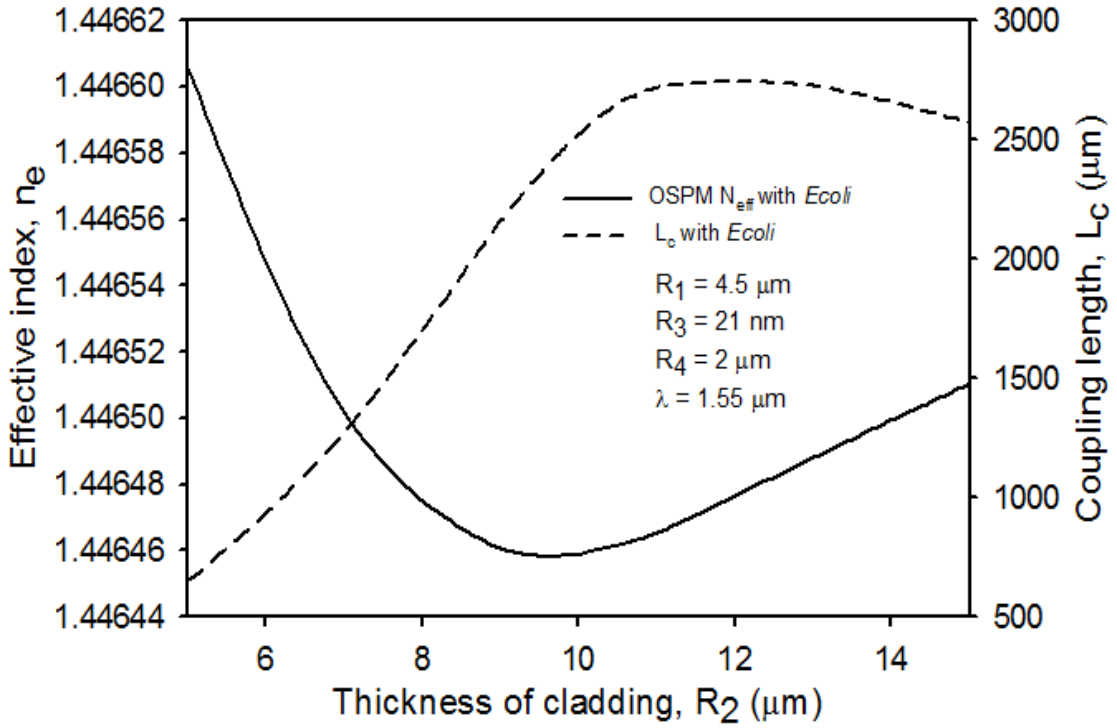

Figure 4.10: Coupling length as a function of the cladding thickness with and without *E.Coli* for an outer medium index, R4 of 1.449

Next the effect of the coupling length with the cladding thickness is studied. As can be seen from Figure 4.10 the coupling length increases monotonically for small values of thickness and it reaches a maximum around the optimum design condition of R_2=10μm. As can be seen from this Figure the coupling length is maximum at a cladding thickness, R_2=10μm. This can be correlated with Figure 4.2 where the ISPM and the OSPM modes match very closely around 10μm when the outer medium index, R_4 is 1.449. It can also be noticed from Figure 4.10 that the maximum power transfer occurs when the device length is around 2524 μm in presence of *E.Coli*. Hence by carefully selecting the length of the fibre and monitoring power transfer, the presence of *E.Coli* may be identified.

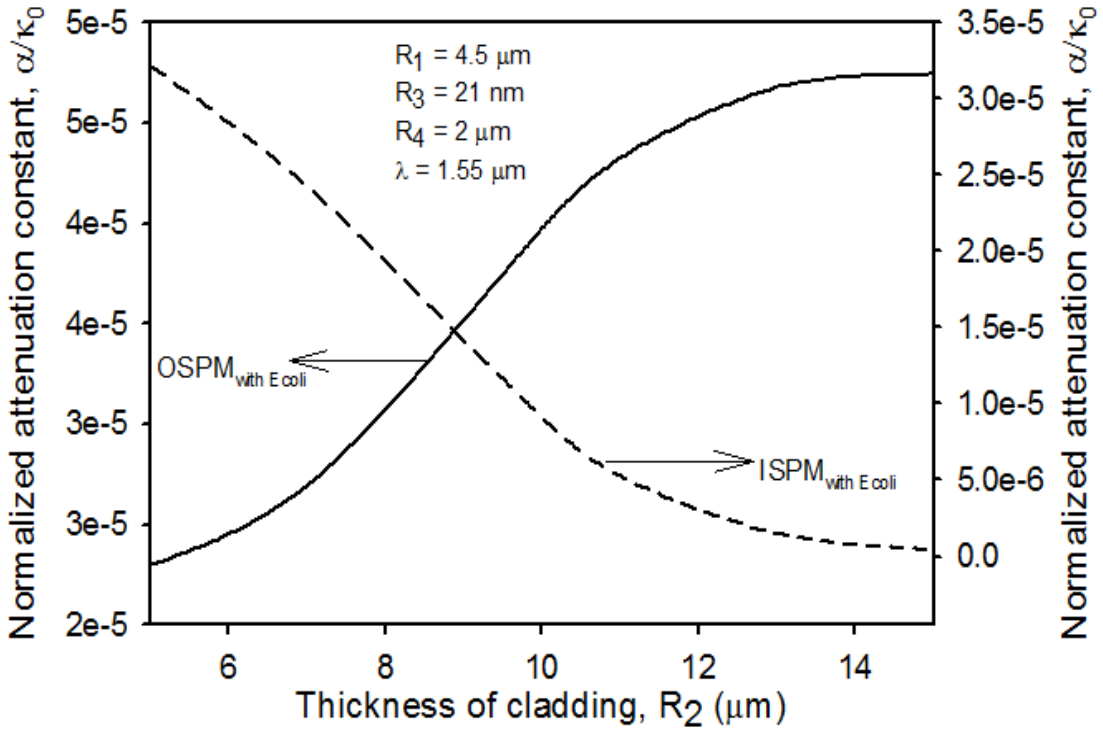

Figure 4.11: Attenuation constant variation with the cladding thickness R_2 for the even and the odd SPMs.

Next, the attenuation characteristics of the inner and outer SPM modes have been calculated by using the vector H-field FEM with perturbation and the variation of the normalized attenuation constant α/k_0 for the oddlike and evenlike SPMs are shown in Figure 4.11 by a solid line and a dashed line, respectively. The inner SPM decays more slowly in the core region and with a lower power confinement in the lossy metal layer, yielding a smaller modal loss compared to the SPM at the outer interface. The evanescent field of outer surface plasmon mode penetrates more into the *E.coli* layer due to higher refractive index of buffer layer, R4 in between outer metal interface and *E.coli* layer hence modal loss increases.

4.1.8 Effect of outer medium

The outer medium layer can be used to increase the sensitivity of sensor by manipulating the power distribution of the guided modes. The concept behind the outer medium layer is that a thin layer with higher refractive index than the core is used to penetrate more power of the mode into the sensing layer.

Finally the structure was slightly modified to study the effect of outer medium, R_4. The thickness of the outer medium, R_4, is increased from 2µm to 3µm. The refractive index of outer medium is varied from 1.440 to 1.453 to predict the coupling between modes.

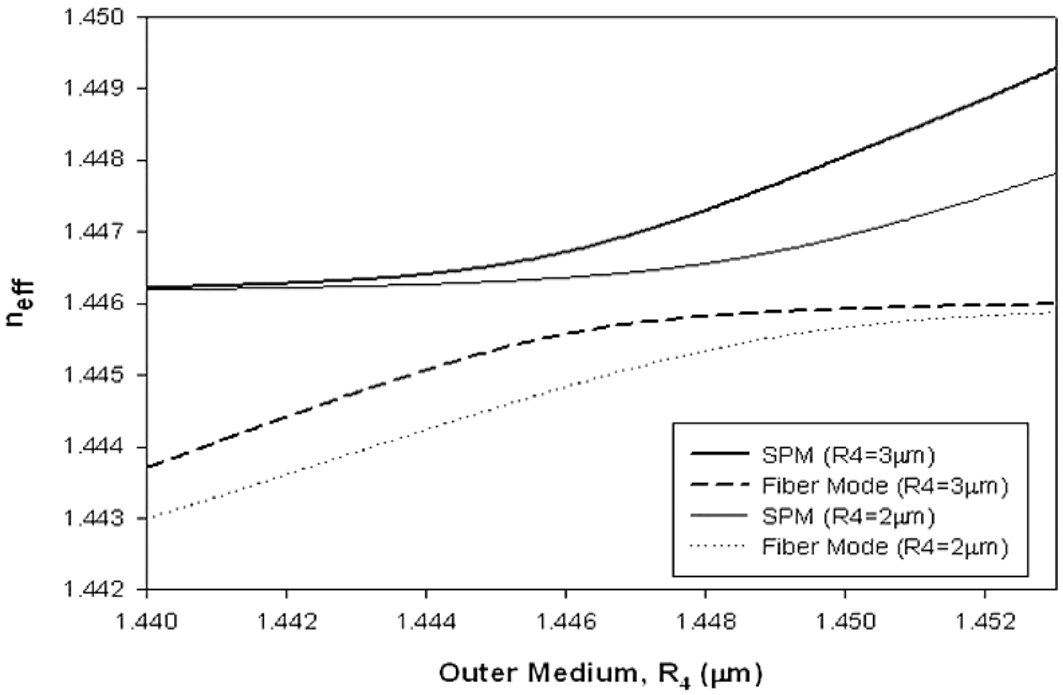

Figure 4.12: Effective index as a function of the outer medium index for the Fibre Mode and (SPM) surface plasmon mode for an outer medium thickness of R4 = 2 & 3µm and cladding thickness, R2 = 5µm.

As shown in Figure 4.12 increase in refractive index of the outer medium increases the effective index of outer SPM, however, effective index of inner SPM doesn't change that much. The propagation constants of the two SPMs are close to phase match only when the outer layer refractive index is 1.449 and 1.446. In this case the cladding thickness, R_2 of 5µm when R_4 is 2µm and 3µm respectively are used. It can be clearly observed that these two

eigenvalue curves do not cross each other. The effective index of the ISPM strongly depends on the outer layer refractive index and increases monotonically. The effective index of the OSPM increases much faster with the changing outer refractive index as the metal layer sees the outer mode.

4.1.9 Power in the *E.coli* region

Finally the biosensor is optimized for the maximum percentage of power in the *E.Coli* region. It can be seen from Figure 4.13 that the maximum detection is possible when the outer medium, R_4 refractive index is 1.449, the thickness of the cladding, R_2 is 10 µm, and the thickness of the outer medium is 2 µm. As the outer medium refractive index is reduced it can be noticed that the percentage of power in the *E.Coli* region is also slowly reducing showing that increased index difference between the *E.Coli* and the outer medium has more power confined in the *E.Coli* region.

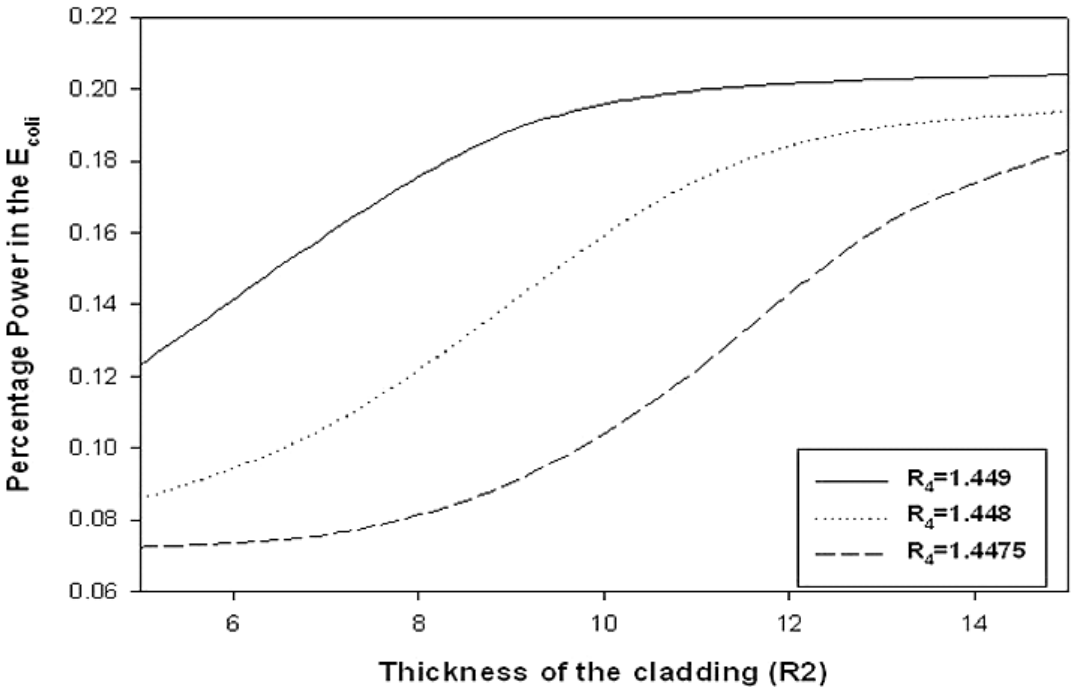

Figure 4.13: Percentage of power in the *E.Coli* (R5) region as a function of cladding thickness for different outer medium refractive indices

4.2 Interaction of metal-clad fibre with surrounding refractive index

A metal-clad fibre is considered to study the optical properties and effect of outer sensing region whose index is varied from 1.30 –1.44 to cover most of the materials that can be used in the biosensing applications [207]. Different metals such as copper, gold and silver are used to excite the surface plasmon modes. The variation of optical parameters of such structures due to the presence of materials that affect the modal field distribution can be utilized in optical sensor applications.

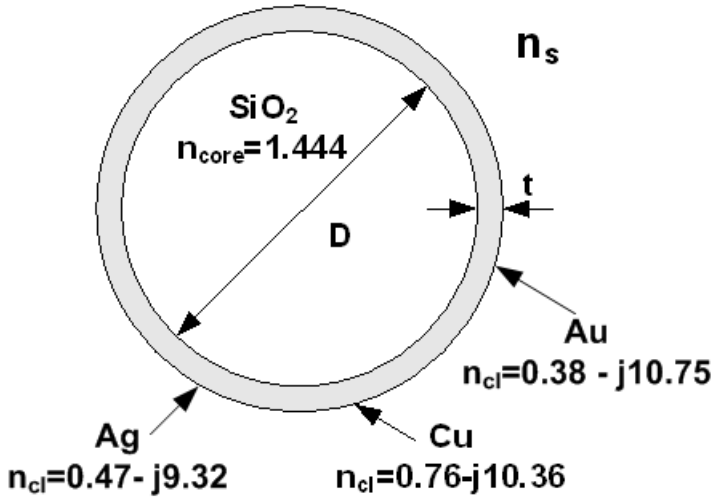

Figure 4.14: Schematic of the Metal-clad fibre structure

Figure 4.14 shows the schematic cross-section of the metal-clad optical fibre with a silica core and a finite copper cladding thickness, *t* is evaluated, where D is the core diameter, the refractive index of the core is taken as n_{core}= 1.444, copper cladding is given by n_{cl}= 0.76-j10.36, and surrounding index medium n_s is taken as 1.34 at an operating wavelength of λ = 1.55 µm. The thickness, *t* of the copper layer was set to 20 nm. The reason thickness, *t* of the copper layer is kept 20 nm and operating wavelength λ = 1.55 µm is because penetration depth of guided mode is greater in to the sensing region under these parameters and thus higher sensitivity can be achieved. Using these values, the performance of the SPR sensor is evaluated through simulating the structure in Figure 4.14.

4.2.1 Optical mode field distribution

Figures 4.15 and 4.16 shows the inner and outer radially polarized surface plasmon modes at core diameter of D = 6 µm. As can be seen from these Figures the inner mode is more confined and the outer mode is more spreaded and much more circular. The superimposed field intensity from the Hx and Hy fundamental supermodes form the radially polarized RP_{01} mode, for a metal-clad silica fibre with a diameter, D = 6 µm and a metal thickness, t = 0.02 µm and a surrounding index of 1.34 is presented here. From Figure 4.16 it can be seen that the optical field decays in both the centre of the fibre and the outer cladding, with the anti-symmetric peak field intensities at the inner silica/copper (where the field is positive) and small negative peak (but this is not visible) at the outer copper interface.

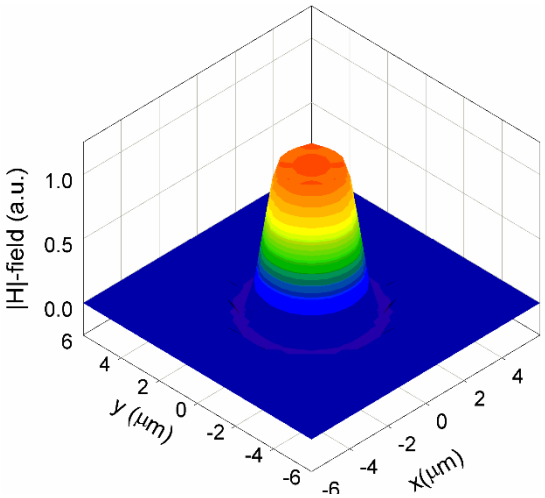

Figure 4.15: Inner radially polarized surface plasmon mode at D = 6 µm.

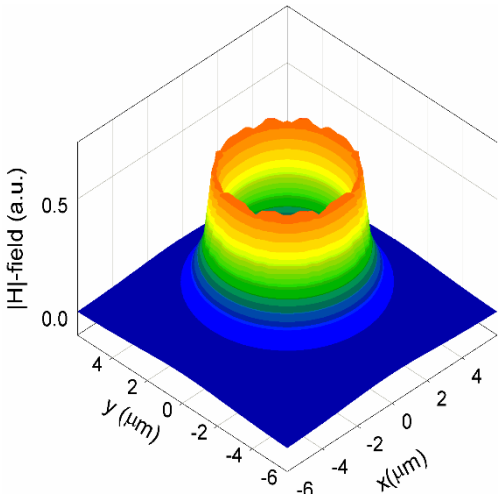

Figure 4.16: Outer radially polarized surface plasmon mode at D = 6µm and ns = 1.34.

4.2.2 Variation of surrounding medium index

Figure 4.17 shows the effective index with the surrounding medium refractive index. In this case the surrounding medium index is varied from 1.30–1.44 to cover most of the materials that can be used in the biosensing applications [207]. As can be seen from Figure 4.17 the outer surface plasmon effective index changes linearly with the increasing index values.

However, as the inner mode does not see the surrounding index the refractive index of the inner mode is not affected.

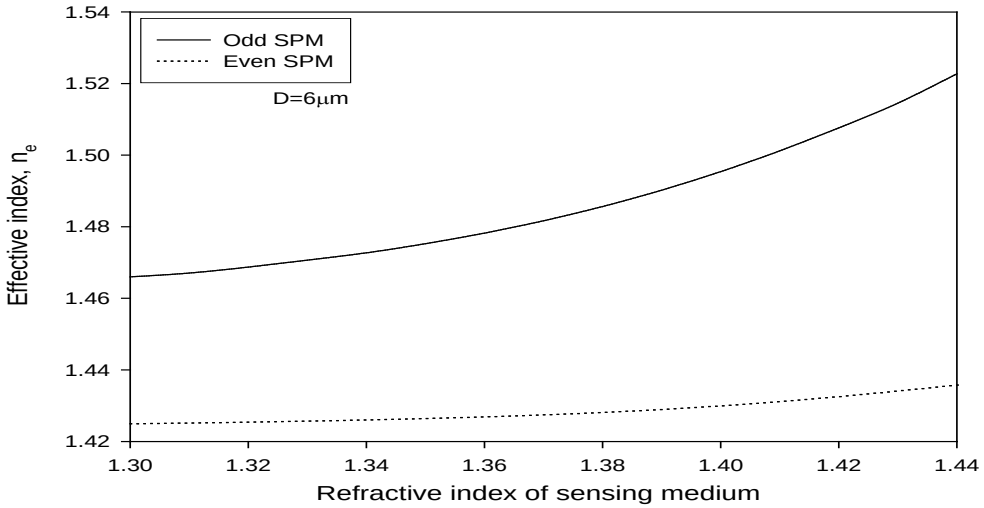

Figure 4.17: Effective index with surrounding medium (n_s) refractive index.

The inner SPM and outer SPM are excited at the inner and outer metal interfaces respectively and outer SPM effective index is higher than that of inner SPM. The evanescent field of outer surface plasmon mode penetrates more into the sensing region due to increasing refractive index of sensing medium hence effective index of outer SPM increases. The inner surface plasmon doesn't penetrate deep into the sensing medium because it is confined near the core region hence the effective index of inner SPM doesn't change and is lower than that of outer SPM.

4.2.3 Effect of modal loss

Next the attenuation characteristics of the above modes have been calculated using the vector H-field Finite Element Method with perturbation and the variation of the normalized attenuation constant, α/k_0 with the surrounding refractive index is presented for a fibre diameter of 6 μm in Figure 4.18. From this Figure it can be seen that as the refractive index of the surrounding medium is increased the modal loss also increases as the mode starts to penetrate more into the surrounding medium. However the modal loss in the inner

silica/copper boundary is constant over a range of surrounding index as the field does not see the outside index. The modal loss here is mainly due to the metal loss at the silica/metal inner interface. It can clearly be seen that as the outside index approaches that of the silica index the modal loss is at its maximum. However, to design practical biosensing devices a compromise must be found between the modal loss and the amount of penetration that is needed within the surrounding index medium. This can be attributed to the sensitivity of the biosensor that is needed for different biomedical applications.

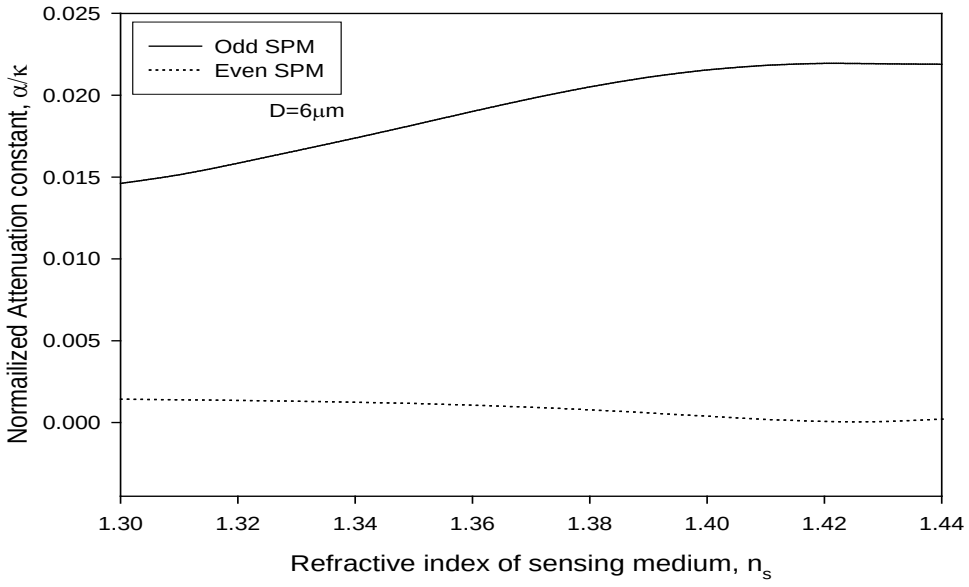

Figure 4.18: Attenuation with surrounding refractive index.

The inner SPM decays more slowly in the core region and with a lower power confinement in the lossy metal layer, yielding a smaller modal loss compared to the SPM at the outer interface. The evanescent field of outer surface plasmon mode penetrates more into the sensing medium hence modal loss increases with the increasing refractive index. The inner surface plasmon doesn't penetrate deep into the sensing medium because it is confined near the core region hence modal loss remains unchanged with the increasing refractive index of sensing medium.

4.2.4 Power in the sensing medium

Figure 4.19 shows the percentage power with the surrounding medium refractive index. In this case the surrounding medium index is varied from 1.30–1.44. As can be seen from Figure 4.19 percentage power in the sensing medium also increases with the increase in the surrounding index. However the percentage power in the inner silica/copper boundary is constant over a range of surrounding index as the field does not see the sensing medium index. It can clearly be seen that as the outside index approaches that of the silica index the power in the sensing medium is at its maximum.

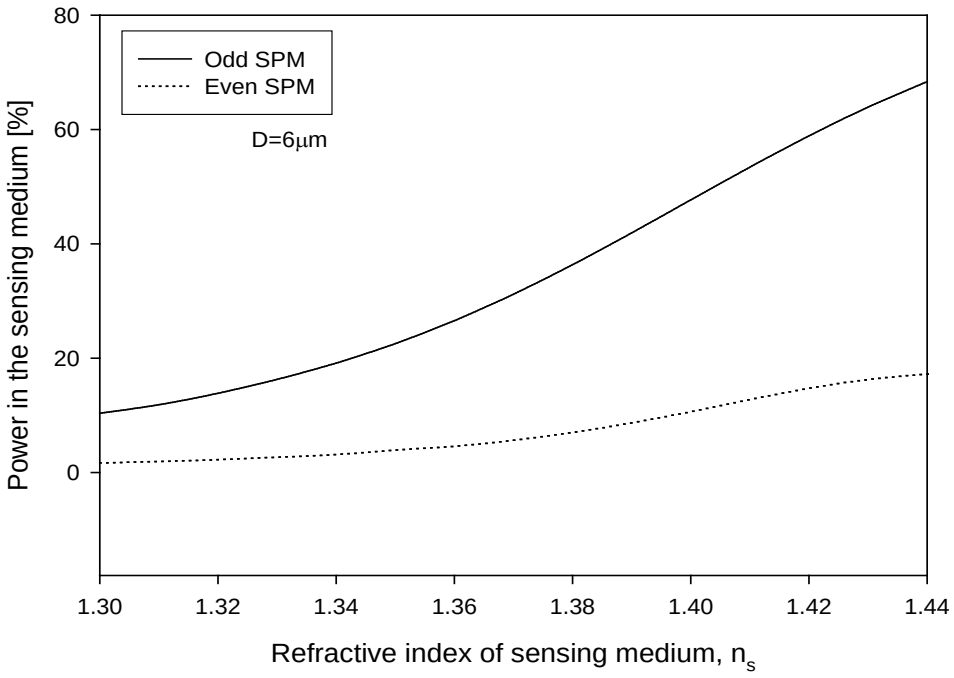

Figure 4.19: Percentage Power with surrounding medium (n_s) refractive index.

The power confinement in the sensing medium is more when outer surface plasmon mode is excited at the outer metal interface. The outer surface plasmon mode evanescent field penetrates more into the sensing region due to increase in refractive index of sensing medium hence the power confinement is high in the sensing medium and low in the core region.

However, the inner surface plasmon mode is confined near the core region hence the power confinement in the core region is high and low in the sensing medium.

4.3 Detection of acetone using metal-clad fibre sensor

Acetone is a chemical that is found in the human bodies and naturally in the environment. It can be produced by industries too. Many conditions can lead to higher than average amounts of acetone in the body. People who can have higher amounts of acetone in their bodies for example, diabetics, babies, pregnant women, and people who exercise, diet, have physical trauma, or drink alcohol.

The metal-clad sensor can be utilized to ascertain whether the patient is suffering from diabetic ketoacidosis, a prospective serious complication that occurs when people with diabetics do not take adequate quantities of insulin and will be used in homes by diabetics to find out whether they require more insulin. A metal-clad fibre as shown in figure 4.14 is considered to study the optical properties and effect of acetone as an outer surrounding material by using different metals such as copper, gold and silver to excite the surface plasmon modes. The variation of optical parameters of such structures due to presence of materials that effect the modal field distribution can be utilized in optical sensor applications. At first, we used the modal approach to calculate the effective refractive index, mode attenuation constant and outer cladding power for guided modes in the sensing section.

4.3.1 Modal field profile along y-axis

A metal-clad fibre with diameter of D = 6 μm and a finite metal thickness, *t*, with acetone material around the metal cladding has been considered at an operating wavelength of 1.55μm. The field profile of the fundamental H_x odd-like optical supermode along the y-axis, for different values of the metal thickness, t, have been investigated and are shown in Figure 4.20. As can be seen from this Figure 4.20, for a metal thickness of 0.2 μm (as shown by a solid

line), the field profile has similar properties to those obtained for an infinite cladding fibre, where the field has a maximum intensity at the dielectric/metal interface and decays rapidly in the metal region, except a small negative peak is clearly visible at the copper/acetone interface, due to the weak coupling between the two non-synchronous SPMs. As the metal thickness decreases, the maximum field intensity increases anti-symmetrically at both the interfaces, with the highest maximum being at the silica/copper interface.

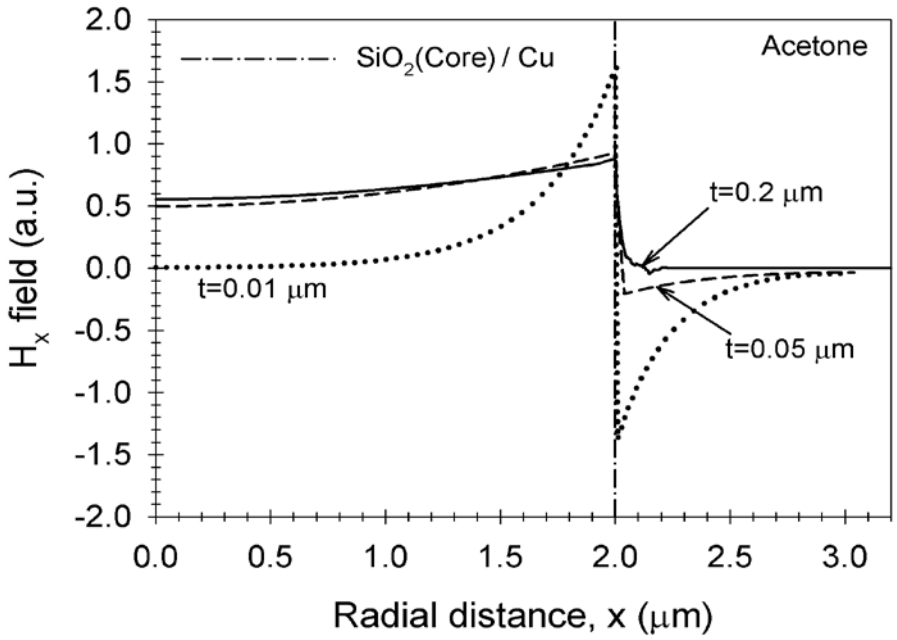

Figure 4.20: H_x field profiles along the y-axis with metal thickness for acetone in the outer cladding.

4.3.2 Effective index change with increase in thickness of metal

The variation in the effective index of outer surface plasmon mode for a fibre diameter of 6 μm, covered by a copper, silver and gold metal layer respectively and further covered by acetone as the sensing medium at an operating wavelength of 1.55μm has been studied and presented in Figure 4.21

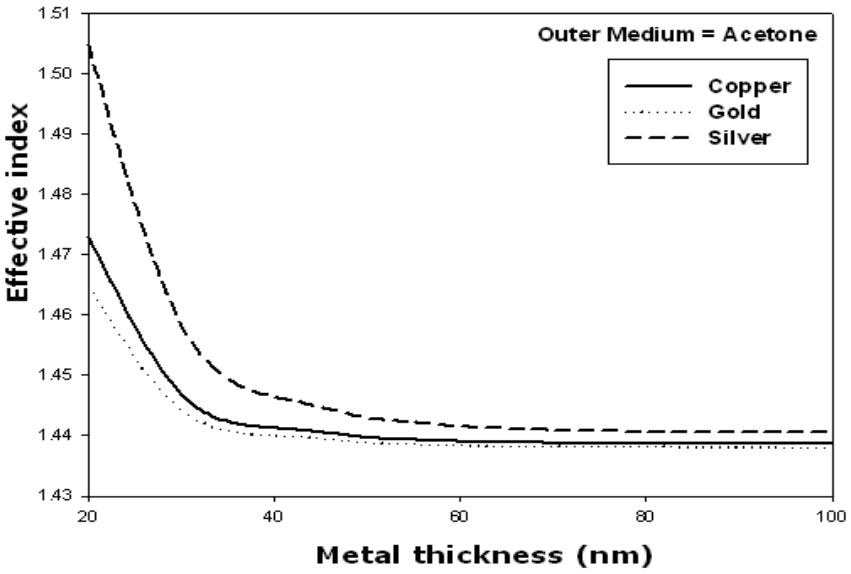

Figure 4.21: Effective index variation with metal thickness for D = 6 µm.

It can be seen that for a large metal thickness, *t*, two SPMs exist at inner and outer metal circular boundaries and when the two dielectric materials are different, their propagation constants are different, and therefore they do not interact to form a supermode. However, as the metal thickness, *t*, is reduced, there is stronger coupling between the SPMs and two supermodes, with odd and even like maximum field intensities at the two interfaces, being formed. The first supermode has a higher propagation constant and is confined near the outer metal interface with the higher refractive index and has an odd-like field profile. As can be seen from the effective index curve shown in Figure 4.21, when the metal thickness, *t*, decreases below 50 nm, the effective index of the odd-like supermode increases rapidly. On the other hand, the second supermode is confined near the inner metal interface with the lower refractive index and has an even-like field profile. The even-like second supermode is dominated by the effective index of the inner metal dielectric interface, and being close to cut-off, as the metal thickness decreases, the even-like mode becomes unbounded. The effective index of the even-type SPM is below the cut-off and therefore is not presented here. When silver is considered as a metal the effective index of acetone is higher as compared to copper and gold respectively.

4.3.3 Effect of attenuation constant with metal thickness

Next, the variation of the normalized attenuation constant of the H_x odd-like optical supermode has been calculated. From the Figure 4.22 it can be seen in all cases that when the metal thickness, *t*, is less than 50 nm the modal loss of odd like SPM is higher. The attenuation constant of odd like SPM decreases with an increasing thickness of the metal film because field doesn't see the outside index. When gold is considered as a metal the attenuation constant of modes is lower as compared to copper and silver respectively.

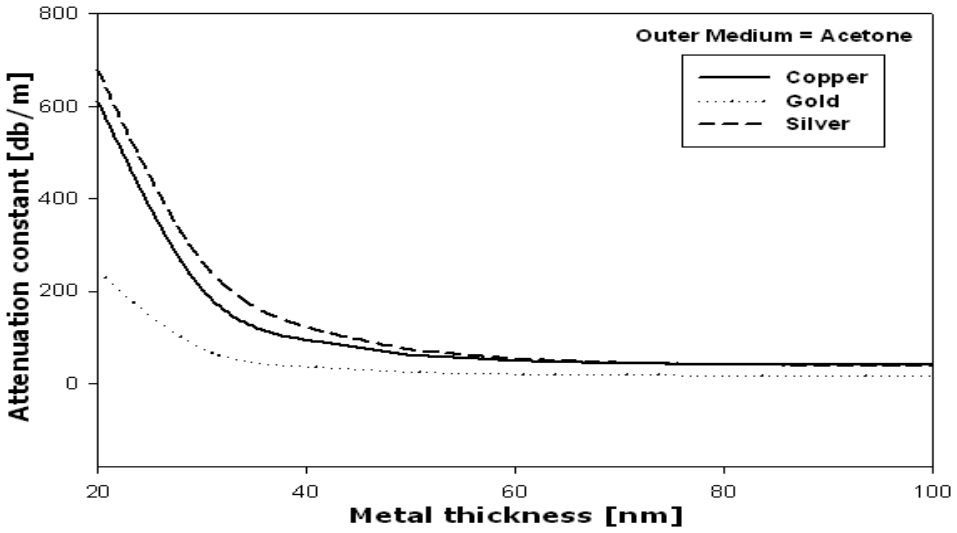

Figure 4.22: Modal loss with metal thickness for D = 6 µm.

As the metal thickness below 50 nm is decreased the modal loss also increases as the mode starts to penetrate more into the surrounding medium. The modal loss here is mainly due to the metal loss at the silica/metal outer interface. It can clearly be seen that at metal thickness of 20 nm modal loss is at its maximum. The outer SPM penetrates more into the sensing medium and with a higher power confinement in the lossy metal layer, yielding a higher modal loss to the SPM at the outer interface.

4.3.4 Effect of power with the thickness of metal layer

The power in the sensing medium also depends on the thickness of the metal layer which is an important design parameter of the structure, which may strongly influence the sensor performance. It is clear from Figure 4.23 when the metal thickness decreases power increases in the sensing medium due to coupling of modes. The power is more in the sensing region when the silver is considered as metal as compared to copper and gold respectively.

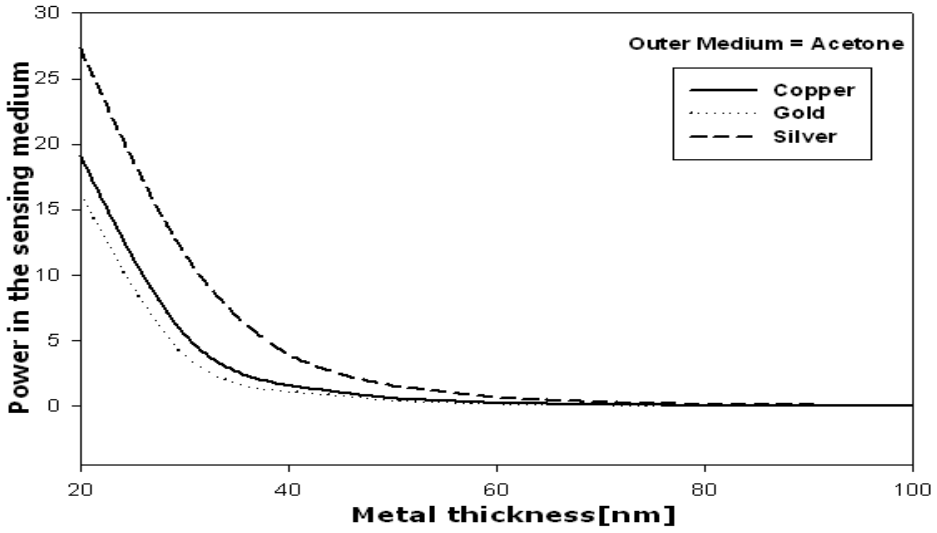

Figure 4.23: Percentage power in acetone with metal thickness for D = 6 µm.

The power confinement in the sensing medium is more when outer surface plasmon mode is excited at the outer metal interface. The outer surface plasmon mode evanescent field penetrates more into the sensing region due to thin metal film hence the power confinement is high in the sensing medium and low in the core region.

4.4 Summary

A finite-element approach based on a full-vectorial **H**-field formulation in conjunction with the perturbation technique has been used to study the surface plasmon resonance based fibre optic biosensors to detect *E.Coli*. The SPM_S propagating in the above waveguide and the study of their propagation and attenuation characteristics, with the variation of the metal layer

thickness and outer layer thickness is investigated. It has been shown that by changing the refractive index of the outer medium, R_4 the effective index of the inner and the outer surface plasmon modes can be matched to achieve better coupling efficiency. The effect of coupling length, modal confinement and modal loss are studied with and without the presence of *E.coli* in the outer medium. We have also shown the differential coupling length and differential attenuation for the cases of with and without *E.Coli*.

Moreover above numerical methods have been used to study the detailed optical properties such as the optical mode field distribution, the effective index and the attenuation constant of a metal-clad silica fibre with finite metal-clad thickness surrounded by another outer cladding. The variations of the above optical properties with the change of the surrounding materials are very important in several applications, such as optical fibre sensors and biosensors. For finite metal thickness, the SPMs exist at both the inner and outer interfaces. By adjusting the metal thickness and refractive index values of the cladding layers, the odd and even-type coupled SPMs can be formed and exploited for various biosensing applications.

5

NANOSTRUCTURE OPTICAL BIOSENSORS

5.1 Mach–Zehnder nanowire biosensor for detection of *E.coli*

Silica nanowires [208] offer several advantages over other types of nanowires since they are based on materials used in the most important photonic and opto-electronic applications within the visible and the near-infrared ranges and as a result their optical properties are familiar [209].

Light guided along the optical nanowire leaves a large fraction of the guided field outside the wire as evanescent waves [210], [211] making it highly sensitive to the index change of the surrounding medium. Phase shift of the guided mode caused by index change of the surrounding medium is used as a criterion for sensitivity estimation. Our simulation shows that optical nanowire waveguides are very promising for developing high-sensitivity optical sensors of significantly reduced sizes.

In the aforementioned work, changes in the optical field profile, the power confinement, and the propagation constant of the guided optical mode along the sensing arm have been studied. In the present work, the aforementioned structure has been analyzed using the more rigorous and versatile FEM approach and the variation of the effective index; the optical power distribution of the guided optical mode in both the reference and the sensing arm of the sensor have been studied, by optimizing the sensitivity of important silica nanowire

parameters, such as the fibre core diameter, the specimen refractive index, the wavelength, and the temperature.

5.2 Mach–Zehnder based sensor structure

The proposed Mach–Zehnder-based biosensor system is formed by using two uniform silica nanowires: one used as a reference arm and the other as a sensing arm is presented in Figure 5.1(a). Both arms are immersed in aqueous solution and the surface of the sensing arm is silanized and biomodified with specific receptors for higher selective detection. A layer around the wire is formed by the complex of chemical linker, antibody and *E.Coli* respectively as shown in the cross section of the composite waveguide in Figure 5.1(b).

The chemical linker is MUDA [mercapto undecanoic acid], its RI is 1.463 and thickness is 1.69nm and is used as linker for antibody (RI is 1.41 and thickness is 2.98nm) and the target antigen is *E.coli* with average RI of 1.37 and average thickness of 0.4 – 0.7 microns [212].

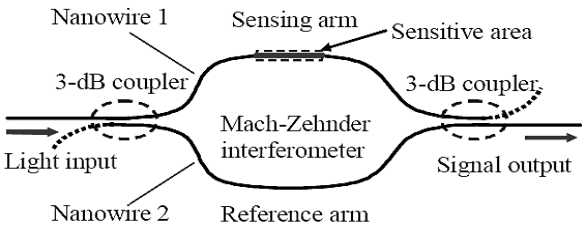

(a)

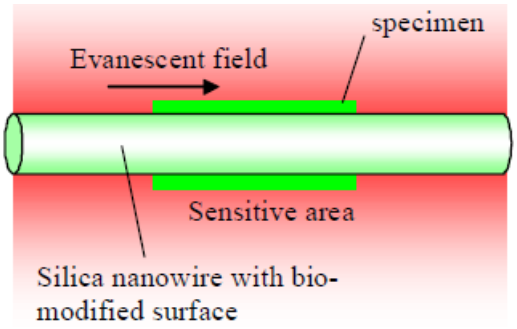

(b)

Figure 5.1: Schematic diagram of (a) the proposed sensor and (b) the cross section view of the composite waveguide, with a specimen layer.

A probe light that is launched through the nanowire propagates through the first 3 dB coupler, operating as an optical splitter, which divides it between the sensing and the reference arms, and it finally recombines via the second 3 dB coupler, working as an optical combiner, as shown in Figure 5.1(a). The phase shift caused by the index change due to the specimen placed in the sensing arm is numerically calculated and evaluated from the simulated signal output of the lower nanowire, as presented in Figure 5.1(a).

5.2.1 Modal Solution

Initially, the optical properties of the reference and the sensing arm of the single mode silica nanowires immersed in aqueous solution have been examined, where the latter is coated with the linker, antibody and *E.coli* under detection and the 3-D optical field profile of the mode of the two arms, for a core diameter, D, of 400 nm is presented in Figure 5.2.

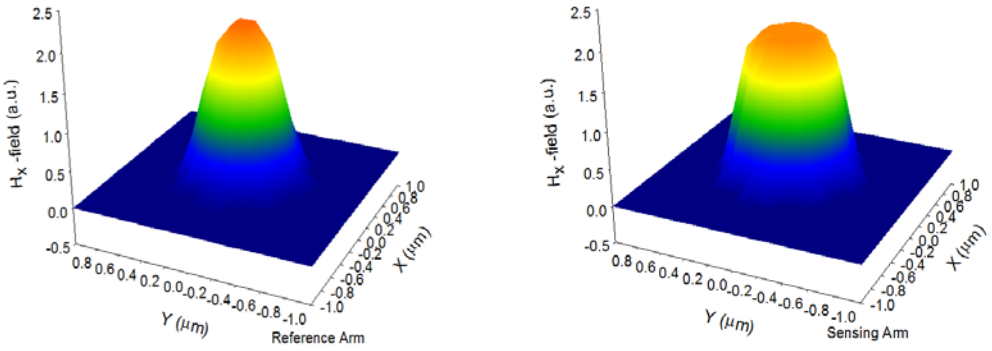

Figure 5.2: (a) 3-D field profile of the Hx mode for the reference and the sensing arm for D = 400 nm

The refractive index of the single-mode silica nanowire and the aqueous solution were considered to be 1.482 and 1.355, respectively, at an operating wavelength of 325 nm [213].

As can be seen from the field profiles of the optical mode for a core diameter, D, of 400 nm, in the reference arm shown in Figure 5.2 (a), the optical field is more confined in the silica

core and the aqueous solution does not have much effect on the field profile. However, for a core diameter, D, of 400 nm, in the sensing arm shown in Figure 5.2 (b) a small change in the refractive index profile produces a larger change in the field profile. As can be concluded evanescent field in the sensing arm expands more outside due to change of refractive index in the aqueous solution.

The optical field confinement in the reference and the sensing arms can be better viewed from the normalized field profile along the horizontal (x)-axis, as presented in Figure 5.3 for nanowire core diameter, D, of 150 nm. As can be seen from the earlier curves in Figure 5.3, the normalized optical fields for the reference and the sensing arms have small variation in the optical field profile.

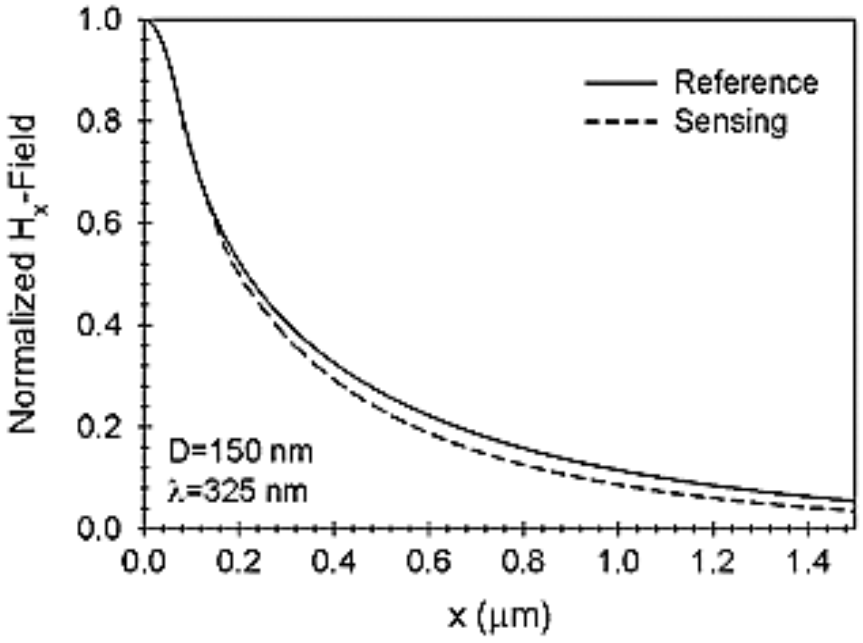

Figure 5.3: H_x along the x axis for a fibre diameter of D = 150 nm.

5.2.2 Effective Index Variation

Next, the variation of the effective reactive index of H_x^{11} in the reference and the sensing arms with the silica nanowire diameter, D, has been examined, and the results are presented in Figure 5.4. Here, the effective index of the reference arm and the effective index difference

between the two arms is plotted against core diameter, over a range of 100 nm to 800 nm. As can be seen from the aforementioned characteristics, as diameter, D, decreases, the effective index also reduces, and the rate of reduction slowly increases. The effective index difference between the reference and the sensing arm is presented in Figure 5.4. It is shown in the Figure 5.1, the effective index difference between the reference and the sensing arm decreases with the increase of the core diameter. However, for a core diameter, D, of 100 nm, peak value in Δn_{eff} is obtained and as the core diameter increases the effective index difference decreases.

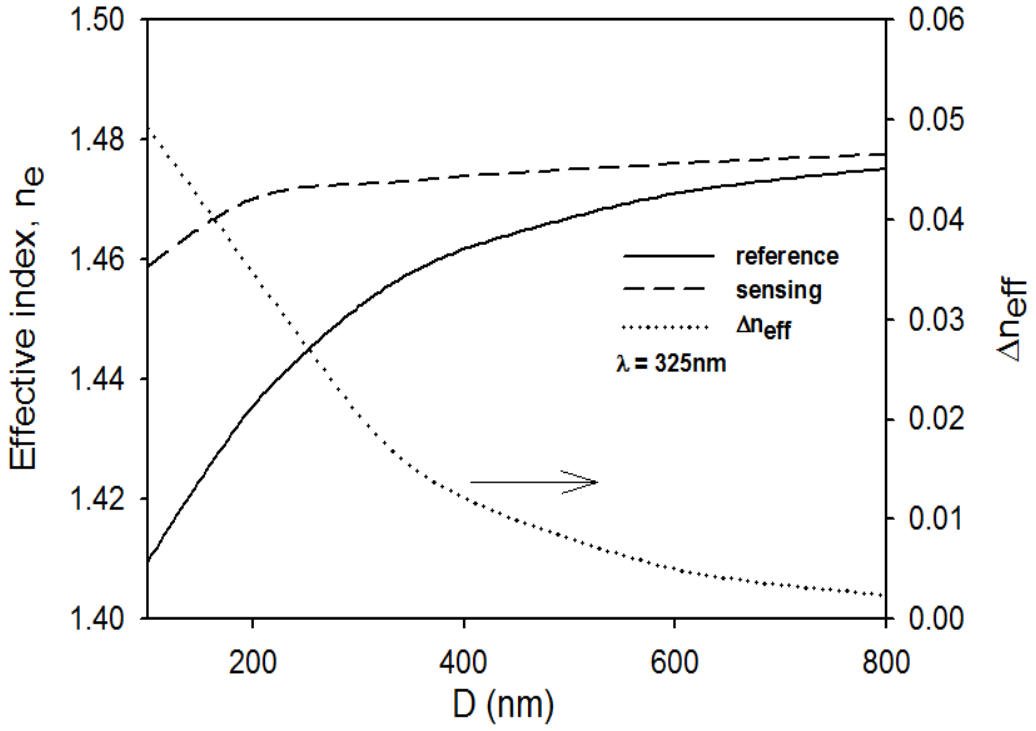

Figure 5.4: Effective index (n_e) and effective index difference (Δn_{eff}) between the reference and sensing arms as a function of the fibre diameter (D).

The effective index of the sensing arm is higher than the reference arm. It is due to increase of refractive index in the sensing arm with the addition of linker, antibody and *E.coli*. It can be noted that as the nanowire diameter is increased, the effective index asymptotically approaches that of the Silica refractive index, when most of optical power is confined in the Silica core. The effective index is dependent on the refractive index of surrounding medium.

Therefore, single mode nanowires are suitable for sensing elements and sensitive to the index change of the surrounding medium.

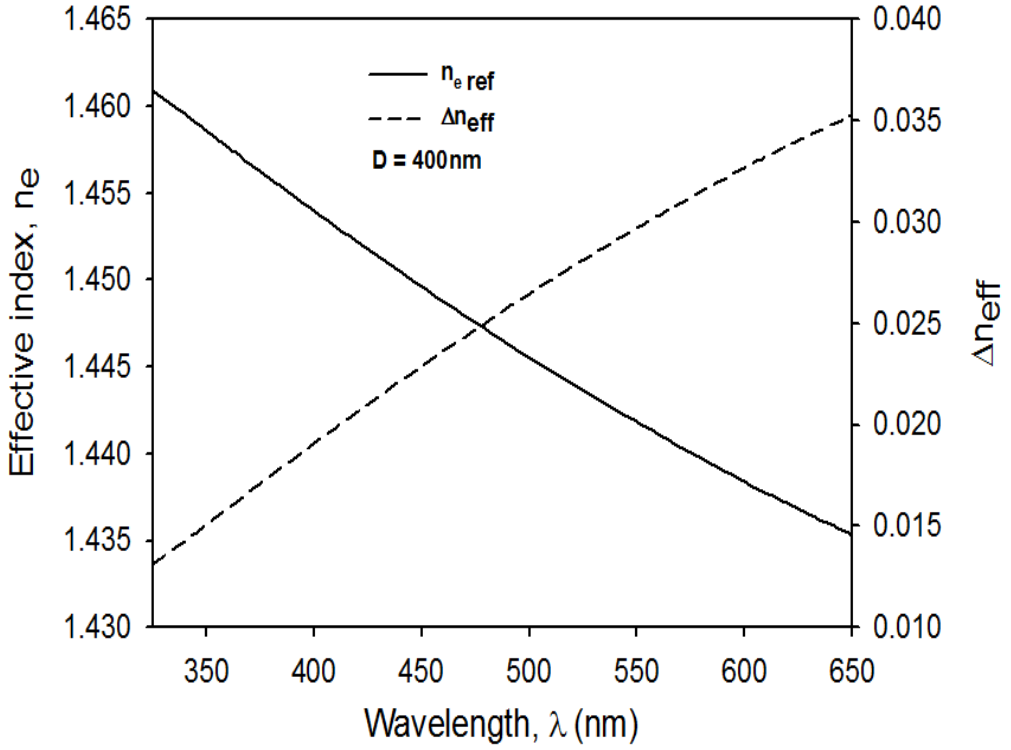

Figure 5.5: Change in effective index (n_e) and effective index difference (Δn_{eff}) as a function of the wavelength (λ)

Next, the effective index for the reference arm and the effective index difference between the reference and the sensing arms are presented, with the variation of the wavelength, in Figure 5.5. As can be seen from the Figure 5.5, the effective index of reference arm decreases with the increase of the wavelength and the effective index difference increases linearly with the increase of the wavelength for core diameter of 400 nm. When the wavelength increases, the mode is weakly confined and penetrates more into the sensing region of the sensing arm hence increases the effective index. However, when the wavelength decreases, the mode is well confined and decays more into the core region hence decreases the effective index of sensing arm.

5.2.3 Power confinement

Further, the power fraction in the aqueous solution for the reference and the sensing arm has also been studied with the variation of the nanowire core diameter and the result is presented in Figure 5.6. As can be seen from the aforementioned characteristics, for a core diameter, D, of 100nm the field extends mostly in the aqueous solution for both the reference and the sensing arms. However sensing arm exhibits more power in the aqueous solution than the power in the aqueous solution of reference arm. It is due to refractive index change in the aqueous solution of sensing arm when target antigen (*E.Coli*) is attached to immobilised antibody. As the value of D is increased further, the power in the aqueous solution is reduced since the field is more confined in the core region.

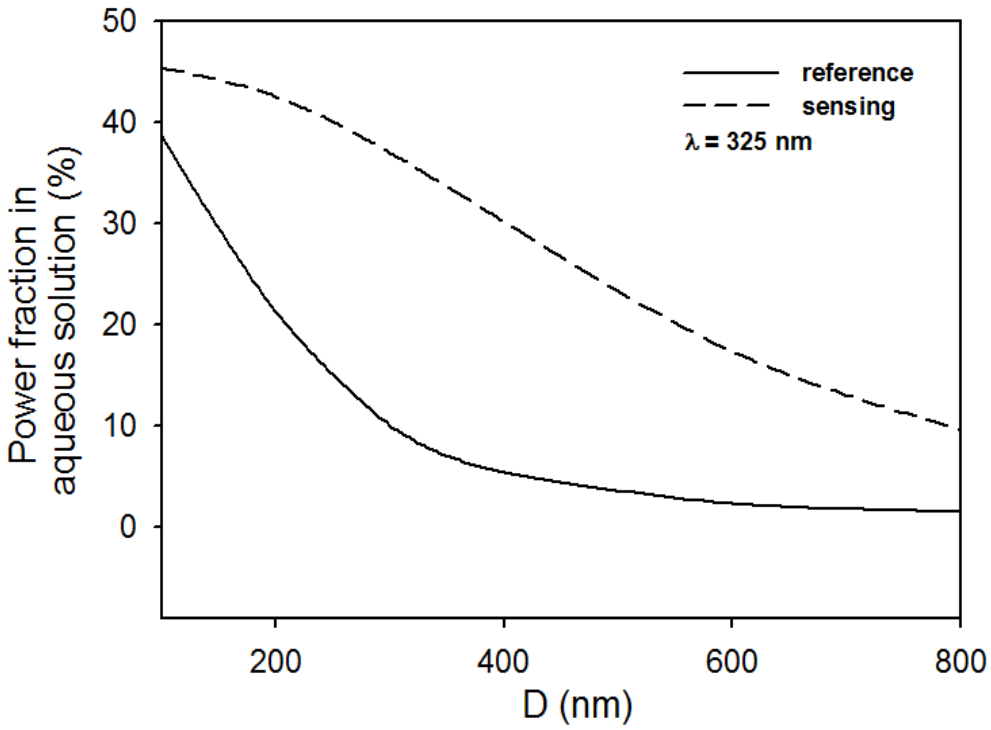

Figure 5.6: Power fraction in aqueous solution for the sensing and the reference arms as a function of the fibre diameter (D).

The change of the power fraction in the different regions of the sensing arm has been studied and is presented in Figure 5.7. As can be seen from the characteristics, shown in Figure 5.7, when the wavelength increases, the mode is weakly confined, and hence, less power is seen in the core region and more power is present in the cladding aqueous region. The mode is well confined for smaller wavelength values and more power is present in the core silica region. However, as the wavelength increases, the mode becomes weakly confined and more power is present in the aqueous solution region compared to the silica core region.

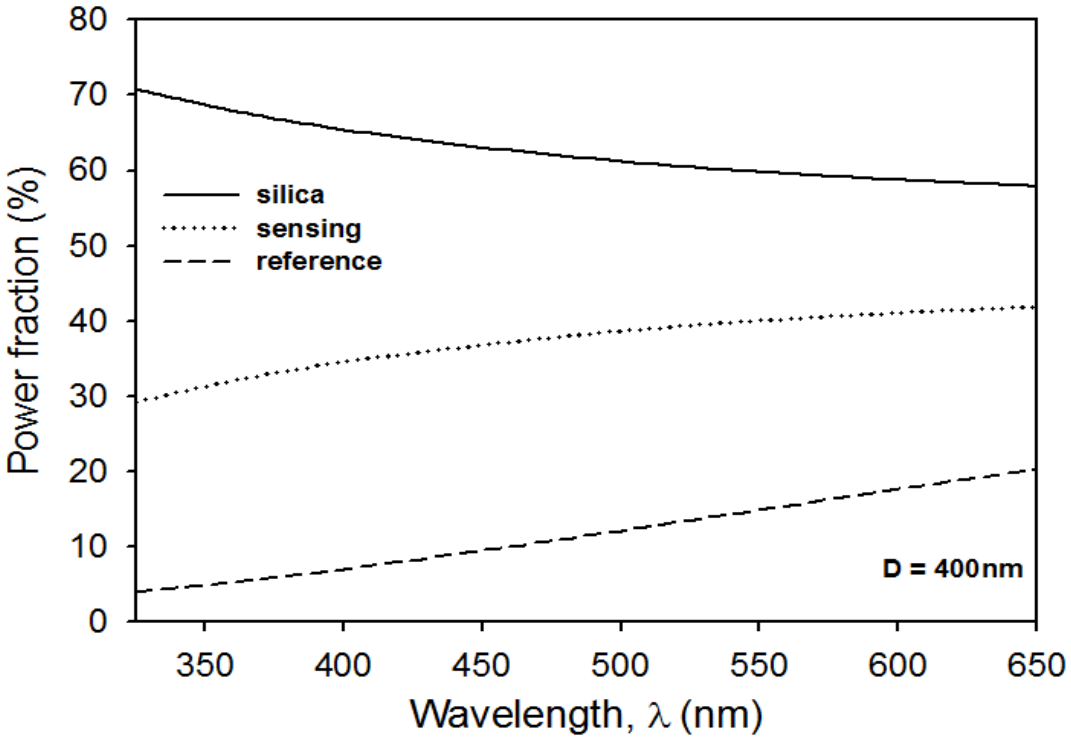

Figure 5.7: Power fraction for the sensing arm as a function of wavelength for a fibre diameter of D = 400 nm

5.2.4 Effect of thickness

Next, the change in the propagation constant β of sensing arm and the power fraction in the aqueous solution of sensing arm as a function of the *E.Coli* thickness, for a core diameter of D = 400 nm, have been investigated and are presented in Figure 5.8. As the *E.Coli*

thickness increases, both the propagation constant and the power fraction in the sensing arm decrease linearly.

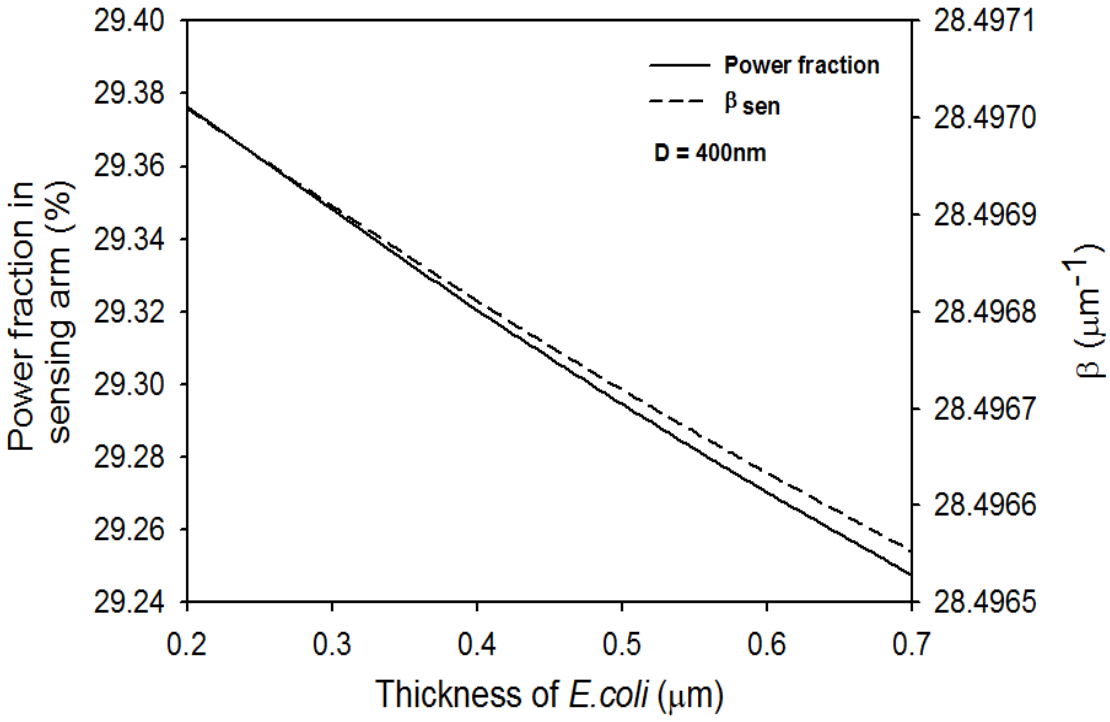

Figure 5.8: Change in propagation constant (β) and power fraction in the E.coli with the variation of the E.coli thickness.

As the thickness of *E.coli* increases the power fraction in the sensing arm and propagation constant of the sensing arm mode decreases with the increase in thickness of *E.coli*. This is due to the penetration of evanescent field into the sensing region decreases with increase of *E.coli* thickness. With the increase of sensing layer thickness evanescent field will not penetrate deep into the sensing region. However smaller nanowires with diameter of 100 nm and 200 nm may be used to penetrate more evanescent field into the sensing region.

5.2.5 Sensitivity

The effective index change is produced either by a change of cover medium refractive index (homogeneous sensing) or by a change of thickness of *E.coli* which is immobilized on nanowire (surface sensing). Adlayer thickness and change of cover medium refractive index affects the effective index of the propagating optical mode. Measurement of sensitivity depends on

optical field distribution in the sensing medium therefore the most important design task is to maximize the sensitivity of the biosensor.

Figure 5.9 shows the change in effective index and waveguide sensitivity decreases with the increase in diameter, D, of silica nanowire. The larger effective index variation and waveguide sensitivity is achieved at a D = 100 nm. The greater the change in Δn_{eff} more sensitive the biosensor will be. Therefore, when D = 100nm maximum index difference is achieved. When the nanowire dimension becomes too large, most of the power is confined in the silica core and a smaller effective index difference is achieved hence lesser sensitivity.

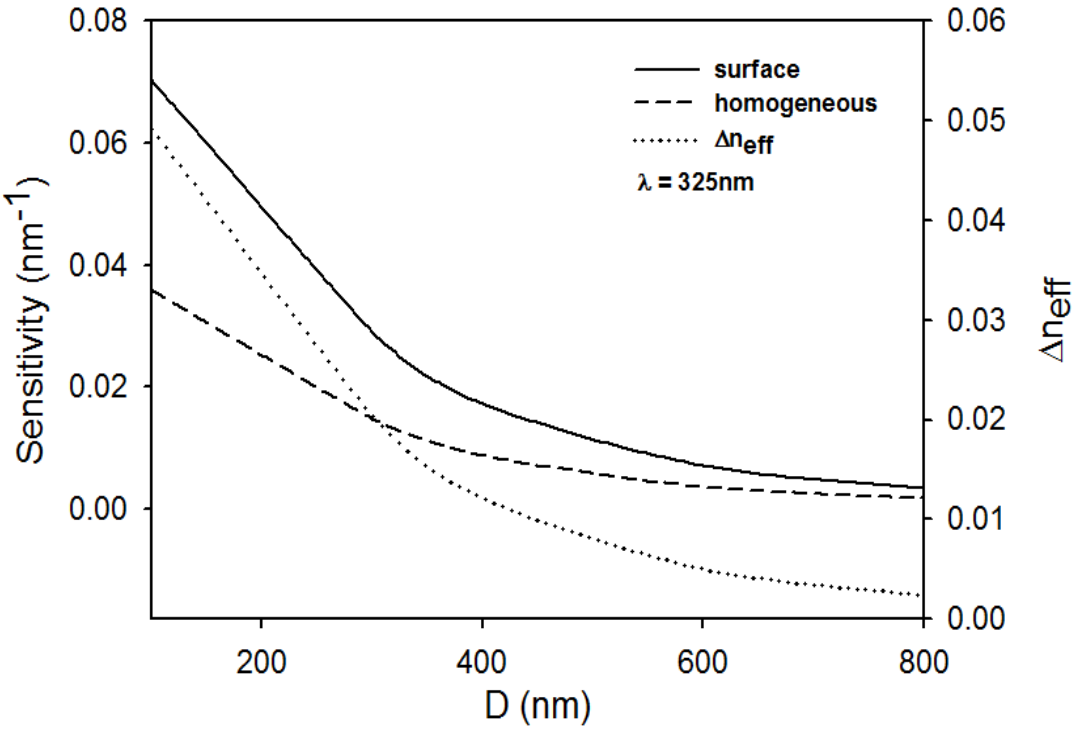

Figure 5.9: Variation of effective index difference, Δn_{eff} and waveguide sensitivity with Diameter, D (nm), of silica nanowire.

When designing a sensor, the sensitivity is a very important parameter to evaluate the device performance. To study the sensitivity of our device, we use the sensor to detect the change in the effective index of mode with the change in the refractive index of surrounding medium. When there is an extremely small index change around the nanowire, the guided light is changed in its optical phase. We assumed the sensing area length, L = 75µm. Calculated Δn_{eff}

is about 0.0131/μm at the wavelength of 325 nm induced by coating the nanowire with *E.coli* layer for a 400nm diameter silica nanowire.

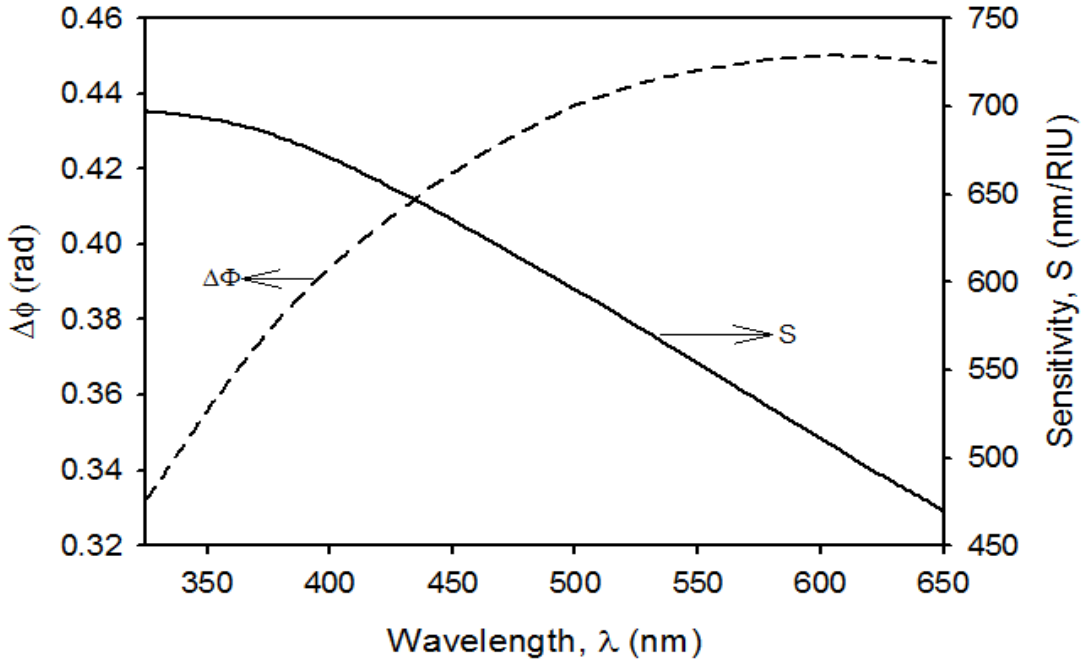

Figure 5.10: Sensitivity of the sensor as a function of the wavelength

The phase shift (Δϕ) of the sensing arm can be obtained as;

$$\Delta\phi = \frac{2\pi}{\lambda} L \Delta n_{eff} \qquad (5.1)$$

Where L is the effective length of sensitive area and Δn_{eff} is the effective index difference between the sensing arm and the reference arm, respectively. It is shown in the Figure 5.10a that the sensitivity of the device decreases with the increase in the wavelength and higher sensitivity of 697nm/RIU is achieved at wavelength of 325 nm. For comparison, the sensitivity of conventional Mach–Zehnder sensors based on integrated planar waveguides is much lower [209], showing that much higher sensitivity, or equivalently much smaller size can be achieved when sensing with silica nanowires.

5.3 Slot-waveguide biosensor for detection of DNA hybridisation.

Slot waveguides present an interesting alternative when compared to rib or strip waveguide based biosensors where light is predominantly guided in the high index material. The light thus has little interaction with the biomaterial. This is a drawback for biosensing applications where small refractive index variations caused by biomolecular interactions are monitored. In case of slot waveguide, light is confined in a low index slot region sandwiched between two high index rails. Due to the discontinuity of the electric field at the interface between the rails and slot, a significant fraction of the electromagnetic field is localized in the slot.

The sensitivity of an optical waveguide sensor relies on the amount of light in the medium to be sensed. Due to the increased amount of power confined in the slot region higher sensitivities will be achieved as compared to other waveguide based biosensors.

Author of [128] has compared conventional slot waveguide, slot rib waveguides and Si wire for sensing of aqueous solution. However the work presented here is based on the slot waveguide micro ring resonation for the detection of DNA Hybridization - binding of complementary DNA strands (targets) to DNA probes. Moreover we have calculated wavelength shift, device sensitivity, detection Limit, and power density and compared with the experimental work published in [214], [215], [216] and [217].

In the present work, the **H**-field Finite Element Method (FEM) based full-vector formulation is used for the solution of the TE and TM Slot Waveguide modes where the TE mode is highly confined in the slot region as compared to TM mode. In the FEM, a problem domain can suitably be divided into a patchwork of a finite number of subregions called “elements”. Each of the elements can have different shapes and sizes and by using many elements a complex problem can be accurately represented. In using the aforementioned approach, the field distribution in the transverse plane is obtained by the application of the variational formulation in the region. More recently, slot waveguide based biosensors have been

investigated using Finite difference time domain method (FDTD) and Finite Element Method [218,219,220].

In the present work by optimising the slot waveguide parameters such as the slot width, guide width and guide height a compact biosensor is proposed. The aim of this work is to provide a novel comprehensive analysis defining the modal characteristics, effective index variation of ssDNA and dsDNA, surface sensitivity and power confinement in the DNA layer of a slot waveguide biosensor with a nanoscale cross-section, and in doing so, the effects of the critical size of such waveguide are also presented. To undertake such analysis, an accurate and numerically efficient vector-**H**-field finite-element method (VFEM) [221] is used to calculate the propagation constant, effective index, power confinement factor and the full-vectorial modal field profiles of the waveguide. The full-vectorial electric field (**E**) is also derived from the vector **H**-field obtained to characterize modal properties of such waveguides.

5.3.1 Slot waveguide structure

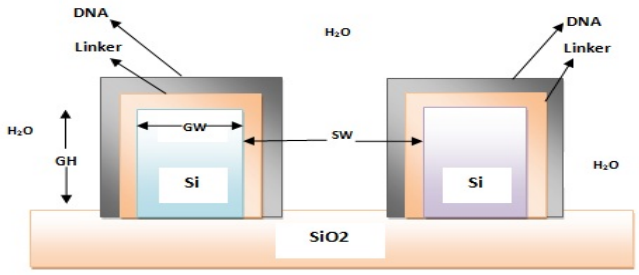

Figure 5.11: Slot Waveguide Biosensor

A slot waveguide is investigated for the biosensing applications. The slot waveguide is formed by two Si wires close to each other having nanometer dimensions as shown in Figure 5.11. Refractive index (RI) of silicon, silicon oxide and water is taken as 3.476, 1.444 and 1.31

respectively at an operating wavelength of 1550nm. The sensing structure is first coated with a linker layer (silanes) whose refractive index is taken as 1.42 [222] having a thickness of t=1 nm. The refractive index of ssDNA and dsDNA is taken as 1.456 and 1.53 [223] respectively. The thickness of the DNA probe layer is taken as n=8 nm and remains unchanged when binding of complementary DNA strands (targets) to DNA probes happens i.e., only refrective index changes from 1.456 (ssDNA) to 1.53 (dsDNA).

A waveguide height, GH = 320 nm and high index region width, GW = 180 nm [128], slot width, SW = 100 nm, linker layer thickness of t=1 nm and DNA probe thickness of n=8 nm is considered for the initial simulation study.

5.3.2 Modal solutions

In the study of modal field profile, the H-field based VFEM is used to obtain the modal solutions of such a waveguide. For this study, due to the availability of two-fold symmetry of the waveguide structure, only a half of the structure is considered, in which more than 80,000 irregular sized first order triangular elements have been employed to represent the waveguide structure. It takes about 2 minutes cpu time on a dual-core Pentium processor computer running solaris platform.

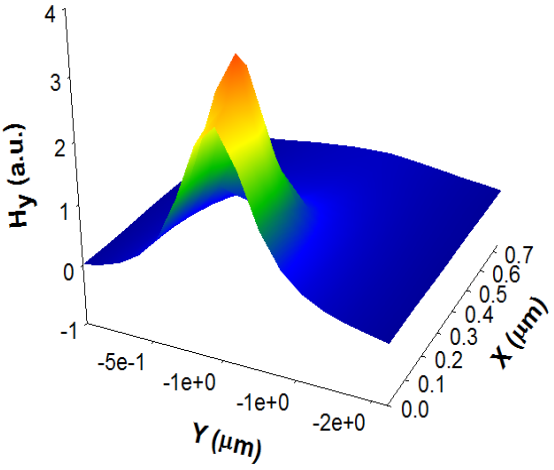

Figure 5.12: H_y field of the H_y11 mode

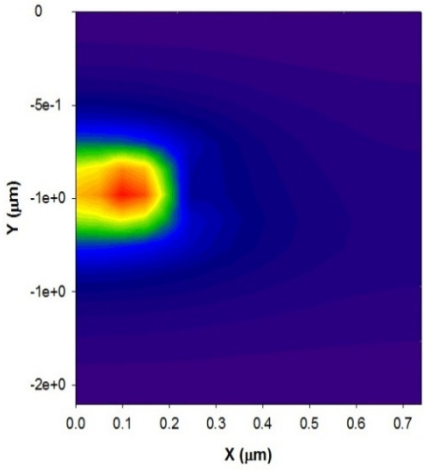

Figure 5.13: H_y Contour of H_y11 mode

The structure supports both fundamental quasi-TE and quasi-TM modes. For the quasi-TE mode the Hy field component is dominant, and H_x and H_z are the nondominant components. The dominant H_y field component of the Hy11 mode is shown in Figure 5.12 for the waveguide width, GW = 180 nm and height, GH = 320 nm

In its contour plot as shown in Figure 5.13 it is clearly visible that the modal confinement is much stronger in the slot region. Due to the large index contrast at interfaces, the normal electric field undergoes a large discontinuity, which results in a field enhancement in the slot region.

5.3.3 Effective index variation

The variation in the effective index of the fundamental H^y_{11} mode for a slot waveguide has been studied. The effective index, n_{eff}, of a given mode is a normalized propagation parameter, which can be defined by $n_{eff} = \beta_0/k_0$, where β_0 is the propagation constant of that mode and k_0 is the free space wavenumber defined as $k_0 = \omega (\varepsilon_0\mu_0)^{1/2} = 2\pi/\lambda$. The various simulations are carried out to yield the maximum effective index difference so that maximum waveguide sensitivity is achieved and small size compact biosensor is designed.

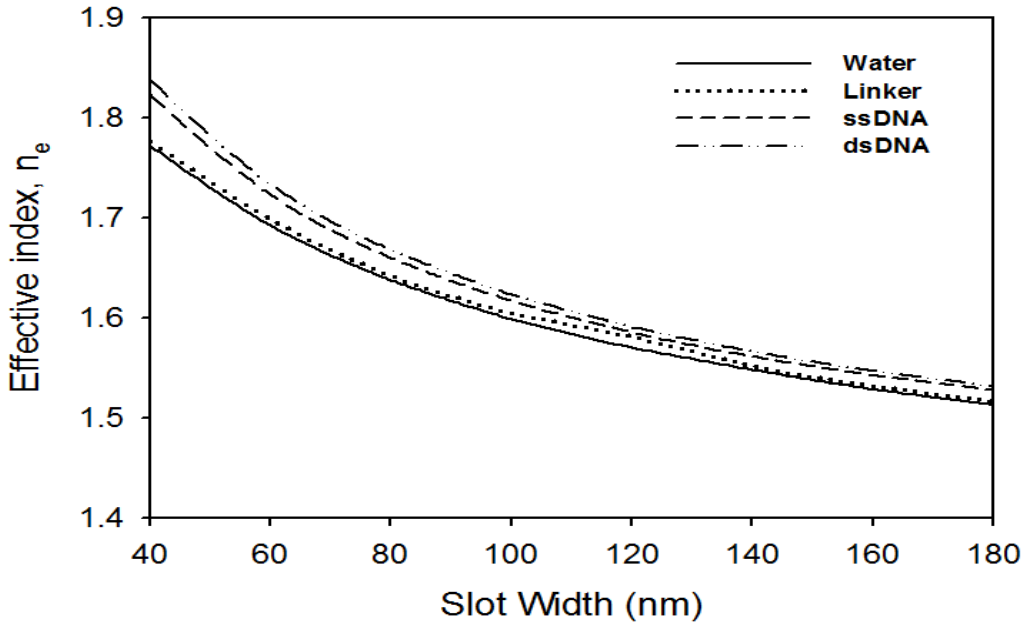

Figure 5.14: Variations of the effective index, n_{eff}, with the Slot width for TE Mode

For biosensing applications effective index change is an important design parameter. In Figure 5.14 variations of the effective index (n_{eff}) with the slot width for the fundamental H^{y}_{11} mode is presented. A waveguide height, GH = 320 nm and high index region width and GW = 180 nm is considered for the study of simulations. In Figure 5.14, solid line represents the water as the sensing medium, dotted line represents linker layer (thickness t=1 nm and RI = 1.42), and water as the sensing layers, dashed line represents linker layer, ssDNA (thickness n=8 nm and RI = 1.456), and water as the sensing layers and dash dotted line represents linker layer, dsDNA (thickness n=8 nm and RI = 1.53) and water as the sensing layers. In all the cases it shows the effective index decreases with the increase in slot width because when the slot gap is small a stronger coupling occurs and hence increases the effective index. It is also shown that the effective index is higher when the sensing medium is dsDNA as represented by dash dotted line in the Figure 5.14.

5.3.4 Sensitivity

In sensor development, sensitivity is an important parameter to evaluate the sensor performance. Fundamentally, sensitivity is determined by the strength of light-matter interaction. For an optical label-free sensor, sensitivity can be divided into waveguide sensitivity and device sensitivity. Device sensitivity is defined as the ratio of the change in the transducing optical parameter to the effective index change, while waveguide sensitivity is the ratio of the effective index change to the change in the waveguide parameter affected by analytes.

5.3.4.1 Waveguide sensitivity

The effective index change is produced either by a change of cover medium refractive index (homogeneous sensing) or by a change of thickness of DNA layer which is immobilized on waveguide surface (surface sensing). Measurement sensitivity depends on optical field distribution in the sensing medium, so one of the most important design task is the waveguide optimization in order to maximize its sensitivity.

Adlayer thickness and change of cover medium refractive index affects the effective index of propagating optical mode. The thickness of the DNA probe layer is taken as 8 nm and remains unchanged when binding of complementary DNA strands (targets) to DNA probes happens and the refractive index of ssDNA and dsDNA is taken as 1.456 and 1.53 respectively.

Waveguide sensitivity can be written as;

$$S = \Delta n_{eff} / RI \tag{5.3}$$

Where RI is the DNA layer refractive index and Δn_{eff} is the effective index difference when ssDNA and dsDNA is present. The effective index difference is achieved by simulating first by adding ssDNA layer on top of linker layer and then replacing ssDNA by dsDNA layer.

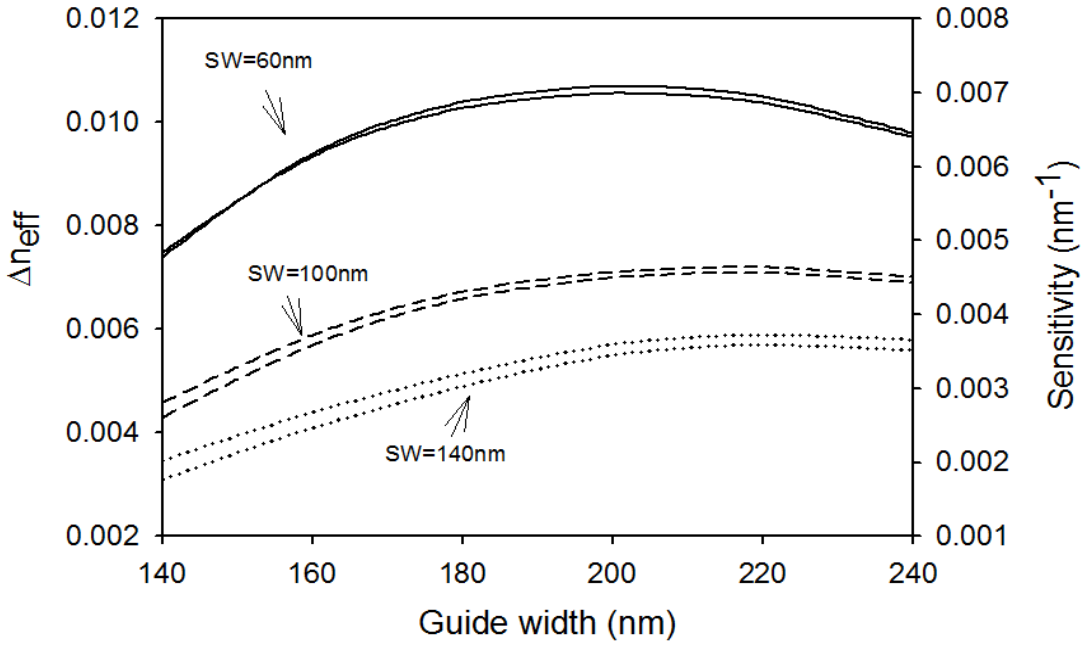

Figure 5.15: Variation of effective index difference, Δn_{eff} and waveguide sensitivity with guide width

A waveguide height, GH = 320 nm is fixed and SW = 60, 100 and 140 nm is varied. The sensing layers are linker layer (thickness t=1 nm and RI = 1.42), ssDNA (thickness n=8 nm and RI = 1.456), and water respectively. We have then replaced ssDNA layer with the dsDNA (thickness n=8 nm and RI = 1.53) to achieve the difference between the two.

Figure 5.15 shows larger effective index variation and waveguide sensitivity is achieved at a guide width = 220 nm when the slot width is 60nm, 100nm and 140nm respectively. The greater the change in Δ_{neff} more sensitive the biosensor will be. Therefore, when guide width is between 200nm and 220nm maximum index difference is achieved. Although, a smaller slot width shows a more sensitive design, however, considering the fabrication techniques available today, a 100 nm slot-width would be suitable design [224].

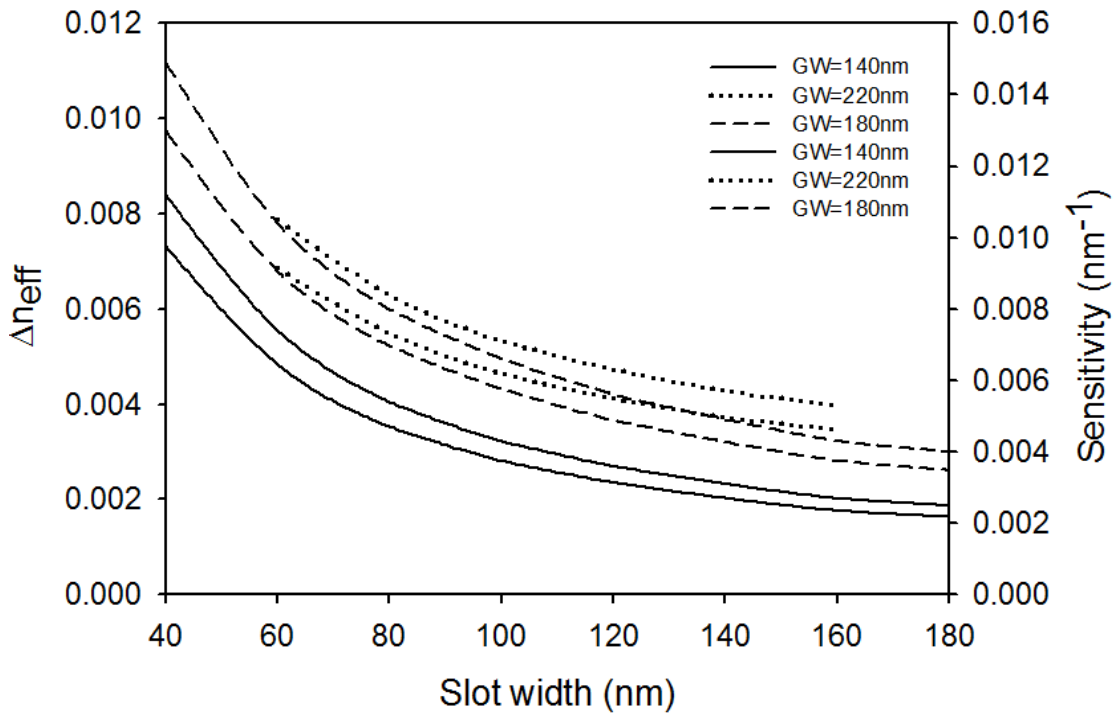

Figure 5.16: Variation of effective index difference, Δn_{eff} and waveguide sensitivity with slot width

Figure 5.16 shows variation of effective index difference and waveguide sensitivity with the slot width. The effective index difference, Δn_{eff} , as well as waveguide sensitivity decreases with the increase in the slot width due to presence of DNA layers. A waveguide height, GH = 320 nm is fixed and GW = 140, 180 and 220 nm is varied. The sensing layers are linker layer (thickness t=1 nm and RI = 1.42), ssDNA (thickness n=8 nm and RI = 1.456), and water respectively. We have replaced ssDNA layer with the dsDNA (thickness n=8 nm and RI = 1.53) to achieve the difference between the two. A large effective index variation is achieved when the slot width is less than 100 in all cases.

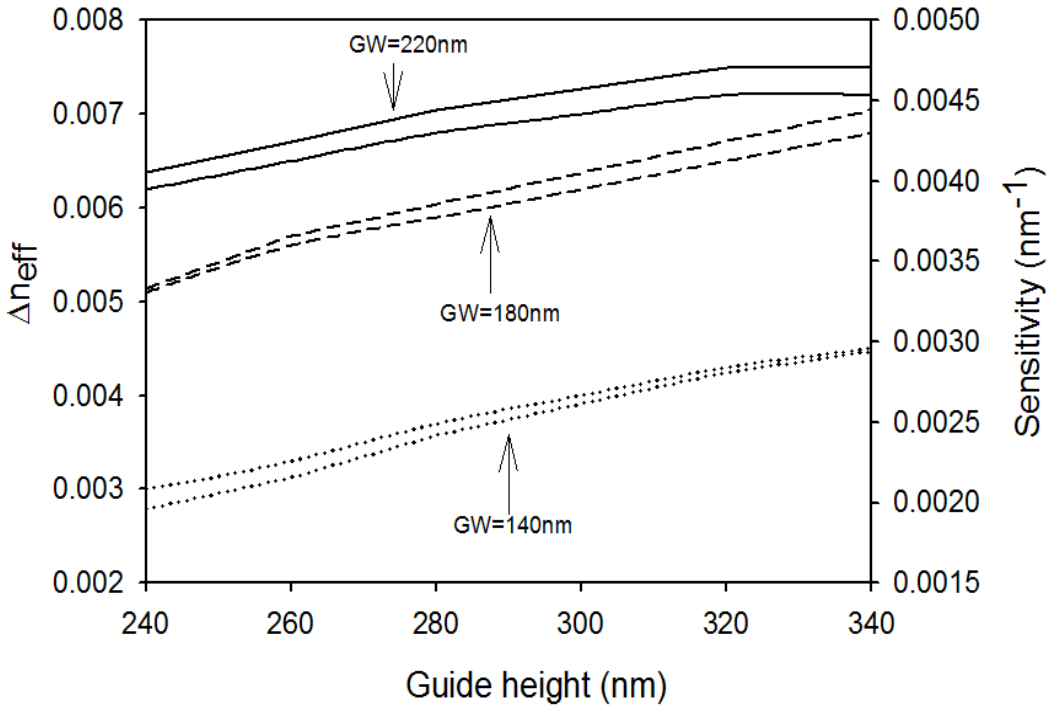

Figure 5.17: Variation of effective index difference, Δn_{eff} and waveguide sensitivity with guide height

Figure 5.17 shows variation of effective index difference, Δn_{eff} , and waveguide sensitivity with the guide height. When guide width is between 180nm and 220nm and slot width is 100nm maximum effective index difference can be achieved as compared to a guide width 140nm. The effective index difference increases with the increase in guide height. However if the waveguide dimension becomes too large, most of the power would be then confined in the Si core and a smaller effective index difference can be achieved hence less sensitivity and less confinement in the slot region. A line needs to be drawn to achieve a compact and smaller biosensor therefore guides height between 320nm and 340nm are the desirable dimensions.

A comparison is made with the structure simulated in [219]. The parameters of slot waveguide structure in [219] have Slot width = 100 nm, Guide width = 220 nm, and Guide height = 250 nm. The refractive indices of the silicon and the silicon oxide are 3.48 and 1.46, respectively.

In total, they have used about 100 00 mesh elements for full structure. When same parameters are simulated using our method calculated effective indices are shown in Figure 5.18 below. For this study, due to the availability of two-fold symmetry of the waveguide structure, only a half of the structure is considered, in which 80,000 triangular elements have been employed to represent the waveguide structure. The cover medium refractive index is equal to 1, 1.33 1.444, 1.456 and 1.530 for air, aqueous solution, silicon oxide, ssDNA and dsDNA respectively.

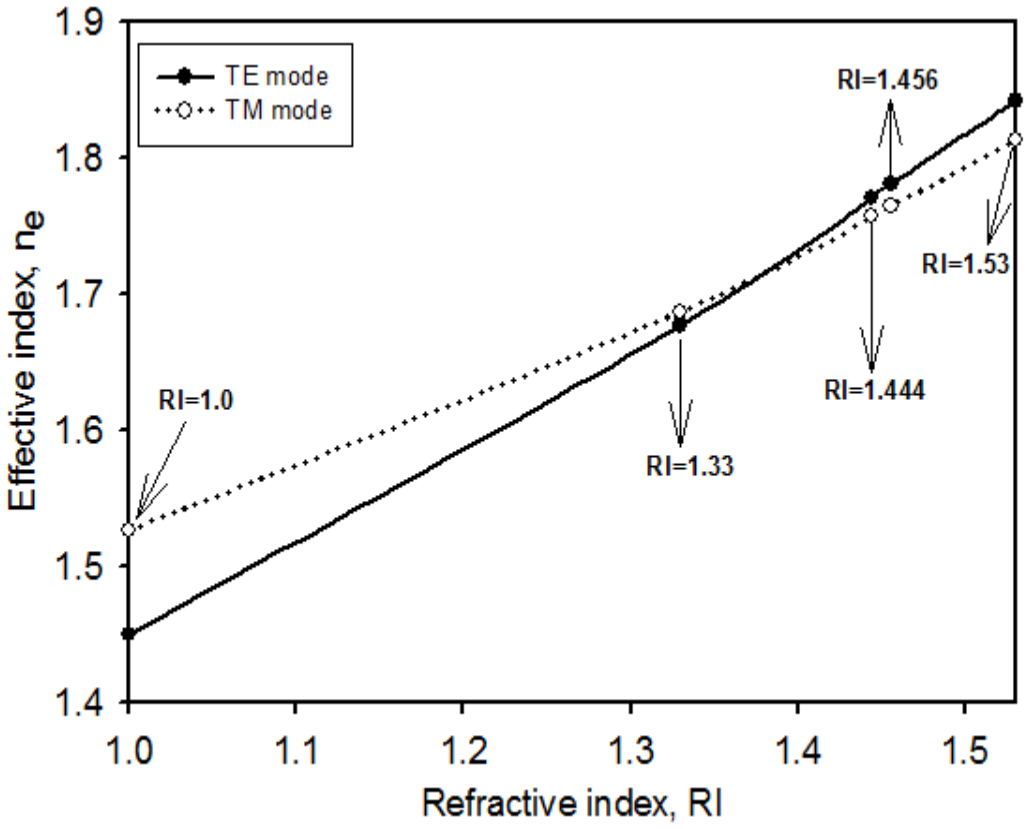

Figure 5.18: Variation of Effective index, n_e with RI

The effective index of TE and TM mode increases with the increase in the refractive index of cover medium. When cover medium refractive index is equal to 1, 1.33 and 1.444 a strong decrease in the effective index of the quasi-TE mode is measured whereas the effective index of the quasi-TM mode is less affected. This behaviour is direct evidence that, for the quasi-TE mode, light is indeed concentrated in the low-index region because of the field discontinuity.

However, when cover medium refractive index is equal to 1.456 and 1.530 the effective index of the quasi-TE mode is getting higher than the quasi-TM mode. The field still is concentrated in the low-index region of quasi-TE mode but the increase in its effective index is due to increase in the cover medium refractive index including the slot gap region. Therefore, if refractive index of the low-index region is increased the quasi-TE mode effective index is increased and gets higher than the quasi-TM mode.

When cover medium index is equal to 1.0 the calculated effective index is 1.757767 for the quasi-TM mode and 1.611924 for the quasi-TE mode at the operating wavelength of 1545 nm in [219]. When same parameters are simulated using our method the calculated effective indices are 1.5271 for the quasi-TM mode and 1.4509 for the quasi-TE at the operating wavelength of 1545 nm. This difference in effective indices of the quasi-TM mode and the quasi-TE mode is maybe due to difference in x-side and y-side total length of the structure. The x-side total length of 0.500 μm including guide width of 0.220 μm and y-side total length of 1.500 μm including height of 0.250 μm is set in our structure. In [219] there is no mention of total length in the x-side and the y-side of the structure. However, when x-side total length is reduced from 0.500 μm to 0.330 μm and y-side total length increased from 1.500 μm to 2.050 μm the effective index of the quasi-TE mode is increased from 1.4509 to 1.62540.

5.3.4.2 Device Sensitivity

Device sensitivity only depends on device properties, and waveguide sensitivity is relevant to waveguide structures regardless of the type of devices. Based on the definition, device sensitivity is related to the variation of transducing optical parameters, and thus depends on the transducing method. For the resonant wavelength shift scheme, it is expressed as

$$S = \Delta\lambda/\Delta n \tag{5.4}$$

$$\Delta\lambda = \frac{\Delta n_{eff} * \lambda_{res}}{n_g} \tag{5.5}$$

Where Δ_{neff} is the change of the effective index caused by the analyte binding, λ_{res} is the resonance wavelength and n_g is the group index and its value is 1.81264 at wavelength of 1550nm as shown in Figure 5.19 when silicon width is 220nm, height is 320 nm and slot width is 100 nm.

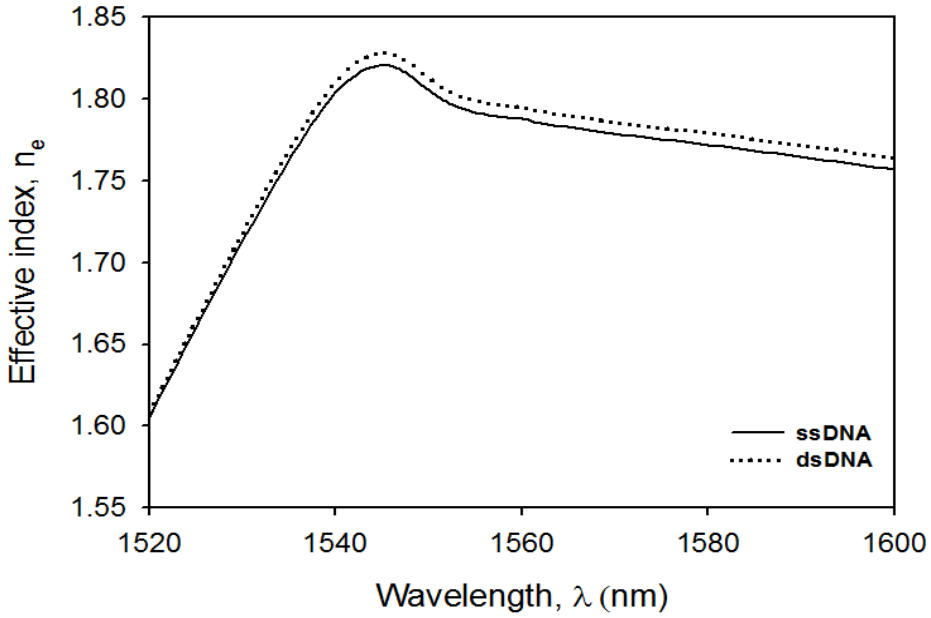

Figure 5.19: Variation of effective index with wavelength

As a function of slot width and guide width the effective index of the waveguide was simulated once for ssDNA and once for dsDNA. By using Eq 5.3, the difference in effective index $\Delta n_{eff} = n_{eff,ssDNA} - n_{eff,dsDNA}$ was used to calculate the expected wavelength shift of the slot waveguide.

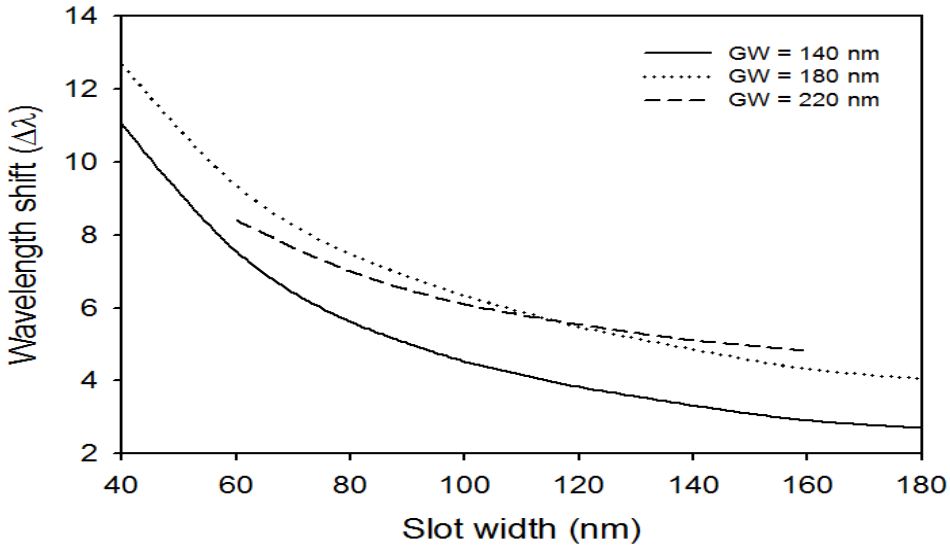

Figure 5.20: Variation of wavelength shift with slot width

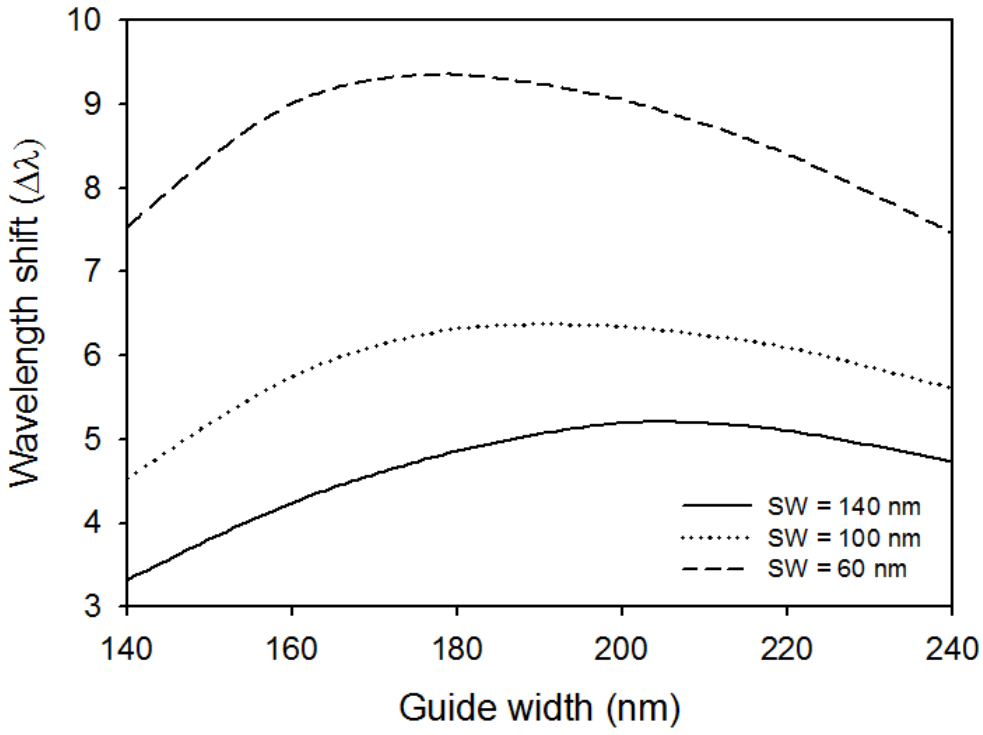

Figure 5.21: Variation of wavelength shift with guide width

Figures 5.20 and 5.21 show the calculated resonance wavelength shift as a function of slot width and guide width. In this range of the parameters, the sensitivity increases with decreasing slot width. When silicon width is 220nm, height is 320 nm and slot width is 100 nm our simulation shows that the effective refractive indices of ssDNA and dsDNA are 1.80549

and 1.81264 respectively with 6.12nm resonance wavelength shift, and sensitivity of 856 nm/RIU is achieved.

In our sensor, a large resonance wavelength shift is caused by large light-matter interaction and by decreasing the slot width. A comparison is made with the following structures [215], [216] and [214] respectively. In case of [215] where Slot width = 100 nm, Guide width = 210 nm, Guide height = 220 nm, RI = 1.45 and a wavelength shift is 5.4 nm. When same parameters are simulated using our method a wavelength shift of 5.56 nm is achieved. This difference is due two different numerical methods are applied in simulating the structure. The authors in [215] have used FIMMWAVE for theoretical simulations and don't have any mention of mesh elements employed in simulating the structure. We have applied H-field Finite Element Method (FEM) based full-vector formulation in calculating the effective indices of the TE and TM modes of slot waveguide structure in which 80,000 triangular elements have been employed. Despite the difference in values of effective indices and resonance wavelength shift we have a similar sort of trend in optimising the slot width and guide width of the slot waveguide. Higher values of resonance wavelength shift are calculated when slot width is less than 100nm as shown in the Figure 5.20 and same is the case with structure simulated in [215]. Similarly, higher values of resonance wavelength shift are calculated when guide width is between 180nm and 240nm as shown in the Figure 5.21. Other parameters like quality factor in [215] has not been studied because it needs either Beam Propagation Method (BPM) or FDTD method for calculating the quality factor values which is not the focus and objective of this work and will be taken into consideration in the future work.

In case of [216] where Slot width = 200 nm, Guide width = 400 nm, Guide height = 300 nm, RI = 1.45 and a wavelength shift is 3 nm. A wavelength shift of 4.2nm is achieved in our simulations when using same values of slot waveguide as in [216]. The difference in comparing

results is because of two different numerical methods applied in simulating the structure. The authors in [216] have calculated numerical values of wavelength shift experimentally.

Different results of wavelength shift is achieved when same slot waveguide parameters as in case of [214] are used (Slot width = 200 nm, Guide width = 500 nm, RI of ssDNA = 1.456, RI of dsDNA = 1.53 and a wavelength shift of 3.634 nm). The authors of [214] have used FDTD numerical method in simulating the structure which isn't the objective of this research work.

5.3.5 Sensor Detection Limit

Sensor detection limit (DL) is another important parameter to characterize the sensor performance. DL is the smallest change in the refractive index which is equal to the resonance wavelength resolution divided by the sensitivity [215]. The DL can be deduced by taking into account the noise in the transduction signal, σ, i.e., the minimum resolvable signal: DL = σ/S, where S is the sensitivity. For an optical RI-based label-free sensor, DL in units of refractive index units (RIU) is naturally used to quantify the sensor performance, which enables a rough comparison of the sensing capability among different optical technologies and structures. [126]. We follow the convention of using 3 standard deviations σ of the total system noise as a measure of the sensor resolution [227].

$$R = 3\sigma = 1.2 \text{ pm} \tag{5.6}$$

Improvement in the DL can be accomplished by increasing the sensitivity or reducing the noise level. Sensitivity can be enhanced by increasing the light-matter interaction. For our sensor, the detection limit is 1.43×10^{-6} RIU.

5.3.6 Power confinement

The confinement factor in any particular area normalized to the total power, which is obtained by integrating the Poynting vector, from the H-and E fields as given below:

$$S_z = \int\int_{\Omega} \{E \times H\}\, dxdy \qquad (5.7)$$

The waveguide sensitivity depends on the optical field confinement factor in the sensing medium. Quasi-TE mode supported by a slot waveguide is highly confined in the gap region and its confinement factor in the DNA layer is typically around 10-12%, which means a very large sensitivity to cover index change. Quasi-TM mode is significantly less sensitive to cover index change and its confinement factor is only around 4-5%.

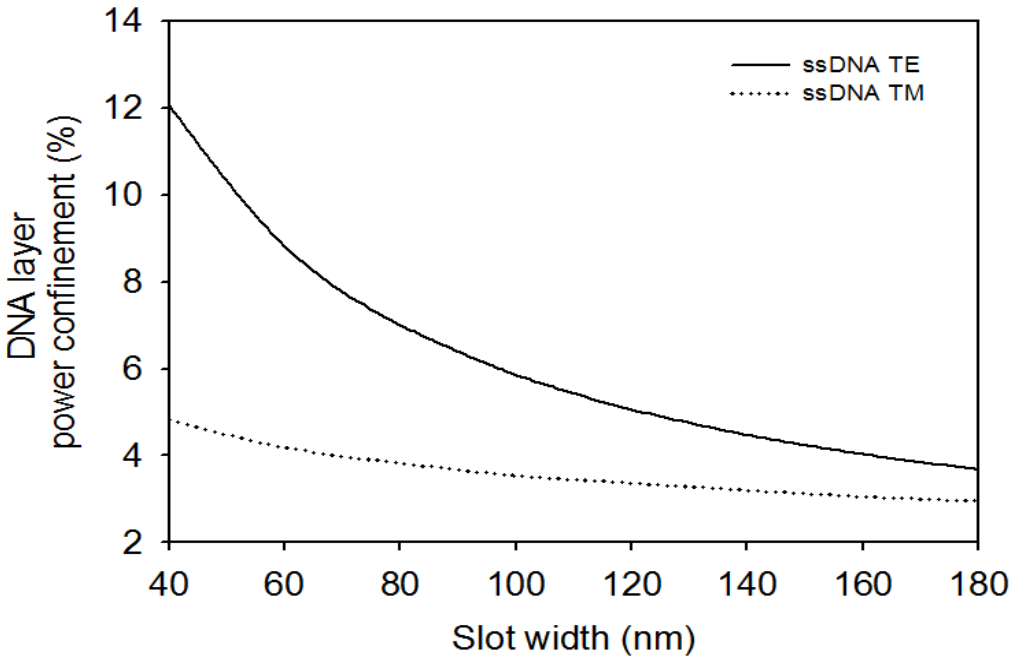

Figure 5.22 (a): Power confinement factor in ssDNA layer

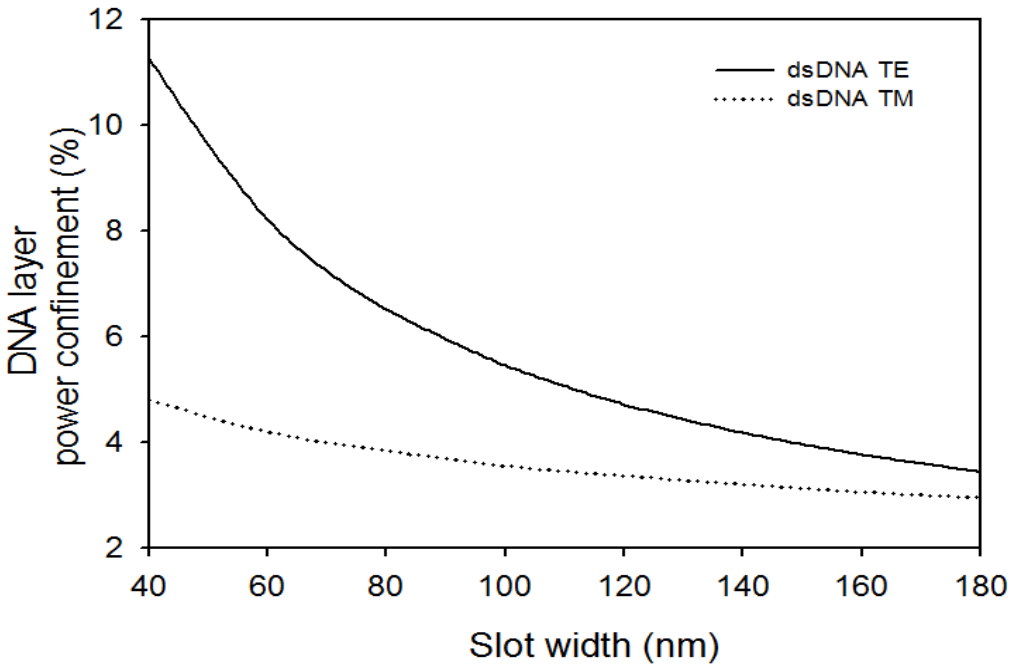

Figure 5.22 (b): Power confinement factor in dsDNA layer

As shown in Figure 5.22 (a) and 5.22 (b), the difference in the field confinement between ssDNA and dsDNA is small and that is why the curves are plotted separately otherwise they overlap with each other.

TE mode has more power confinement due to normal electric field undergoes a large discontinuity, which results in a field enhancement in the slot region when the slot width is smaller. However, TM mode has less power confinement in the slot region because optical power is localised more in the high index region and less confined in the slot region.

The slot width is varied from 40 nm to 180 nm keeping guide width as 220 nm and guide height as 320 nm. The highest power confinement is achieved when slot width is 40 nm and sensing medium is ssDNA. When the slot gap is smaller, stronger coupling occurs and hence more power confinement. However, it is important to remember the fabrication limitations that the slot width less than 100nm are not easy to fabricate and hence slot width of 100nm is the minimum desirable width for the design of our biosensor [224].

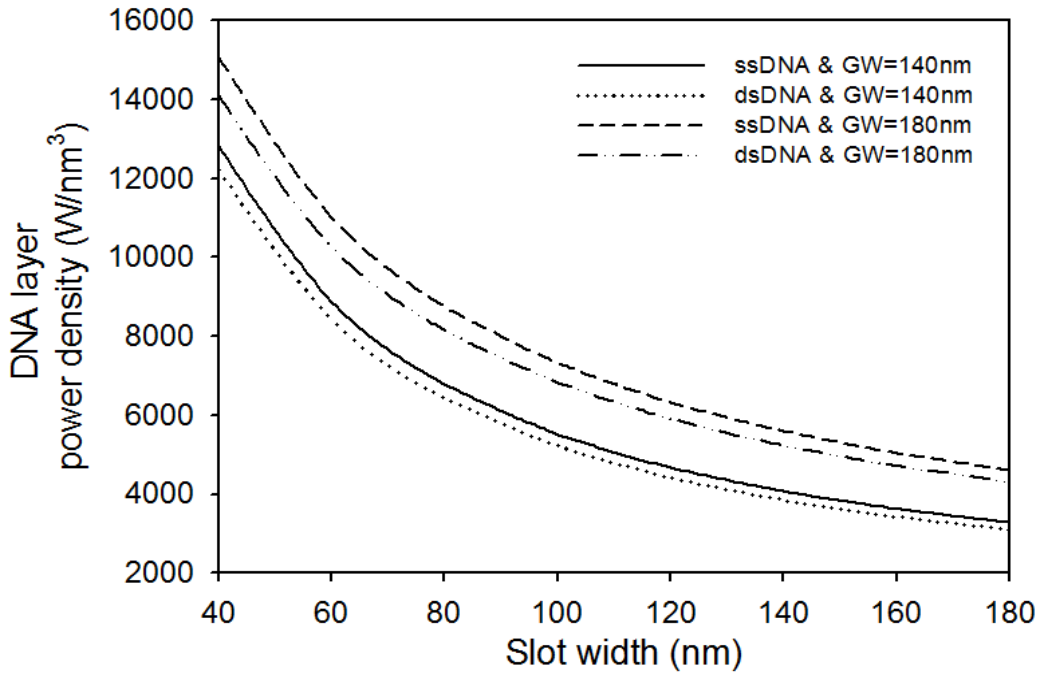

Figure 5.23: Variation of power density in DNA layer with the slot width for TE mode

Another important parameter in the design of such biosensors is the slot power density, which is defined as the power confinement in the sensing medium divided by the sensing medium area [220]. Figure 5.23 shows the variation of the slot power density for different slot widths keeping constant guide width of 140nm and 180nm respectively and guide height of 320nm. The guide width of 140nm and 180nm is compared in order to achieve better results. The power density is a maximum when the slot width is smaller and guide width is 180nm. Smaller the slot widths better the coupling efficiency. Power density is higher when the sensing medium is ssDNA as compared to dsDNA in both the cases of guide widths. When the index contrast is high the normal electric field undergoes a large discontinuity, which results in a field enhancement in the slot region therefore more power confinement in the slot region in case of ssDNA as compared with dsDNA.

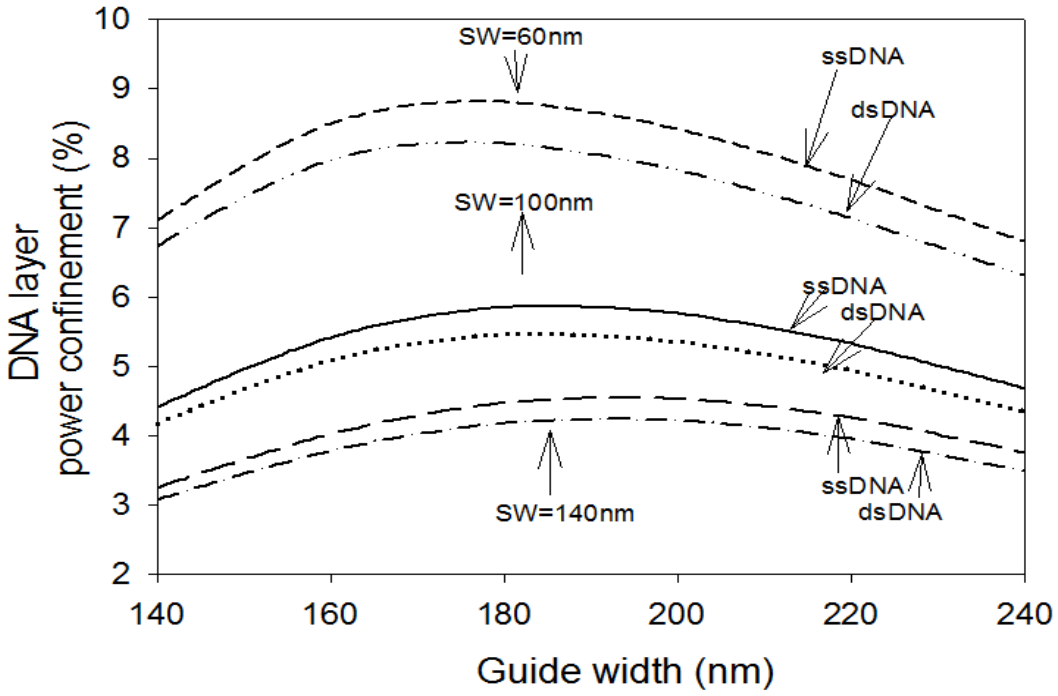

Figure 5.24: Variation of power density in DNA layer with the guide width for TE mode

Next the effect of power confinement is measured by varying the guide width and keeping the sloth widths as 60nm, 100nm and 140nm and guide height as 320 nm. The maximum power confinement is achieved when guide width is 180nm and slot width is 60nm as shown in Figure 5.24. Then followed by guide width of 180 and slot width of 100nm. However slot width of 60nm is not easy to fabricate therefore slot width of 100nm and guide width of 180nm is an ideal combination for achieving maximum power confinement. Again, it is evident that power confinement is higher when the sensing medium is ssDNA as compared to dsDNA in all the cases of varying slot widths due to its high index contrast with the guide.

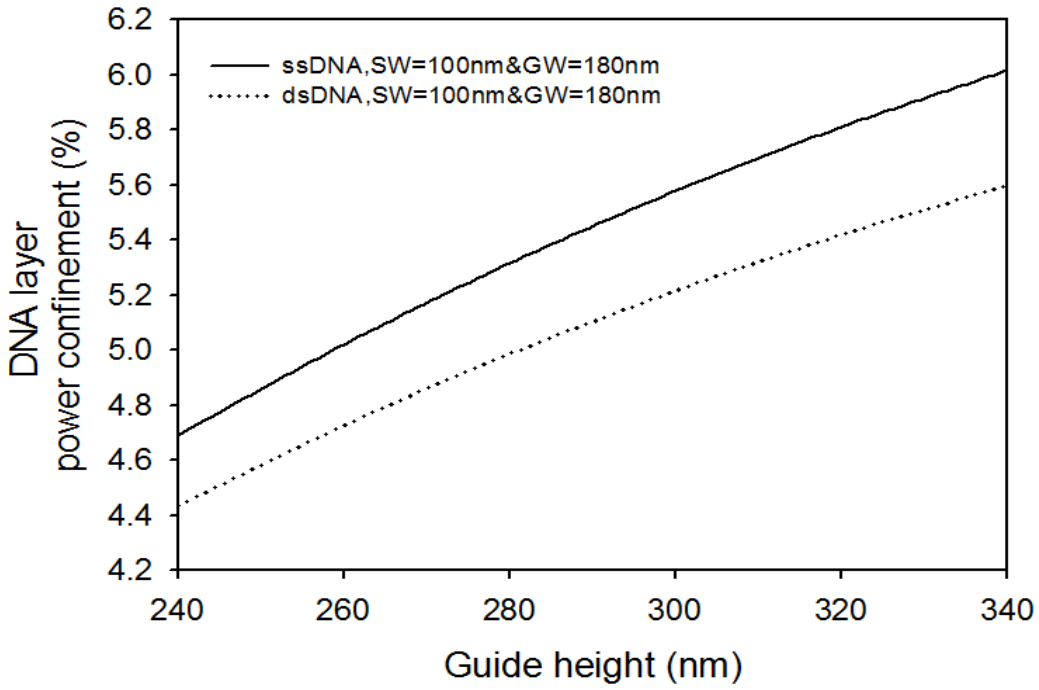

Figure 5.25: Variation of power density in DNA layer with the guide height for TE mode

Further, the guide height is varied whilst keeping slot width as 100 nm and guide width as 180 nm which is the best possible combination as shown above in Figure 5.15 and Figure 5.16. The power confinement increases with the increase in guide height as shown in the Figure 5.25. As the waveguide dimension becomes large, most of the power would be confined in the Si core however due to restrictions in guide width and slot width we see power confinement in the DNA layer increases with the guide height. Most of the easily available wafers are of H=220nm, and slot waveguide of other heights needs to be fabricated specifically.

Comparing Figures 5.23, 5.24 and 5.25 with Figures 5.15, 5.16 and 5.17 it appears power confinement and sensitivity can be achieved with the same design parameters where sensitivity is maximum we can also see power confinement is maximum in all the cases.

5.4 Simulation results for non-vertical sidewall slot waveguide

In this section we present the results of a non-vertical sidewall slot waveguide structure (slanted-shaped slot waveguide) as shown in Figure 5.26. Numerical simulations of the possible mode field, the power confinement, and the sensitivity are carried out for different waveguide geometry such as non-vertical sidewall width, slot width, guide height and guide width, operating wavelengths and cladding materials. The simulation study here is based on a comparison of non-vertical sidewall slot waveguide with the conventional slot waveguide structure defined above in the Figure 5.11.

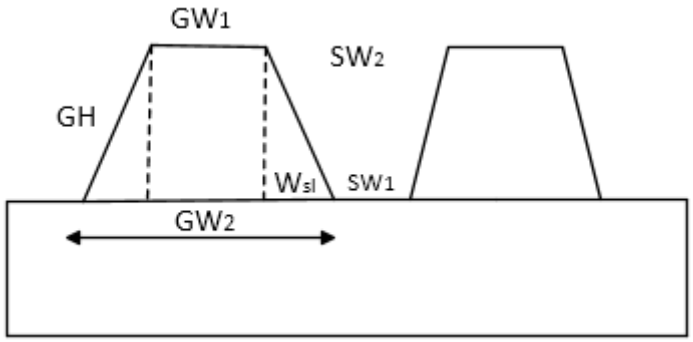

Figure 5.26: Non-vertical sidewall slot waveguide biosensor

Refractive index (RI) of silicon, silicon oxide and water is taken as 3.476, 1.444 and 1.34 respectively at an operating wavelength of 1550nm. The sensing structure is first coated with a linker layer (silanes) whose refractive index is taken as 1.42 [222] having a thickness of t=1 nm. The refractive index of ssDNA and dsDNA is taken as 1.456 and 1.53 [223] respectively. The thickness of the DNA probe layer is taken as n=8 nm and remains unchanged when binding of complementary DNA strands (targets) to DNA probes happens i.e., only refrective index changes from 1.456 (ssDNA) to 1.53 (dsDNA).

A waveguide height, GH = 320 nm and high index region width, GW = 180 nm [128], slot width, SW = 100 nm, linker layer thickness of t=1 nm and DNA probe thickness of n=8 nm is considered for the initial simulation study. The structure supports both fundamental quasi-TE and quasi-TM modes. For the quasi-TE mode the Hy field component is dominant, and H_x and

H_z are the non-dominant components. The dominant H_y field component of the Hy11 mode is studied using the full-vectorial finite element method and its contour plot is shown in Figure 5.27 for the waveguide width, GW = 180 nm and height, GH = 320 nm.

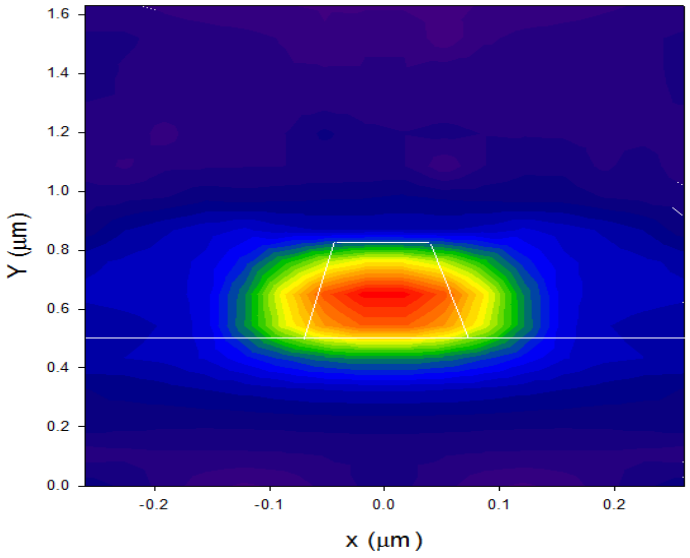

Figure 5.27: H_y Contour of H_y11 mode

The contour plot of dominant H_y field component of the Hy11 mode is shown in Figure 5.27 for the waveguide width, GW = 180 nm and height, GH = 320 nm. It is clearly visible that the modal confinement is much stronger in the slot region. Due to the large index contrast at interfaces, the normal electric field undergoes a large discontinuity, which results in a field enhancement in the slot region.

5.4.1 Effect of non-vertical sidewall

The change of effective index as induced by non-vertical sidewalls is calculated in the Figure 5.28. When varying the width of non-vertical sidewalls the effective mode index of quasi-TE mode in a slot waveguide (GW_1=180nm, GH=320nm and SW=100nm) increases dramatically with the increase of non-vertical sidewalls width. The increase in effective index with non-vertical sidewalls is an indication of an enhanced optical confinement.

A linear dependence of effective index change on non-vertical sidewalls has been observed. Non vertical sidewalls influence on effective index is stronger for quasi-TE because the

relevant electric field has its maxima along the vertical interfaces between silicon guide and gap region.

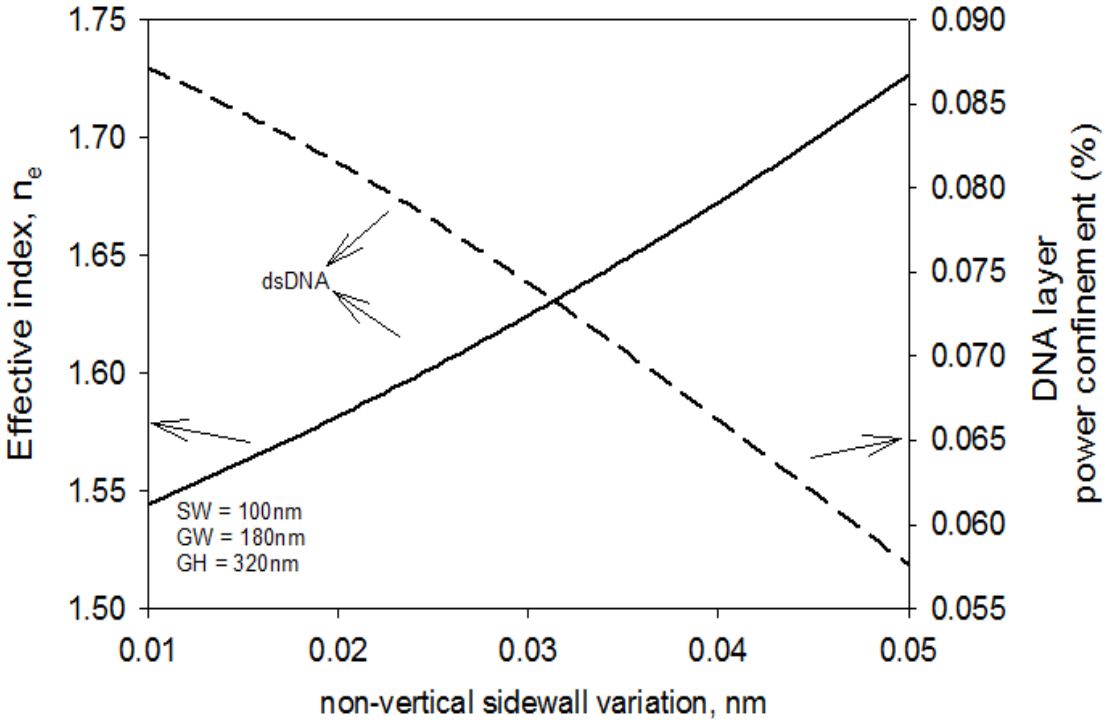

Figure 5.28: Effective mode index and power confinement in a non-vertical slot waveguide with RI of dsDNA = 1.53 as function of W_{sl} (non-vertical sidewall variation).

With an increase of non-vertical sidewall width power confinement decreases in the cover medium i.e. DNA layer due to enhanced optical field confinement along the vertical interfaces between the silicon guide and the gap region. Therefore, most of field remains between the silicon guide and the gap region which leads to less confinement in the cover medium. Hence this shape will have an impact on the sensor performance when compared to conventional slot waveguides whereby power confinement in the cover medium is higher.

5.4.2 Effect of slot width

Next, effect of varying slot width is studied with fixed dimension of 320nm height (GH), 180nm top-width (GW_1), and 280nm bottom-width (GW_2) at an operating wavelength of 1550nm as shown in Figure 5.29.

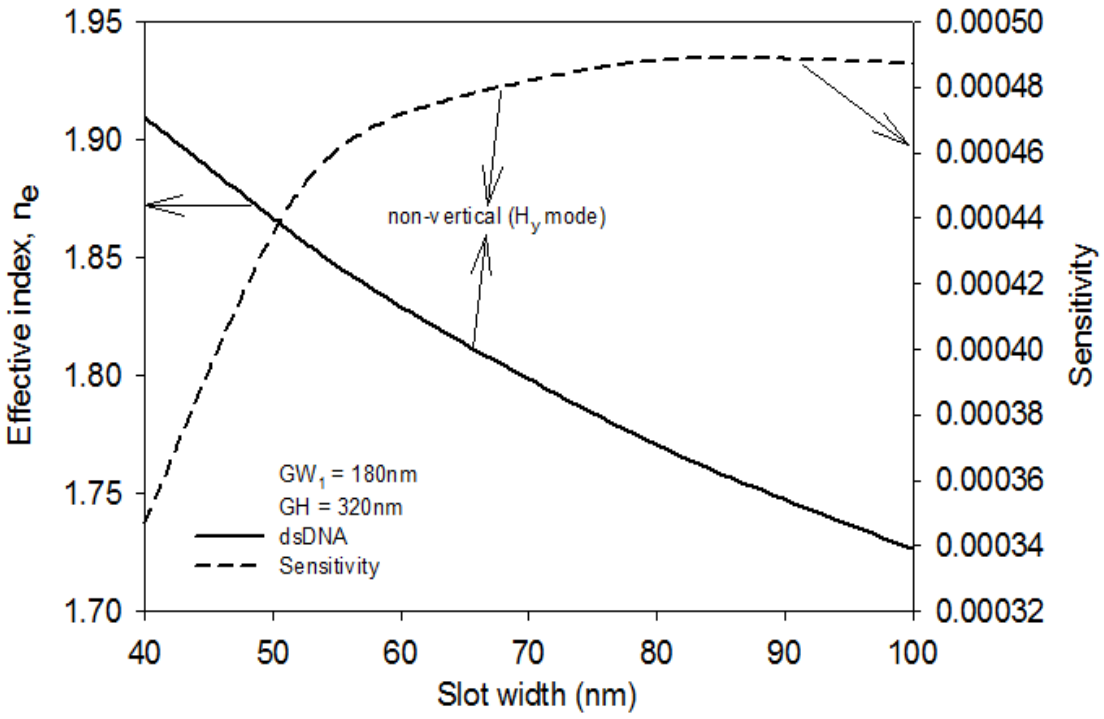

Figure 5.29: Effective mode index in a non-vertical slot waveguide with RI of dsDNA = 1.53 as function of slot width.

The sensing layers are linker layer (thickness t=1 nm and RI = 1.42), ssDNA (thickness n=8 nm and RI = 1.456), and water respectively. We have then replaced ssDNA layer with the dsDNA (thickness n=8 nm and RI = 1.53) to achieve the effective index difference for calculating the sensitivities.

The effective index of the structure is decreased when the slot width is increased. Therefore, there is less confinement of the optical field in the guiding region at a large slot width.

Due to less confinement of the optical field in the guiding region sensitivity of the sensor increases with the increase in the slot width. However, the sensitivity of the non-vertical sidewall structure is less than the vertical sidewall structure as shown in Figure 5.30.

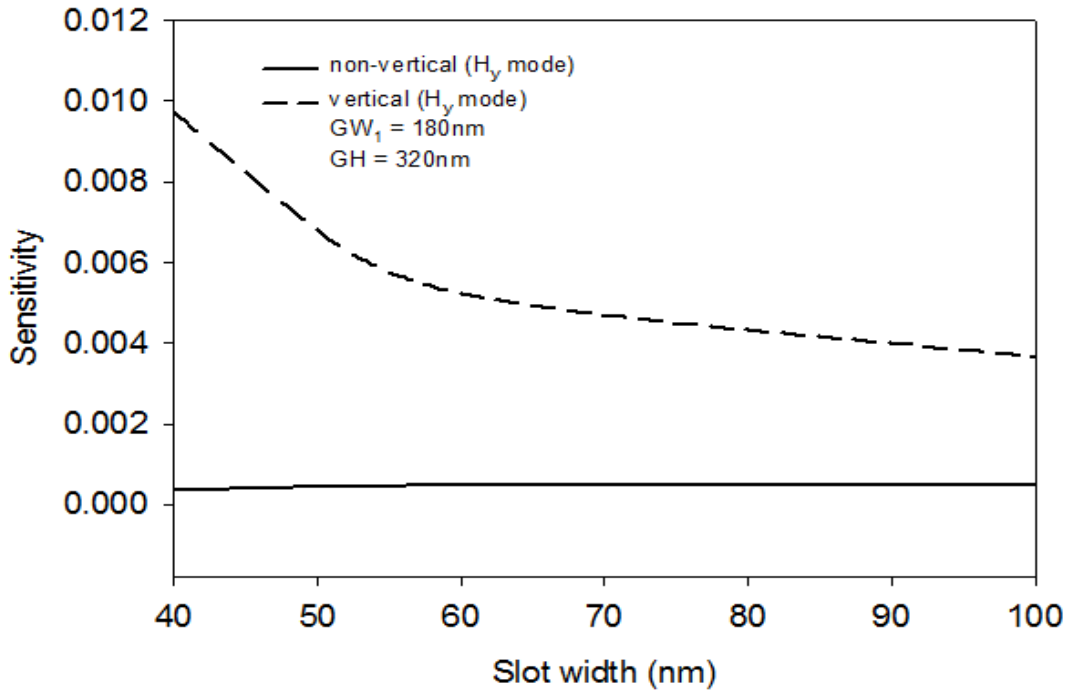

Figure 5.30: Sensitivity in a non-vertical and vertical slot waveguide as function of slot width.

The non-vertical sidewalls significantly degrade the conventional slot waveguide sensitivity because less evanescent field extends into the sensing region. Thus, the high power confinement in the cladding is the key parameter to achieve better sensitivity.

5.4.3 Effect of guide height

Figure 5.31 shows the power confinement in the sensing layer i.e. DNA layer as a function of variable guide height whilst keeping slot width as 100 nm and guide width as 180 nm. The power confinement increases with the increase in guide height. As the waveguide dimension becomes large, most of the power would be confined in the Si core however due to restrictions in guide width and slot width we see power confinement in the DNA layer increases with the guide height.

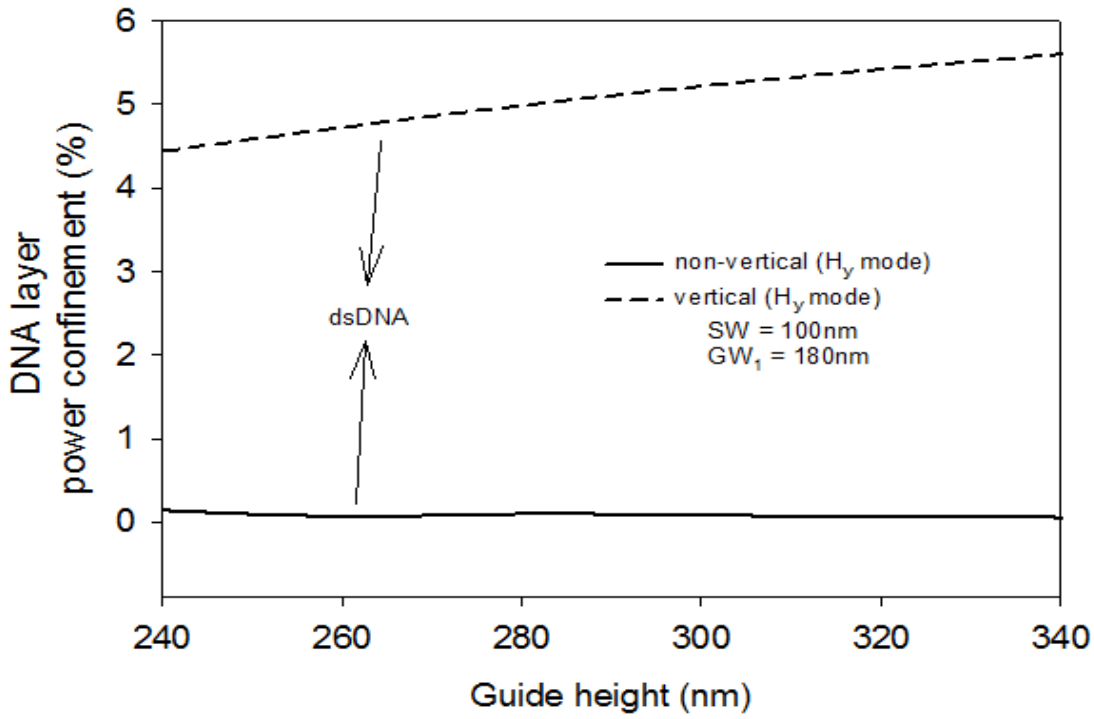

Figure 5.31: Variation of power confinement in DNA layer with the guide height for TE mode

The Figure 5.31 shows a comparison of power confinement in the DNA layer in non-vertical vs vertical structure. Due to non-vertical sidewalls the maximum optical field confinement remains along the vertical interfaces between the silicon guide and the gap region and hence less evanescent field extends into the sensing region which is the reason for degraded power confinement in the DNA layer with the non-vertical sidewall structure.

Figure 5.32 shows variation of waveguide sensitivity with the guide height for non-vertical and vertical structures with fixed guide width of 180nm and slot width of 100nm. The sensitivity increases with the increase in guide height. However if the waveguide dimension becomes too large, most of the power would be then confined in the Si core and a smaller effective index difference can be achieved hence less sensitivity and less confinement in the slot region.

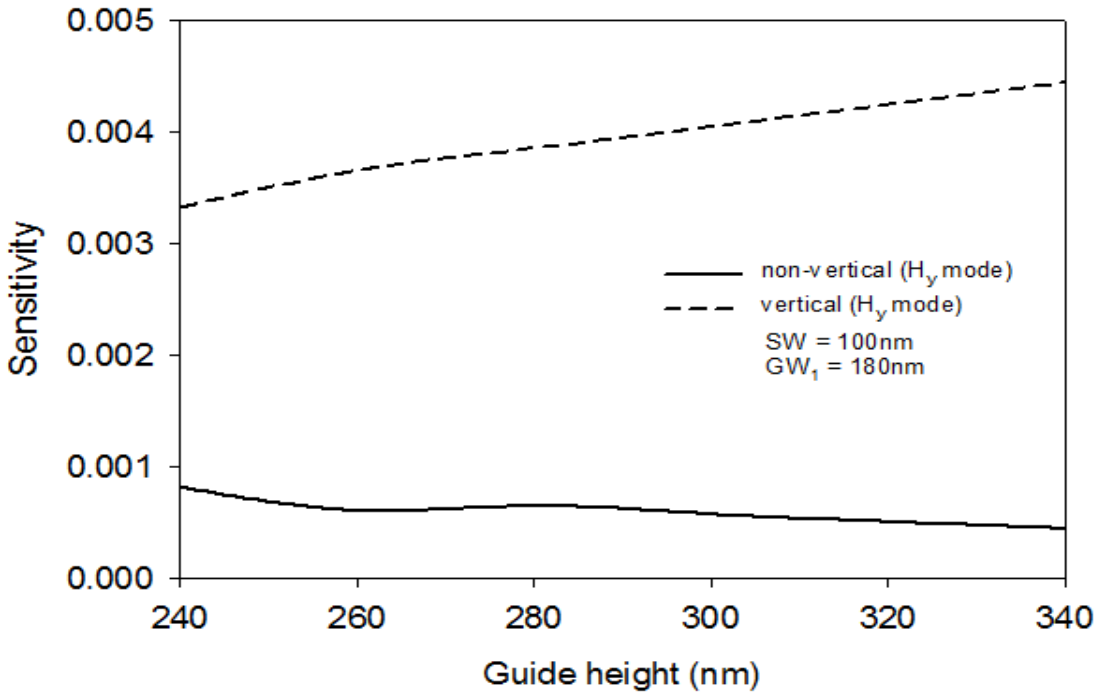

Figure 5.32: Variation of waveguide sensitivity with guide height

Again, a comparison of sensitivities is drawn between the non-vertical and vertical structures and it proves that the sensitivity of vertical structures are higher than the non-vertical one's.

5.4.4 Effect of guide width

Figure 5.33 shows a comparison of power confinement in DNA layer for non-vertical and vertical sidewalls. The vertical sidewall structure achieves higher power confinement in the DNA layer than the non-vertical sidewall structure. It is expected that as the waveguide dimension becomes large, most of the power would be confined in the core. However, it can be noted that, the power confinement in the sensing region is higher between guide width of 180nm and 220nm, because the height of the core was restricted to 320 nm. If the height of the core also becomes larger, then the power confinement in the core could approach 100%. It can be observed here that as the width is reduced, the power confinement in the core also reduces.

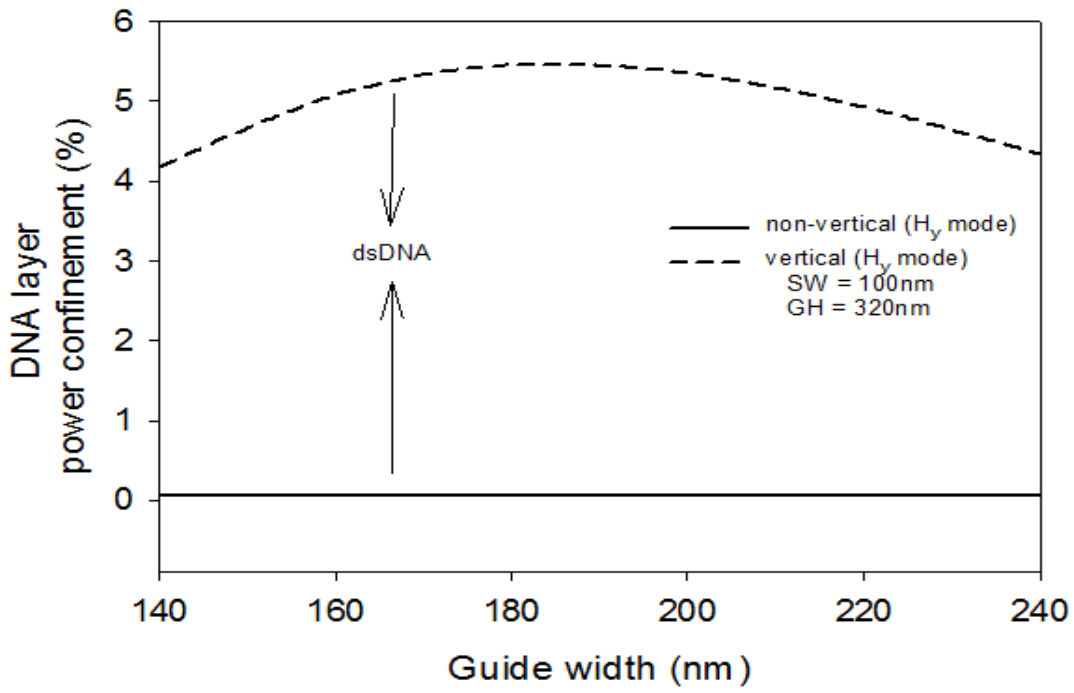

Figure 5.33: Variation of power confinement in DNA layer with the guide width for TE mode

Next, the sensitivity is calculated for vertical and non-vertical structures with fixed slot width of 100nm and guide height of 320nm as shown in Figure 5.34. It is evident that sensitivity of vertical guide is much higher than the non-vertical guide due to higher power confinement in the sensing region which allows more evanescent field interaction with the sensing material. Most of modal field in non-vertical sidewall structure remains confined between the guide and the gap region which leads to less penetration in the cover medium hence less sensitive's are achieved.

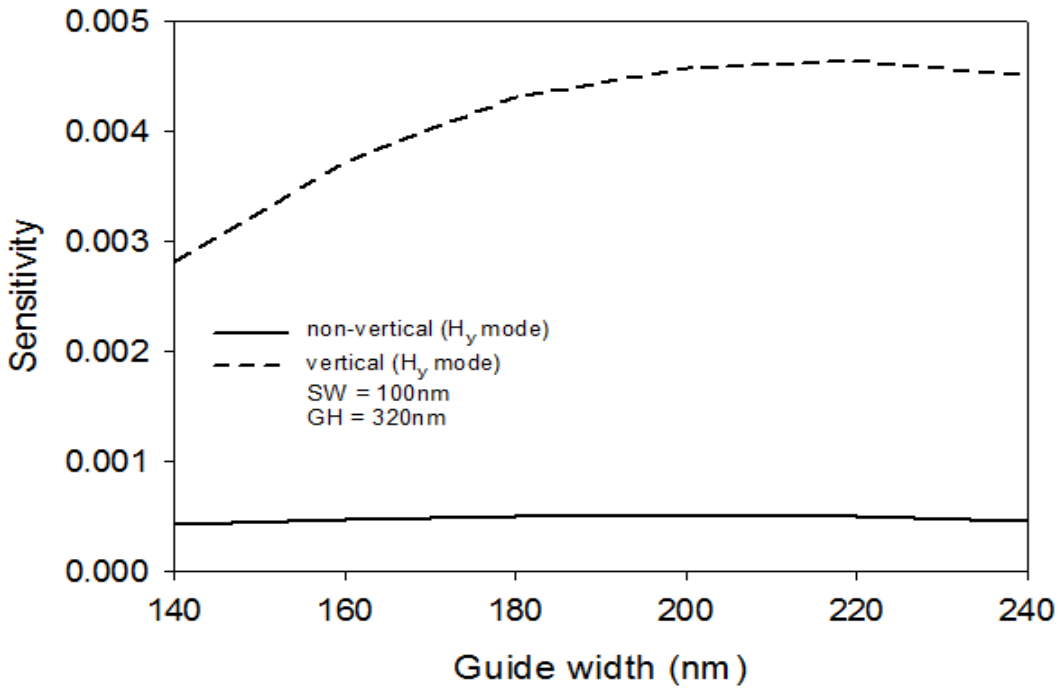

Figure 5.34: Variation of sensitivity in non-vertical and vertical sidewall structures with the guide width for TE mode

5.4.5 Effect of refractive index variation

It can be observed from Figure 5.35 that the power confinement of the vertical slot waveguide exploiting quasi-TE mode is greater than that of the non-vertical slot waveguide, and this value increases when the refractive index of the cladding material is increased. The power confinement in the cladding region is improved when increasing the refractive index of the cladding material for both vertical and non-vertical slot waveguides.

For the quasi-TE mode, light is indeed concentrated in the low-index region because of the field discontinuity for both vertical and non-vertical structure. However, the field still is highly concentrated in the low-index region of quasi-TE mode for non-vertical sidewall structure as compared to vertical sidewall structure. Therefore, less field penetrates into cladding region of the non-vertical slot waveguide and hence less power confinement in this region.

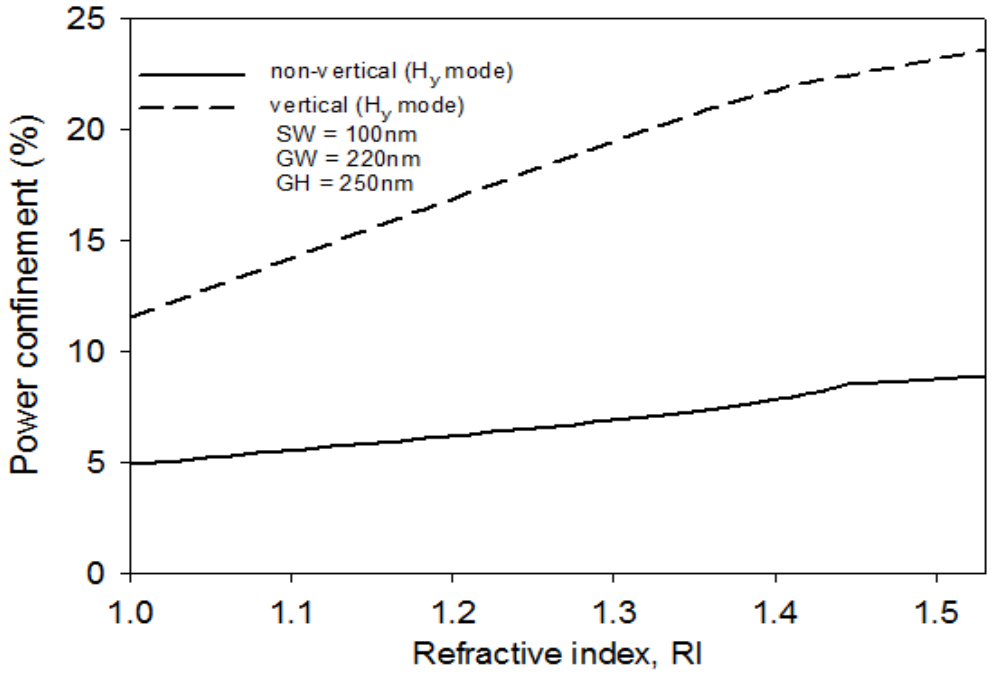

Figure 5.35: Variation of power confinement in DNA layer with the variation of cladding refractive index for TE mode

5.4.6 Effect of wavelength

The power confinement in the cladding region is greater when the operating wavelength increases, as shown in Figure 5.36.

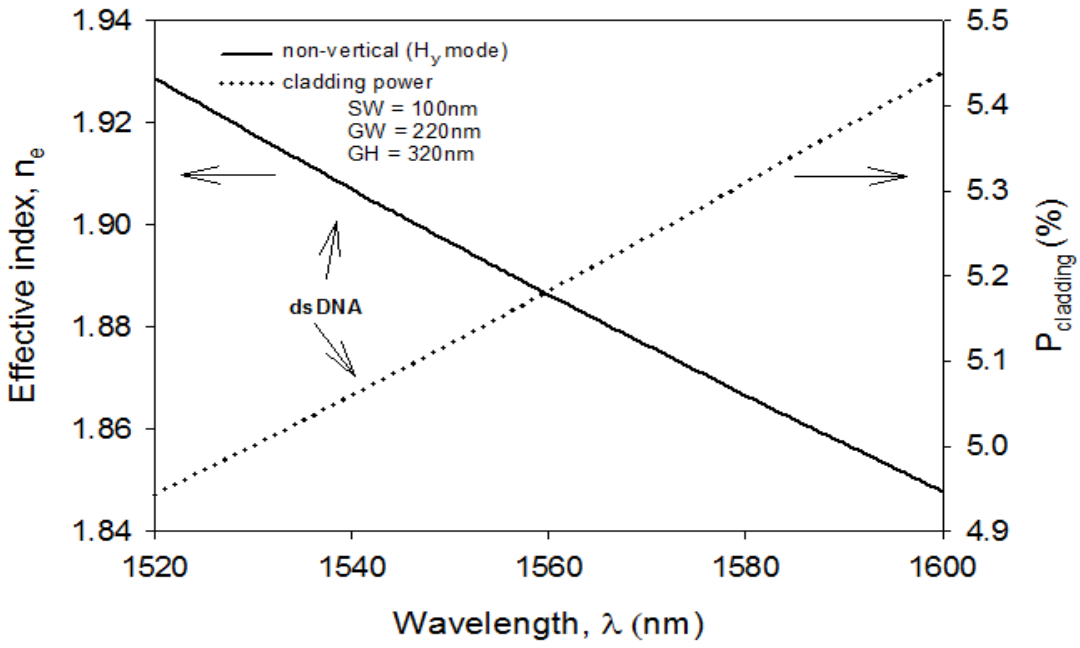

Figure 5.36: Variation of effective index and power confinement in DNA layer with non-vertical sidewall at an operating wavelength range from 1520 to 1600nm for TE mode.

The effective index of the structure is decreased when the operating wavelength is increased. Therefore, there is less confinement of the optical field in the guiding region at a large wavelength.

The vertical sidewall slot waveguide structure have been proved to be very sensitive to detect the DNA hybridisation than the non-vertical sidewall structures especially when a quasi-TE mode is considered. The analysis in this work shows that non-vertical sidewall slot waveguide have an enhancing effect on the mode confinement with mode intensity maximum moves towards the region where the rails are wider and the slot is narrower. However, non-vertical structures degrade the performance of sensitivity for sensor which need more penetration of evanescent field into the cover sensing region towards the top of the waveguide.

5.5 Summary

A rigorous finite element-based full vectorial H-field formulation has been used for the study of the optical properties of silica nanowires in a simulated Mach–Zehnder-based optical sensor for detecting biomaterial specimens such as E.coli. The variation of the effective index, propagation constant, power fraction in the different regions of the reference and the sensing arms of the aforementioned device with the variation of the nanowire size and the specimen refractive index, temperature, and wavelength are studied thoroughly as they are very important parameters in determining the sensitivity of the proposed optical sensors based on such a configuration.

In the next part of the above chapter the finite-element approach based on a full-vectorial H-field formulation has been used to study the slot waveguide biosensor to detect the DNA hybridisation. The optical field profiles, the effective index change, power confinement factor and power density in the DNA layer have been studied and an optimised slot waveguide sensor with maximum sensitivity is proposed. In this work we have proposed a method to detect DNA hybridisation. When the complementary strand DNA

attaches with the probe DNA, we see a change in the effective index and power confinement.

By keeping the fabrication limitation into consideration slot width of 100nm is a minimum desirable width for the design of a biosensor. Moreover, guide width of 180nm to 220nm and guide height of 320nm gives us the compact and smaller size biosensor with maximum waveguide sensitivity, maximum effective index difference and maximum power confinement factor in the DNA layer.

6

CONCLUSION AND FUTURE WORK

6.1 Conclusion

The primary objective of this research work has been to develop, implement and apply effectively a numerical modelling technique which can be used to model, design, optimise and characterize label free optical biosensors for detection of various biomolecular interactions at optical frequencies in light of practical limitations such as fabrication and experimental results. The objectives outlined have been successfully achieved with a detailed analysis of results during the entire work. In this work, a numerical method based on finite element formulation has been extensively used to accurately characterise various types of optical biosensors and study their optical properties.

The background knowledge of label free optical biosensors is of paramount importance for understanding their underlying principles, mechanisms, architectures and immobilization techniques is discussed and served in chapter 2. The discussion started with the introduction of biosensors in order to know and fully understand its working principle. It has followed with classification of optical biosensors based on sensing mechanism, sensing architectures and detection protocols. We have adopted an evanescent wave sensing mechanism for detection of biomolecular interactions. Sensitivity is an important parameter to evaluate the sensor performance and the factors that affect sensitivity has been identified. The design goal for achieving high sensitivity is to design a structure that allows as much of the field as possible to reside in the sensing medium. For this reason various architectures of optical biosensors

with comparison are elaborated that allowed interaction of guided mode with the sensing medium so that the minimum detectable change in the sensing medium changes the effective refractive index of mode and thus to a change of the output signal. Interface between the sensor surface and the chemical or a biological system is a key component of the optical biosensors. The physical and chemical properties of the interface play an important role in achieving optimal recognition of the target and limiting the nonspecific adsorption. Immobilizations of bioreceptors such as enzymes, antibodies, nucleic acids, proteins on the functionalized surface are discussed. The performance of a biosensor comes from its ability to immobilize receptors while maintaining their natural activity, the bioavailability of the receptors to targets in solution and a low nonspecific adsorption to the solid support. These specifications govern the specificity and sensitivity of such devices and can be tailored by an appropriate choice of the interface where the bioreceptors are immobilized.

Chapter 3 is devoted to the methodology adopted for modelling and simulation of metal-clad fibre, silica nanowire and slot-waveguide based biosensors. The full vectorial H-field based variational formulation has been implemented in the numerical tool is applied to analyse the effects of various design parameters of optical biosensor devices by varying and resolving the problem repeatedly, while an appropriate output metric is recorded. Graphs are built relating the parameters to the results, from which optimum parameters are picked according to fabrication limitations. In this formulation, the magnetic field vector H is naturally continuous across the waveguide interfaces and also the associated natural boundary condition is that of an electric wall, which is very convenient to implement in many practical waveguide problems. Key primary concepts such as discretisation of the domain, the shape functions and the element matrices were explained in detail in this chapter. Since the shape functions provide only an approximate representation of the true fields, it is necessary to increase the number of elements or nodal points to reduce the resulting error. In doing so, the numerical model becomes a closer representation of the real physical problem. However, with this H-field

formulation, the appearance of the spurious (non-physical) modes along with the physical modes is a key problem. The penalty function method was incorporated to eliminate these spurious modes by imposing the condition ($\nabla \cdot H = 0$). The finite element method has been proven to be a very powerful method of finding the field profiles and propagation characteristics of the guided modes of most waveguides used across the broader electromagnetic spectrum.

The design of label free optical sensors based on optical fibre is a quite attractive area due to the intrinsic features of optical fibres, including small size, robustness, low cost and immunity to electromagnetic interference. Implementation of numerical methods for the modelling and characterisation of metal-clad optical biosensors for the detection of E.Coli and range of refractive indexes of other biomolecules is shown in chapter 4. A full-vectorial H-field formulation in conjunction with the perturbation technique has been used to study the surface plasmon resonance based fibre optic biosensors to detect *E.Coli*. The newly developed polar coordinate discretization used here has matched accurately the circular layers of the waveguide, and the optical field profiles and optical power confinement were rigorously presented for each layer. The surface plasmon modes propagating in the above waveguide and the study of their propagation and attenuation characteristics, with the variation of the metal layer thickness and outer layer thickness is investigated. For finite metal thickness, the SPMs exist at both the inner and outer interfaces. By adjusting the metal thickness and refractive index values of the cladding layers, the odd and even-type coupled SPMs can be formed and exploited for various biosensing applications. The metal-clad optical biosensors for the detection of E.Coli is a circularly symmetric structure and contains core, cladding, gold, outer medium and water layers respectively. The refractive index of outer medium is varied from 1.440 to 1.453 to study the coupling between the inner surface plasmon mode (ISPM) and the outer surface plasmon mode (OSPM). The propagation constants of the two SPMs are close at refractive indices of 1.449, 1.448 for cladding thickness

of 5µm and 10µm respectively. In this case the outer medium thickness was fixed at 2µm. The coupling length is an important parameter in investigating the phase matching condition of the fibre mode and the surface plasmon mode. The maximum coupling length is observed when it is phased matched. When the cladding thickness is 5µm the inner and the outer SPMs are very strongly coupled hence the difference between their propagation constant is large giving a shorter coupling length. However, when the cladding thickness is 15µm the inner and the outer surface plasmon modes are weakly coupled and hence the difference between their propagation constant is small giving rise to an increased coupling length. It has been analysed that the maximum detection is possible when the outer medium refractive index is 1.449, the thickness of the cladding is 10µm, and the thickness of the outer medium is 2µm.

Chapter 5 is focused on studying optical properties of silica nanowires for detecting specimens such as *E.coli*. The optical field profiles, effective index difference, propagation constant difference and power fraction of reference and sensing arms of the Mach-Zehnder based interferometer sensor are discussed with the variation of the nanowire diameter, specimen refractive index and wavelength. They are very important parameters in determining the sensitivity of the proposed biosensor. Due to the presence of *E.coli* in an aqueous solution it is has been analysed evanescent field in the sensing arm expands more outside because of change of refractive index in the aqueous solution. Because of this change in refractive index, effective index of guided mode decreases with the decrease of core diameter and the increase of the wavelength. For a core diameter, D, of 100nm the field extends mostly in the aqueous solution for both the reference and the sensing arms. However sensing arm exhibits more power in the aqueous solution than the power in the aqueous solution of reference arm. It is due to refractive index change in the aqueous solution of sensing arm when target antigen (E.Coli) is attached to the immobilised antibody. The greater the change in Δ_{neff} more sensitive the biosensor will be. Therefore, when D = 100nm maximum index difference is achieved.

When nanowire dimension becomes too large most of the power is confined in the silica core and a smaller effective index difference is achieved hence lesser sensitivity.

In the next part of the chapter 5 we have proposed a method to detect DNA hybridisation using an optimised slot waveguide sensor. When the complementary strand DNA attaches with the probe DNA, we see a change in the effective index and power confinement. The various simulations are carried out to yield the maximum effective index difference so that maximum waveguide sensitivity is achieved and small size compact biosensor is designed. The effective index decreases with the increase in slot width because when the slot gap is small a stronger coupling occurs and hence increases the effective index. The greater the change in Δ_{neff} more sensitive the biosensor will be. The effective index difference, $\Delta_{n_{eff}}$, as well as waveguide sensitivity decreases with the increase in the slot width due to presence of DNA layers. In this sensor, a large resonance wavelength shift is caused by large light-matter interaction and by decreasing the slot width. When silicon width is 220nm, height is 320nm and slot width is 100nm our simulation shows that the effective refractive indices of ssDNA and dsDNA are 1.80549 and 1.81264 respectively with 6.12nm resonance wavelength shift, and sensitivity of 856nm/RIU is achieved. Improvement in the Detection Limit can be accomplished by increasing the sensitivity or reducing the noise level. For this sensor, the detection limit achieved is 1.43x10-6 RIU.

6.2 Future work

Modelling of optical biosensor is a rich source of mathematical challenges. The main components of biosensors are based on well-understood physical processes as well as chemical and biological reactions, all of which are amenable to mathematical modelling using ordinary and partial differential equations.

Chapter 5 refers to an interferometer structure using nanowires. However, the results presented correspond to the change in modal effective index in one arm of the interferometer and not in the changes in the interferogram. Simulations of the interferogram (as a function of the wavelength) and estimate the sensitivity of the sensor from the interferogram will be carried out in the future work.

Traditional diagnostic methods are not very powerful methods when it comes to cancer detection at very early stages. As well, some of the screening methods are quite costly and not available for everyone. Therefore, the development of technology that is specific and reliable for detecting cancers at early stages and is easily accessible so that it can function as the first-line guidance is of importance.

Biomarkers in relation with nanotechnology and biosensors have opened up a new era of early cancer diagnosis and precise drug delivery. Proteins, antibody fragments, DNA fragments, and RNA fragments are the base of cancer biomarkers and have been used as targets in cancer detection and monitoring. Various nanowires have also been applied to biomarker detection including silicon nanowires [228-230], In2O3 nanowires [231], gold nanowires [232], [233], and conducting polymer nanowires [234].

DNA sensors are highly concerned due to their important function of transferring genetic codes in living cells. Once the DNA sensor is reduced down to cell scale, it would be possible to detect signs of the early DNA damage that can lead to cancers. The DNA sensor presented in the chapter 5 of thesis has been proved to be label-free and fast. Aiming at the in-cell DNA

detection, the miniature sensor with the same structure is a new research direction of great interest. The numerical methods based on Finite Element Method applicable to study of DNA sensor as outlined in the chapter 5 with a view to optimising sensor design process will be applied first to detect the in-cell DNA.

Nanowire sensors based biosensors have been considered as one of the appropriate methods for disease detection and label-free detection of cancer biomarkers is possible. Therefore, numerical methods discussed in the thesis can be used to design, analyse and optimise the label-free optical biosensors for detection of cancer biomarkers in future.

Appendices

Appendix A: Finite element analysis of quarter structure of Metal Clad Optical Fibre

Polar Mesh Generation

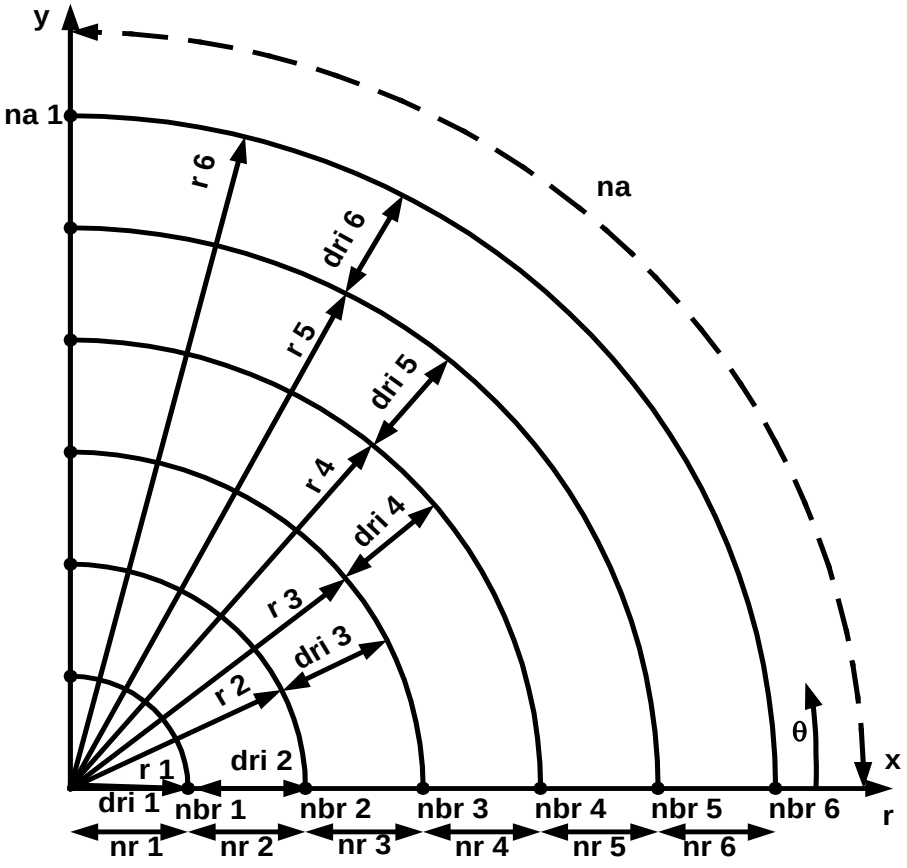

Quarter structure of Optical Fiber

subroutine gend1(np,ne,nop,cord,ibnd,dlc,nrt)

Variables used in the subroutine

nmt = number of radial layers

nrt = number of radial elements

npr = number of radial nodes

na: number of azimuthal elements

na1: number of azimuthal nodes

np: number of nodes

ne: number of triangular elements.

r(i): r1..r6: radius of each radial layer

nr(i): nr1.. nr6: element divisions for each radial layer

nbr(i): nbr1..nbr6: radial boundary nodes for each layer

dri(i): dri1..dri6: radius difference

dr(i): dr1.. dr6= radial element resolution for each layer where **dr(i)=dri(i)/nr(i)**

da: azimuthal element resolution: $da = \frac{\pi}{2 * na}$

k: node variable, **k=1..np**

polc(k,1): stores the magnitude of the nodal polar coordinate

polc(k,2): stores the phase of the nodal polar coordinate

Assignment of nodes for layer 1

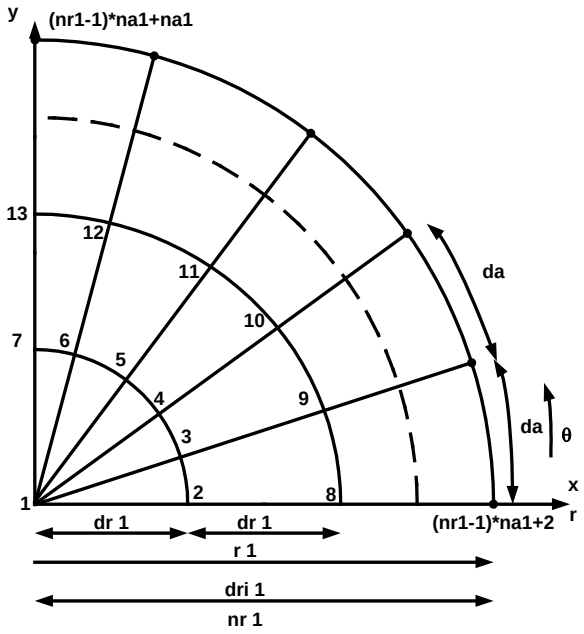

Boundary nodes for each layer

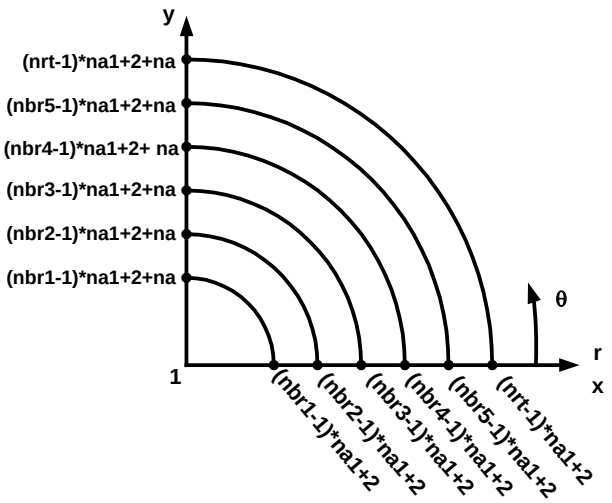

sr=dr(1) *{Initialisation of the radial length: sr}*

```
do 200 ir=1,nrt
drr=dr(1)                          {Radial resolution for the inner layer}
do 210 im=1,nmt
if (ir.ge.nbr(im-1)) drr=dr(im)    {Assignment of radial resolution for each ring layer}
 210      continue


sp=0.0d0                           {Initialisation of the azimuthal length, sp}
do 220 iz=1,na1
k=(ir-1)*na1+iz
k=k+1                              { node  index variable}
polc(k,1)=sr                       {Nodal magnitude}
polc(k,2)=sp                       {Nodal phase}
sp=sp+da                           {Radial length increment}
220      continue
sr=sr+drr                          {Azimuthal length increment}
200      continue
```

Assignment of element global nodes, element number and material index

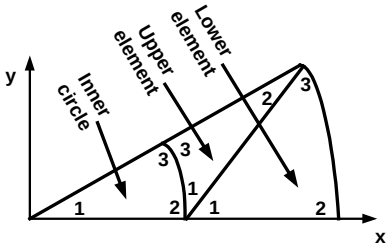

Local node numbering

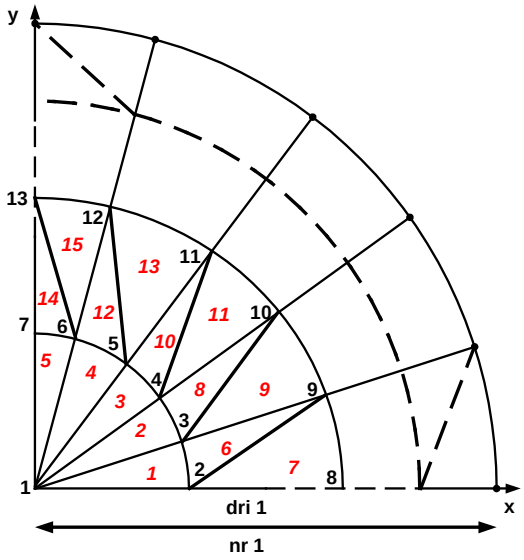

Global nodal and element numbering for the inner layer

do 400 ir=1,nrt *{total number of radial elements}*

do 400 iz=1,na *{total number of azimuthal elements}*

if(ir.eq.1) then *{node numbers for the elements in the first inner ring: Elements1..5}*

kr=iz

nop(kr,1)=1 {*Global node number for the 1st local node of the inner circle*}

nop(kr,2)=iz+1 {*Global node number for the 2nd local node of the inner circle*}

nop(kr,3)=iz+2 *{Global node number for the first local node of the inner circle}*

nop(kr,4)=1 {*Material index for the elements in the inner circle*}

endif

k1=(ir-1)*na+na+iz+k3 *{element index for the upper elements}*

k2=k1+1 *{element index for the lower elements}*

k3=k3+1 *{element index for the lower elements}*

nop(k1,1)=(ir-1)*na1+iz+1 {*Global node number for the 1st local node of the upper element*}

nop(k1,2)=ir*na1+iz+1 {*Global node number for the 2nd local node of the upper element*}

nop(k1,3)=ir*na1+iz+2 {*Global node number for the 3rd local node of the upper element*}

nop(k2,1)=(ir-1)*na1+iz+1 {*Global node number for the 1st local node of the lower element*}

nop(k2,2)=ir*na1+iz+2 {*Global node number for the 2nd local node of the lower element*}

nop(k2,3)=(ir-1)*na1+iz+2 {*Global node number for the 3rd local node of the lower element*}

if(ir.le.nbr(1)) nop(k1,4)=1 *{Material index for the inner layer}*

if(ir.ge.nbr(1).and.ir.lt.nbr(2)) nop(k1,4)=2 *{Material index for the 1st ring layer}*

if(ir.ge.nbr(2).and.ir.lt.nbr(3)) nop(k1,4)=3 *{Material index for the 2nd ring layer}*

if(ir.ge.nbr(3).and.ir.lt.nbr(4)) nop(k1,4)=4 *{Material index for the 3rd ring layer}*

if(ir.ge.nbr(4).and.ir.lt.nbr(5)) nop(k1,4)=5 *{Material index for the 4th ring layer}*

if(ir.ge.nbr(5)) nop(k1,4)=5 *{Material index for the 5th ring layer}*

nop(k2,4)=nop(k1,4) *{Material index for the corresponding lower elements of each ring layer}*

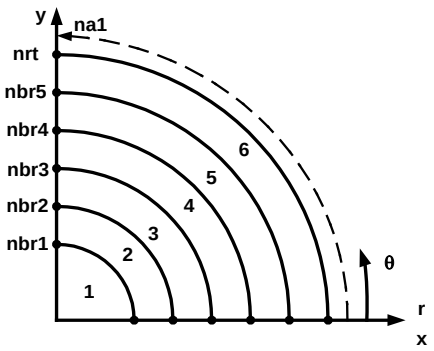

400 continue

Assignment of boundary nodes

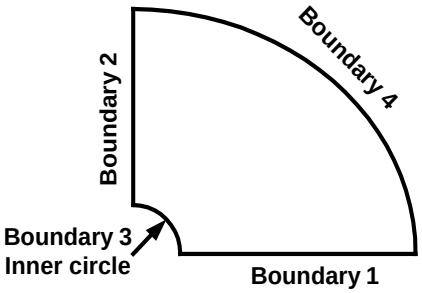


```
ibnd(1,1)=1                    {Initialization of boundary nodes for each boundary
ibnd(2,1)=1
ibnd(3,1)=1
ibnd(4,1)=1

do 420 i=1,na1                 {Assignment of boundary nodes for boundary 4}
ibnd(4,i)=i+nrt*na1            {Assignment of boundary nodes for boundary 3}
ibnd(3,i)=i
420     continue

do 430 i=1,nrt
ibnd(1,i+1)=(i-1)*na1+2        {Assignment of boundary nodes for boundary 1}
ibnd(2,i+1)=i*na1+1            {Assignment of boundary nodes for boundary 2}
430     continue
```

Dielectric constant for each material index

Real part

dlc(1)=anco

dlc(2)=ang

dlc(3)=ans

dlc(4)=ango

dlc(5)=anc

Complex refractive index

Assigned in the main program

IF (icm.eq.1) canm=cmplx(anco,altco)

IF (icm.eq.2) canm=cmplx(ang,altg)

IF (icm.eq.3) canm=cmplx(ans,alts)

IF (icm.eq.4) canm=cmplx(ango,altgo)

IF (icm.eq.5) canm=cmplx(anc,0.0d0)

*where **canm** is the complex refractive index variable*

Transformation from polar to rectangular coordinates

do 230 i=1,np

cord(i,1)=polc(i,1)*dcos(polc(i,2))

cord(i,2)=polc(i,1)*dsin(polc(i,2))

230 continue

Figure below shows the element discretization for a three layer fibre:

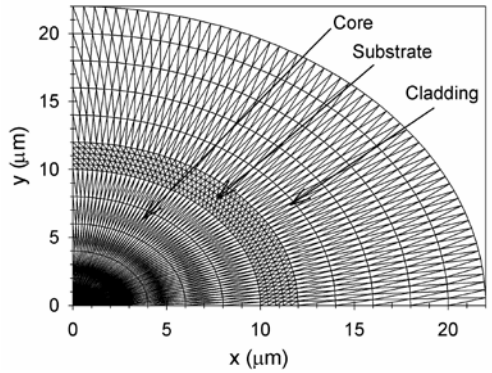

Material variation in the azimuthal generation

The easiest way to change the material of a circular layer in the azimuthal direction is to assign the number of total azimuthal elements to be a multiple of the azimuthal partition.

Example

Assume the 3rd layer to be partioned into 1/5 with material 4 and 4/5 with material 3 as shown below:

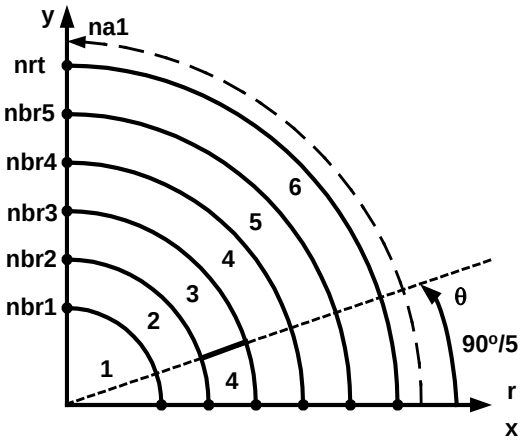

The total number of azimuthal elements, **na** should be a multiple of 5. Therefore the statements for the assignment of material index to the different layers will be changed to:

```
if(ir.le.nbr(1)) nop(k1,4)=1
```

if(ir.ge.nbr(1).and.ir.lt.nbr(2)) nop(k1,4)=2

if(ir.ge.nbr(2).and.ir.lt.nbr(3)) then

if(iz.le.(na/5)) nop(k1,4)=4 *{Material index4 for the 1/5 of the azimuthal section}*

if(iz.gt.(na/5)) nop(k1,4)=3 *{Material index3 for the remaining 4/5 of the azimuthal section}*

endif

if(ir.ge.nbr(3).and.ir.lt.nbr(4)) nop(k1,4)=4

if(ir.ge.nbr(4).and.ir.lt.nbr(5)) nop(k1,4)=5

if(ir.ge.nbr(5)) nop(k1,4)=5

nop(k2,4)=nop(k1,4)

By using the above approach only the material contribution in the azimuthal direction is controlled.

To control mesh refinement in the azimuthal direction, the number of azimuthal elements, **na**, should be subdivided according to the partition eg. ***naz1***, ***naz2***, where

na=naz1+naz2.

Further azimuthal arc lengths (in rad) are also required such as ***az1*** and ***az2***, where

az1+az2= π/2

Next an azimuthal resolutions ***daz1*** and ***daz2*** are required to be defined where:

daz1=naz1/az1

daz2=naz2/az2

In the coordinate assignment section of the subroutine the following statement should be added in the loop

if (iz.lt.na1) da=daz1

if (iz.ge.na1) da=daz1

Appendix B: Finite element analysis of waveguide

Mesh Generation Subroutine

Directional coupler structure

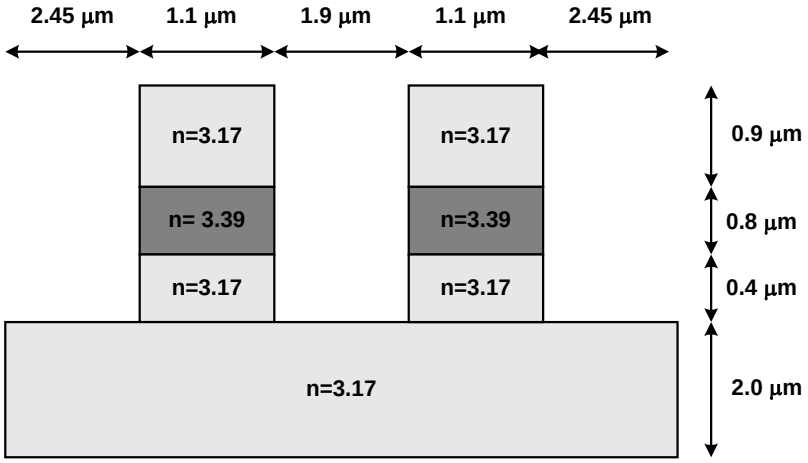

Fig.1

Input waveguide structure

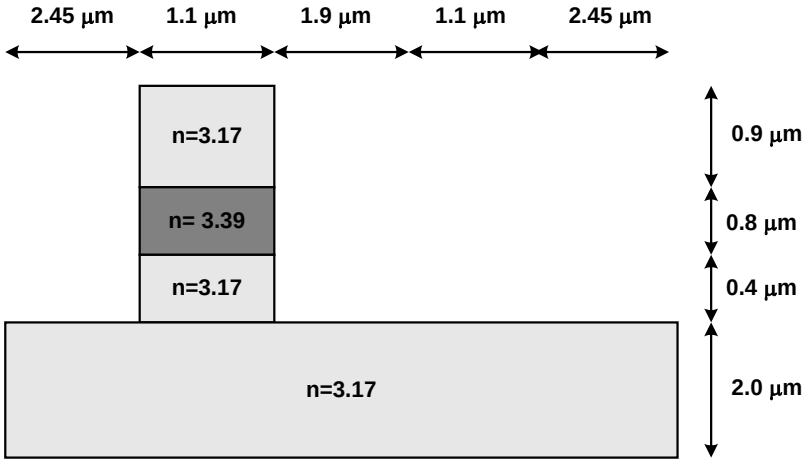

Fig.2

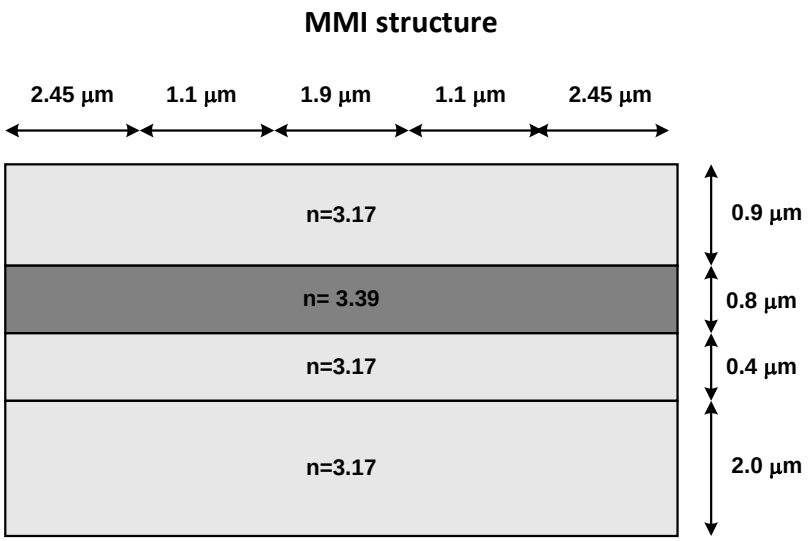

Fig.3

The above structures are to be used for the input/ output waveguides and MMI region of the MMI 3dB coupler.

Finite Element discretization for Input waveguide structure

The input waveguide structure is subdivided into 8 and 9 main divisions along the x- and the y-axis thus giving 8x9 rectangular blocks as shown in Fig.4.

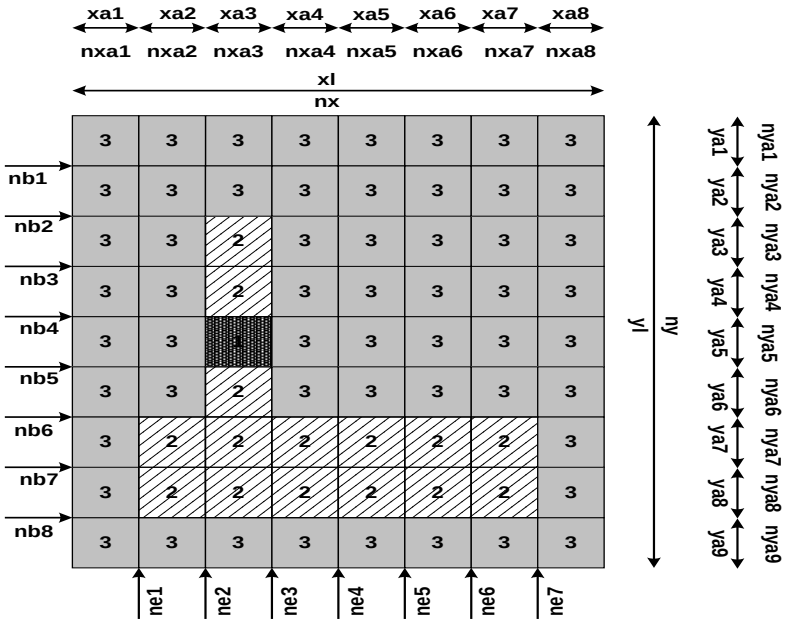

Fig.4

The number of elements in each of the main divisions along the x and the y direction are named nxa1..nxa8 and nya1..nya8, respectively and given in the COMMON BLOCK statement as follows

data nx/70/, nxa1/5/, nxa2/5/, nxa3/15/, nxa4/10/, nxa5/10/, nxa6/15/, nxa7/5/, nxa8/5/

data ny/60/, nya1/5/, nya2/5/, nya3/5/, nya4/20/, nya5/5/, nya6/5/, nya7/5/, nya8/5/, nya9/5/

where nx and ny is the total number of elements in the x and the y direction, respectively.

The variables ne1..ne7 and nb1..nb8 is a count of the nodes along the boundaries, at the end of each main division, in the x and y direction, respectively.

The dimensions for each main division of elements is also given in the BLOCK DATA statement as:

data xa1/1.0d0/, xa2/2.45d0/, xa3/1.1d0/, xa4/0.95d0/

data xa5/0.95d0/,xa6/1.1d0/,xa7/2.45d0/,xa8/1.0d0/

data ya1/1.0d0/, ya2/1.0d0/, ya3/0.45d0/,ya4/0.45d0/, ya5/0.8d0/,ya6/0.4d0/, ya7/1.0d0/, ya8/1.0d0/, ya9/1.0d0/

The material index shown in each block, corresponds refractive index of each block, where the refractive indices are also given the BLOCK DATA as:

data an1/3.39d0/ an2/3.17d0/, an3/1.0d0/

Assignment of nodes

Each main division shown in Fig.4 is subdivided according to the number of elements as shown in Fig.5

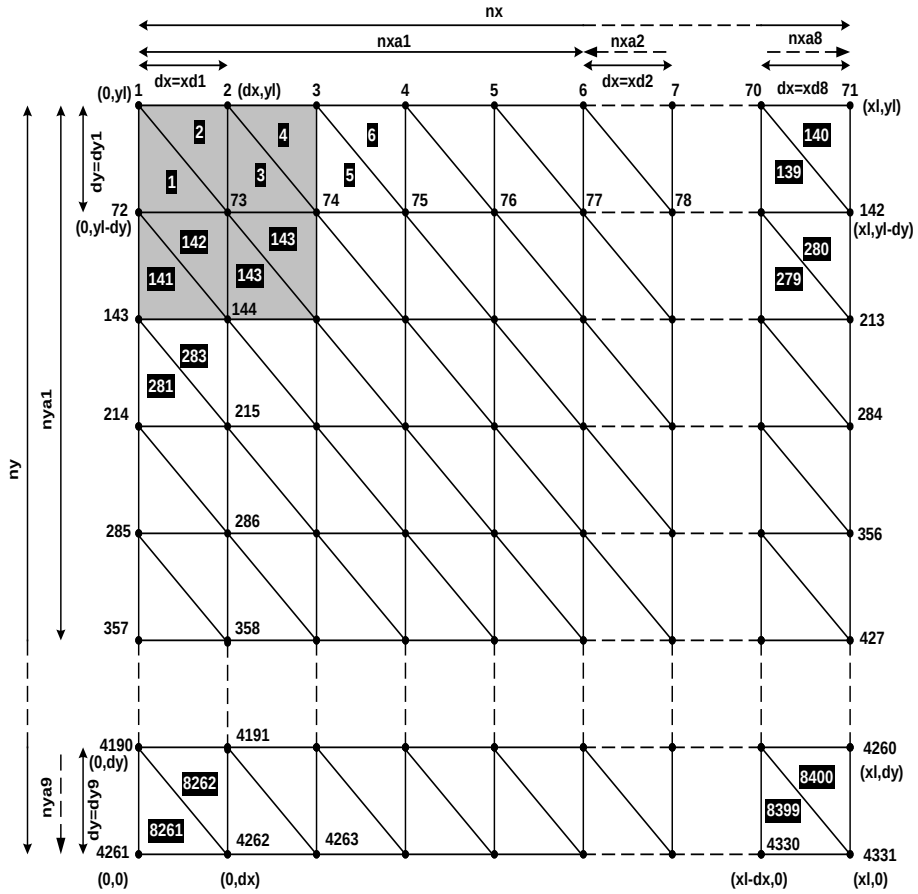

Fig.5

The resolution **dx** and **dy** for each main division along the x- and the y-axis respectively is defined as the length of each main division divided by the number of elements in that division.

For example by considering the 1st main division along the x-axis the resolution **dx** is defined by **dx=xa1/nxa1**. Similarly, for the first main division along the y-axis starting from the top of the structure the resolution **dy** is given by: **dy=ya1/nya1.**

In the FORTRAN program the resolution for each main division, xd1..xd8 and dy1..dy9, in the x and the y direction, is achieved as follows:

```
xd1=xa1/dble(float(nxa1))
 xd2=xa2/dble(float(nxa2))
xd3=xa3/dble(float(nxa3))
xd4=xa4/dble(float(nxa4))
xd5=xa5/dble(float(nxa5))
xd6=xa6/dble(float(nxa6))
 xd7=xa7/dble(float(nxa7))
xd8=xa8/dble(float(nxa8))

  dy1=ya1/dble(float(nya1))
 dy2=ya2/dble(float(nya2))
 dy3=ya3/dble(float(nya3))
dy4=ya4/dble(float(nya4))
 dy5=ya5/dble(float(nya5))
  dy6=ya6/dble(float(nya6))
dy7=ya7/dble(float(nya7))
dy8=ya8/dble(float(nya8))
 dy9=ya9/dble(float(nya9))
```

The next step is to determine a count of the sum of the nodes along the boundaries, at the end of each main division, in the x and y direction, (ne1..ne7 and nb1..nb8), respectively, with in order to assign the nodes for each element. The top-left corner node is considered as the first node of the structure. The above counting is determined as follows:

```
nb1=nya1+1
nb2=nb1+nya2
nb3=nb2+nya3
nb4=nb3+nya4
nb5=nb4+nya5
nb6=nb5+nya6
nb7=nb6+nya7
nb8=nb7+nya8
nb9=nb8+nya9
ne1=nxa1+1
ne2=ne1+nxa2
ne3=ne2+nxa3
ne4=ne3+nxa4
ne5=ne4+nxa5
ne6=ne5+nxa6
ne7=ne6+nxa7
ne8=ne7+nxa8
sy=yl
```

Next, the coordinates at each nodal point are assigned by forming a loop initially along the y- and then along the x-axis as follows.

```
do 100 i=1,ny1
```

```
 if(i.le.nya1) dy=dy1
if(i.gt.nya1) dy=dy2
if(i.ge.nb2) dy=dy3
 if(i.ge.nb3) dy=dy4
if(i.ge.nb4) dy=dy5
 if(i.ge.nb5) dy=dy6
 if(i.ge.nb6) dy=dy7
  if(i.ge.nb7) dy=dy8
    if(i.ge.nb8) dy=dy9
   sx=-xd1
    do 110 j=1,nx1
  if(j.le.ne1)dx=xd1
   if(j.gt.ne1)dx=xd2
   if(j.gt.ne2)dx=xd3
 if(j.gt.ne3)dx=xd4
   if(j.gt.ne4)dx=xd5
 if(j.gt.ne5)dx=xd6
     if(j.gt.ne6)dx=xd7
     if(j.gt.ne7)dx=xd8
     k=(i-1)*nx1+j
     cord(k,1)=sx+dx
     sx=sx+dx
     cord(k,2)=sy
  110 continue
     sy=sy-dy
  100 continue
```

Using the above loop the node numbering starts from the top-left corner of the structure, moves from left to right **nx1** and **ny1** correspond to the total number of nodes along the x and the y direction respectively, and calculated by:

```
nx1=nx+1

ny1=ny+1
```

Therefore, the total number of nodes of the structure, **np**, can be calculated from

```
np=nx1*ny1
```

In the above loop the resolution **dx** and **dy** is defined according to the node defined by **i** and **j** index and the x,y coordinates are stored in the array:

cord(k,m)

where k is the node number

And m=1 and m=2 correspond to the x and the y coordinate of each node.

It should be noted that the length in the x and the y direction xl and yl respectively are calculated by:

```
xl=xa1+xa2+xa3+xa4+xa5+xa6+xa7+xa8

yl=ya1+ya2+ya3+ya4+ya5+ya6+ya7+ya8+ya9
```

By considering the highlighted rectangular blocks in Fig.5 the nodes are assigned as shown in Fig.6.

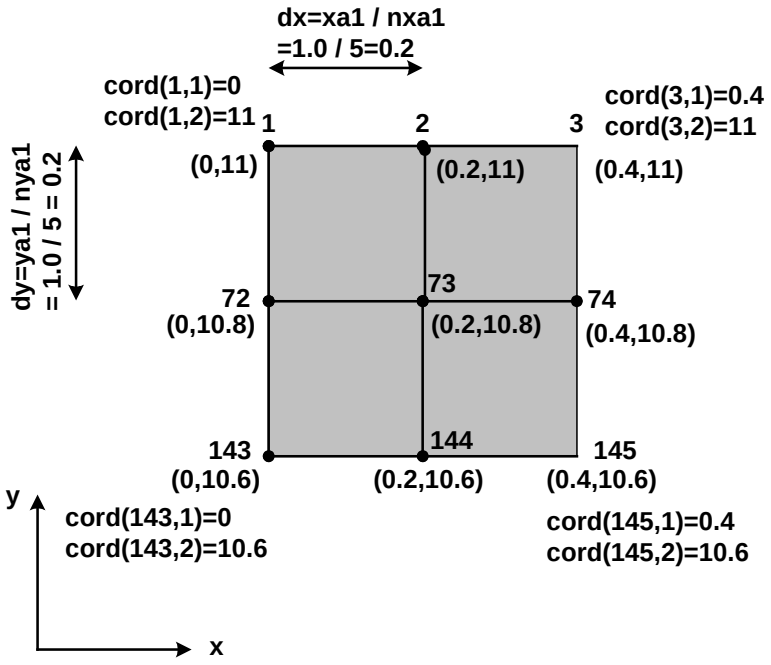

Fig.6

Assignment of elements

As it has been shown above, the waveguide structure has been divided into rectangular elements, according to the mesh refinement given. Further, these elements are subdivided into triangular elements. The triangular elements are numbered, starting with the lower triangle of the first left top-rectangular element, as shown in Fig.7.

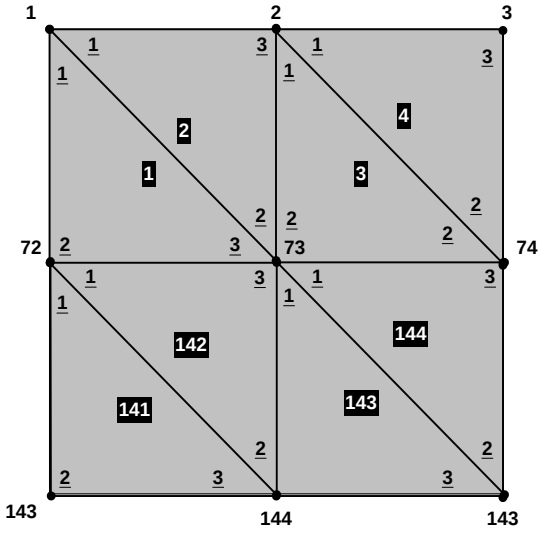

Fig.7

The highlighted numbers correspond to the element number and the numbers assigned to the nodal points are the node numbers.

The edges of the triangular element are assigned with local node numbers 1, 2, and 3, and each local node number corresponds to a global node number, as shown in Fig.7.

For example, for element 1, the local node numbers 1, 2, and 3, correspond to the global node numbers 1, 72, and 73, respectively. Similarly, for element 142, the local node numbers correspond to the global node numbers72, 144 and 73.

The element numbers are assigned using the following code:

```
do 200 i=1,ny
do 200 j=1,nx
k=(i-1)*nx+j
k2=k*2
k1=k2-1
nop(k1,1)=(i-1)*nx1+j
nop(k1,2)=i*nx1+j
nop(k1,3)=i*nx1+j+1
nop(k2,1)=(i-1)*nx1+j
nop(k2,2)=i*nx1+j+1
nop(k2,3)=nop(k1,1)+1
200 continue
```

The global node numbers for each elements are stored in the array:

nop(k,j)

where **k=k1, k2**.

k1 and k2 is the index for the lower and the upper triangle for each rectangular element.

J=1..3

Where 1, 2, and 3 is the element local node number.

Therefore global node numbers for element 1 are stored as:

nop(1,1)=1

nop(1,2)=72

nop(1,3)=73

Assignment of element material number

By considering Fig.4 each main block has a particular element material index number according to the structure. These material index numbers are assigned utilizing the count of the nodes along the boundaries, ne1..ne7 and nb1..nb8, as explained earlier. The assignment of the material index number is accomplished using the following FORTRAN code:

```
 do 200 i=1,ny
do 200 j=1,nx
 k=(i-1)*nx+j
 k2=k*2
  k1=k2-1
nop(k1,1)=(i-1)*nx1+j
  nop(k1,2)=i*nx1+j
 nop(k1,3)=i*nx1+j+1
nop(k2,1)=(i-1)*nx1+j
 nop(k2,2)=i*nx1+j+1
```

```
   nop(k2,3)=nop(k1,1)+1
c            calculate material data
nop(k1,4)=3
  if(j.ge.ne2.and.j.lt.ne3.and.i.ge.nb2.and.i.lt.nb4) nop(k1,4)=2
  if(j.ge.ne2.and.j.lt.ne3.and.i.ge.nb4.and.i.lt.nb5) nop(k1,4)=1
  if(j.ge.ne2.and.j.lt.ne3.and.i.ge.nb5.and.i.lt.nb6) nop(k1,4)=2
  if(j.ge.ne1.and.j.lt.ne7.and.i.ge.nb6.and.i.lt.nb8) nop(k1,4)=2
  nop(k2,4)=nop(k1,4)
 200 continue
```

Bibliography

[1] D. Ivnitski, I. Abdel-Hamid, P. Atanasov, and E. Wilkins. Review: Biosensors for detection of pathogenic bacteria. Biosensors Bioelectron., 14:599–624, 1999.

[2] Buzby, Jean C., and Tanya Roberts. "The economics of enteric infections: human foodborne disease costs." Gastroenterology 136.6 (2009): 1851-1862.

[3] Mariusz Tichoniuk, Marta Ligaj and Marian Filipiak, "Application of DNA Hybridization Biosensor as a Screening Method for the Detection of Genetically Modified Food Components", Sensors 2008, 8, 2118-2135

[4] IUPAC Compendium of Chemical Terminology 2nd Edition (1997). (1992), International Union of Pure and Applied Chemistry: Research Triangle Park, NC.

[5] Gorton, Lo, ed. Biosensors and modern biospecific analytical techniques. Vol. 44. Elsevier Science Limited, 2005.

[6] Clark, L. C. & Lyons, C. (1962). Electrode systems for continuous monitoring in cardiovascular surgery. Annals of the New York Academy of Sciences, 102, 1, 29-45.

[7] Justino, I. L. C., Rocha-Santos, A. T. & Duarte, C. A. (2010). Review of analytical figures of merit of sensors and biosensors in clinical applications. Trends in Analytical Chemistry, 29, 10, 1172—1183.

[8] Yogeswaran, U. & Chen, S. M. (2008). A review on the electrochemical sensors and biosensors composed of nanowires as sensing material. Sensors, 8, 290-313.

[9] Ghoshal, S., Mitra, D., Roy, S., & Majumder, D. D. (2010). Biosensors and biochips for nanomedical applications: A review. Sensors & Transducers Journal, 113, 2, 1-17.

[10] Martín-Palma, J. R., Manso, M. & Torres-Costa, V. (2009). Optical biosensors based on semiconductor nanostructures. Sensors, 9, 5149-5172.

[11] Vo-Dinh, T. & Cullum, B. (2000). Biosensors and biochips: advances in biological and medical diagnostics. Fresenius Journal of Analytical Chemistry, 366, 540–551.

[12] Challenges in biocatalysis for enzyme-based biofuel cells J Kim, H Jia, P Wang - Biotechnology advances, 296– 308 , 2006 – Elsevier

[13] Kim R. Rogers Molecular Biotechnology February 2000, Volume 14, Issue 2, pp 109-129 Principles of Affinity-Based Biosensors

[14] S.F. D'Souza, Nuclear Agriculture and Biotechnology Division, Bhabha Atomic Research Centre, Trombay, Mumbai 400085, India Biosensors and Bioelectronics Volume 16, Issue 6, August 2001 Elsevier, Pages 337–353

[15] Matthew A Cooper, Optical biosensors: where next and how soon, Drug Discovery Today Elsevier, Volume 11, Issues 23–24, December 2006, Pages 1061–1067

[16] T. Vo-Dinh, B. J. Tromberg, G. D. Griffin, K. R. Ambrose, M. J. Sepaniak, E. M. Gardenhire, "Antibody-based fiberoptics biosensor for the carcinogen benzo(a)pyrene", Appl. Spectrosc., vol. 41, pp. 735-738, 1987.

[17] Vo-Dinh, T.; Nolan, T.; Cheng, Y.E.; Sepaniak, M.J.; Alarie, J.P. "Phase-resolved fiberoptics fluoroimmunosensor", Appl. Spectrosc., vol. 44, pp. 128-134, 1990

[18] Smith, L. M.; Saunders, J. Z.; Kaiser, R. J.; Hughes, P.; Dodd, C. R.; Cornell, C. R.; Heiner, C.; Kent, S. B. H.; Hood, L. E. "Fluorescence Detection in Automated DNA Sequence Analysis," Nature, vol. 321, pp. 674-679, 1986

[19] Homola, J.; Yee, S. S.; Gaugliz, G. "Surface plasmon resonance sensors: review," Sens. Actuators B, vol. 54, pp. 3-15, 1999

[20] Flanagan, M. T.; Pantell, R.H. "Surface plasmon resonance and immunosensors," Electron. Lett., vol. 20, pp. 968-970, 1984

[21] Isola, N. R.; Stokes, D. L.; Vo-Dinh, T. "Surface enhanced Raman gene probe for HIV detection", Anal. Chem., vol. 70, pp. 1352-1356, 1998

[22] Vo-Dinh, T.; Stokes, D. L.; Griffin, G. D.; Volkan, M.; Kim, U. J.; Simon, M. I. "Surfaceenhanced Raman scattering (SERS) method and instrumentation for genomics and biomedical analysis", J. Raman Spectrosc. vol. 30, pp. 785-793, 1999

[23] Yotter, R. A.; Lee, L. A.; Wilson, D. M.; "Sensor technologies for monitoring metabolic activity in single cells – part II: nonoptical methods and applications", IEEE Sensors Journal, vol. 4, pp. 395-411, 2004

[24] V.M.N. Passaro, F. Dell'Olio, F. De Leonardis, "Review Electromagnetic field photonic sensors," Progress in quantum electronics, vol. 30,pp. 45-47, 2006

[25] C. Chao and L.J. Guo, "Biochemical sensors based in polymer," App. Phy. Lett., vol. 83, no. 8, 1527-1529, Aug. 2003

[26] V.M.N. Passaro, F. Dell'olio, "Guided-wave optical biosensors," Sensors, vol. 7, pp. 508-536, 2007

[27] V.M.N. Passaro, F. Dell'Olio, F. De Leonardis, "Ammonia optical sensing by microring resonators," Sensors, vol. 7, pp. 2741-2749, 2007

[28] Jae Ho Shin,Sang Yong Yoon,In Jun Yoon,Sung Hyuk Choi,Sung Dong Lee,Hakhyun Nam Sensors and Actuators B Elsevier: Chemical Volume 50, Issue 1, 15 July 1998, Pages 19–26

Potentiometric biosensors using immobilized enzyme layers mixed with hydrophilic polyurethane

[29] Joseph Wang, Amperometric biosensors for clinical and therapeutic drug monitoring: a review, Journal of Pharmaceutical and Biomedical Analysis, Elsevier, Volume 19, Issues 1–2, February 1999, Pages 47–53

[30] SV Dzydevich, AA Shuľga, AP Soldatkin, Conductometric biosensors based on cholinesterases for sensitive detection of pesticides, Journal of Electroanalysis Volume 6, Issue 9, pages 752–758, September 1994

[31] J.L.Arlett, E.B.Myers & M.L.Roukes, Comparative advantages of mechanical biosensors, Nature Nanotechnology 6,203–215 (2011)

[32] Kumaran Ramanathan, Principles and applications of thermal biosensors, Biosensors and Bioelectronics Elsevier, Volume 16, Issue 6, August 2001, Pages 417–423

[33] Matthew A Cooper (2009), Label-Free Biosensors Techniques and Applications

[34] Matthew A Cooper, Label-free screening of bio-molecular interactions, Analytical and Bioanalytical Chemistry, November 2003, Volume 377, Issue 5, pp 834-842

[35] Matthew A Cooper, Optical biosensors: where next and how soon, Drug Discovery Today Elsevier, Volume 11, Issues 23–24, December 2006, Pages 1061–1067

[36] Cooper, M.A. Non-optical screening platforms: the next wave in label-free screening?Drug Discov. Today. 2006.11(23/24): 1068-1074

[37] Matthew A Cooper (2009), Label-Free Biosensors Techniques and Applications

[38] Byungchul Jang and Arjang Hassibi, "Biosensor Systems in Standard CMOS Processes: Fact or Fiction?" IEEE TRANSACTIONS ON INDUSTRIAL ELECTRONICS, VOL. 56, NO. 4, APRIL 2009

[39] R. Thewes, C. Paulus, M. Schienle, F. Hofmann, A. Frey, R. Brederlow, P. Schindler-Bauer, M. Augustyniak, M. Atzesberger, B. Holzapfl, M. Jenkner, B. Eversmann, G. Beer, M. Fritz, T. Haneder, and H.-C. Hanke, “Integrated circuits for the biology-to-silicon interface,” in Proc. 34th Eur. Solid-State Device Res. Conf., Sep. 2004, pp. 19–28.

[40] S. D. Keighlev, P. Li, P. Estrela, and P. Migliorato, “Optimization of DNA immobilization on gold electrodes for label-free detection by electrochemical impedance spectroscopy,” Biosens. Bioelectron., vol. 23, no. 8, pp. 1291–1297, Mar. 2008.

[41] M. Bisoffi, B. Hjelle, D. C. Brown, D. W. Branch, T. L. Edwards, S. M. Brozik, V. S. Bondu-Hawkins, and R. S. Larson, “Detection of viral bioagents using a shear horizontal surface acoustic wave biosensor,” Biosens. Bioelectron., vol. 23, no. 9, pp. 1397–1403, Apr. 2008.

[42] "Label-Free Optical Biosensors: An Introduction," B.T. Cunningham, Label Free Biosensors - Techniques and Applications, edited by M. Cooper, Cambridge University Press, 2008.

[43] Xu, D-X., et al. "Label-free Evanescent Field Biosensors Using Silicon Photonics Technology." Lasers and Electro-Optics Society, 2007. LEOS 2007. The 20th Annual Meeting of the IEEE. IEEE, 2007.

[44] Homola, J., Present and future of surface plasmon resonance biosensors. Analytical and Bioanalytical Chemistry, 2003. 377(3): p. 528-539

[45] Phillips, K.S. and Q. Cheng, Recent advances in surface plasmon resonance based techniques for bioanalysis. Analytical and Bioanalytical Chemistry, 2007. 387(5): p. 1831-1840.

[46] Ferguson, J.A., T.C. Boles, C.P. Adams, and D.R. Walt, A fiber-optic DNA biosensor microarray for the analysis of gene expression. Nature Biotechnology, 1996. 14(13): p. 1681-1684.

[47] Bosch, M.E., A.J.R. Sanchez, F.S. Rojas, and C.B. Ojeda, Recent development in optical fiber biosensors. Sensors, 2007. 7(6): p. 797-859.

[48] Potyrailo, R.A., S.E. Hobbs, and G.M. Hieftje, Optical waveguide sensors in analytical chemistry: today's instrumentation, applications and trends for future development. Fresenius Journal of Analytical Chemistry, 1998. 362(4): p. 349-373.

[49] Blair, S., Chen, Y., Resonant-enhanced evanescent-wave fluorescence biosensing with cylindrical optical cavities. Applied Optics, 2001 40(4): p. 570-582.

[50] Boyd, R. W., Heebner, J. E., Sensitive Disk Resonator Photonic Biosensor. Applied Optics, 2001 40(31): p. 5742-5747.

[51] Claes, Tom, J. Girones Molera, Katrien De Vos, Etienne Schacht, Roel Baets, and Peter Bienstman. "Label-free biosensing with a slot-waveguide-based ring resonator in silicon on insulator." Photonics Journal, IEEE 1, no. 3 (2009): 197-204.

[52] Densmore, A., D.X. Xu, P. Waldron, S. Janz, P. Cheben, J. Lapointe, A. Delage, B. Lamontagne, J.H. Schmid, and E. Post, A silicon-on-insulator photonic wire based evanescent field sensor. IEEE Photonics Technology Letters, 2006. 18(21-24): p. 2520-2522.

[53] X. Fan, I. M. White, S. I. Shopova, H. Zhu, J. D. Suter, and Y. Sun, “Sensitive optical biosensors for unlabeled targets: A review,” Anal. Chim. Acta 620, 8–26 (2008).

[54] Chao, Chung-Yen, and L. Jay Guo. "Design and optimization of microring resonators in biochemical sensing applications." Journal of lightwave technology Vol 24, No. 3 (2006): 1395.

[55] Dell'Olio, Francesco, and Vittorio MN Passaro. "Optical sensing by optimized silicon slot waveguides." Opt. Express 15, no. 8 (2007): 4977-4993.

[56] I. M. White, H. Zhu, J. D. Suter, N. M. Hanumegowda, H. Oveys, M. Zourob, and X. Fan, "Refractometric sensors for lab-on-a-chip based on optical ring resonators," IEEE J. Sensors 7, 28–35 (2007).

[57] Han, Ming, and Anbo Wang. "Temperature compensation of optical microresonators using a surface layer with negative thermo-optic coefficient." Optics letters 32, no. 13 (2007): 1800-1802.

[58] Murthy, Chaitanya R., and Andrea M. Armani. "Mass Transport Effects in Suspended Waveguide Biosensors Integrated in Microfluidic Channels." Sensors 12, no. 11 (2012): 14327-14343.

[59] B. Liedberg, C. Nylander, and I. Sundstrom, "Surface plasmon resonance for gas detection and biosensing", Sensors and Actuators, vol. 4, pp. 299-304, 1983.

[60] J. van Gent, P.V. Lambeck, H.J.M. Kreuwel, G.J. Gerritsma, E.J.R. Sudholter, D.N. Reinhoudt, and T.J.A. Popma, "Optimization of a chemooptical surface plasmon resonance based sensor", Applied Optics, vol.29, pp. 2843-2849, 1990.

[61] M. A. Cooper, "Optical biosensors in drug discovery," Nat. Rev. Drug Discovery 1 (2002) 515–528.

[62] E. Stenberg, B. Persson, H. Roos, and C. Urbaniczky, "Quantitative determination of surface concentration of protein with surface plasmon resonance using radiolabeled proteins", Journal of Colloid and Interface Science, vol. 143, pp. 513-526, 1991.

[63] G. Dougherty, "A compact optoelectronic instrument with a disposable sensor based on surface plasmon resonance", Measurement Science and Technology, vol. 4, pp. 697-699, 1993.

[64] S. Ekgasit, A. Tangcharoenbumrungsuk, F. Yu, A. Baba and W. Knoll, "Resonance shifts in SPR curves of nonabsorbing, weakly absorbing, and strongly absorbing dielectrics", Sensors and Actuators B, vol. 105, pp.532-541, 2005.

[65] J.J. Chyou, C.S. Chu, F.C. Chien, C.Y. Lin, T.L. Yeh, R.C. Hsu and S.J. Chen, "Precise determination of the dielectric constant and thickness of a nanolayer by use of surface plasmon resonance sensing and multiexperiment linear data analysis", Applied Optics, vol. 45, pp. 6038-6044, 2006.

[66] H.P. Chiang, C.W. Chen, J.J. Wu, H.L. Li, T.Y. Lin, E.J. Sanchez and P.T. Leung, "Effects of temperature on the surface plasmon resonance at a metal-semiconductor interface", Thin Solid Films, vol. 515, pp. 6953-6961, 2007.

[67] J.L. Person, F. Colas, C. Compere, M. Lehaitre, M.L. Anne, C. Boussard-Pledel, B. Bureau, J.L. Adam, S. Deputier and M. Guilloux-Viry, "Surface plasmon resonance in chalcogenide glass based optical system", Sensors and Actuators B, vol. 130, pp. 771-776, 2007.

[68] W. Feng, L. Shenye, P. Xiaoshi, C. Zhuangqi and D. Yongkun, “Reflective type configuration for monitoring the photobleaching procedure based on surface plasmon resonance”, J. Opt. A: Pure Appl. Opt., vol. 10, 095102, 2008.

[69] R. C. Jorgenson and S. S. Yee, “A fiber-optic chemical sensor based on surface plasmon resonance”, Sensors and Actuators B, vol. 12, pp. 213-220, 1993.

[70] R. D. Harris and J. S. Wilkinson, “Waveguide surface plasmon resonance sensors”, Sensors and Actuators B, vol. 29, pp. 261-267, 1995.

[71] W. B. Lin, N. Jaffrezic-Renault, A. Gagnaire, and H. Gagnaire, “The effects of polarization of the incident light-modeling and analysis of a SPR multimode optical fiber sensor”, Sensors and Actuators A, vol. 84, pp. 198-204, 2000.

[72] R. Slavík, J. Homola, J. Ctyroký, and E. Brynda, “Novel spectral fiber optic sensor based on surface plasmon resonance”, Sensors and Actuators B, vol. 74, pp. 106-111, 2001.

[73] M. Piliarik, J. Homola, Z. Maníková, and J. Ctyroký, “Surface plasmon resonance sensor based on a single-mode polarization-maintaining optical fiber”, Sensors and Actuators B, vol. 90, pp. 236-242, 2003.

[74] D. J. Gentleman, L. A. Obando, J. F. Masson, J. R. Holloway, and K. Booksh, “Calibration of fiber optic based surface plasmon resonance sensors in aqueous systems”, Analytica Chimica. Acta, vol. 515, pp. 291-302, 2004.

[75] A. K. Sharma and B. D. Gupta, “Absorption-based fiber optic surface plasmon resonance sensor: a theoretical evaluation”, Sensors and Actuators B, vol. 100, pp. 423-431, 2004.

[76] M. Mitsushio, S. Higashi and M. Higo, “Construction and evaluation of a gold-deposited optical fiber sensor system for measurements of refractive indices of alcohols”, Sensors and Actuators A, vol. 111, pp. 252-259, 2004.

[77] Y. Kim, W. Peng, S. Banerji, and K. S. Booksh, "Tapered fiber optic surface plasmon resonance sensor for analyses of vapor and liquid phases", Optics Letters, vol. 30, pp. 2218-2220, 2005.

[78] A. K. Sharma and B.D. Gupta, “On the sensitivity and signal to noise ratio of a step-index fiber optic surface plasmon resonance sensor with bimetallic layers”, Optics Communications, vol. 245, pp. 159-169, 2005.

[79] B. D. Gupta and A.K. Sharma, “Sensitivity evaluation of a multi-layered surface plasmon resonance-based fiber optic sensor: A theoretical study”, Sensors and Actuators B, vol. 107, pp. 40-46, 2005.

[80] Rajan, S. Chand, and B. D. Gupta, “Fabrication and characterization of a surface plasmon resonance based fiber-optic sensor for bittering component—Naringin”, Sensors and Actuators B, vol. 115, pp. 344-348, 2006.

[81] N. Diaz-Herrera, O. Esteban, M.C. Navarrete, M.L. Haitre and A. Gonzalez-Cano, “In situ salinity measurements in seawater with a fibre-optic probe”, Meas. Sci. Technol., vol. 17, pp. 2227-2232, 2006.

[82] A.K. Sharma, Rajan Jha, and B.D. Gupta, “Fiber-optic sensors based on surface plasmon resonance: a comprehensive review”, IEEE Sensors Journal, vol. 7, pp. 1118-1129, 2007.

[83] E. Kretchmann and H. Reather, “Radiative decay of non-radiative surface plasmons excited by light”, Naturforsch, vol. 23, pp. 2135-2136, 1968.

[84] S. A. Zynio, , A. V. Samoylov, E. R. Surovtseva, V. M. Mirsky, and Y. M. Shirsov, “Bimetallic layers increase sensitivity of affinity sensors based on surface plasmon resonance”, Sensors, vol. 2, pp. 62-70, 2002.

[85] A. K. Sharma and B.D. Gupta, “On the performance of different bimetallic combinations in surface plasmon resonance based fiber optic sensors”, Journal of Applied Physics, vol. 101, pp. 093111-1-6, 2005.

[86] A. K. Sharma, Rajan and B.D. Gupta, “Influence of dopants on the performance of a fiber optic surface plasmon resonance sensor”, Optics Communications, vol. 274, pp. 320-326, 2007

[87] J. Homola and R. Slavik, “Fibre-optic sensor based on surface plasmon resonance”, Electronics Letters, vol. 32, pp. 480-482, 1996.

[88] H.Y. Lin, W.H. Tsai, Y.C. Tsao and B.C. Sheu, “Side-polished multimode fiber biosensor based on surface plasmon resonance with halogen light”, Applied Optics, vol. 46, pp. 800-806, 2007.

[89] L.Y. Cheng, T.Y. Chia, T.W. Hu, H.T. Shan, C.K. Shao and L.S. Chuan, “The enhancement method of optical fiber biosensor based on surface plasmon resonance with cold plasma modification”, Sensors and Actuators B, vol. 133, pp. 370-373, 2008.

[90] M.H. Chiu, C.H. Shih and M.H. Chi, “Optimum sensitivity of single-mode D-type optical fiber sensor in the intensity measurement”, Sensors and Actuators B, vol. 123, pp. 1120-1124, 2007.

[91] M.H. Chiu and C.H. Shih, “Searching for optimal sensitivity of single-mode D-type optical fiber sensor in the phase measurement”, Sensors and Actuators B, vol. 131, pp. 596-601, 2008.

[92] D.J. Gentleman and K.S. Booksh, “Determining salinity using a multimode fiber optic surface plasmon resonance dip-probe”, Talanta, vol. 68, pp. 504-515, 2006.

[93] H. Suzuki, M. Sugimoto, Y. Matsui and J. Kondoh, “Effects of gold film thickness on spectrum profile and sensitivity of a multimode-optical-fiber SPR sensor”, Sensors and Actuators B, vol. 132, pp. 26-33, 2008.

[94] K. Kurihara, H. Ohkawa, Y. Iwasaki, O. Niwa, T. Tobita and K. Suzuki, “Fiber-optic conical microsensors for surface plasmon resonance using chemically etched single-mode fiber”, Analytica Chimica Acta, vol. 523, pp.165-170, 2004.

[95] T. Abrahamyan and Kh. Nerkararyan, “Surface plasmon resonance on vicinity of gold-coated fiber tip”, Physics Letters A, vol. 364, pp. 494-496, 2007.

[96] A. Hassani and M. Skorobogatiy, “Design criteria for microstructured-optical-fiber-based surface-plasmon-resonance sensors”, J. Opt. Soc. Am. B, vol. 24, pp. 1423-1429, 2007.

[97] B. Gauvreau, A. Hassani, M.F. Fehri, A. Kabashin and M. Skorobogatiy, “Photonic bandgap fiber-based surface plasmon resonance sensors”, Optics Express, vol. 15, pp. 11413-11426, 2007.

[98] F. Prieto, B. Sep ´ ulveda, A. Calle, et al., “An integrated optical interferometric nanodevice based on silicon technology for biosensor applications,” Nanotechnology, vol. 14, no. 8, pp. 907–912, 2003.

[99] A. Ymeti, J. S. Kanger, R. Wijn, P. V. Lambeck, and J. Greve, “Development of a multichannel integrated interferometer immunosensor,” Sensors and Actuators B, vol. 83, no. 1–3, pp. 1–7, 2002.

[100] A. Densmore, D.-X. Xu, P. Waldron, et al., “A silicon-oninsulator photonic wire based evanescent field sensor,” IEEE Photonics Technology Letters, vol. 18, no. 23, pp. 2520–2522, 2006.

[101] C. G. Poulton, M. A. Schmidt, G. J. Pearce, G. Kakarantzas, and P.St. J. Russell, “Numerical study of guided modes in arrays of metallic nanowires,” Opt. Lett., vol. 32, pp. 1647–1649, 2007.

[102] L. Tong, L. Hu, J. Zhang, J. Qiu, Q. Yang, J. Lou, Y. Shen, J. He, and Z. Ye, “Photonic nanowires directly drawn from bulk glasses,” Opt. Exp., vol. 12, pp. 82–87, 2006.

[103] M. Law, D. J. Sirbuly, J. C. Johnson, J. Goldberger, R. J. Saykally, and P. D. Yang, “Nanoribbon waveguides for subwavelength photonics integration,” Science, vol. 305, pp. 1269–1273, 2004.

[104] C. J. Barrelet, A. B. Greytak, and C. M. Lieber, “Nanowire photonic circuit elements,” Nano Lett., vol. 4, pp. 1981–1985, 2004.

[105] P. Debackere, S. Scheerlinck, P. Bienstman, and R. Baets, “Surface plasmon interferometer in silicon-on-insulator: Novel concept for an integrated biosensor,” Opt. Exp., vol. 14, pp. 7063–7072, 2006.[106] M. A. Foster, A. C. Turner, M. Lipson, and A. L. Gaeta, “Nonlinear optics in photonic nanowires,” Opt. Exp., vol. 16, no. 2, pp. 1300–1320, 2008.

[107] L. Tong, R. R. Gattass, J. B. Ashcom, S. He, J. Lou, M. Shen, I. Maxwell, and E. Mazur, “Subwavelength diameter silica wires for low-loss optical wave guiding,” Nature, vol. 426, pp. 816–819, 2003.

[108] J. Bures and R. Ghosh, “Power density of the evanescent field in the vicinity of a tapered fiber,” J. Opt. Soc. Am. A 16, 1992-1996 (1999).

[109] L. M. Tong, J. Y. Lou, and E. Mazur, “Single-mode guiding properties of subwavelength-diameter silicaand silicon wire waveguides,” Opt. Express 12, 1025-1035 (2004)

[110] White, Ian M., and Xudong Fan. "On the performance quantification of resonant refractive index sensors." Optics Express 16.2 (2008): 1020-1028.

[111] Suter, Jonathan D., et al. "Thermal characterization of liquid core optical ring resonator sensors." Applied optics 46.3 (2007): 389-396.

[112] Armani, Andrea M., et al. "Label-free, single-molecule detection with optical microcavities." Science 317.5839 (2007): 783-787.

[113] Serpengüzel, A., S. Arnold, and G. Griffel. "Excitation of resonances of microspheres on an optical fiber." Optics Letters 20.7 (1995): 654-656.

[114] Barrios, Carlos A., María José Bañuls, Victoria González-Pedro, Kristinn B. Gylfason, Benito Sánchez, Amadeu Griol, Angel Maquieira, Hans Sohlström, Miquel Holgado, and R. Casquel. "Label-free optical biosensing with slot-waveguides." Optics letters 33, no. 7 (2008): 708-710

[115] I. M. White and X. Fan, BOn the performance quantification of resonant refractive index sensors,[Opt. Express, vol. 16, no. 2, pp. 1020–1028, Jan. 2008.

[116] V. R. Almeida, Q. Xu, C. A. Barrios, and M. Lipson, B Guiding and confining light in void nanostructures, [Opt. Lett., vol. 29, no. 11, pp. 1209–1211, Jun. 2004

[117] McCammon, J. Andrew. "Theory of biomolecular recognition." Current opinion in structural biology 8.2 (1998): 245-249.

[118] Kahn, Kalju, and Kevin W. Plaxco. "Principles of Biomolecular Recognition." Recognition Receptors in Biosensors (2010): 3-45.

[119] Choi, Martin MF. "Progress in enzyme-based biosensors using optical transducers." Microchimica Acta 148.3 (2004): 107-132.

[120] Letant, Sonia E., et al. "Enzyme immobilization on porous silicon surfaces." Advanced Materials 16.8 (2004): 689-693

[121] Kuswandi, Bambang, Roberto Andres, and Ramaier Narayanaswamy. "Optical fibre biosensors based on immobilisedenzymes." Analyst 126.8 (2001): 1469-1491

[122] Donahue, Amber C., and Maher Albitar. "Antibodies in Biosensing." Recognition Receptors in Biosensors (2010): 221-248

[123] Ginsburg, Geoffrey S., and Jeanette J. McCarthy. "Personalized medicine: revolutionizing drug discovery and patient care." TRENDS in Biotechnology 19.12 (2001): 491-496.

[124] Soper, Steven A., et al. "Point-of-care biosensor systems for cancer diagnostics/prognostics." Biosensors and Bioelectronics 21.10 (2006): 1932-1942.

[125] Eguchi, Masakatsu, and Michael Kahn. "Design, synthesis, and application of peptide secondary structure mimetics." Mini Reviews in Medicinal Chemistry 2.5 (2002): 447-462.

[126] Lam, Kit S., and Manat Renil. "From combinatorial chemistry to chemical microarray." Current opinion in chemical biology 6.3 (2002): 353-358.

[127] Sadler, Kristen, and James P. Tam. "Peptide dendrimers: applications and synthesis." Reviews in Molecular biotechnology 90.3 (2002): 195-229.

[128] Sawyer, T. K., and M. Chorev. "Peptide revolution: genomics, proteomics and therapeutics." BioTechniques 34.3 (2003): 594-599.

[129] Tothill, Ibtisam E. "Peptides as molecular receptors." Recognition Receptors in Biosensors (2010): 249-274.

[130] Welling, Gjalt W., et al. "Synthetic antibody fragment as ligand in immunoaffinity chromatography." Journal of Chromatography A 512 (1990): 337-343.

[131] MA, James S. "Unnatural amino acids in drug discovery." Chimica oggi 21.6 (2003): 65-68.

[132] Nakamura, Chikashi, et al. "Detection of porphyrin using a short peptide immobilized on a surface plasmon resonance sensor chip." Biosensors and Bioelectronics 16.9 (2001): 1095-1100.

[133] Tothill, I. E., and A. P. F. Turner. "Biosensors: New developments and opportunities in the diagnosis of livestock diseases." Proceedings Series (1998).

[134] Emili, Alia Qureshi, and Gerard Cagney. "Large-scale functional analysis using peptide or protein arrays." Nature biotechnology 18.4 (2000): 393-397.

[135] Jelinek, Raz, and Sofiya Kolusheva. "Carbohydrate biosensors." Chemical Reviews-Columbus 104.12 (2004): 5987-6016.

[136] Ju, Huangxian, Xueji Zhang, and Joseph Wang. "Carbohydrate Detection Using Nanostructured Biosensing." NanoBiosensing (2011): 393-424.

[137] Siontorou, Christina G., and Fragiskos A. Batzias. "Carbohydrate detection failure analysis via biosensoring." Instrumentation and Measurement, IEEE Transactions on 57.12 (2008): 2856-2867.

[138] de Paz, Jose L., and Peter H. Seeberger. "Recent advances in carbohydrate microarrays." QSAR & Combinatorial Science 25.11 (2006): 1027-1032.

[139] Ju, Huangxian, Xueji Zhang, and Joseph Wang. "Carbohydrate Detection Using Nanostructured Biosensing." NanoBiosensing (2011): 393-424.

[140] Hahn, Sinuhe, Susanne Mergenthaler, Bernhard Zimmermann, and Wolfgang Holzgreve. "Nucleic acid based biosensors: the desires of the user." Bioelectrochemistry 67, no. 2 (2005): 151-154.

[141] Grennan, B., N. A. O'sullivan, R. Fallon, C. Carroll, T. Smith, M. Glennon, and M. Maher. "PCR-ELISAs for the detection of Campylobacter jejuni and Campylobacter coli in poultry samples." Biotechniques 30, no. 3 (2001): 602-610

[142] Maher, Majella, Cathriona Finnegan, Evelyn Collins, Brid Ward, Cyril Carroll, and Martin Cormican. "Evaluation of culture methods and a DNA probe-based PCR assay for detection of Campylobacter species in clinical specimens of feces." Journal of clinical microbiology 41, no. 7 (2003): 2980-2986

[143] O'Connor, L., J. Joy, M. Kane, T. Smith, and M. Maher. "Rapid polymerase chain reaction/DNA probe membrane-based assay for the detection of Listeria and Listeria monocytogenes in food." Journal of Food Protection® 63, no. 3 (2000): 337-342.

[144] Pfaller, Michael A. "Molecular approaches to diagnosing and managing infectious diseases: practicality and costs." Emerging Infectious Diseases 7, no. 2 (2001): 312

[145] Su, Xiao-Li, and Yanbin Li. "A self-assembled monolayer-based piezoelectric immunosensor for rapid detection of Escherichia coli O157: H7." Biosensors and Bioelectronics 19, no. 6 (2004): 563-574

[146] Lazcka, Olivier, F. Campo, and F. Xavier Muñoz. "Pathogen detection: A perspective of traditional methods and biosensors." Biosensors and Bioelectronics 22, no. 7 (2007): 1205-1217.

147] Cooper, Matthew A. "Optical biosensors in drug discovery." Nature Reviews Drug Discovery 1, no. 7 (2002): 515-528.

[148] Homola, Jiri, ed. Surface plasmon resonance based sensors. Vol. 4. Springer, 2006.

[149] Norde, Willem. "Adsorption of proteins from solution at the solid-liquid interface." Advances in colloid and interface science 25 (1986): 267-340

[150] Dugas, Vincent, Abdelhamid Elaissari, and Yves Chevalier. "Surface Sensitization Techniques and Recognition Receptors Immobilization on Biosensors and Microarrays." Recognition Receptors in Biosensors (2010): 47-134.

[151] Frederix, Filip, Kristien Bonroy, Gunter Reekmans, Wim Laureyn, Andrew Campitelli, Mikhael A. Abramov, Wim Dehaen, and Guido Maes. "Reduced nonspecific adsorption on covalently immobilized protein surfaces using poly (ethylene oxide) containing blocking agents." Journal of biochemical and biophysical methods 58, no. 1 (2004): 67-74

[152] Zourob, Mohammed, ed. Recognition receptors in biosensors. Springer, 2010.

[153] Van Der Merwe, P. Anton. "Surface plasmon resonance." Protein–Ligand Interactions: A Practical Approach (2000): 3-50

[154] Jason-Moller, Laure, Michael Murphy, and JoAnne Bruno. "Overview of Biacore systems and their applications." Current Protocols in Protein Science (2006): 19-13.

[155] Dugas, Vincent, Abdelhamid Elaissari, and Yves Chevalier. "Surface Sensitization Techniques and Recognition Receptors Immobilization on Biosensors and Microarrays." Recognition Receptors in Biosensors (2010): 47-134.

[156] Brogan, Kathryn L., Kristie N. Wolfe, Patricia A. Jones, and Mark H. Schoenfisch. "Direct oriented immobilization of F (ab') antibody fragments on gold." Analytica chimica acta 496, no. 1 (2003): 73-80.

[157] Bagiyan, G. A., I. K. Koroleva, N. V. Soroka, and A. V. Ufimtsev. "Oxidation of thiol compounds by molecular oxygen in aqueous solutions." Russian chemical bulletin 52, no. 5 (2003): 1135-1141.

[158] Jason-Moller, Laure, Michael Murphy, and JoAnne Bruno. "Overview of Biacore systems and their applications." Current Protocols in Protein Science (2006): 19-13.

[159] Savage, D., Mattson, G., Desai, S., Nielander, G., Morgensen, S., Conklin, E., Avidin-Biotin Chemistry: A Handbook,Pierce Chemical Company, Rockford, IL 1992, pp. 1–23.

[160] Holmberg, Anders, Anna Blomstergren, Olof Nord, Morten Lukacs, Joakim Lundeberg, and Mathias Uhlén. "The biotin-streptavidin interaction can be reversibly broken using water at elevated temperatures." Electrophoresis 26, no. 3 (2005): 501-510.

[161] Knopp, Dietmar, Dianping Tang, and Reinhard Niessner. "Review: bioanalytical applications of biomolecule-functionalized nanometer-sized doped silica particles." Analytica chimica acta 647, no. 1 (2009): 14-30.

[162] Tong, Xinchun, and Lloyd Smith. "Solid-phase method for the purification of DNA sequencing reactions." Analytical chemistry 64, no. 22 (1992): 2672-2677.

[163] Turkova, Jaroslava. "Oriented immobilization of biologically active proteins as a tool for revealing protein interactions and function." Journal of Chromatography B: Biomedical Sciences and Applications 722, no. 1 (1999): 11-31.

[164] Lofas, Stefan, and Alan Mcwhirter. "The art of immobilization for SPR sensors." Surface Plasmon Resonance Based Sensors (2006): 117-151.

[165] Homola, Jiri, Sinclair S. Yee, and Günter Gauglitz. "Surface plasmon resonance sensors: review." Sensors and Actuators B: Chemical 54, no. 1 (1999): 3-15.

[166] Alves, I. D., C. K. Park, and V. J. Hruby. "Plasmon resonance methods in GPCR signaling and other membrane events." Current protein & peptide science 6, no. 4 (2005): 293.

[167] Haensch, Claudia, Stephanie Hoeppener, and Ulrich S. Schubert. "Chemical modification of self-assembled silane based monolayers by surface reactions." Chemical Society Reviews 39, no. 6 (2010): 2323-2334.

[168] Lewis, Penelope A., Rachel K. Smith, Kevin F. Kelly, Lloyd A. Bumm, Scott M. Reed, Robert S. Clegg, John D. Gunderson, James E. Hutchison, and Paul S. Weiss. "The role of buried hydrogen bonds in self-assembled mixed composition thiols on Au {111}." The Journal of Physical Chemistry B 105, no. 43 (2001): 10630-10636.

[169] Kidoaki, Satoru, and Takehisa Matsuda. "Adhesion forces of the blood plasma proteins on self-assembled monolayer surfaces of alkanethiolates with different functional groups measured by an atomic force microscope." Langmuir 15, no. 22 (1999): 7639-7646.

[170] Dugas, Vincent, Abdelhamid Elaissari, and Yves Chevalier. "Surface Sensitization Techniques and Recognition Receptors Immobilization on Biosensors and Microarrays." Recognition Receptors in Biosensors (2010): 47-134.

[171] Love, J. Christopher, Lara A. Estroff, Jennah K. Kriebel, Ralph G. Nuzzo, and George M. Whitesides. "Self-assembled monolayers of thiolates on metals as a form of nanotechnology." Chemical Reviews-Columbus 105, no. 4 (2005): 1103-1170.

[172] Schreiber, Frank. "Structure and growth of self-assembling monolayers." Progress in surface science 65, no. 5 (2000): 151-257.

[173] Vericat, C., M. E. Vela, and R. C. Salvarezza. "Self-assembled monolayers of alkanethiols on Au (111): surface structures, defects and dynamics." Phys. Chem. Chem. Phys. 7, no. 18 (2005): 3258-3268.

[174] Dowling, D. P., K. Donnelly, M. L. McConnell, R. Eloy, and M. N. Arnaud. "Deposition of anti-bacterial silver coatings on polymeric substrates." Thin Solid Films 398 (2001): 602-606.

[175] Kandimalla, Vivek Babu, Vijay Shyam Tripathi, and Huangxian Ju. "Immobilization of biomolecules in sol–gels: biological and analytical applications." Critical Reviews in Analytical Chemistry 36, no. 2 (2006): 73-106.

[176] P Chiriac, A., I. Neamtu, L. E Nita, and M. T Nistor. "Sol gel method performed for biomedical products implementation." Mini Reviews in Medicinal Chemistry 10, no. 11 (2010): 990-1013.

[177] MacCraith, Brian D., and Colette McDonagh. "Enhanced fluorescence sensing using sol-gel materials." Journal of Fluorescence 12, no. 3 (2002): 333-342.

[178] Singh, A. K., A. W. Flounders, J. V. Volponi, C. S. Ashley, K. Wally, and J. S. Schoeniger. "Development of sensors for direct detection of organophosphates. Part I: immobilization, characterization and stabilization of acetylcholinesterase and organophosphate hydrolase on silica supports." Biosensors and Bioelectronics 14, no. 8 (1999): 703-713.

[179] Jeronimo, Paula CA, Alberto N. Araujo, and M. Conceicao BSM Montenegro. "Optical sensors and biosensors based on sol–gel films." Talanta 72, no. 1 (2007): 13-27.

[180] E. J Marcatili, “Dielectric rectangular waveguide and directional coupler for integrated optics,” Bell Syst. Tech. J., vol. 48, no. 21, pp. 2071–2102,1969.

[181] R. Knox and P. P. Toulios, “Proceedings of MRI symposium on submillimeter waves,” J. Fox Ed., New York: Brooklyn Polytechnic Press, 1970.

[182] H. Shigesawa and M. Tsuji, “A new equivalent network method for ana- lyzing discontinuity properties of open dielectric waveguides,” IEEE Trans. Microwave Theory Tech., vol. 37, no. 1, pp. 3–14, 1989.

[183] M. Koshiba, Optical Waveguide Analysis. New York: McGraw-Hill, 1992.

[184] M. Koshiba, Analysis Methods for Electromagnetic Wave Problems. Lon- don: Artech House, 1990.

[185] I. Goyal, R. Gallawa, and A. Ghatak, “Improved variational analysis of in- homogeneous optical waveguides using airy functions,” J. Lightwave Tech- nol., vol. 11, no. 10, pp. 1575–1578, 1993.

[186] A. Wexler, “Computation of electromagnetic fields,” IEEE Trans. Mi- crowave Theory Tech., vol. 17, no. 8, pp. 416–439, 1969.

[187] M. Feit, J. Fleck Jr., “Computation of mode properties in optical fiber waveguides by a propagating beam method,” Appl. Opt., vol. 19, no. 7, pp. 1154–1164, 1980.

[188] H. Nolting and R. Marz, “Results of benchmark tests for different numerical BPM algorithms,” J. Lightwave Technol., vol. 13, no. 2, pp. 216–224, 1995.

[189] K. Chiang, “Review of numerical and approximate methods for the modal analysis of general optical dielectric waveguides,” Opt. Quantum Electron., vol. 26, no. 3, pp. 113–134, 1994.

[190] D. Yevick and B. Hermansson, “New formulations of the matrix beam prop- agation method: application to rib waveguides,” IEEE J. Quantum Electron., vol. 25, no. 2, pp. 221–229, 1989.

[191] P. Buah, B.M.A Rahman, and K.T.V Grattan, “Numerical study of soliton switching in active three-core nonlinear fiber couplers,” IEEE J. Quantum Electron., vol. 33, no. 5, pp. 874–878, 1997.

[192] J. B. Davies, Numerical Techniques for Microwave and millimeter-wave passive structures, T. Itoh Ed. New York: Wiley, 1989.

[193] J. M. Jin, The finite element method in electromagnetics. New York: Wiley,1993.

[194] R. Mearz, Integrated optics: design and modeling. London: Artech House,1995.

[195] N. Mabaya, P. Lagasse, and P. Vandenbulcke, “Finite element analysis waveguides of optical,” IEEE Trans. Microwave Theory Tech., vol. 29, no. 6, pp. 600–605, 1981.

[196] P. Daly, “Finite element approach to propagation in elliptical and parabolic waveguides,” Int. J. Numer. Methods Eng., vol. 20, no. 4, pp. 681–688, 1984.

[197] R. Wu and C. Chen, “A scalar variational conformal mapping technique for weakly guiding dielectric waveguides,” IEEE J. Quantum Electron., vol. 22, no. 5, pp. 603–609, 1986.

[198] M. Koshiba, K. Hayata, and M. Suzuki, “Approximate scalar finite-element analysis of anisotropic optical waveguides with off-diagonal elements in a permittivity tensor,” IEEE Trans. Microwave Theory Tech., vol. 32, no. 6, pp. 587–593, 1984.

[199] Z. Csendes and P. Silvester, “Numerical solution of dielectric loaded waveguides: I-finite-element analysis,” IEEE Trans. Microwave Theory Tech., vol. 18, no. 12, pp. 1124–1131, 1970.

[200] W. English and F. Young, “An E vector variational formulation of the maxwell equations for cylindrical waveguide problems,” IEEE Trans. Mi- crowave Theory Tech., vol. 19, no. 1, pp. 40–46, 1971.

[201] M. Hano, “Finite-element analysis of dielectric-loaded waveguides,” IEEE Trans. Microwave Theory Tech., vol. 32, no. 10, pp. 1275–1279, 1984.

[202] M. Koshiba, K. Hayata, and M. Suzuki, “Finite-element formulation in terms of the electric-field vector for electromagnetic waveguide problems,”IEEE Trans. Microwave Theory Tech., vol. 33, no. 10, pp. 900–905, 1985.

[203] A. Berk, “Variational principles for electromagnetic resonators and waveguides,” IRE Trans. Anntenas Propag., vol. 4, no. 2, pp. 104–111, 1956.

[204] B.M.A Rahman and J.B. Davies, “Finite-element analysis of optical and microwave waveguide problems,” IEEE Trans. Microwave Theory Tech., vol. 32, no. 1, pp. 20–28, 1984.

[205] A. Konrad, “High-order triangular finite elements for electromagnetic waves in anisotropic media,” IEEE Trans. Microwave Theory Tech., vol. 25, no. 5, pp. 353–360, 1977.

[206] M. Koshiba, K. Hayata, and M. Suzuki, “Improved finite-element formula- tion in terms of the magnetic field vector for dielectric waveguides,” IEEE Trans. Microwave Theory Tech., vol. 33, no. 3, pp. 227–233, 1985.

[207] B.M.A Rahman and J. Davies, “Penalty function improvement of waveguide solution by finite elements,” IEEE Trans. Microwave Theory Tech., vol. 32, no. 8, pp. 922–928, 1984.

[208] Su X and Zhang J, “Comparison of surface plasmon resonance spectroscopy and quartz crystal microbalance for human IgE quantification”, Sens. Actuators B100, 311-316, 2004.

[209] Osmond R I W, Kett W C, Skett S E, and Coombe E R, “Protein heparin interactions measured by BIAcore 2000 are affected by the method of heparin immobilization”, Anal.Biochem. 301, 00 199-207, 2002.

[210] Nath N, Chilkoti A, “Label-free biosensing by surface plasmon of nanoparticles on glass: optimization of nanoparticles size”, Anal. Chem 76, pp. 5370-5378, 2004.

[211] Buchanan, R, L., & Doyle, M. P. (1997). Foodborne disease significance of Escherichia coli and other enterohemorrhagic E. coli. Food Technology, 51, 69-76.

[212] Gannon V P, Rashed M, King R K, and Thomas E J, "Detection and characterization of the eae gene of Shiga-like toxin-producing Escherichia coli using polymerase chain reaction," Vol. 31, no. 5, pp. 1268-1274, 1993

[213] Padhye N V and Doyle M P, "Escherichia coli Q157:H7: epidemiology, pathogenesis and methods for detection in food" Journal of food protections, Vol. 55, no. 7, pp. 555-565, 1992.

[214] DeMarco D R, Saaski E W, McCrae D A and Lim D V, "Rapid detection ofEscherichia coli O157:H7 in ground beef using a fibre-optic biosensor, Journal of food protection, Vol. 62, no. 7, pp. 711-716, 1999.

[215] Rand G A, Ye J, Brown C W, and Letcher S V, "Optical biosensors for food pathogen detection". Food Technology, Vol 56, no. 3, pp. 32-37, 2002.

[216] Kai E, Ikebukuro K, Hoshina S, Watanabe H and Karube I, "Detection of PCR products of Escherichia coli O157:H7 in human stool samples using surface plasmon resonance (SPR)", FEMS Immunology & Medical Microbiology, Vol. 29, no.4, pp. 283-288, 2000.

[217] Byung-Keun O H, Young-Kee K, Min Bae Y, Hong Lee W, and Jeong-Woo C, "Detection of E.coli O157:H7 using immunosensor based on surface plasmon resonance," Journal of microbiology and biotechnology, Vol. 12, no. 5, pp 780-786,2002.

[218] Zervas M N, Surface plasmon-polariton waves guided by thin metal films," Opt. Lett.Vol 16, pp. 720-722, 1991.

[219] Foster M W, Ferrel D J, and Lieberman R A, "Surface plasmon resonance biosensor miniaturization", Proc. SPIE 2293, pp. 122-131, 1994.

[220] Homola J and Slavik R, "Fibre-optic sensor based on surface plasmon resonance", Electron. Lett. Vol. 32, pp. 480-482, 1996.

[221] Swaminathan A, Irudayaraj J, and Ryan T "Self-assembled monolayer-based surface plasmon immunosensor for detection of E. coli O157:H7". Biosensors and Bioelec. Vol 21, No 7, pp 998-1006, 2005.

[222] Yu C, Ganjoo A, Jain H, Pantano C, and Irudayaraj J, "Towards a mid-IR biosensor: Detection and fingerprinting of pathogens on chalcogenide films" Analytical Chem. Vol. 78, No. 8, pp. 2500-2506, 2005.

[223] Ctyroky J, Homola J, and Skalsky M, "Modelling of surface plasmon resonance waveguide sensor by complex mode expansion and propagation method," Opt. Quantum Electron., Vol. 29, pp. 301-311, 1997.

[224] Reisinger A, "Charactersitics of optical guided modes in lossy waveguides," Appl. Opt, Vol 12, pp. 1015-1025, 1973.

225] Rahman B M A and Davies J B, “Finite-element solution integrated optical waveguides,” J Lightwave Technology, Vol.2, pp. 682-688, 1984.

[226] Esteban O, Alonso R, Navarrete C, and Gonzalez-Cano A “Surface plasmon excitation in fiber-optics sensors: a novel theoretical approach,” J Lightwave Technology Volume 20, Issue 3, Mar 2002 Page(s): 448 - 453

[227] Brun, Caroline, and Caroline Hagege. "Normalization and paraphrasing using symbolic methods." In Proceedings of the second international workshop on Paraphrasing-Volume 16, pp. 41-48. Association for Computational Linguistics, 2003.

[228] Laffel, Lori. "Ketone bodies: a review of physiology, pathophysiology and application of monitoring to diabetes." Diabetes/metabolism research and reviews 15, no. 6 (2000): 412-426.

[229] C. G. Poulton, M. A. Schmidt, G. J. Pearce, G. Kakarantzas, and P. St. J. Russell, “Numerical study of guided modes in arrays of metallic nanowires,” Opt. Lett., vol. 32, pp. 1647–1649, 2007.

[230] L. Tong, L. Hu, J. Zhang, J. Qiu, Q. Yang, J. Lou, Y. Shen, J. He, and Z.Ye, “Photonic nanowires directly drawn from bulk glasses,” Opt. Exp., vol. 12, pp. 82–87, 2006.

[231] M. Law, D. J. Sirbuly, J. C. Johnson, J. Goldberger, R. J. Saykally, and P. D. Yang, “Nanoribbon waveguides for subwavelength photonics integration,” Science, vol. 305, pp. 1269–1273, 2004.

[232] C. J. Barrelet, A. B. Greytak, and C. M. Lieber, “Nanowire photonic circuit elements,” Nano Lett., vol. 4, pp. 1981–1985, 2004.

[233] P. Debackere, S. Scheerlinck, P. Bienstman, and R. Baets, “Surface plasmon interferometer in silicon-on-insulator: Novel concept for an integrated biosensor,” Opt. Exp., vol. 14, pp. 7063–7072, 2006.

[234] M. A. Foster, A. C. Turner, M. Lipson, and A. L. Gaeta, “Nonlinear optics in photonic nanowires,” Opt. Exp., vol. 16, no. 2, pp. 1300–1320, 2008.

[235] L. Tong, R. R. Gattass, J. B. Ashcom, S. He, J. Lou, M. Shen, I.Maxwell, and E. Mazur, “Subwavelength diameter silica wires for low-loss optical wave guiding,” Nature, vol. 426, pp. 816–819, 2003.

[236] B. M. A. Rahman and J. B. Davies, “Finite-element solution of inte- grated optical waveguides,” J. Lightw. Technol., vol. LT-2, no. 5, pp. 682–688, Oct. 1984.

[237] B. J. Luff, J. S. Wilkinson, J. Piehler, U. Hollenbach, J. Ingenhoff, and N. Fabricius, “Integrated optical Mach–Zehnder biosensor,” J. Lightw. Technol., vol. 16, no. 4, pp. 583–592, Apr. 1998.

[238] J. Lou, L. Tong, and Z. Ye, “Modeling of silica nanowires for optical sensing,” Opt. Exp., vol. 13, no. 6, pp. 2135–2140, 2005.

[239] J. Bures and R. Ghosh, “Power density of the evanescent field in the vicinity of a tapered fiber,” J. Opt.Soc. Am. A 16, 1992-1996 (1999).

[240] L. M. Tong, J. Y. Lou, and E. Mazur, “Single-mode guiding properties of subwavelength-diameter silica and silicon wire waveguides,” Opt. Express 12, 1025-1035 (2004)

[241] Ren, Hai-Cang, Frank Vollmer, Stephen Arnold, and Albert Libchaber. "High-Q microsphere biosensor-analysis for adsorption of rodlike bacteria." Optics express 15, no. 25, 17410-17423, 2007

[242] P. Klocek, Handbook of Infrared Optical Materials. New York: Marcel Dekker, 1991.

[243] P. Schiebener, J. Straub, J. M. H. Levelt Sengers, and J. S. Gallagher, “Refractive index of water and steam as function of wavelength, temperature and density,” J. Phys. Chem. Ref. Data, vol. 19, pp. 677–717, 1990.

[244] Francesco Dell’Olio and Vittorio M. N. Passaro, “Optical sensing by optimized silicon slot waveguides”, Opt.Express, Vol. 15, No. 8, Apr 2007.

[245] Vittorio M. N. Passaro , Francesco Dell'Olio, Caterina Ciminelli and Mario N. Armenise, "Efficient Chemical Sensing by Coupled Slot SOI Waveguides",Sensors and Actuators B: Chemical Volume 150, Issue 1, 21 September 2010, pp 417-424

[246] Francesco Dell’Olio and Vittorio M. N. Passaro, “Optical sensing by optimized silicon slot waveguides”, Opt.Express, Vol. 15, No. 8, Apr 2007.

[247] Kirankumar R. Hiremath, "Analytical modal analysis of bent slot waveguides," J. Opt. Soc. Am. A 26, 2321-2326 (2009)

[248] B. M. A. Rahman, and J. B. Davies, “Finite element solution of integrated optical waveguides,” J. Lightwave Technol. 2(5), 682–688 (1984).

[249] Michelle Duval Malinsky, K. Lance Kelly, George C. Schatz, and Richard P. Van Duyne, "Chain Length Dependence and Sensing Capabilities of the Localized Surface Plasmon Resonance of Silver Nanoparticles Chemically Modified with Alkanethiol Self-Assembled Monolayers",J. Am. Chem. Soc., 2001, 123 (7), pp 1471–1482

[250] Xiaohui Li, Ziyang Zhang, Shenying Qin, Tao Wang, Fangfei Liu, Min Qiu, and Yikai Su, "Sensitive label-free and compact biosensor based on concentric silicon-on-insulator microring resonators", Applied Optics, Vol. 48, Issue 25, pp. F90-F94 (2009)

[251] Vittorio M. N. Passaro , Francesco Dell'Olio, Caterina Ciminelli and Mario N. Armenise, "Efficient Chemical Sensing by Coupled Slot SOI Waveguides",Sensors and Actuators B: Chemical Volume 150, Issue 1, 21 September 2010, pp 417-424

[252] T. Claes, J. G. Molera, K. De Vos, E. Schacht, R. Baets, P. Bienstman, "Label-Free Biosensing with a slot waveguide based ring resonator in Silicon on Insulator", IEEE Photonics Journal, Vol. 1, No. 3, pp. 197-204

[253] Carlos A. Barrios, Maria Jose Banuls, Victoria Gonzalez-Pedro, Kristinn B. Gylfason,Benito Sanchez, Amadeu Griol, A. Maquieira, H. Sohlstrom, M. Holgado, and R.

Casquel, “Label-free optical biosensing with slot-waveguides”, Optics Letters, Vol. 33, Issue 7, pp. 708-710

[254] C.Koos,P.Vorreau,T.Vallaitis,P.Dumon,W.Bogaerts,R.Baets,B.Esembeson,I.Biaggio,T.Michinobu, F.Diederich, W. Freude, and J. Leuthold, “All-optical high-speed signal processing with silicon-organic hybrid slot waveguides” , Nat. Photon., vol. 3, no. 4, pp. 216–219, Apr. 2009.

[255] K. Palmer and D. Williams, “Optical properties of water in the near infrared”, J. Opt. Soc. Amer., vol. 64, no. 8, pp. 1107–1110, Aug. 1974.

[256] Xudong Fan ,Ian M. White, Siyka I. Shopova, Hongying Zhu, Jonathan D. Suter, Yuze Sun, "Sensitive optical biosensors for unlabeled targets: A review", Analytica Chimica Acta, Volume 620, Issues 1-2, 14 July 2008, Pages 8-26

[257] C. F. Carlborg, K. B. Gylfason, A. Kazmierczak, F. Dortu, M. J. Banuls Polo, A. Maquieira Catala, G. M. Kresbach, H. Sohlstrom, T. Moh, L. Vivien, J. Popplewell, G. Ronan, C. A. Barrios, G. Stemme and W. van der Wijngaart, "A packaged optical slot-waveguide ring resonator sensor array for multiplex label-free assays in labs-on-chips", Lab Chip, 2010, 10, 281-290

[258] Peng, G.; Tisch, U.; Haick, H. Detection of nonpolar molecules by means of carrier scattering in random networks of carbon nanotubes: toward diagnosis of diseases via breath samples. Nano Lett. 2009, 9, 1362-1368.

[259] Hahm, J.; Lieber, C. Direct ultrasensitive electrical detection of DNA and DNA sequence variations using nanowire nanosensors. Nano Lett. 2004, 4, 51-54.

[260] Patolsky, F.; Zheng, G.; Hayden, O.; Lakadamyali, M.; Zhuang, X.; Lieber, C. Electrical detection of single viruses. Proc. Natl. Acad. Sci. USA 2004, 101, 14017-14022.

[261] Zheng, G.; Patolsky, F.; Cui, Y.; Wang, W.; Lieber, C. Multiplexed electrical detection of cancer markers with nanowire sensor arrays. Nat. Biotechnol. 2005, 23, 1294-1301.

[262] Li, C.; Curreli, M.; Lin, H.; Lei, B.; Ishikawa, F.; Datar, R.; Cote, R.; Thompson, M.; Zhou, C.Complementary detection of prostate-specific antigen using In2O3 nanowires and carbon nanotubes. J. Am. Chem. Soc. 2005, 127, 12484-12485.

[263] Cusmà, A.; Curulli, A.; Zane, D.; Kaciulis, S.; Padeletti, G. Feasibility of enzyme biosensors based on gold nanowires. Mater. Sci. Eng.: C 2007, 27, 1158-1161.

[264] Basu, M.; Seggerson, S.; Henshaw, J.; Jiang, J.; del A Cordona, R.; Lefave, C.; Boyle, P.; Miller, A.; Pugia, M.; Basu, S. Nano-biosensor development for bacterial detection during human kidney infection: Use of glycoconjugate-specific antibody-bound gold nanowire arrays (GNWA).Glycoconj. J. 2004, 21, 487-496.

[265] Fan, Y.; Chen, X.; Trigg, A.; Tung, C.; Kong, J.; Gao, Z. Detection of microRNAs using target- guided formation of conducting polymer nanowires in nanogaps. J. Am. Chem. Soc. 2007,129, 5437-5443.